100 YEARS
ASTM
A PROVEN PARTNERSHIP

EFFECTS OF PRODUCT QUALITY AND DESIGN CRITERIA ON STRUCTURAL INTEGRITY

RICHARD C. RICE
DOUGLAS E. TRITSCH
EDITORS

STP 1337

STP 1337

Effects of Product Quality and Design Criteria on Structural Integrity

R. C. Rice and D. E. Tritsch, Editors

ASTM Stock #: STP1337

ASTM
100 Barr Harbor Drive
West Conshohocken, PA 19428-2959

Printed in the U.S.A.

Library of Congress Cataloging-in-Publication Data

Effects of product quality and design criteria on structural integrity / R.C. Rice and D.E. Tritsch, editors.

(STP: 1337) "ASTM Stock Number: STP1337."

Proceedings of the Symposium on Effects of Product Quality and Design on Structural Integrity, held May 5, 1997, in St. Louis, Mo., sponsored by ASTM Committee E8 on Fatigue and Fracture.

Includes bibliographical references and index.

ISBN 0-8031-2485-6

1. Materials - Fatigue - Congresses. 2. Structural stability - Congresses. 3. Structural design - Congresses. I. Rice, Richard C. II. Tritsch, D.E. (Douglas E.), 1957- . III. ASTM Committee E-8 on Fatigue and Fracture. IV. Symposium on Effects of Product Quality and Design on Structural Integrity (1997: Saint Louis, Mo.) V. Series: ASTM special technical publication: 1337.

TA409.E34 1998

624.1'7 - dc21 98-45739

CIP

Peer Review Policy

Each paper published in this volume was evaluated by two peer reviewers and at least one editor. The authors addressed all of the reviewers' comments to the satisfaction of both the technical editor(s) and the ASTM Committee on Publications.

To make technical information available as quickly as possible, the peer-reviewed papers in this publication were prepared "camera-ready" as submitted by the authors.

The quality of the papers in this publication reflects not only the obvious efforts of the authors and the technical editor(s), but also the work of these peer reviewers. The ASTM Committee on Publications acknowledges with appreciation their dedication and contribution of time and effort on behalf of ASTM.

Printed in Scranton, PA
November 1998

Foreword

The Symposium on Effects of Product Quality and Design on Structural Integrity was held 5 May, 1997 in St. Louis, MO. The symposium was sponsored by ASTM Committee E8 on Fatigue and Fracture. Richard C. Rice, with Battelle Columbus Laboratories in Columbus, OH, and Douglas E. Tritsch, with the University of Dayton Research Institute in Dayton, OH, served as cochairmen of the symposium and are editors of this publication.

This symposium was originally planned as two independent symposia, titled "The Design Criteria to Assure Structural Integrity" and "The Effects of Product Quality on Structural Durability." The ultimate decision to merge these two symposia was based on their shared emphasis on enhancing the service life of structures. Therefore, the two symposia were consolidated into a one-day symposium with the above name.

Contents

Overview

This special technical publication (STP) includes papers submitted and accepted from the Symposium on the Effects of Product Quality and Design Criteria on Structural Integrity, which was held in St. Louis at the Regal Riverfront Hotel on 5 May, 1997. The first half of the symposium focused on the benefits to be gained (in terms of reduced life-cycle costs and increased performance) from improvements in the initial quality of engineering materials, components, and structures. Today's fatigue-critical structures are being designed closer to design limits than ever before. Small initial flaws or defects in these structures may go undetected in routine nondestructive inspections, and yet they may substantially reduce safe operating lifetimes. Initial quality improvement represents an attractive means for minimizing the high costs associated with nuisance in-service fatigue cracking problems and increasing the reliability of these components within their normal operating envelope.

The first six papers included in this STP address different aspects of product quality as it relates to structural integrity. The paper by Bhansali, et al., shows the influence that changes in production processing had on the susceptibility to corrosion damage and loss in fatigue strength of a laminated high-strength stainless steel assembly. The next paper, by Nikbin, addresses the challenge of achieving structural integrity in high-temperature applications using fracture mechanics methodologies, and in this instance at least, shows the primary sources of variability in crack growth rates to be due to fabrication methods, testing practices, and basic material creep properties. The paper by Rice and Deschapelles describes the marked improvements in fatigue resistance of 7050 thick plate that were achieved through reductions in mid-plane microporosity. The article by Stephens, et al., addresses another quality issue, specifically the influence of density and porosity size and shape on the fatigue properties of a high-strength powder metallurgy steel. Tipton's paper focuses on the complexities of assessing the low-cycle fatigue quality of a coiled tubing product. And finally, the paper by Champagne includes a graphic description of performance problems that can occur in a nickel base fastener system and provides practical guidance on steps that can be taken to alleviate these quality problems.

The last five papers in this STP address the influence of design criteria on structural integrity. The paper by Duffy describes an investigation of the effects of changes in plating and shot peening design criteria on the fatigue properties of 4340 steel plate. The next paper, by Petrou and Perdikaris, examines the influence of design criteria on the fatigue behavior of scale-model reinforced concrete bridge decks subjected to moving loads. The paper by Sémète, et al., describes a fracture mechanics analysis that was completed on cast duplex stainless steel elbows containing surface cracks of varying depth. The article by Watanabe describes some of the design criteria and analysis procedures that have been used to develop and maintain reliable commercial transport aircraft. And finally, the paper by Wiesner and Scheumann addresses the design criteria currently used with low-temperature storage tanks to ensure crack arrest and avoid brittle failure.

The editor would like to thank the authors, referees, symposium session chairpersons, the organizing committee, and the ASTM staff for making this publication possible. The organizing committee included R. C. Rice, Battelle, cochairperson; D. Tritsch, University of Dayton Research Institute; cochairperson; E. Tuegel, APES; and A. Fatemi, University of Toledo.

Richard C. Rice

Engineering Mechanics,
Battelle,
Columbus, Ohio 43201-2693

Kirit J. Bhansali,[1] Gang Liu,[2] Scott M. Grendahl,[3] Victor K. Champagne,[3] and Marc S. Pepi[3]

EFFECT OF INTERGRANULAR SURFACE ATTACK ON THE FATIGUE AND CORROSION PROPERTIES OF AM-355 CRT MATERIAL

REFERENCE: Bhansali, K. J., Liu, G., Grendahl, S. M., Champagne, V. K., and Pepi, M. S., **"Effect of Intergranular Surface Attack on the Fatigue and Corrosion Properties of AM-355 CRT Material,"** *Effects of Product Quality and Design Criteria on Structural Integrity, ASTM STP 1337,* R. C. Rice and D. E. Tritsch, Eds., American Society for Testing and Materials, 1998.

ABSTRACT: A dynamic part, consisting of a stack of laminates, failed in the field after an unexpectedly short life. Failure analysis showed that a multitude of fatigue cracks originated from a combination of corrosion and fretting. Recent changes in the production process of the laminates resulted in the presence of an intergranular (IG) morphology on the surface. Due to the criticality of this part's application, a better understanding of the influence of varying degrees of IG attack on fatigue properties was pursued. Coupon specimens were machined from actual components with different surface IG conditions and were subjected to fatigue testing. Results showed a direct relationship between the number of cycles to failure and the severity of surface IG attack. Potentiodynamic polarization measurements indicated that a sample with IG attack had a lower breakdown potential and an unstable passivation behavior as compared to that without an IG attack. The detrimental effects of surface IG attack on the crack initiation process, endurance limit and corrosion resistance is discussed in terms of the stress concentration and breakdown of the passivation layer.

KEYWORDS: AM-355, fatigue, fretting, corrosion, corrosion potential, passivation

Introduction

The precipitation hardenable stainless steel, AM-355, has been considered a good candidate for aerospace structural applications because of its high strength, good corrosion and oxidation resistance, and excellent formability [1-6]. AM-355 alloys, produced by the Allegheny Ludlum Steel Corp. (Pittsburgh, PA), can be fabricated into

[1] U. S. Army Aviation Troop Command, St. Louis, Missouri 63120
[2] Westar Corporation, St. Louis, Missouri 63044
[3] U.S. Army Research Laboratory, Aberdeen Proving Ground, Maryland 21005

different product forms and heat-treated to various microstructures to meet a relatively wide range of mechanical property requirements [2]. The main rotor strap pack of an Army helicopter is assembled from a stack of 0.014 inch (0.36 mm) thick laminates made from AM-355 material in the cold rolled and tempered (CRT) condition. The strap pack is used to transfer loads between the main rotor hub and the blade and as such is subjected to very severe fatigue loads. A schematic of the helicopter main rotor hub assembly depicting the location and loading of the strap pack is shown in Fig. 1.

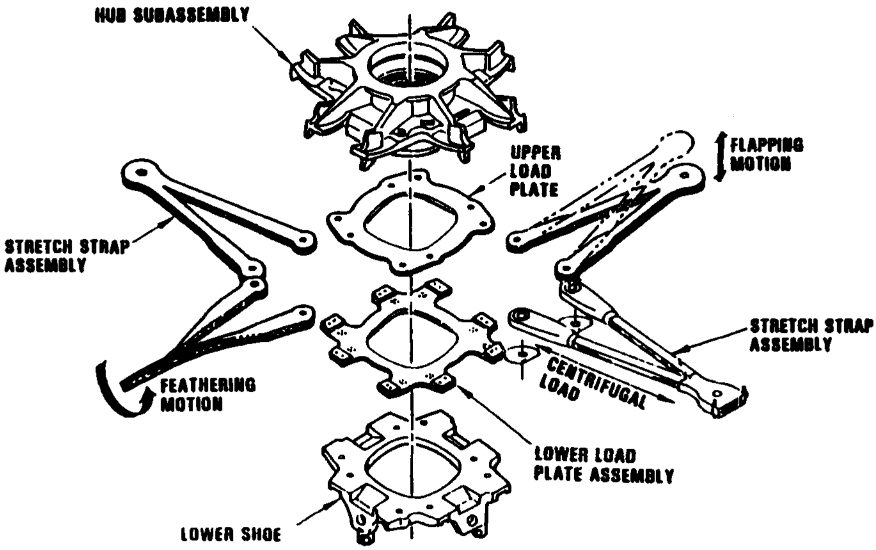

Figure 1. Schematic of the main rotor hub assembly showing strap pack location and loading conditions.

Although AM-355 CRT material would be expected to have excellent fatigue strength and good corrosion-resistance [1-4], many strap laminates in-service were found to be susceptible to corrosion/fatigue damage and failed at a significantly lower life than their original design. Failure analysis showed that crack initiation was predominantly at corrosion pits which contained some residual elements (Cl, S, Na, K, etc.) and/or foreign particles (Al_2O_3, SiO_2) [7, 8]. Recent analyses revealed that some laminates displayed severe IG networks on the surface and these particles tend to lodge within the IG grooves [8].

Surface IG morphology on AM-355 CRT strap laminates was the result of a prior pickling operation performed during primary processing of the material. The severity of the IG attack is not known on the original qualified part because the IG morphology was not visible at the time of production with a 40x optical lens or detectable by normal non-destructive inspections. Further, the final surface finishing process utilized on the qualified part may have removed the IG surface morphology through the utilization of an automated Super Sanding machine. Recently, a hand finishing operation utilizing Scotch Brite pads replaced the Super Sanding machine in the production line and some surface anomalies were noticed during visual inspection. These anomalies were most likely caused by entrapped particles within the IG network on the surface that fretted during subsequent strap laminate assembly packing [8]. Based on these facts, a question was raised if the fatigue/corrosion problems in the field with the AM-355 CRT material could be attributed to the surface IG attack.

The purpose of this investigation was to examine the role of the surface IG attack on the fatigue and corrosion properties of AM-355 CRT strap material. Selected laminates with varying degrees of IG attack were fatigue tested to evaluate their endurance limits. The samples with IG and without IG (polished) were subjected to potentiodynamic polarization measurement to evaluate the pitting corrosion resistance and passivation behavior. It was shown that the surface IG attack reduced the fatigue strength and pitting corrosion resistance of AM-355 CRT strap material.

Material and Experimental Procedures

Material used in this study was AM-355 CRT material taken from the actual strap pack assembly laminates. The detailed composition of AM-355 material was published in reference [6]. The test specimens were carefully selected from the laminates with varying degrees of the IG attack, categorized as heavy IG attack, moderate IG attack, and light IG attack as listed in Table 1. Dog-bone shaped specimens were machined from the laminate legs in the longitudinal direction as specified in the engineering test requirement. Fig. 2 depicts the area of the laminates from where the specimens were taken.

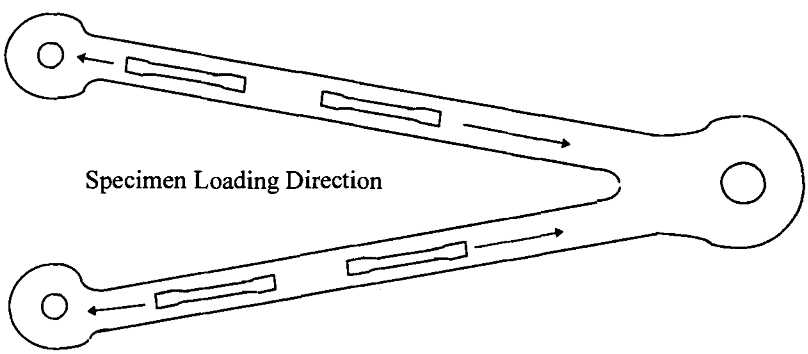

Figure 2. Schematic of a strap pack laminate showing the area where dog bone specimens were obtained.

Each sample with a gage length of 2.5 inches (6.35 cm) was fabricated with the same processing and tooling in order to minimize the effects of machining. The specimens were edge broke with 800 grit emery cloth. The dimensions of each sample were precisely measured by a Mitutoyo Mikematic 100E Micrometer. The tensile and axial fatigue tests were carried out on an Instron 8502 servohydraulic machine under ambient conditions (25°C, 50% relative humidity). The tensile testing was performed with a strain rate of 0.05 in/min (0.127 cm/min). The fatigue testing was performed with a sinusoidal frequency of 25 Hz at a load ratio (P_{min}/P_{max}) of 0.05. Each fatigue test was systematically stopped upon breaking or when a total of 3 million cycles was reached. Subsequently, the cyclic stress amplitude was plotted against the number of loading cycles. The fracture surfaces of the fatigue specimens were examined in detail using a Jeol JSM-840 scanning electron microscope (SEM), operated at 15 kV, to characterize and examine the crack path morphology, crack initiation, crack propagation and failure mode.

Potentiodynamic polarization measurements were performed on samples, exposing 1 cm^2 to the deaerated 3.56 wt% NaCl solution, in accordance with the ASTM Standard G 61. The samples with moderate IG and without IG attack (polished) were tested in order to get the anodic polarization curves to evaluate the passivation behavior and localized pitting corrosion resistance. All samples were taken from the same strap laminate in order to eliminate the effects of material and processing. The IG attack on the surface was removed by grinding with dry 400-grit and polishing with dry 600-grit SiC paper. Finally, the samples were ultrasonically degreased in acetone and immediately rinsed with methanol and dried prior to exposing to the deaerated 3.56 wt.% NaCl solution.

Results

A set of optical micrographs depicting different IG attacks (light, moderate, and heavy) on the surface are shown in Fig. 3. The light IG condition is the normal surface condition of the laminates. As shown in Fig. 3 the sample designated as light IG attack did not display any grain boundary network on the surface. A very light etched morphology, mainly located at the triple point of grain boundaries, was evident. In contrast, for the heavy IG attack sample the grain boundary network was clearly visible and completely covered the surface. In some areas, the surface IG attack was so heavy that a few small grains, surrounded by large grains, were almost etched away. The average depth of the IG attack on the surface was measured by a high resolution optical microscope and the results are listed in Table 1. The increase in the severity of surface IG attack was accompanied with increasing depth/density of the IG network on the surface. It should be noted that the IG attack varied in depth, depending on the size, shape and the number of grains in the area. As shown in Table 1, the heavy surface IG condition had a much deeper surface attack than the others. The maximum of 250 μinch (6.35 μm) in-depth on both sides in the heavy IG condition is approximately equivalent to 3.6 % of the total cross-section thickness (0.014 inches, 0.36 mm) of the strap laminate.

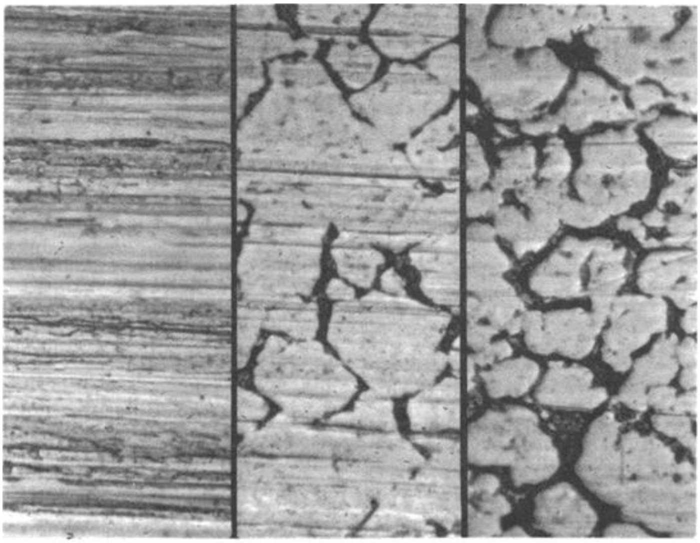

A B C

Figure 3 - Optical micrographs showing the surface morphology in a) light IG, b) moderate IG, and c) heavy IG conditions. Mag. 1000x.

TABLE 1--Average Depth of the Different IG Attacks on the Surface

Condition	Light IG Attack	Moderate IG Attack	Heavy IG Attack
Average Depth, μinch (μm)	0 ~ 75 (0 ~ 1.9)	75 ~ 150 (1.9 ~ 3.81)	150 ~ 250 (3.81 ~ 6.35)

Tensile properties of AM-355 CRT laminates with different degrees of IG attack on the surface are presented in Table 2. For a comparison, the minimal tensile requirement for the strap laminate of the component is also given in Table 2. Results showed that all tested samples meet the minimum tensile requirement of the laminate material regardless of the surface IG attack conditions. It indicated that the different degrees of IG attack on the surface did not appear to have a significant effect on the tensile properties of the material.

TABLE 2 -- Tensile Properties of AM - 355 CRT Laminates with Different IG Attacks

(1 ksi = 6.895 MPa)

Specimen Condition	Ultimate Tensile σ_{UTS}, ksi	Yield Strength σ_y, ksi	Elongation δ, %
Light IG Attack	246	205	17
Moderate IG Attack	245	188	18
Heavy IG Attack	241	211	17
Required Properties (min.)	220	180	10

Fatigue test results for the samples with moderate IG and light IG attack are given in Fig. 4. The data were plotted with "best-fit" approximations according to the equation

$$y = (a + b \ln(x) + c/x^2) \tag{1}$$

which was acquired from curve-fitting software. As shown in Fig. 4, a significant difference in fatigue strength in the high cyclic (traditionally $N > 10^6$ cycles) regime is evident. The mean fatigue strength at $N = 3 \times 10^6$ cycles for the samples with light IG attack is measured to be ~70 ksi (482 MPa), R=0.05. For the samples with moderate IG attack the corresponding fatigue strength is only ~58 ksi (400 MPa). A 20% reduction in fatigue strength at $N = 3 \times 10^6$ cycles is observed for the samples with moderate IG attack as compared to the samples with light IG attack. Such a large decrease in fatigue strength for the laminate with moderate IG attack would be expected to have a significant negative impact on its service-life due to the extreme dynamic loading conditions. However, the difference in fatigue resistance appears to decrease with increasing applied stress (Fig. 4). At ~10^4 cycles, the samples with moderate IG attack had a fatigue resistance close to that of the light IG specimen. This seems to indicate less dependence of surface IG attack conditions on the fatigue resistance in the low cyclic regime (traditionally $N < 10^4$ cycles), which is consistent with the findings in many steel alloys regarding notch effects on fatigue behavior [9]. Because of the limited number of specimens, the sample with heavy IG attack was only subjected to fatigue loading to study the fatigue crack initiation and propagation behavior.

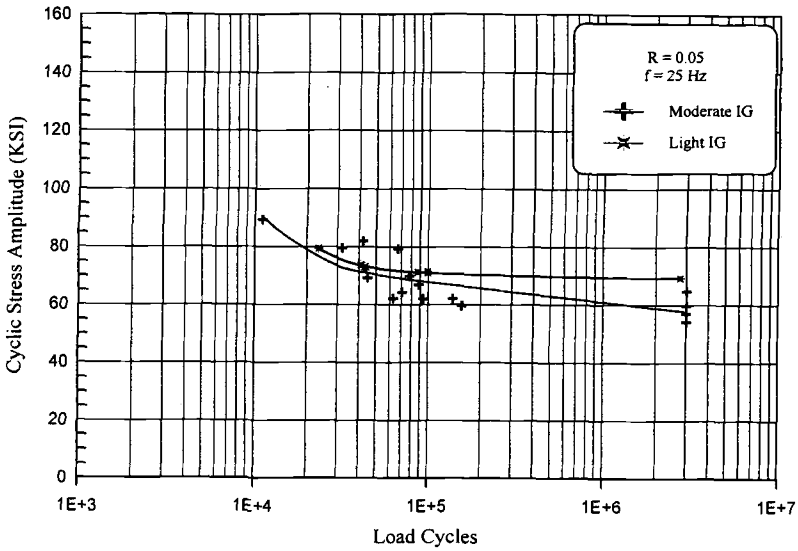

Figure 4 - Comparison of fatigue strength in different IG conditions. (1 ksi = 6.895 MPa).

The specimens with light IG attack failed predominantly from machined edge defects. Fig. 5 shows a typical fatigue fracture surface with a crack origin at the edge scratches. The edge finishing performed on the specimen caused scratches perpendicular to the specimen length. In production, a similar automated edge finishing technique is utilized to break the edges of the stamped laminates. These scratches would be expected to be the origins of fatigue crack initiation. No crack initiations or secondary cracks, resultant from the surface IG attack, were observed on the fracture surface. As shown in Fig. 6, the specimen did not display any IG attack morphology on the surface and the crack path along its edge appeared to be transgranular.

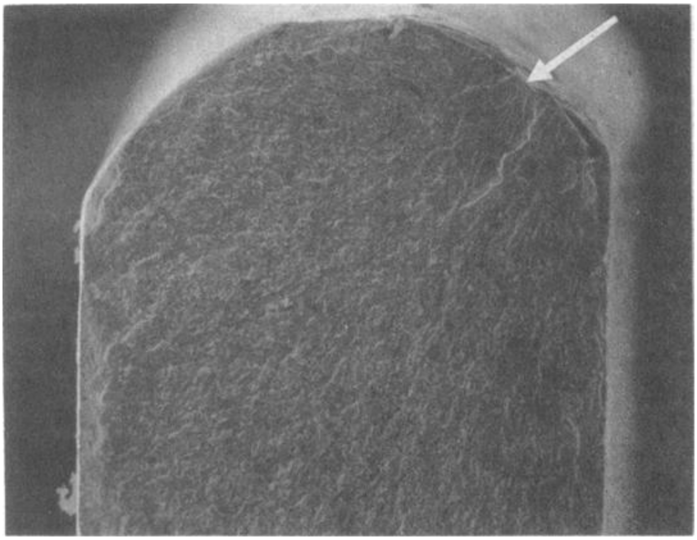

Figure 5 - SEM fractograph showing an edge origin, indicated by an arrow (light IG condition). Mag. 250x.

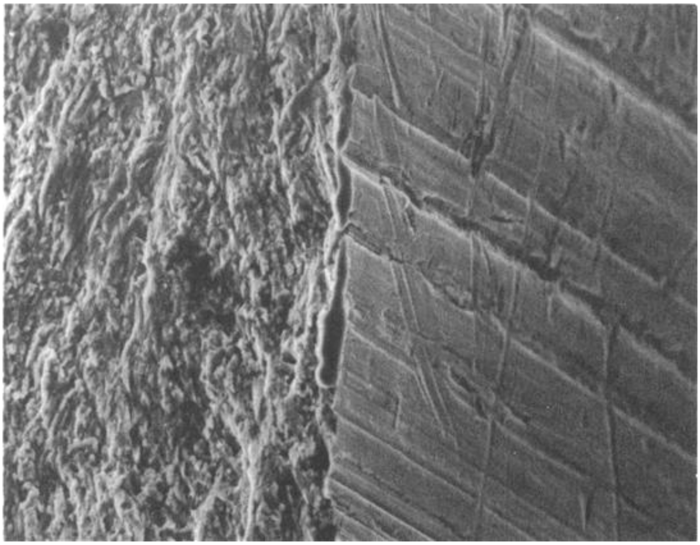

Figure 6 - SEM fractograph showing lack of IG edge (light IG condition). Mag. 750x.

Crack initiations and secondary cracking, either at machined edges or surface flaws of the IG network, were observed on the specimens with moderate IG attack. Surface edge scratches, introduced during finishing, served as favorable crack initiation sites. However, the fatigue cracks were found to propagate along the network at surface flaws attributed to the IG attack. In-service failures are complicated by fretting and crevice corrosion issues (from the clamped stack of laminates). However, the effect of the IG attack on the surface remains as the area of principal concern. As shown in Fig. 7 (arrows denote IG morphology along edges), the IG attack on the surface allows the fatigue crack front to propagate along the IG network near the surface. Furthermore, there were significant secondary cracks revealed on the fracture surface adjacent to the main crack front. These secondary cracks also appeared to be resultant from the surface IG attack. Fig. 8 shows that a few grains were entirely removed, as the crack progressed around them. This suggested that the boundaries of these grains were either weakened or already cracked due to the moderate IG attack.

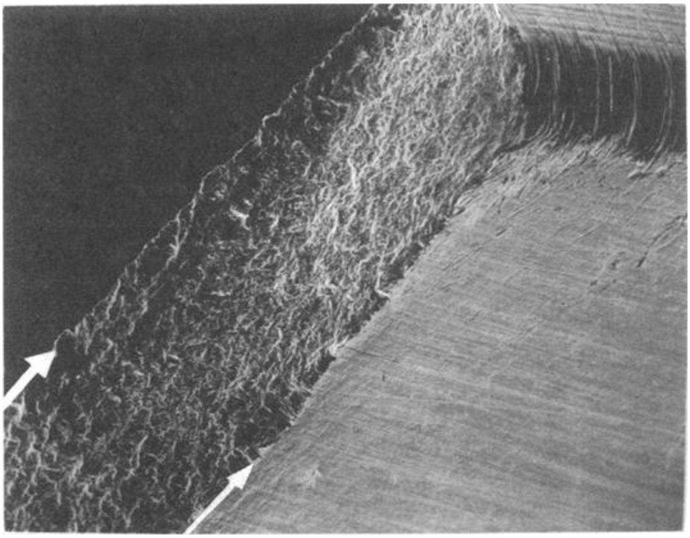

Figure 7 - SEM fractograph showing fatigue by edge IG (moderate IG condition). Mag. 100x.

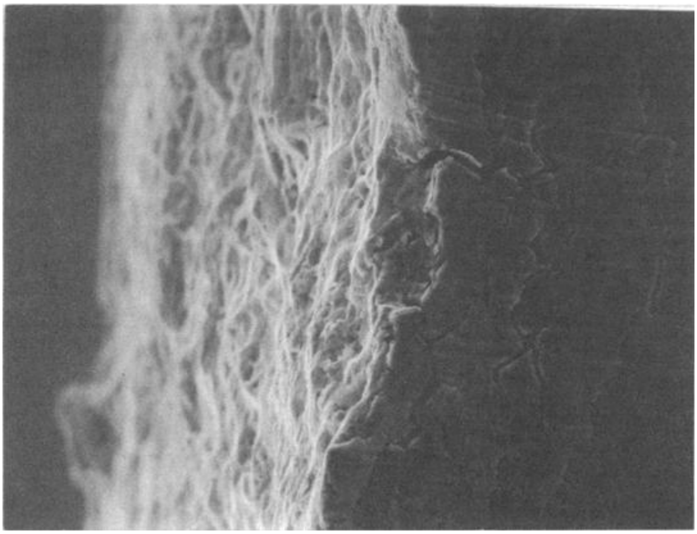

Figure 8 - SEM fractograph showing removed grain on the edge (moderate IG condition). Mag. 750x.

For the samples with heavy IG attack, fatigue cracks initiated predominantly on the surface flaws of the IG network, as shown in Fig. 9. Closer examination revealed an IG morphology at the origin (Fig. 10). The IG network appeared to be the preferred crack initiation site. A rough fracture morphology along the edge of crack path was observed and the crack growth at both edges was along attacked grain boundaries. The depth and severity of the heavy IG surface attack close to the fracture surface are shown in Fig. 11. Clearly, multiple secondary cracks were initiated at the IG network and the cracks propagated along the grain boundaries. A few removed edge grains were also observed on the edge fracture surface (Fig. 11).

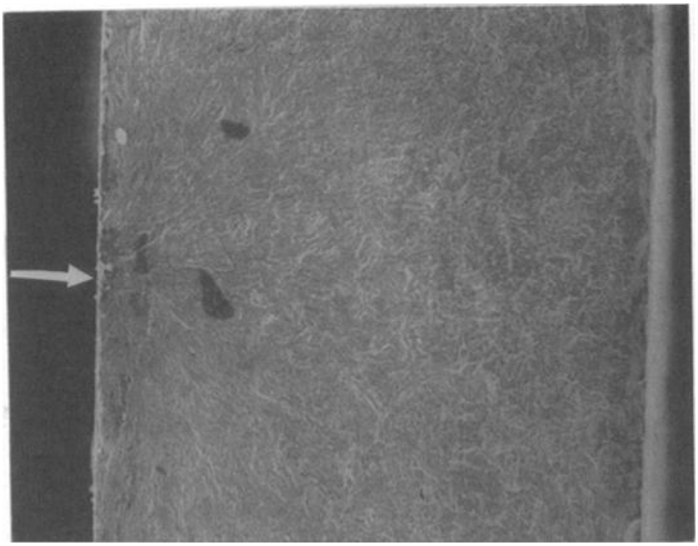

Figure 9 - SEM fractograph showing surface failure origin, indicated by an arrow (heavy IG condition). Mag. 250x.

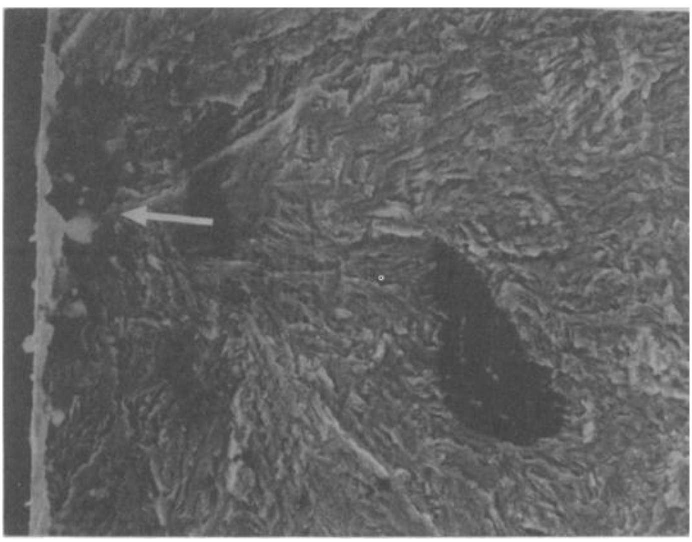

Figure 10 - SEM fractograph showing IG morphology at origin (heavy IG condition). Mag. 1000x.

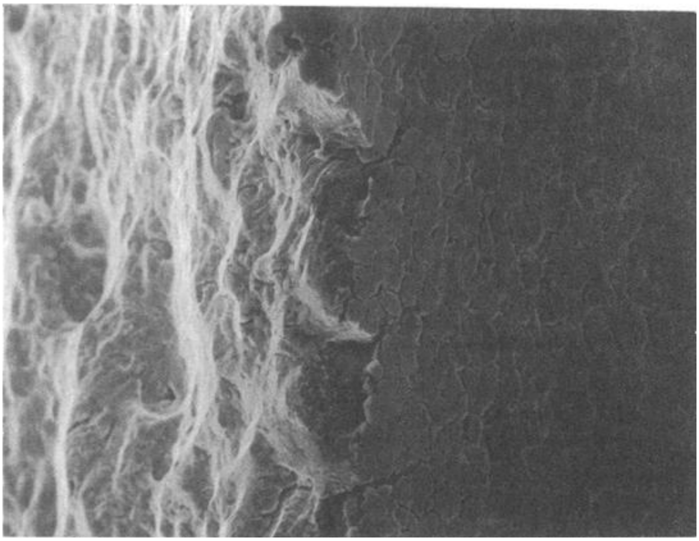

Figure 11 - SEM fractograph showing removed edge grains and secondary cracking origins (heavy IG condition). Mag. 500x.

Fig. 12 shows the results of potentiodynamic polarization measurement for the samples with and without IG attack. Only the positively increasing scans are shown in Fig. 12 in order to evaluate the passive current density, I_p, and breakdown potential for pitting corrosion, E_{bp}. Both curves demonstrate passive behavior followed by transpassive behavior. The sample with IG attack had a value of E_{bp} = 360 mV, but no stable constant current in the passive region can be determined. Accordingly, the current density of the sample with IG attack was increased by one order of magnitude, from about 0.1 $\mu A/cm^2$ to 1 $\mu A/cm^2$, before transpassivation occurred. For the sample without IG attack (polished) the breakdown potential, E_{bp}, was about 520 mV, which was higher by 160 mV as compared to the sample with IG attack. Meanwhile, a constant current density in the passive region was determined to be ~8 $\mu A/cm^2$. Based on the polarization measurements, the sample with IG attack exhibits an unstable passivation behavior and had a low passivation breakdown potential, indicative of a lower corrosion resistance and increased susceptibility to pitting corrosion as compared with the sample without IG attack.

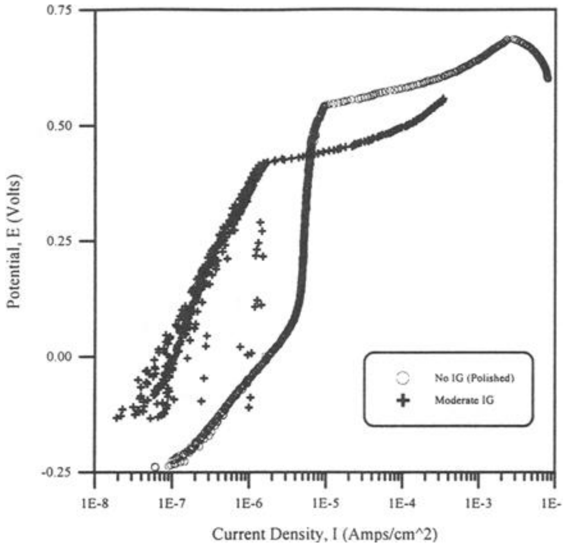

Figure 12 - Anodic polarization curves of the samples with IG attack and polished.

Discussion

An IG network is caused by a preferential attack at the grain boundaries on the surface, which is a typical surface defect similar to rounded "microcracks" uniformly distributed on the surface. It is reasonable to expect that these "microcracks" will result in a local stress concentration at the crack-tip. In metal, the stress concentration effect, i.e., a notch effect, on fatigue properties has been studied for several decades. The notch sensitivity is dependent on material properties and notch size. In this case, it is strongly dependent on density and depth of the IG network on the surface. Figure 13 shows the fatigue behavior of the laminates with different degrees of IG attack compared to preliminary fatigue curves of the laminates at stress concentrations of $K_t = 1$ and K_t > or = 2 [10]. Clearly, all fatigue data measured from the samples with varying IG conditions fall completely within the bounds of fatigue curves between $K_t = 1$ and K_t > or = 2. The increasing severity of IG attack on the surface has shown a similar effect as increasing stress concentration on the fatigue properties of the materials.

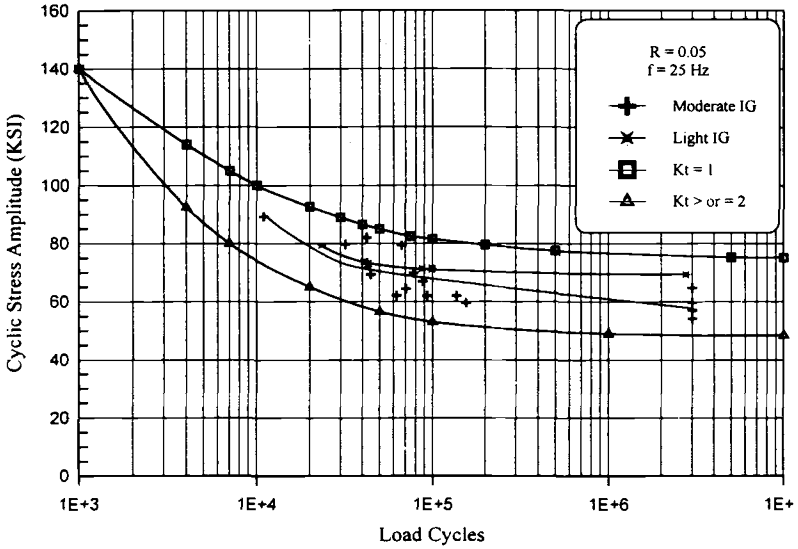

Figure 13 - A comparison of fatigue behavior in different IG conditions with fatigue curves at $K_t = 1$ and K_t > or = 2. (1 ksi = 6.895 MPa).

The total fatigue life of a sample is the sum of the crack initiation life and crack propagation life. In the high cyclic regime, most of the life is taken up with crack initiation. Cyclic plastic deformation results in local damage, such as slip steps, to form microcracks at crack initiation sites. Any pre-existent flaws on the surface, such as, scratches, nicks, machining marks, and even inclusions, can serve as heterogeneous nucleation sites resulting in accelerated crack initiation. In this study, the samples, subjected to cyclic fatigue, have different degrees of IG attack on the surface. The surface IG attack serves not only as a fatigue crack initiation site, but also can be treated as premature surface microcracking. No slip steps are necessary to develop microcracks. With increasing IG attack on the surface, the increase in stress concentration at the root of the IG network will result in easier crack initiation. Also, a fatigue crack front can easily follow the attacked grain boundaries near the surface, and less energy is needed to propagate the crack. As a result, a lower fatigue life is expected. However, in the low cyclic regime, where crack propagation dominates, only a small fraction of the life involves crack initiation. Further, the localized yield at the crack-tip may cause the crack to blunt and thereby reduce the stress concentration at the crack-tip. Consequently, the surface IG condition would not be expected to play an important role in determining fatigue life. This is consistent with our experimental results in Fig. 13. For most high strength steels [9], notch sensitivity is related to the surface conditions and increases with increasing alloy strength. The crack initiation sites in the as-cold rolled 301 and 304 alloys were found to be predominantly cracked inclusions, which are largely affected by the surface material with high residual stress levels or with stress raising roll marks [11].

It was verified by the polarization measurement that the surface IG attack had a significant effect on the resistance of AM-355 CRT laminate against pitting corrosion. In general, current density in the passive region is related to the thickness of the passive film, while the change in current density is dependent on the stability of the passive film. E_{pb} is more indicative of the film's integrity/quality. The "jump" in current density observed from about 0.1 $\mu A/cm^2$ to 1 $\mu A/cm^2$ for the specimen with IG attack indicates that the passive film is not stable. In addition, The E_{pb} was lower by about 150 mV indicative of lower resistance to corrosion pitting for the specimen with IG attack. Since all samples were run in deaerated NaCl solutions, the as-received sample with IG attack would be expected to have a slightly lower pitting current than the polished sample, reflecting that the polishing has removed a pre-existing passive layer.

For the AM-355 CRT laminate material, the major IG network was determined to be formed during an acid pickling operation. This was verified by the primary manufacturer. As suggested by Bergman and Palty [4], the possible mechanism for the IG attack in the AM-355 material is the presence and distribution of the incoherent carbide precipitates at grain boundaries. If the final temper is designed to achieve a maximum strength, the combination of incoherent and coherent precipitates in the microstructure could further result in a lower corrosion resistance [4]. Although the distribution and percentage of both precipitates in the AM-355 CRT laminates are unknown, the IG attack on the surface of the laminates implied that the processing and final temper could attribute to weakened grain boundaries, showing a similar phenomenon to the "sensitization" of some 300 type stainless steels [12, 13]. Even though the pickling is a production process with controlled cycle, time, temperature, speed and acid range, the variations in each step could result in different degrees of IG attack. In addition, the subsequent surface finishing and cleaning processes may further increase the variations of IG attack. As a result, the IG attack on the surface may accelerate the localized corrosion because of the easy attraction of the residual chemicals from the laminate cleaning process and the unstable passivation behavior. Also, the IG network tends to lodge foreign particles which can cause a localized chemical reaction involved the breakdown of the passive film in the field. In this regard, eliminating the surface IG morphology may be helpful in reducing the corrosion attack and fatigue damage of the laminate in service.

Conclusions

This study has shown that surface IG condition plays an important role in fatigue strength and corrosion-resistance of AM-355 CRT materials. Based on the experimental results, the following conclusions have been reached:

1. An increase in the surface IG attack on the AM-355 CRT laminates results in a decrease in fatigue strength. The drop in fatigue strength at $N = 3 \times 10^6$ cycles combined with increasing IG attack on the surface is attributed to a preferred crack initiation at IG network and crack propagation along the attacked grain boundaries. However, the IG

attack does not appear to have a significant effect on the fatigue behavior in the low cyclic regime.

2. The AM-355 CRT laminate with IG attack has shown a low breakdown potential and an unstable passive layer as compared to the laminate without IG attack. This suggests that the laminate with IG attack on the surface has a lower resistance to pitting corrosion.

3. It would be advantageous to remove the IG attack via an automated production process to reduce or eliminate the detrimental effects presented within this work.

Acknowledgments

The authors wish to thank Mr. J. Kelley, Army Research Laboratory (ARL), Aberdeen Proving Ground, MD, and Mr. B. Waterson, Worcester Polytechnic Institute, Worcester, MA, for making significant contributions in acquiring the data presented within this paper and Dr. J. Beatty (ARL) for helpful discussions on this study.

References

[1] Aggen, G. N., "AM-355: High-Strength Stainless," The Iron Age, April 2, 1959.

[2] Technical Bulletin, "AM-350/AM-355 Precipitation Hardening Stainless Steels," Allegheny Ludlum Steel Corporation, Pittsburgh, PA, 1963.

[3] Bergman, P. A., "AM 355 for Gas Turbine Engines," Metal Progress, Vol. 79, 1961, pp. 79-85.

[4] Bergman, P. A. and Palty, A. E., "Development of Corrosion Resistance in AM355," Transactions of ASM, ASM International, Materials Park, OH, Vol. 56, 1963, pp. 728-743.

[5] MIL-HDBK-5G, Vol. 1, Chapter 2, 1994, pp. 117-122.

[6] Aerospace Structural Metals Handbook, prepared by Metals and Ceramics Information Center, Beaverite Products Inc., New York, NY, Vol. 2, Section 1505, 1994.

[7] "QDR Strap Pack Phase I Final Report," McDonnell Douglas Helicopter Systems, May 1995.

[8] Grendahl, S. M. and Champagne, V. K., "Analysis of the Strap Pack Laminate Surface Anomalies," U.S. Army Research Laboratory, 26 October 1995.

[9] "Fundamentals of Metal Fatigue Analysis," J. Bannantine, J. Comer, and J. Handrock, Eds., Prentice-Hall, Inc., 1990, 124-144.

[10] Preliminary test data. McDonnell Douglas Helicopter Systems. 1995.

[11] Wright, R. N., "The High Cycle Fatigue Strength of Commercial Stainless Steel Strip," Material Science and Engineering., Vol. 22, 1975, pp. 223-230.

[12] Freedman, A. H., "An Accelerated Stress Corrosion Test for High-Strength Ferrous Alloys," Journal of Materials, Vol. 5, 1970, pp. 431-466.

[13] Dayal, R. K. and Gnanamoorthy, J. B., "Corrosion Failure of Stainless Steel Components During Surface Pretreatment," Handbook of Case Histories in Failure Analysis, K. A. Esaklul Ed., ASM International, Materials Park, OH, Vol. 2, 1993, pp. 506-508.

K M Nikbin[1]

CONSIDERATION OF SAFETY FACTORS IN THE LIFE EXTENSION MODELLING OF COMPONENTS OPERATING AT HIGH TEMPERATURES

REFERENCE: Nikbin, K. M., **"Consideration of Safety Factors in the Life Extension Modelling of Components Operating at High Temperatures,"** *Effects of Product Quality and Design Criteria on Structural Integrity, ASTM STP 1337,* R. C. Rice and D. E. Tritsch, Eds., American Society for Testing and Materials, 1998.

ABSTRACT: The appraisal of high temperature structural integrity and design and life extension of engineering components, using fracture mechanics methodologies, is dependent on available material properties derived from short term tests. The scatter attributed to fabrication, geometry, testing, material creep properties could vary by up-to a factor of ±2.5. The parameter C* adopted in 'The standard test method for measurement of creep crack growth rates in metals' (ASTM STP E1457-92) and also in the R5 [1-2] and A16 [3-4] crack growth assessment procedures, can vary by a further factor of ±3.3 using differing experimental methods for its estimation. The NSW [5-6] model which describes cracking behaviour over the plane stress/strain range identifies this variability in terms of crack tip constraint. It is concluded from the NSW model (Nikbin, Smith and Webster [5,6]) that for creep ductile materials a factor of 25 in crack growth rates would bound the creep cracking data and an additional factor of up-to 10 would be added when transient and initiation behaviour prior steady crack growth were to be included in the life predictions.

KEYWORDS: Fracture Mechanics, Creep, Crack Growth, Constraint, Life Assessment, Scatter, Structural Integrity, K, C*

Introduction

Manufacturer's recommendations and their past experience have usually been the basis for designing of vital engine components such as turbine blades, vanes and discs and in less critical engineering components such as gas steam pipes, pressure vessels and in weldments which might contain pre-existing defects. In recent times however crack growth initiation and failure analyses have become more acceptable as an independent design and remaining life assessment methodology [1-9]. The development of high temperature fracture mechanics concepts [5,6,10-11] through which the time dependent effects of creep could be modelled uses experimental uniaxial and crack growth data from simple laboratory tests specimens in order to predict failure times under operating conditions. The improvement in non-destructive inspections and testing methods (NDT) to determine the existence of smaller and smaller defects has given rise to a need for looking at both an initiation/incubation period and a steady crack growth period [12,13] in structural assessment procedures.

Life extension calculations require detailed knowledge of past service records and

[1]Mechanical Engineering Department, Imperial College, London SW7 2BX, UK.

postulated future operations together with 'appropriate' mechanical properties of the virgin and service-aged conditions.

The life assessment codes[1-4,7-9] differ in the amount of data that they present in their data banks.ASME N-47[7] and French code RCC-MR [8] both tabulate physical properties of alloys together with yield stress-temperature diagrams and isochronous stress-strain curves. In some cases lower bound data and in other cases average data are presented. Design (i.e. factored for safety) strain range-endurance curves and stress rupture plots are provided for calculation of damage summation. In addition, RCC-MR provides cyclic stress-strain data and also the product of stress and strain range for Neuber-type calculations.

The British Standard document BSPD 6539 (1994) [9] also contains some specialised data for creep crack growth assessments. In contrast, the Nuclear Electric's R5 [1] procedure does not supply elevated temperature data, except where specifically used to validate the procedures. Instead, the user is referred to other data compendia such as the Nuclear Electric R66 data-base, or is encouraged to determine properties on material relevant to the investigation in hand.

Despite the proliferation of data produced on creep and creep/fatigue crack growth the recommended design procedures have remained static over the past thirty years and have only acted as guidelines. For example the ASME Code N47 [7] for un-cracked components, which is a part of the pressure vessel design code acted as a preliminary guidance until consensus had been reached by experience in the field to make it a mandatory code. Relatively recently however two new design procedures has been put forward to redress this status quo. These are notably the French RCC-MR Rules [8], based on un-cracked components and the British R5 high temperature procedures [2] based on cracked components. Other specialised life assessment methods have also been developed but have been used for the present on a voluntary basis. Most notably the proposed French A16 [4-5] procedure used in the life assessment of cracked components. This procedure is in principle the same as British R5 except that it derives the relevant parameters such as the reference stress from a different information base. The variation in deriving the relevant parameters are in themselves an additional source of scatter.

The application of all these design rules is served by the existence of previous test information obtained in high temperature tests. The quality and acceptability of the test data will depend on the inherent and man-made scatter of the data and the accuracy of the analysis. Attempts to co-ordinate and unify data validation and procedures are being made in many European projects in order to standardise the different methods [14-16].

In this paper high temperature data is appraised to bound the level of scatter that could be expected from laboratory tests. The data correlation and the bounds of data scatter were obtained by means of linear regression analysis. The 95% confidence limit (taken to correspond to a standard deviation +2s) was calculated by means of the standard statistical formulae for standard deviation from m data points given by

$$s = \sqrt{\sum_{i=1}^{m} \frac{(xi - \bar{x})^2}{m-1}} \tag{1}$$

Also the application of the fracture mechanics non-linear parameter C* [5,11,17], implemented in a number of testing and assessment codes [1,4], to the prediction of initiation and growth of cracks at high temperatures is examined to consider the differences that exist in its evaluation. A crack growth model (known as the NSW model) derived from C* [5,6] is considered and is shown to be capable of describing the time dependant ductile creep initiation and crack growth data and predicting upper and lower bounds of the cracking behaviour at high temperatures. In addition the transition periods experienced at the initial stages of crack growth is also bound using the extension of NSW model [11,12].

Scatter from testing methods, and material variability

Engineering materials, experiencing high temperature failures under operating conditions, can range from light aluminium alloys, low alloy steels to nickel-based super-alloys. All have one common problem related to fabrication and usage. Variations in the microstructure during the production, operation and during testing when over-ageing and material degradation may occur could produce dissimilar or unexpected cracking behaviour. It is usually difficult to quantify this scatter and only a statistical calculation could determine this range. Where weldments and other matrix incompatibilities are introduced with the possible presence of micro-cracks and their probable interaction, this will further add to the variability and inconsistency of data.

Crack initiation and propagation in high temperature tests for any one material are unique due to the following reasons; The statistical distribution of crack growth and damage accumulation is influenced by many test parameters such as fabrication, plasticity, temperature, creep ductility, overageing, loading frequency, minimum to maximum stress R-ratio, hold time, specimen thickness and size and possibly other time dependent environmental effects. In any one laboratory the number of tests with a particular test condition is very small therefore no homogenous data base exists. In attempting to compare and analyse the intrinsically non-linear data from different laboratories further exacerbates the problem and increased scatter ensues.

The high temperatures testing procedures of these materials are an important source of scatter even though recent high temperature testing procedure ASTM E1457 has been introduced to redress the situation. The experimental techniques, potential drop measurements, optical crack growth readings and different methods for measuring the load-line creep displacement of the specimen also contribute to this source of error. It has been established [15-16] that individual creep tests in one laboratory not only differs from test to test using exactly the same parameters but vary even more when tests are compared to those performed in different establishments. More strict adherence to standardised test methods would improve the data comparison but not entirely eradicate it, as has been shown in the strictly controlled round Robin tests [15-16].

A number of techniques can be adopted to quantify the data scatter and material variation. Statistical methods [18] using random generator techniques, can be applied to bound the data. The test variables can be taken to be random and a probabilistic distribution established from available data, and then applied to a deterministic crack propagation model. Equally using experimental data an upper and lower bound can be established by from a comprehensive data base of relevant material and test conditions. The recommended divergence [14] for basic uniaxial creep data is ± 2.5. Consequently the material constants needed for the subsequent analysis will have a substantial error band associated with it.

The C* integral concept

The arguments for correlating high temperature crack growth data essentially follow those of elasto-plastic fracture mechanics methods. For creeping situations [5,6] where elasticity dominates the stress intensity factor may be sufficient to predict crack growth. However as creep is a non-linear time dependent mechanism even in situation where small scale creep may exist linear elasticity my not be the answer. By using the J definition to develop the fracture mechanics parameter C* it is possible to correlate time-dependent crack growth using non-linear fracture mechanics concepts.

A simplified expression for stress dependence of creep is given by a power law equation which is often called the Norton's creep law and is comparable to the power law hardening material giving;

$$\varepsilon = A\sigma^N \tag{2}$$

and by analogy for a creeping material

$$\dot{\varepsilon} = C\sigma^n$$

$$\text{or} \quad \frac{\dot{\varepsilon}}{\dot{\varepsilon}_0} = \left(\frac{\sigma}{\sigma_0}\right)^n \tag{3}$$

where A, N, C, n, $\dot{\varepsilon}_0$ and σ_0 are material constants. Equation 3 is used to characterise the steady state (secondary) creep stage where the hardening by dislocation interaction is balanced by recovery processes. The typical value for n is between 3 and 10 for most metals. When N=n for creep and plasticity the assumption is that the state of stress is characterised in the same manner for the two conditions. The stress fields characterised by *K* in elasticity will be modified to the stress field characterised by the J integral in plasticity in the region around the crack tip. In the case of large scale creep where stress and strain rate determine the crack tip field the C* parameter is analogous to J. The C* integral has been widely accepted [15-22] as the fracture mechanics parameter for this purpose.

As the J integral characterises the stress and strain state, the C* integral is also expected to characterise the stress and strain rate around a crack. For a non-linear creeping material, the asymptotic stress and strain rate fields are expressed by equations

$$\sigma_{ij} = \sigma_o \left(\frac{C(t)}{I_n \sigma_0 \dot{\varepsilon}_0 r}\right)^{1/(n+1)} \tilde{\sigma}_{ij} \tag{4}$$

$$\dot{\varepsilon}_{ij} = \dot{\varepsilon}_o \left(\frac{C^*}{I_n \sigma_0 \dot{\varepsilon}_0 r}\right)^{n/(n+1)} \tilde{\varepsilon}_{ij} \tag{5}$$

Therefore the stress and strain rate fields of non-linear viscous materials are also HRR [5,6] type fields with I_n being the non-dimensional factor of n, and $\tilde{\sigma}_{ij}$ and $\tilde{\varepsilon}_{ij}$ are functions of angle θ and n, and are normalised to make their maximum equivalent stress and strain unity. By analogy also with the energy release rate definition of J , the C* integral can be obtained from

$$C^* = \frac{1}{B}\frac{dU^*}{da} \tag{6}$$

where B is the thickness, da is the crack extension and U^* is the rate of change of the potential energy dU*/dt. From the view of an energy balance, the C* integral is the rate of change of potential energy with crack extension. Experimentally C* can be calculated [5,6,16] from the general relationship

$$C^* = (P\dot{\Delta}_c / WB_n)F \tag{7}$$

where $\dot{\Delta}_c$ is the load-line creep displacement rate, F is a non-dimensional factor which can be obtained from limit analysis techniques, B_n is the net thickness of the specimen with side-groove and W is the width. In general equation (7) is used to estimate the values of C* for tests in the laboratory. The other methods available is one based on reference stress concepts [11], the C[t] derivation [19] that also uses the specimen's creep deformation rate. Reference stress procedures are also employed to evaluate C* for feature and actual component tests where the load-line deformation rate is not available [11,22]. By determining;

$$C^* = \sigma_{ref}.\dot{\varepsilon}_{ref}\left(\frac{K}{\sigma_{ref}}\right)^2 \tag{8}$$

where ε_{ref} is the creep strain rate at the reference stress, σ_{ref} and K is the stress intensity factor. Usually it is most convenient to employ limit analysis to obtain σ_{ref} from

$$\sigma_{ref} = \sigma_y \frac{P}{P_{lc}} \tag{9}$$

where P_{lc} is the collapse load of a cracked body and σ_y is the yield stress. The value of P_{lc} will depend on the collapse mechanism employed.

Scatter relating to C* estimations procedures

Creep cracking behaviour can be described under two regimes of fracture. In one extreme where the available creep ductility is low, failure is creep brittle and the resulting elastic stress fields will dominate [13,19]. Where creep ductility is high and the crack-tip singular field is non-linearly constrained, the parameter C* is found to be appropriate [5,6,17]. The steady state parameter C* or its equivalent C[t] [17,19] which has been adopted in ASTM E1457 and in the R5 [1-2] and A16 [3-4] crack growth assessment procedures is widely accepted as the parameter which best describes the cracking behaviour in the ductile cracking regime for power law hardening materials. However no agreement exists as to the method for C* evaluation in specimens and components.

There are differences of opinion as to exact interpretation and validity ranges of C* for the creep ductile regime and furthermore the accurate numerical evaluation of these parameters is largely dependent on the creep model employed, be it the Norton's creep law or other creep models which could also include the primary and the tertiary regions modelled on the actual material uniaxial behaviour. All these factors give rise to differences in evaluating C*. Comparison of the differing methods of calculating C* have been performed [5,20,21] and in general it has been observed that the experimental estimate for C* gives conservative values [21] compared to the numerical methods. However further work is needed for an acceptable validation.

It has been established [5,6,17,19] that the material creep strain rate is the dominant factor in the development of the stress/strain fields local to the crack tip and this in turn controls the damage development and crack extension in the structure. In consequence the monitoring of this variable during tests and utilising it in the estimation procedures for C* has shown the most success and show the least scatter. This is to be expected since damage development and crack growth in individual tests will be inherently described by the time dependent deformation processes that occur during the particular test which encompasses the variation in material properties at the crack tip with respect to time. It is therefore argued that by using an agreed method for experimental estimation of the parameter C* in standard testing using creep displacement rates or by using the reference stress/strain rate technique [11] in component shaped specimens short term tests, the extent of scatter in the analysis can be reduced and a more consistent defect assessment procedure can be carried out.

FIG. 1-2 compare the differences in evaluation of the results of a round Robin exercise [15-16] on creep crack growth test carried out on 1CrMoV steels ate 550 °C. FIG. 1 shows the resulting analysis where crack growth data on compact tension (CT), single edge notch tension (SENT) centre cracked panel (CCP) and single edge notch bend (SENB) specimens are plotted versus C*. The data in FIG.1 was separately analysed by the individual institutions and the figure is presented in this paper unchanged. There are differences in units employed as well as use of different methods for data reduction and analysis. The scatter band in FIG. 1 which measures in the region of a factor 100 is clearly unacceptable.

The different organisation then sent Imperial College their actual raw data, all relevant information about the test methods, specimen dimensions, loading, total load-line displacement readings, potential drop crack readings, and their initial and final crack lengths measured from the fracture surface. Imperial College undertook to do the analysis using the raw data and the results are shown in FIG. 2. It is clear that when a unified method of reducing the data, calculating the cracking and the creep displacement rates and finally estimating the C* parameter is adopted the scatter band drops appreciably to about a factor of 10 (or approximately ±3.5). Superimposing the two FIGS. 1 and 2 in FIG. 3 and using the same units highlights the fact that both crack growth rate measurements as well as C* estimations are sources for scatter. In FIG. 2 the reduced scatter of data suggests that the use of unified method, using as its basis equation (2), allows differentiation between the crack growth rate behaviour of different variables in terms of constraint. In particular the best fit lines (drawn for the steady state region of cracking which disregards the initial 'tail') for different geometries show differences in cracking rates which FIG. 1 would not be able to show.

The region where the scatter seems to be largest is found in the initial transient period of crack growth where it has been shown [12,13] that until there is sufficient damage build up at the crack tip the crack growth rate is in the transient/incubation region and no steady state cracking will be observed.

FIGS. 4 and 5 show further comparisons of the analysis methods using equations (7,8) as the basis for the calculations, for standard CT specimens and tubes of 21/4Cr1Mo steel at 600 °C [22] under tensile and internal pressure. This gives an example of

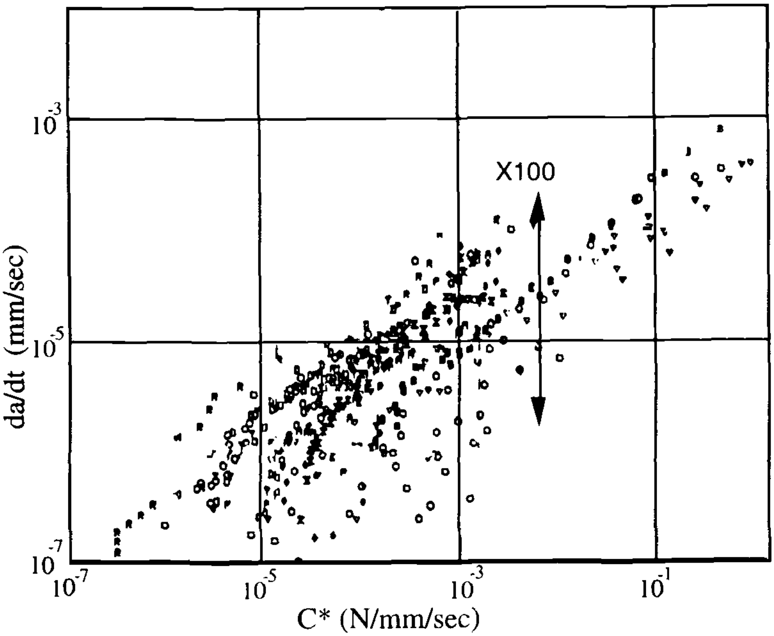

Figure 1: Crack growth rate correlation versus C* analysed by different laboratories [19] showing large scatter in tests carried out on a 1 CrMoV steel at 550 °C using different geometries and specimens sizes .

comparing data generated standard laboratory specimens from to feature test data of components shaped specimens. There is clearly a geometry effect due to the constrait differences between the specimens. The scatter band of 10 in the steady cracking range are similar to those seen in FIG. 2. It is clear that for more complicated component structures the use of different methods of the relevant variables, such as evaluating equation (9), and choice of basic material property data will further increase the scatter range.

From measurements and observations of data of crack growth versus C* [5,6,15,16], obtained from a number of engineering material it is safe to assume that for any particular test condition a divergence a factor of about 10 encompass the data. Therefore any distinguishable crack growth variation from the mean attributed to other test variables estimation should also contain an error band of about a factor of 10.

A model to describe the transient and steady crack growth data

The application of C* in crack growth analysis is well established and no attempt will be made in this paper to develop it in detail. Analysis of the crack growth using steady state values of C* is more relevant in the case of ductile creep crack growth [5,19] where the creep strain rate $\dot{\varepsilon}$ is governed by Norton's creep law given in equation (2). From both theoretical and experimental standpoints a relevant and an appropriate correlating relationship has been put forward describing C^* and creep crack growth in the form of

$$\dot{a} = D_o C^{*\phi} \tag{10}$$

where $\phi = (n/n+1)$ and for materials with $n > 10$, ϕ is approximately 1, D_0 is a material constant, and C^* is the non-linear creep parameter describing the state of stress

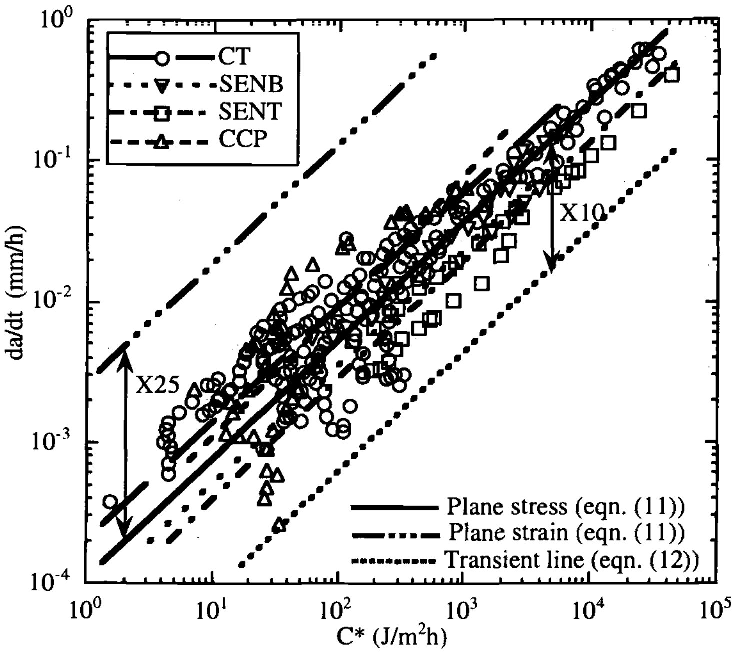

Figure 2: Unified evaluation of crack growth rate in a 1CrMoV steel tested at 550 °C as a function of C* [16]. Showing the best fits for the data from four geometries and the upper/lower bounds of Equations (11) and (12).

ahead of a crack tip in a creeping body. In addition it has been found [5,6] by using a creep process zone as the basis for the model, that for a wide range of materials equation (10) is most sensitive to creep failure strain and that it can be represented approximately in plane stress by the approximate NSW model as

$$\dot{a}_s = \frac{3C^{*0.85}}{\varepsilon_f^*} \tag{11}$$

where $\dot{a}_s$ is the steady crack growth rate in mm/h, ε_f^* is failure strain as a fraction and C* is in MJ/m^{2}h. The relevant ductility needed for crack growth could be reduced in the limit by a further factor of ε_f^*/50 in the plane strain regime [5,6]. This range describes the effects of constraint on crack growth due to both material properties and size/geometric factors. The factor 50 which is an estimate of the bounds ranging from uniaxial to a tri-axial state of stress bounds the scatter range prevalent in crack growth of engineering alloys in the range of creep brittle to creep ductile regime [6].

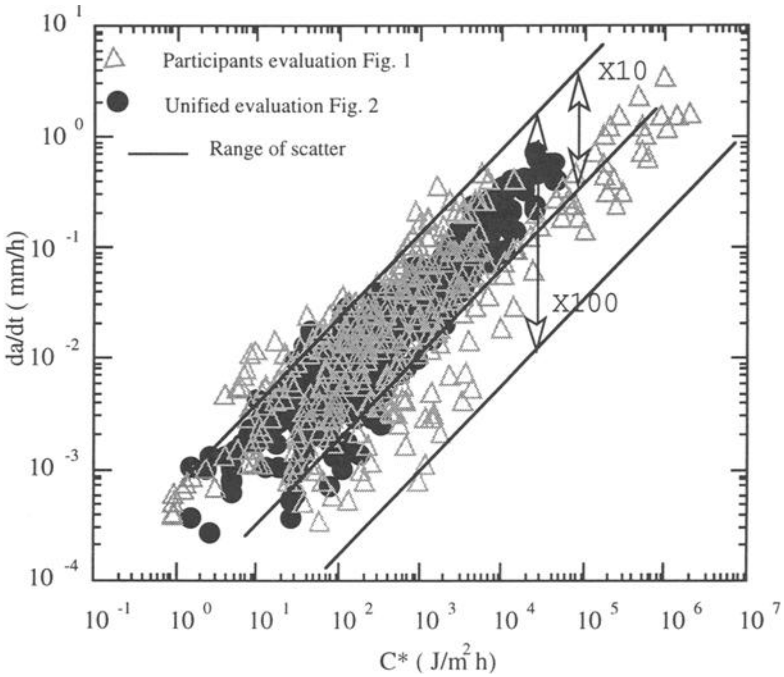

Figure 3 : Comparison of scatter using the data in FIGS. (1 and 2)

The initial stage cracking prior steady growth exhibit a transient phenomena, as observed in FIGS. 2,4,5. It has been modelled [12,13] assuming a transient period where creep damage needs to develop from an elastic state of stress before steady cracking could occur. This extension of the NSW model can be approximated terms of;

$$\dot{a}_o \approx \dot{a}_s /(n+1) \tag{12}$$

where $\dot{a}_o$ is the initial crack growth rate and n is the creep index in Norton's creep law (equation (2)). The value of n for engineering materials is in the range of 5-10 which suggests that effectively $\dot{a}_o$ can be taken as about 1/10 as a lower bound of the steady state creep cracking rate described by equation (11). Alternatively this period can be translated to an initiation time t_i to a steady state crack growth conditions by [12,13];

$$t_i = r_c /(3\dot{C}*^{0.85}) \tag{13}$$

where r_c is the creep process zone with a size in the region of one grain size. As the limits of crack detection is at best 100μm then r_c can be taken as the minimum size of a

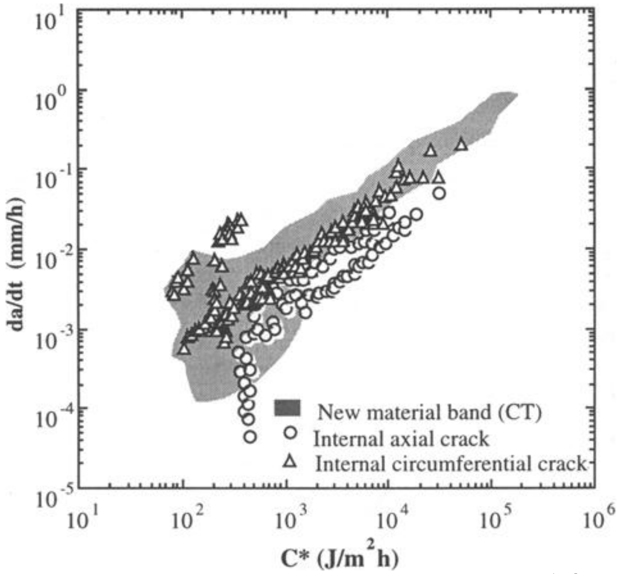

FIG. 4: Crack growth in new 21/4Cr1Mo steel tubes containing internal circumferential and internal axial cracks under pressure loading compared with CT data band [22] at 600 ^{O}C.

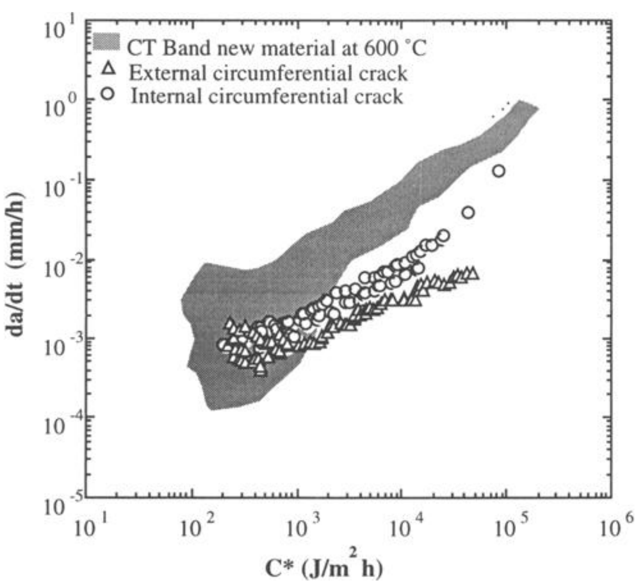

FIG. 5: Crack growth in new 21/4CR 1Mo steel tubes containing internal and external circumferential cracks under tensile loading compared with CT data band [22] at 600 ^{O}C.

detectable crack which gives a conservative value for t_i since for most practical circumstances the accuracy of crack detection is rarely less than 0.5 mm.

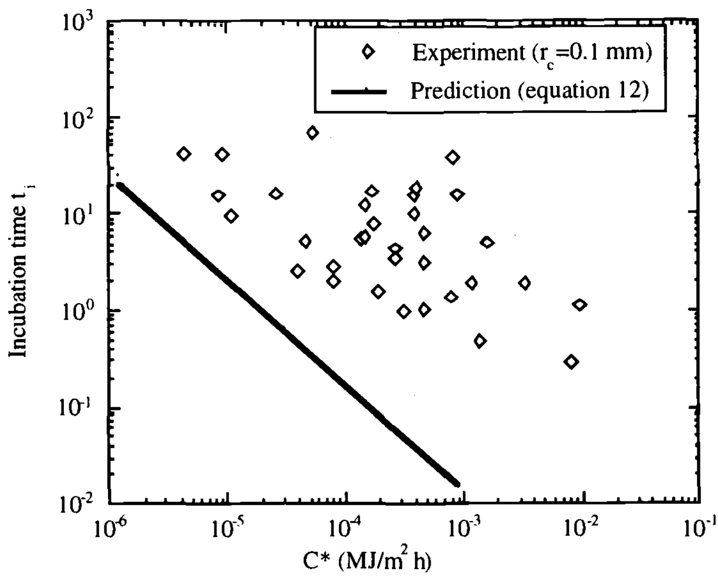

Figure 6: Experimental and predicted incubation times eqn. (12) for 1 CrMoV steel tested at 550 °C.

In the incubation region of crack growth the model predicts an approximate relationship between crack growth rate and r_c and ε_f* (equations (13)). The predictions of initiation times derived from equation (13) and readings of experimental crack initiation times assuming r_c to be 100 μm are shown plotted in FIG. 6 versus C* for the 1CrMoV steel. The steady state line from equation (13) is conservative. If plane strain upper-bounds were to be considered the prediction s would show the shortest incubation time making t_i excessively conservative.

Discussion

Different interpretation of data and method of analysis will contribute to the source of scatter in deterministically based initiation and propagation analyses. In design and residual life assessment this can be accounted for account by incorporating relevant safety factors. The improvement of this safety factor will result from the rational procedure for treating the scatter in the data. The number of test variables and the extent to which they affect the final results have to be considered so that the analysis can be translated into further improvements in design and residual life applications. Expert knowledge based methodology using relevant information related to the particular problem could be used in conjunction with a model for crack growth prediction to estimate life in components.

As an example for the 1CrMoV steel lines are plotted in FIG. 2 to show the bounds for plane stress and plane strain, using the approximate equation (11), and the transient cracking predictions in equation (12), using a uniaxial failure strain ε_f of 20%. Essentially

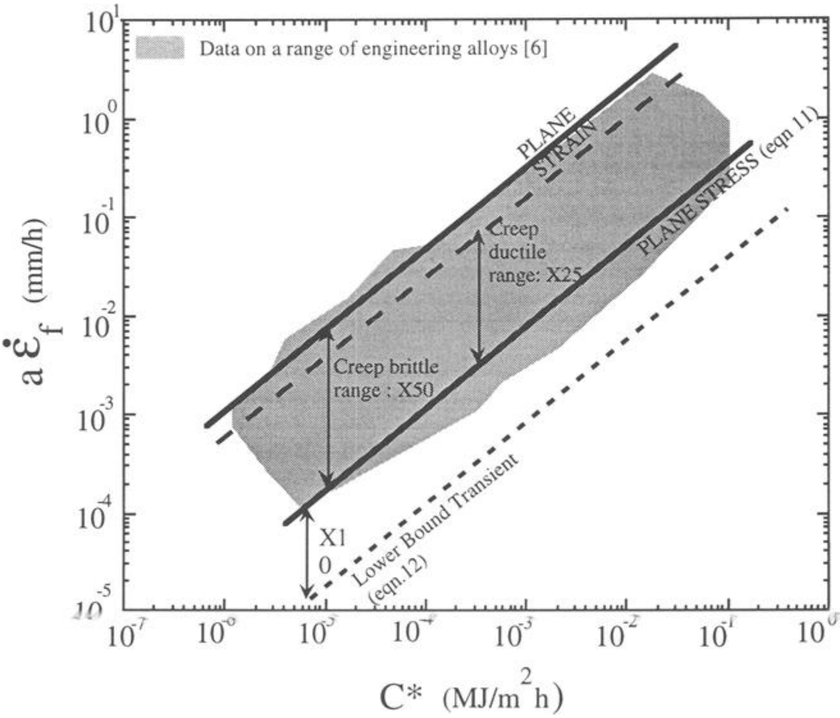

Figure 7: Material independent engineering crack growth assessment diagram over the plane stress/strain and transient upper and lower bounds.

for this steel, cracking is in the plane stress region and the least squares fit of the different geometries show, within the scatter band, geometry effects suggesting differences in crack tip constraint between CT, SENB and SENT geometries. The overlap of the data below the plane stress line is partly due to the approximation in equation (11) but it is also accounted for by the transition region of the cracking describe by equation (12). In this case equation (12) is plotted on FIG. 2 using the plane stress line with the value of $\varepsilon_f^* = \varepsilon_f$, this gives the lower bound for the transition crack growth region. For this case the 'tail' region is also bound by the predictions.

FIG. 7 shows the crack growth rate band of a comprehensive range of engineering materials [6] ranging from creep brittle to creep ductile. The data is normalised with respect to their respective uniaxial ductility and are plotted versus C* using the experimental estimate of C*. The various upper bound factors of safety, predicted by equations (10-12) are also plotted in this FIG. The factor 50 which covers both the creep brittle and creep ductile range of fracture [6] can safely be reduced to 25 for creep ductile engineering materials which satisfy the ASTM E1457 testing conditions.

The regions of the crack growth behaviour therefore which contain an inherent scatter band of approximately a factor 10 (or ±3.3) seem to be covered adequately within the bounds of the present model. FIG. 7 acts as a material independent engineering crack growth assessment diagram. In addition, the transient region assuming that the initial cracking rate is given as $\dot{a}_o \approx \dot{a}_s / 10$ can be introduced as a lower band to bound the initiation and the transition 'tail' region of damage development observed in many testpieces and components. The most conservative line to choose for life prediction would be the plane strain line. However for a narrow range of data sets using specific material, with fixed sizes and geometry an acceptable safety factor of 10 could be used to predict cracking behaviour.

Conclusions

The sources of scatter can be attributed to specimen fabrication, geometry, loading history, material creep properties, as well as laboratory equipment and testing techniques. Raw creep uniaxial data used for modelling and analysis can be bound within a factor of ±2.5. The parameter C*, which is adopted in the ASTM E1457 testing method procedures and R5 [1-2] and A16 [3-4] crack growth assessment procedures, can vary by a factor of ±3.3 using a unified experimental method for its estimation.

The NSW model which describes cracking behaviour over the plane stress/strain range identifies this variability in terms of crack tip constraint. Using this model to predict steady state crack growth rates, the existing creep ductile data in the literature can be bound to within a factor of 25. For the transient and initiation period of unsteady damage development a further factor 10 would bound the data. Further reductions on the upper bound limits can be attained when specific conditions are considered. For circumstances where sufficient data is unavailable a conservative design and remaining life prediction crack growth limit can be obtained by using the upper-bound plane strain prediction line. Creep crack growth testing standards and defect assessment procedures for components should allow for these scatter and cracking ranges when making recommendations for testing methods and/or present models for crack growth prediction.

References

[1] Nuclear Electric (1990) R5: Assessment Procedure for High Temperature response of Structures, *Nuclear Electric, plc Report Issue 1:*, 1990.

[2] Goodall, I. W. (Ed.) 'Assessment Procedure for the High Temperature Response of Structures', *Nuclear Electric procedure R5*, Issue 1, 1990.

[3] Drubay, B., Moulin, D., Faidy, C., Poette, C. and Bhandari, S., ' Defect Assessment Procedure: *a French approach, ASME PVP*, Vol. 266, 113-118, 1993.

[4] Green, D., Moulin, D. and Hooton, D., 'Development of Fracture Assessment Procedures at Elevated Temperature in Europe', in *SISSI 94, Saclay International seminar on structural integrity: Principles of Fracture Mechanics Applications in Nuclear Power Plants*, Centre d'Etudes de Saclay, pp. 59-71, 1995.

[5] Nikbin, K. M., Smith, D. J., & Webster, G. A., 'Prediction of Creep Crack Growth From Uni-Axial Creep Data' *Proc. Roy. Soc., Series A*, 396, 183, 1984.

[6] Nikbin, K. M., Smith, D. J., & Webster, G. A., 'An Engineering Approach to the Prediction of Creep Crack Growth', *J. Eng. Mat. and Tech.*, ASME, 108, 186-191, 1986.

[7] *ASME Boiler and Pressure Vessel Code Case N-47 (29)*, Class 1 components in Elevated Temperature Service, Section III, Division I, ASME, New York, 1991.
[8] *RCC-MR Technical Appendix A3*, Section 1, Subsection Z, Materials Design and Construction Rules for Mechanical Components of FBR Nuclear Test Islands, AFCEN, Paris, 1985.
[9] *British Standards PD 6539*, 'Guide To Methods for The Assessment of The Influence of Crack Growth on the Significance of Defects in Components operating At High Temperatures', *BSI*, London, pp. 1-37, 1994.
[10] Viswanathan, R., 'Damage Mechanisms and Life Assessment Of High Temperature Components', *ASM International*, 1989.
[11] Ainsworth, R. A., 'Approximate Non-Linear Fracture Mechanics Calculations using Reference Stress Techniques, Innovative Approaches to Irradiation Damage and Fracture Analysis', *Proc. Joint ASME/JSME PVP Conf.*, Honolulu, Hawaii, , ASME PVP, 170, July 23-27, pp 13-20, 1989.
[12] Austin, T.S.P. and Webster, G.A., 'Prediction of Creep Crack-Growth Incubation Periods', *Fat. & Fract. Eng. Mats and Structures*, 15 , 1081-1090, 1992.
[13] Nikbin, K. M., The Mechanics of Creep Brittle Materials -2, eds., A.C.F. Cocks, A.R.S. Ponter, *Elsevier Applied Science Publ.*, pp 14-24, 1991.
[14] European Creep Collaborative Committee (ECCC) , 'Data Validation and Assessment Procedures', *Brite/Euram Concerted Action Group, BE5524*, recommendations, Nov., 1995.
[15] Saxena, A., Gibbons, T. B., Hollstein, T, Webster, G. A., Yokobori, T., 'Intercomparison of Creep Crack Growth Data', *Conf. on Harmonizing of Testing Practice for High Temperature Materials. by High Temperature Mechanical Testing Committe'*, ISPRA, Italy, 1990.
[16] Hollstein, T., Webster, G. A. and Djavanroodi, F., 'Creep Crack Growth in 1CrMoV Steel and Alloy 800H: The Results of an EGF Round Robin', *IWM Report T 5/89*, Fraunhoffer-Institut, Freiburg, Dec. 1989.
[17] Saxena, A. and Bassani, J. L. *in Proceedings, 113th AIME Meeting*, Los Angeles, J.M. Wells and J.D. Landes, Eds., pp. 357-383, 1984.
[18] Sire, R. A., Kokarakis, J. E., Well, C. H. and Taylor, R. K., 'A probalistic Structure Life prediction System for Container Ship Repair and Inspection', *Int. J. Pressure Vessel and Piping*, Vol50, Nos.1-3, pp297-316, 1992.
[19] Saxena, A., ' Creep Crack Growth in High Temperature Ductile Materials', *Eng., Fract., Mechanics*, V 40, No. 4/5, pp.721-736, 1991.
[20] Djavanroodi, F. and Webster, G. A., 'Comparisons Between Numerical and Experimental Estimates of the Creep Fracture Mechanics Parameter, C*', Fracture Mechanics: 22nd Symposium (Vol. 1). *ATSM STP 1131. American Society for Testing and Materials*, Philadelphia., pp. 271-283, 1992.
[21] Linkens, D., Busso, E. P., Dean, D. W., 'Prediction of Non-Steady Asymptotic Crack Tip Fields in the Power Law Creeping', *Nuclear Eng. and Design*, 158, pp. 377-385, 1995.
[22] Webster, G. A., Nikbin, K. M., Kaguchi, H., Austin, T. S. P., 'Effects of Service Exposure and Test-Piece Geometry on Creep Crack Growth in Two Low Ally Steels', *Proc. IMechE, Conf.*, London, C494/062/96, pp 289-299, June 1996.

Jorge B. Deschapelles[1] and Richard C. Rice[2]

Improved Fatigue Resistance of 7050 Thick Plate Aluminum Through Minimization of Microporosity

---

REFERENCE: Deschapelles, J. B. and Rice, R. C., **"Improved Fatigue Resistance of 7050 Thick Plate Aluminum Through Minimization of Microporosity,"** *Effects of Product Quality and Design Criteria on Structural Integrity, ASTM STP 1337,* R. C. Rice and D. E. Tritsch, Eds., American Society for Testing and Materials, 1998.

ABSTRACT: This paper illustrates the substantial fatigue life improvements that have been achieved with 7050 heavy gauge plate over the past two decades. The load control fatigue resistance of 7050-T7451 thick plate is shown to decrease with increasing plate thickness at both the plate quarter-thickness (T/4) and mid-thickness (T/2). These reductions in fatigue resistance are shown to be most substantial at the plate mid-thickness, and they are shown to be directly related to the maximum size of remaining micropores.

KEYWORDS: 7050-T7451, aluminum plate, MIL-HDBK-5, load control fatigue properties, microporosity, equivalent stress, thickness effects, process optimization, log-normal distribution.

Background

Alloy 7050 was developed in the early 1970's for the U.S. Navy as a high strength and stress corrosion resistant alloy[3]. One of the original applications for 7050-T73651 plate (temper later changed to T7451) was for the F/A-18 Hornet; bulkheads were machined from 5.68-inch (144-mm) thick 7050 plate.

Starting in 1982, and continuing through 1984, significant problems with mid-thickness porosity were found by Northrop during routine fluorescent penetrant inspections (FPI) [*1*]. The center line porosity problem was common for all of the 7050 plate suppliers. Various meetings between Northrop and specific suppliers were held in early 1984; the focus was on the generation of standards for the acceptance of raw 7050

---

[1] Rolled Products Technical Manager, Century Aluminum Corporation, P.O. Box 98, Ravenswood, West Virginia 26164.

[2] Manager, Structural Integrity Projects Office, Advanced Manufacturing Technology, Battelle, 505 King Avenue, Columbus, Ohio 43201-2693.

[3] Johnson, E. W., "Alcoa Alloy 7050," Alcoa Internal Publication, April 8, 1976.

plate stock[4]. FPI, as well as various other methods for counting and sizing pores, were evaluated as candidate plate inspection procedures. For example, Fig. 1 shows an early attempted correlation between fatigue life and hydrogen content in 7050 plate. These ded an early indication that better degassing practices were needed in order to improve plate quality and increase thick plate fatigue resistance. Fig. 2 shows another attempted correlation between hole size and FPI indication. Poor nondestructive correlations with fatigue resistance such as these led to Northrop's rejection of FPI as an acceptance method for 7050 raw stock plate. In place of nondestructive inspection, a requirement for constant amplitude fatigue testing was established (at a maximum stress of 30 ksi and a stress ratio of 0.10), since it was found to provide the best technical solution for ensuring adequacy of the material and measuring compliance to specifications [*1*]. Fig. 3 shows some of the early data correlating pore size with fatigue resistance[1]. These data helped support the argument that maximum pore sizes no greater than 0.004 to 0.005 inch (100 to 125 μm) were needed to consistently meet the 80 000 cycles to failure minimum fatigue life requirement in the Northrop's new Engineering Order No. EOF 09070[2].

Northrop's specification, combined with high initial failure rates experienced by all 7050 plate suppliers, led to concerted efforts to reduce microporosity through processing improvements on all 7050 thick plate products. By 1989, the pore size distributions on 5- to 6-inch (125- to 150-mm) thick Century Aluminum-Ravenswood Operations (Century) produced plate were substantially improved, and a much clearer understanding had been developed of the pore size ranges that were required to consistently achieve fatigue lives in excess of 100 000 cycles to failure. Fig. 4 illustrates the results of micropore examinations on a collection of 1989-produced plate products that displayed qualification fatigue lives ranging from 111 000 to 238 000 cycles to failure. This study provided further evidence of the strong correlation between reduced 7050 mid-plane microporosity and increased fatigue resistance.

In the early 1990's, the suitability of rolled aluminum plate products for critical aircraft applications was reevaluated by a number of airframe manufacturing groups [*2*][4]. These studies were driven by budgetary constraints that forced cost/performance tradeoff studies of aircraft components traditionally made from forgings and built-up assemblies. Cost elements in these evaluations included:

- the cost of the as-delivered wrought material,
- any costs to control distortion during machining and after heat treatment,
- the cost of shims, rework, and long fabrication sequences,
- the cost (sometimes detailed and exotic) of tooling setups of individual parts,
- the cost of nondestructive inspection, and
- the cost of checking and satisfying dimensional stability and tolerance limits.

These cost considerations, combined with new evidence of reduced porosity levels and improved fatigue resistance of 7050 rolled plate relative to forgings, led many airframe manufacturers to take a second look at this alloy and product form for applications such as wing spars, bulkheads, big bones, and other applications where

---

[4] Kaiser Aluminum Internal correspondence, 1977 - 1988.

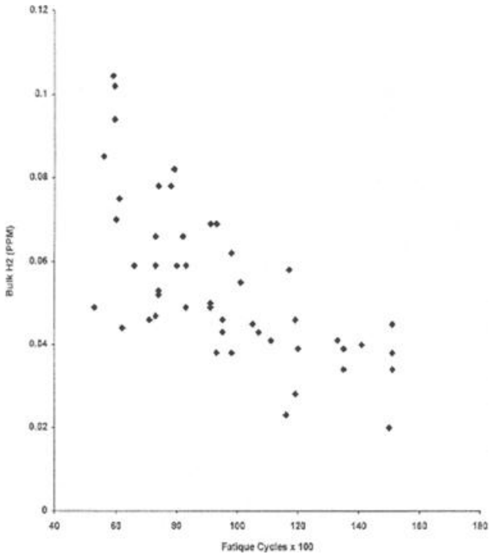

FIG. 1—*Correlation of ingot hydrogen content and fatigue life.*

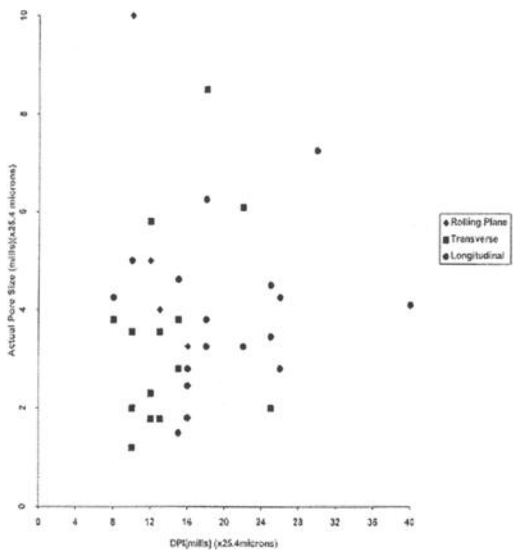

FIG. 2—*Plate pore sizes versus dye penetrant inspection measurements.*

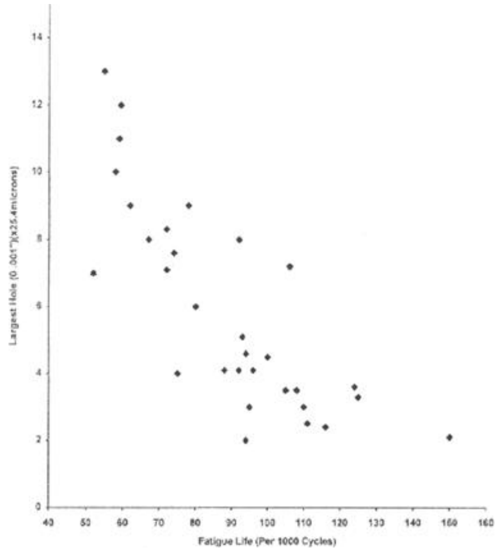

FIG. 3—*7050-T7451 fatigue lives versus T/2 plate pore sizes.*

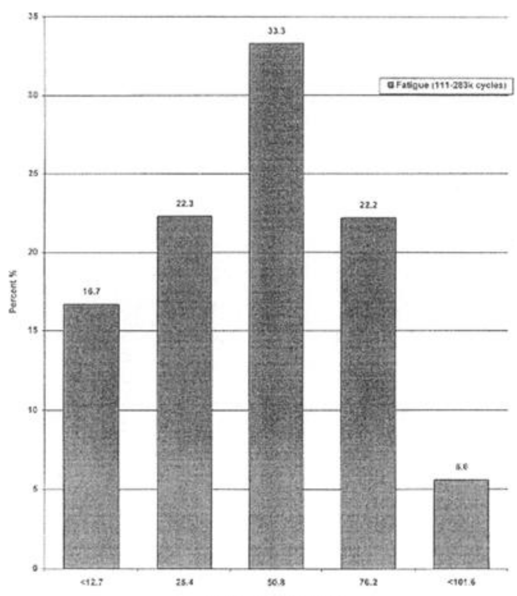

FIG. 4—*Plate pore size distribution in 1989.*

cost/performance tradeoff studies showed promise[5]. Improvements in plate processing equipment also led to increased availability of 7050 plate in thicknesses up to 9 inches (230 mm).

Incremental improvements in the fatigue resistance of Century 7050 thick plate over the past 13 years are shown in Fig. 5, where the percentage of failures versus fatigue cycles for annual collections of receiving inspection tests is shown in the form of a cumulative distribution plot. All of these quality control teswere run at a maximum stress of 30 ksi and a stress ratio of 0.10. These improvements in 7050 thick plate fatigue resistance were achieved through processing improvements that led to incremental reductions in microporosity. Table 1 shows the influence of these systematic changes in casting, hot rolling, and heat treatment on 7050 plate fatigue resistance and the corresponding size range of micropores[4,5].

Table 1 strongly suggests that the processing methods used at Century from 1980 to 1983 contributed to the microporosity problems discovered by Northrop during their FPIs. Since that time period, alternative processing methods were developed at Century through the use of design of experiments (DOE) procedures that led to ongoing reductions in the size range of micropores and marked increases in the percentage of qualification fatigue tests that surpassed 120 000 cycles to failure.

The overall influence of plate processing changes introduced by Century from 1983 to 1995 on the average size of micropores in 7050 thick plate is shown in Fig. 6. The net result has been an 8-fold decrease in nominal pore sizes in 7050 thick plate over a span of 13 years of development work.

Even without evidence, such as that shown in Fig. 3, a correlation between reductions in microporosity and increases in fatigue resistance makes intuitive sense, since it has been known for many years that fatigue crack nucleation is a statistical property that is strongly related to microstructural "defects" such as porosity, and to a lesser extent, to microstructural morphology. Fig. 7 dramatizes this point; two different fracture surfaces are shown, with the crack-nucleating micropore identified in each. The micropores in Figs. 7a and 7b are approximately 0.002 inch (50 μm) and 0.009 inch (230 μm) in diameter, respectively. The fatigue lives of these two specimens, when tested at a maximum stress of 35 ksi (240 MPa) and a stress ratio of 0.10, were 578 662 and 109 227 cycles to failure, respectively. Both of these micropores display features common to the majority of crack initiation sites examined, i.e., they are surface-connected, they are longer in depth (from the specimen surface) than in width (along the specimen surface), and they are irregular in shape. However, about 25 percent of the micropore initiation sites were subsurface, about 30 percent of the fatigue critical micropores were longer at the surface than in depth, and about 20 percent of the fatigue initiating pores were nearly circular in shape. None of these factors were found to influence the resultant fatigue life as strongly as the maximum micropore dimension.

Extensive statistical evidence of the improvement in fatigue resistance of 1994 to 1995 vintage Century 7050 thick plate compared with 1970's vintage plate and forging data is given in this paper, along with a statistical evaluation of the correlation between crack initiation resistance and microporosity.

---

[5] Century Aluminum-Ravenswood Operations Internal Correspondence, 1989 - 1996.

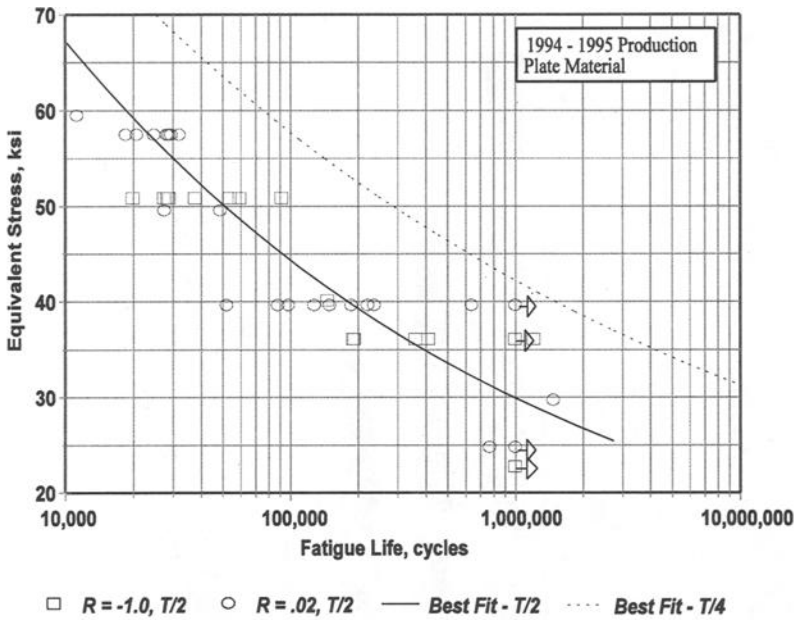

FIG. 5—*Effect of yearly process changes on fatigue life of 5.676-inch (144-mm) thick 7050 plate.*

TABLE 1. Changes in 5 - 6 inch (125 - 150 mm) thick 7050 plate processing have led to significant decreases in microporosity and substantial increases in fatigue crack initiation resistance.

Plate Development Period, year(s)	Casting Variable 1	2	3	4	5	Hot Rolling Variable 1	2	Heat Treatment Method	Average Pore Size Range, inches (μm)	Percentage of Tests with Fatigue Lives >120,000
1980-1983	A	A	A	A	A	A	A	A	N.A.	N.A.
1984-1985	A	B	A	A	A	A	B	A	0.008 - 0.020 (200 - 500)	46
1988-1989	A	C	B	B	A	A	B	A	0.002 - 0.007 (50 - 180)	66
1990-1994	A	C	B	B	B	B	B	A	0.001 - 0.005 (25 - 125)	79
1995	B	D	B	B	B	B	B	B		90
1996	B	D	B	B	C	B	B	B		97

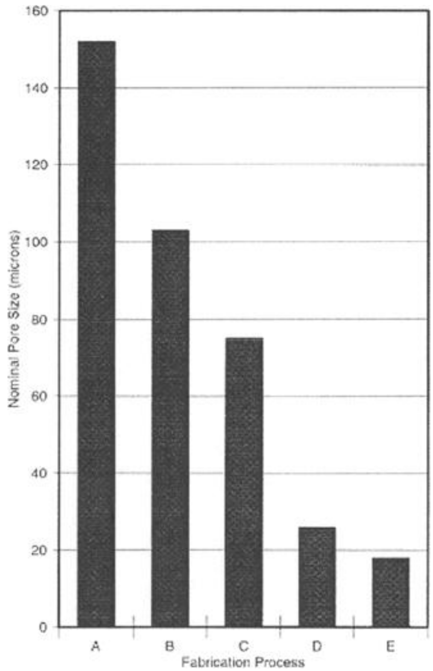

FIG. 6—*Effect of changes in plate fabrication processing on ingot porosity at T/2.*

Experimental Program

Table 2 summarizes the load control test conditions covered in this 7050-T7451 thick plate fatigue evaluation program. Original plate thicknesses varied from 4.00 to 8.50 inches (102 to 216 mm). A total of 116 fatigue tests were performed, as summarized in Appendix A. The test results are arranged in subgroups, first by stress ratio, and second into stress range subgroups.

Test Procedures

All of the load control fatigue tests were completed in accordance with ASTM Practice for Conducting Constant Amplitude Axial Failure Tests of Metallic Materials (ASTM E 466)[6]. These fatigue tests were performed on cylindrical specimens machined with a 1.00 inch (25 mm) gauge length and a 0.30 inch (7.6 mm) diameter test section. The orientation of all specimens within the test plates was L-T. The method of final

[6] ASTM Practice for conducting constant Amplitude Axial Fatigue Tests of Metallic Materials (ASTM E 466).

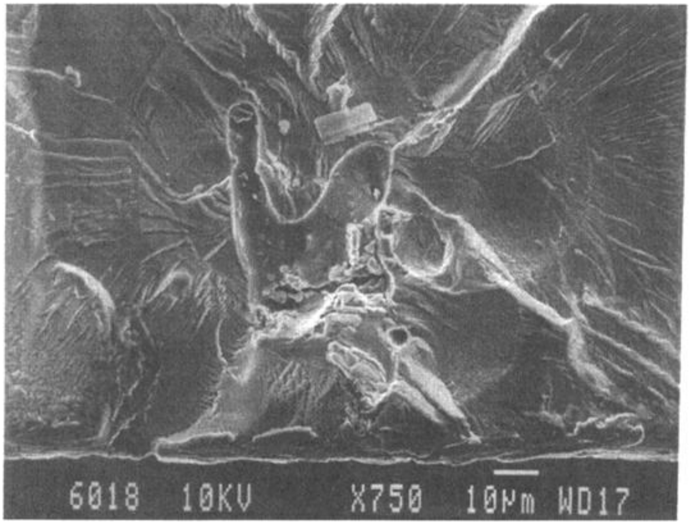

(a) Lot No. 397202, Specimen No. 9, fatigue life of 578,662 cycles

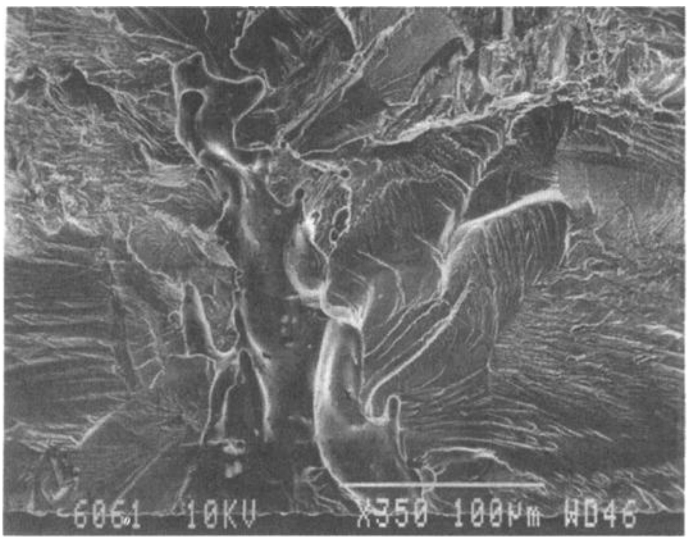

(b) Lot No. 224251, Specimen No. FS2-2, fatigue life of 109,227 cycles

FIG. 7—*SEM photomicrographs of fracture initiation pores.*

TABLE 2. Century 7050-T7451 thick plate load control fatigue data test matrix.

Cyclic Frequency	30 Hz												
Range of Max. Stresses, ksi (MPa)	50 - 60 (345 - 414)		38 - 40 (262 - 276)		35 (241)		30 (207)		25 - 27 (172 - 186)		17 - 22 (117 - 152)		**Specimens per Lot[a]**
Stress Ratio	-1.00	0.02	-1.0	0.02	-1.0	0.02	-1.0	0.02	-1.0	0.02	-1.0	0.02	
Thickness, in. (mm)	**Specimens per Test Condition[a]**												
4.25 (108)	1	2	2										5
4.25 (108)				2	2								4
6.00 (152)			2	2	2	2	2	2					12
4.00 (102)				1*							1*		2*
6.00 (152)									1				1
6.00 (152)											1		1
8.00 (203)			1*	1*					1*		1*		4*
8.00 (203)				1*					1*	2*			4*
8.00 (203)		1*	2*								1*		4*
8.00 (203)		1*	1*							1*	1*		4*
6.00 (152)									2		2		4
4.25 (108)		3*		2*							2*		7*
4.25 (108)			2*						2*	3*			7*
6.50 (165)		2*	1*	3*					2*	3*	3*		14*
6.00 (152)				1*							1*		2*
6.50 (165)		1	2		2								5
7.00 (178)			2		2	2	2						8
8.00 (203)		2*											2*
8.00 (203)		1*		1*			1*	2, 1*					2, 4*
8.00 (203)			2	2	2								6
8.00 (203)						2	2	2					6
8.50 (216)			2		2			2					6
8.00 (203)		2											2
Specimens at R = -1.0	1		12, 8*		12		6, 1*		3, 6*		3, 9*		37, 24*

machining and average surface roughness were not reported. All of the load control tests were run at a cyclic frequency of 30 cycles/second (Hz).

Statistical Data Summary

A statistical summary of the Century 7050 thick plate fatigue data considered in this analysis is provided in Table 3. The sample statistics for the various subgroups are provided in terms of their logarithmic mean and standard deviation. This has been done because of the typical tendency for fatigue data to conform to a log-normal distribution [3,4]. This tendency was evaluated in the case of the Century data by plotting two of the largest data subsets at the T/4 location on log-normal probability paper as shown in Fig. 8. Individual fatigue lives for each maximum stress level for the R = -1.0, load control experiments were plotted according to median ranks [5] for the appropriate sample sizes. If the fatigue data followed a log-normal distribution exactly, all of the data for each maximum stress level would have fallen on a straight line. This was clearly not

TABLE 3. Summary of load control fatigue test data for 7050-T7451 thick plate.

Specimen Location	Stress Ratio	Maximum Stress, ksi (MPa)	Sample Size (Number of Discontinued Tests)	Log (Fatigue Life)	
				Average	Std. Dev.
T/4	-1.0	50.0 (345)	1	4.036	---
		40.0 (276)	12	4.690	0.111
		35.0 (241)	12	5.154	0.180
		30.0 (207)	6	5.722	0.201
		26.0 (179)	3	6.128	0.047
		22.0 (152)	3	6.538	0.065
	0.02	50.0 (345)	5	5.463	0.228
		40.0 (276)	6	6.486	0.081
		35.0 (241)	6	6.657	0.090
		30.0 (207)	8 (5)	7.008[a]	0.051[a]
T/2	-1.0	38.0 (262)	8	4.587	0.205
		30.0 (207)	1	5.166	---
		27.0 (186)	6	5.637	0.313
		17.0 (117)	9 (9)	6.000[a]	---
	0.02	60.0 (414)	1	4.050	---
		58.0 (400)	7	4.408	0.081
		50.0 (345)	2	4.564	0.124
		40.0 (276)	10 (1)	5.273[a]	0.369[a]
		30.0 (207)	1	6.168	---
		25.0 (172)	9 (8)	5.987[a]	0.036[a]

[a] Includes discontinued tests, which reduced the group average and group standard deviation.

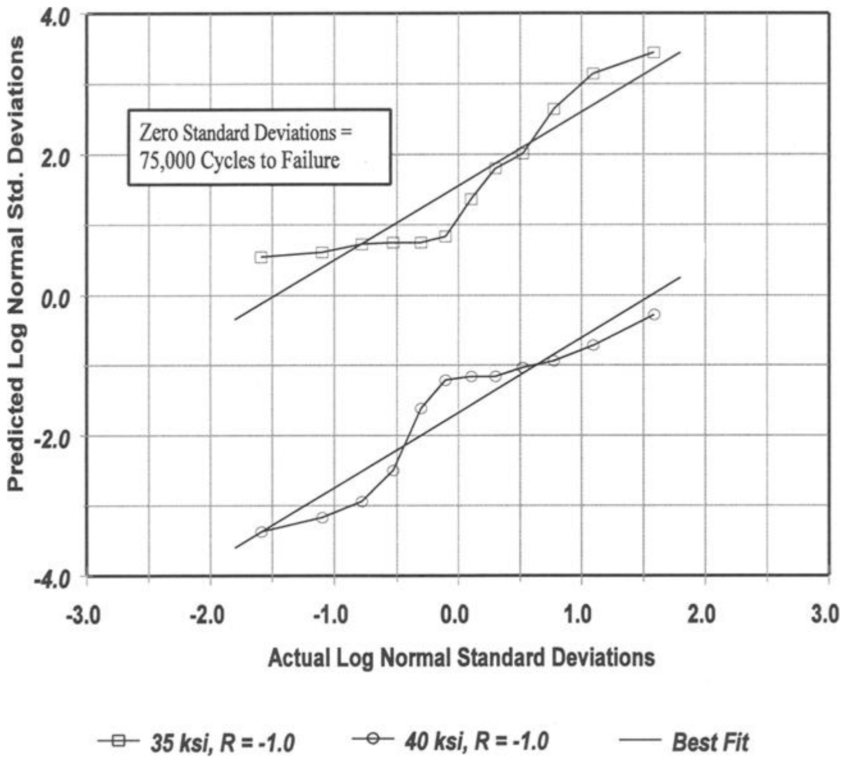

FIG. 8—*Statistical distribution of fatigue lives, T/4 specimen location, R = -1.0,* S_{max} *= 35 and 40 ksi (241 and 276 MPA).*

the case with these data, which suggested that some other variable was influencing the distribution of fatigue lives. The most obvious variable to consider was product thickness, as discussed in the next section.

Load Control Fatigue Data Analysis

Mean stress effects on the load control fatigue data trends were modeled through the use of an equivalent stress parameter developed by Walker [6,7]

$$S_{eq} = S_{max} \bullet (1 - R)^m \quad , \tag{1}$$

where

S_{eq}	=	equivalent stress, ksi
S_{max}	=	maximum cyclic stress, ksi
R	=	stress ratio = S_{min}/S_{max}
S_{min}	=	minimum cyclic stress, ksi
m	=	optimized mean stress exponent.

The exponent, *m*, in Eq. 1 can vary between 0.0 and 1.0. If *m* is set to zero, Eq. 1 implies that the influence of the maximum stress, S_{max} , on fatigue life is independent of the stress ratio, R. If *m* is set to unity, Eq. 1 implies that the influence of the stress range, ΔS, on fatigue life is independent of the stress ratio. Intermediate values of *m* imply a synergistic influence of maximum stress and stress ratio on fatigue life. Optimum values of *m* for most engineering materials have been found to fall in the range of 0.3 - 0.7.

Significantly different trends in stress/fatigue life (S/N) fatigue behavior were observed for the T/4 and T/2 specimen location data, which prompted separate treatment in each of the following subsections. In each case a relationship between fatigue life and equivalent stress was established through optimization of the following expression:

$$\log(N_f) = A_0 + A_1 \cdot \log(S_{eq} - A_2) \qquad (S_{eq}\ ,\ ksi), \tag{2}$$

where

N_f	=	fatigue cycles for failure
A_0	=	optimzed intercept
A_1	=	optimized slope
A_2	=	estimated fatigue limit.

Eq. 2 is mathematically nonlinear when the optimum value of A_2 is greater than zero (which implies a fatigue limit in the S/N fatigue data trends). When the optimum value of A_2 equals zero, Eq. 2 reduces to a log-linear relationship between S_{eq} and fatigue life.

Equivalent Stress Fatigue Analysis

T/4 Location — The Century 7050 thick plate load control fatigue data for specimens removed from the T/4 location are plotted in terms of Eq. 2 in Fig. 9. The optimum mean stress parameter, *m*, (from Eq. 1) for this analysis was found to be 0.65. The best-fit parameters for the fatigue life model described in Eq. 2 was found through iteration as follows:

$$\log(N_f) = 16.41 - 6.624 \cdot \log(S_{eq} - 5.0) \qquad (S_{eq}\ ,\ ksi). \tag{3}$$

There are some minor deviations from the predicted trends of equivalent stress versus fatigue life in Fig. 9, such as the clustering of R = 0.02 data slightly above the mean curve at an equivalent stress of nearly 40 ksi (276 MPa), and the similar clustering of R = 0.02 data slightly below the mean curve at the lowest equivalent stress of nearly 30 ksi (207 MPa). However, it should be noted at this lowest equivalent stress level, that the majority of these observations were discontinued tests, meaning that most of them did not end with specimen failures, and their actual cycles to failure would almost certainly have significantly exceeded their test termination point. Overall, the Walker equivalent stress parameter provided a reasonable representation of the load control fatigue data trends for both stress ratios covering fatigue lives ranging from 10^4 to 10^7 cycles to failure. Therefore, it was used as the basis for construction of stress versus life fatigue data curves and for evaluating the effect of specimen location on fatigue behavior.

The R^2 statistic for the regression defined in Eq. 2 and shown in Fig. 9 was 95.0 percent, with a standard error of estimate, SEE, of only 0.183. The R^2 statistic is higher and the SEE value is lower than the parameters currently defined within Ref. [*8*] for this alloy, product form, and specimen orientation. These statistics indicate an unusually low level of variability in the fatigue resistance of specimens removed from the T/4 location of the Century 7050-T7451 thick plate material.

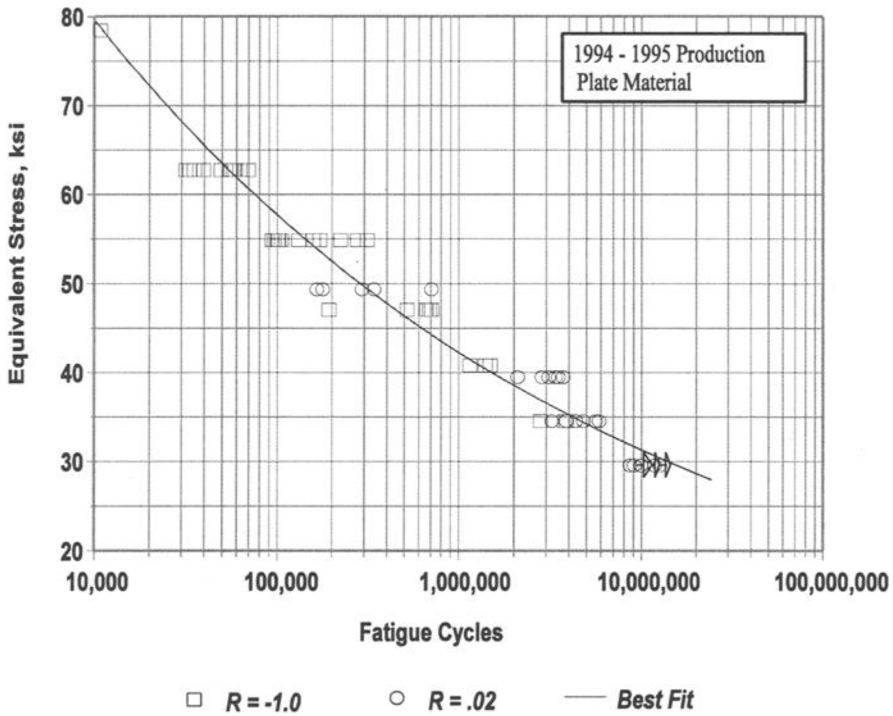

FIG. 9—*Equivalent stress versus fatigue life for Century 7050-T7451 thick plate, T/4 specimen location.*

The symbols shown in Fig. 9 with right-pointing arrows represent one or more discontinued tests, or runouts. Only runout points falling above the mean fatigue curve were included in the regression analysis to avoid artificially high residuals associated with fatigue tests discontinued well before their expected fatigue life.

T/2 Location — The Century 7050 thick plate load control fatigue data for specimens removed from the T/2 location are plotted in terms of Eq. 2 in Fig. 10. The optimum mean stress parameter, *m*, (Eq. 1) for this analysis was 0.42, which was much lower than for the T/4 location material. This lower *m* value indicates a stronger influence of maximum stress on fatigue life and a weaker influence of stress range on fatigue life for the T/2, mid-thickness location, as compared to the T/4 location. The best-fit parameters for the fatigue life model (Eq. 2) were also considerably different for the T/2 location material:

$$\log(N_f) = 12.92 - 4.976 \cdot \log(S_{eq} - 5.0) \qquad (S_{eq}\ ,\ ksi). \qquad (4)$$

In this case, the fatigue limit term of 5.0 ksi in Eq. 4 was not established through an optimization procedure, it was simply set at the same value as in Eq. 3, since it simplified comparisons between the two sets of S/N curves, and Eq. 4 provided a near-optimum fit to the data (the R^2 value for Eq. 4 with A_3 set equal to 5.0 ksi was within 0.2 percent of optimum).

The T/2 S/N fatigue data are plotted in terms of equivalent stress in Fig. 10, along with the fatigue life curve defined in Eq. 4. A comparison of Figs. 9 and 10 shows much less variability in the T/4 fatigue data compared to the T/2 fatigue data. The high level of variability in the fatigue data on specimens removed from the T/2 location is reflected in an R^2 statistic of only 76.4 percent and an SEE of 0.294. It will be demonstrated later in this section that variations in mid-thickness fatigue properties of the 7050-T7451 product as a function of plate thickness contribute greatly to the high level of variability in the overall T/2 dataset.

Stress-Life Fatigue Data Trends

T/4 Location — The equivalent stress/fatigue life formula given in Eq. 3 and shown in Fig. 9 was converted into a maximum S/N plot such as is represented in Ref. [*8*] by inserting the stress ratios used for the Century fatigue testing program into Eq. 3 and calculating estimated fatigue lives for the desired range of maximum stresses. The results of this exercise are shown in Fig. 11.

T/2 Location — In the same manner, the equivalent stress/fatigue life formula given in Eq. 4 and shown in Fig. 10 was converted into maximum stress versus fatigue life curves as shown in Fig. 12. Note the smaller vertical spacing of the two S/N curves for the T/2 data shown in Fig. 12, as compared to the vertical spacing of the two S/N curves for the T/4 data shown earlier in Fig. 11. This comparison provides a pictorial

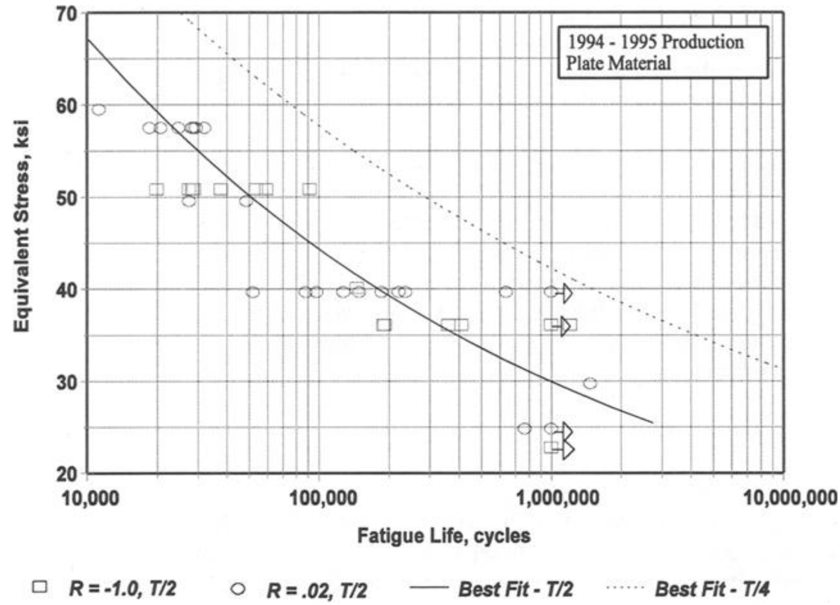

FIG. 10—*Equivalent stress versus fatigue life for Century 7050-T7451 thick plate, T/2 specimen location.*

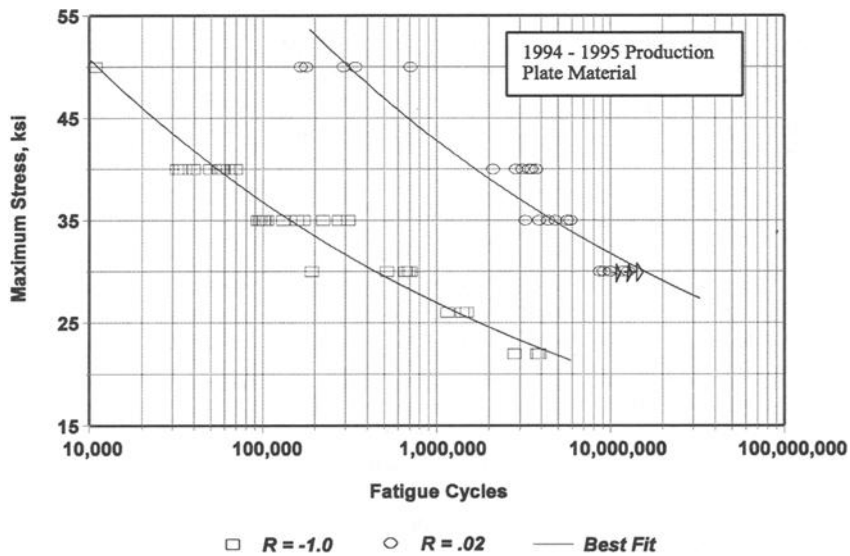

FIG. 11—*Maximum stress versus fatigue life for Century 7050-T7451 thick plate, T/4 specimen location.*

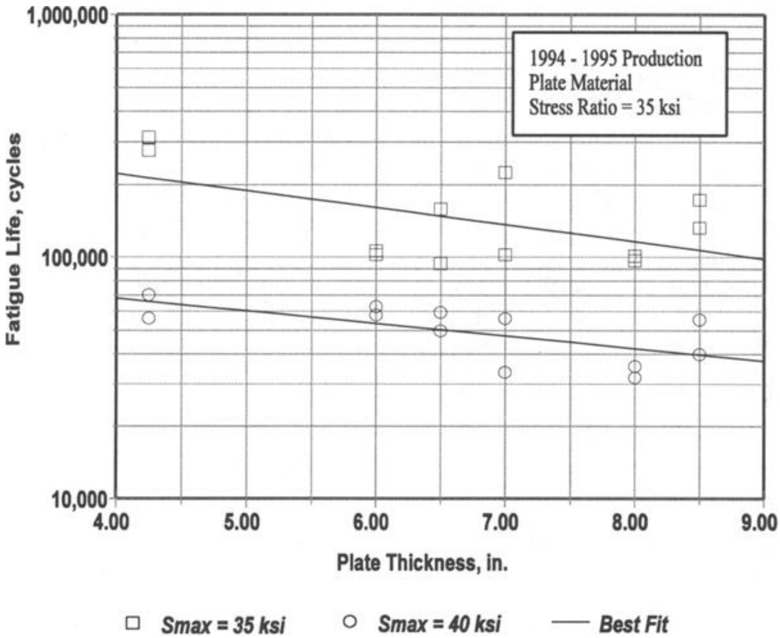

FIG. 12—*Maximum stress versus fatigue life for Century 7050-T7451 thick plate, T/2 specimen location.*

representation of the effect of a smaller optimized m value in the Walker equivalent stress formulation on the resultant maximum stress versus fatigue life curves.

Both S/N fatigue curves (R = -1.0 and R = 0.02) for the T/2 material fall below the T/4 S/N curves. These results illustrate the adverse effect of mid-plane microporosity on the fatigue resistance of 7050-T7451 thick plate. However, as will be shown later in this paper, the current T/2 mean fatigue curves represent a major improvement in fatigue resistance compared to similar curves established 20 years ago on the same alloy and product form. This improvement can be attributed primarily to the processing changes that have been made to substantially reduce the size distributions of mid-plane microporosity.

The smaller separation of the R = -1.0 and 0.02 S/N curves (at a given fatigue life) for the T/2 data compared to the T/4 data leads to another interesting consideration. The point has already been made that the difference in the T/4 and T/2 fatigue properties is likely to result primarily from the residual mid-plane microporosity. If it is assumed that these mid-plane micropores approximate small pre-existing cracks, it is logical to argue that the degradation due to these pre-existing cracks should be more severe in terms of the specimen's crack growth life (i.e., the duration of the fatigue test) for the R = 0.02 condition, than for the R = -1.0 condition, because it has been extensively observed that the compressive portion of a fatigue cycle is largely non-damaging in terms of crack growth.

Effect of Product Thickness on Fatigue Behavior

T/4 Location — A modest influence of product thickness on load control fatigue lives is evident in Fig. 13. This figure shows fatigue cycles to failure for 12 load control fatigue tests run at each of two maximum stress levels of 35 and 40 ksi (241 and 276 MPa). These specimens were removed from the T/4 location within 7050-T7451 alloy plates that ranged in thickness from 4.25 to 8.50 inches (108 to 216 mm). Duplicate tests were run at each stress level on six different lots of material spanning the overall thickness range.

Linear regression analyses on each set of data showed that the effect of plate thickness, t (in.), was significant in both cases, at greater than a 90 percent confidence level. The best-fit linear regression equations for the two stress levels are as follows:

$$\log(N_f) = 5.63 - 0.0705 \cdot t \qquad \text{for } S_{max} = 35\ ksi,\ R = -1.0 \tag{5}$$

and

$$\log(N_f) = 5.04 - 0.0517 \cdot t \qquad \text{for } S_{max} = 40\ ksi,\ R = -1.0 \tag{6}$$

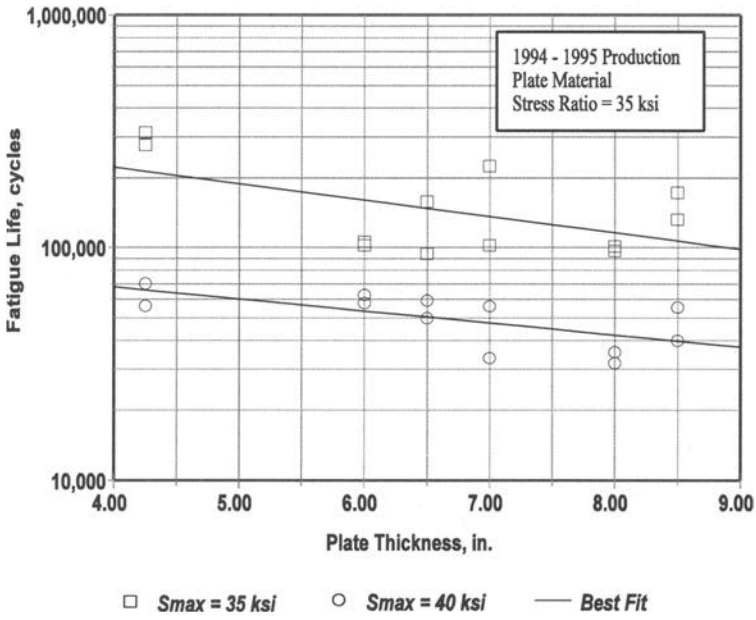

FIG. 13—*Fatigue life versus product thickness for Century 7050-T7451 thick plate, T/4 specimen location.*

Translated to customary units, these equations show expected fatigue lives of approximately 66 000 and 40 000 cycles to failure for 4.25- and 8.50-inch (108- and 216-mm) thick plate, respectively, at 40 ksi (276 MPa) and 214 000 and 111 800 cycles to failure for the same product thicknesses at 35 ksi (241 MPa). Of course, individual fatigue lives are expected to scatter about these average trend lines.

To assess the variability in fatigue lives about these regression lines, an analysis of the residuals (deviations of individual points from their regression line) was completed. The results of these analyses are shown in Fig. 14, which is a log-normal probability plot, similar to Fig. 8, shown previously for the same fatigue data, without regard to product thickness. Since residuals were plotted in this case, rather than actual fatigue lives, it was possible to group the data for the two different (but similar) stress conditions into a single distribution. The close alignment of these data to a straight line reinforces the argument that the scatter in the Century fatigue data can be well represented by a log-normal distribution, as long as the effects of product thickness are taken into account. Deviations from linearity at both extremes of this cumulative distribution plot may suggest problems with this assumption for very low or high probability failures, but there were insufficient

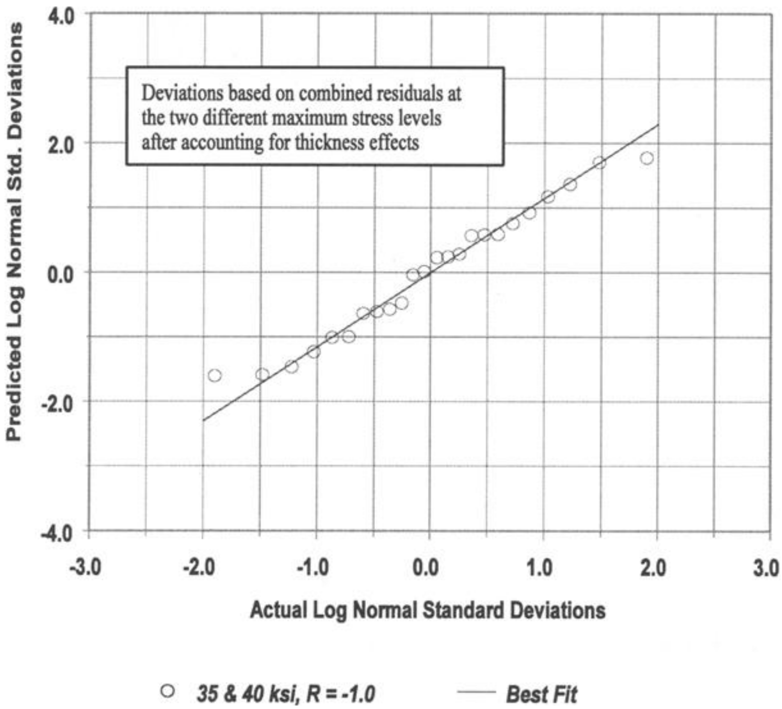

FIG. 14—*Standardized statistical distribution of fatigue lives accounting for thickness effects.*

data to model failure probabilities below about 0.05 or above 0.95 (± 1.64 standard deviations from the mean).

The standard error of estimate (a measure of the variability of the data about the regression line) for the effect of thickness on fatigue life regression was approximately 0.16 on a mean fatigue life (log base 10) of approximately 5.0, which translates to a coefficient of variation (standard deviation divided by the mean) of only about 3.2 percent. This level of variability in fatigue data is quite low compared to many other fatigue data displays for aluminum alloys, such as in MIL-HDBK-5 [*8*].

T/2 Location — Over 50 load control fatigue tests were also performed on specimens removed from the T/2 location of the thick plates, rather than the traditional T/4 location. These tests were completed to evaluate the extent of change in fatigue properties at the plate mid-thickness, where porosity could be expected to be greatest, especially in the thickest plate gauges. The effect of plate thickness on load control fatigue properties is shown in Fig. 15. Each of the curves shown was established through

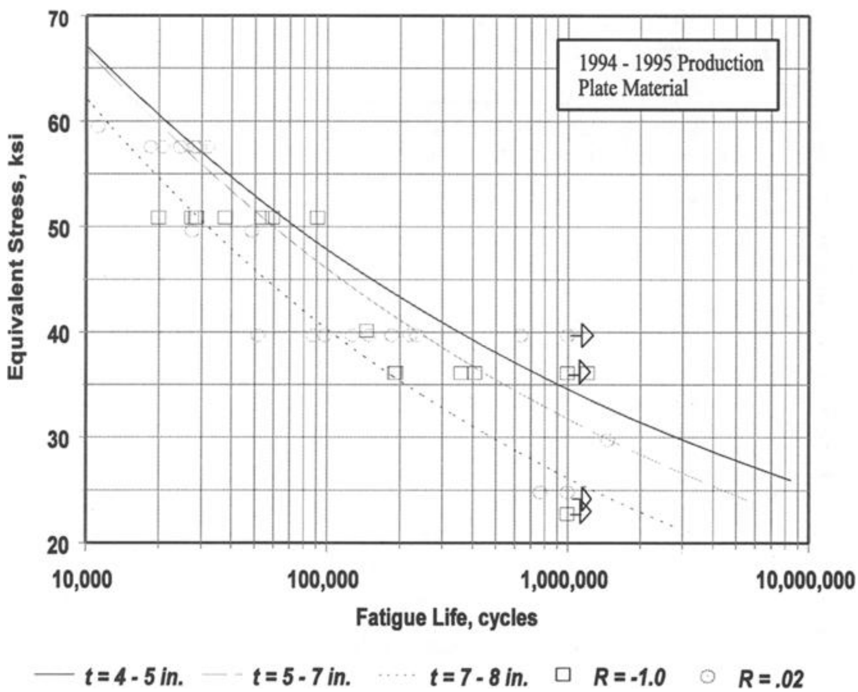

FIG. 15—*Equivalent stress versus fatigue life for Century 7050-T7451 thick plate, T/2 specimen location, product thicknesses of 4.25, 6.50, and 8.00 inches (108, 165, and 203 mm).*

separate equivalent stress analyses on specimens removed from three different thickness ranges of plate material.

Clearly distinct equivalent stress fatigue curves were established for the T/2 material removed from nominally 4.25-, 6.50-, and 8.00-inch (108-, 165-, and 203-mm) thick plate. As expected, the mid-plane fatigue lives were the highest for the 4.25-inch (108-mm) thick plate material, with the T/2 fatigue lives being somewhat lower for the 6.50-inch (165-mm) thickness, and even lower for the 8.00-inch (203-mm) thickness. The difference in mid-plane fatigue properties between the thinnest and thickest plates was only about a factor of two at the highest equivalent stress levels, but the difference in fatigue lives increased to over a factor of five at the lowest equivalent stress levels.

Using the three separate equivalent stress expressions for each of the thickness ranges, three different maximum stress versus fatigue life curves were developed, as shown in Fig. 16. The mathematical expression for the fatigue curves representing the 4.25-inch (108-mm) thick plate material shown in Fig. 16(a) is:

$$\log(N_f) = 15.123 - 6.230 \cdot \log(S_{eq} - 5.0) \tag{7}$$

The equivalent stress equation for the fatigue curves representing the 6.50-inch (165-mm) thick plate material shown in Fig. 16(b) is:

$$\log(N_f) = 15.308 - 6.197 \cdot \log(S_{eq}) \tag{8}$$

The most obvious difference between Eqs. 7 and 8 is the absence of a fatigue limit term in the second equation. With the available data, there was no evidence of a fatigue limit in the 6.50-inch (165-mm) thick plate material. This difference between Eqs. 7 and 8 is evident in Fig. 15, in that the equivalent stress fatigue life trends for the 6.50-inch thick material tend to diverge from the trends for the 4.25-inch (108-mm) thick material at long fatigue lives. The equivalent stress equation for the fatigue curves representing the 8.00-inch (203-mm) thick material shown in Fig. 16(c) is:

$$\log(N_f) = 13.538 - 5.317 \cdot \log(S_{eq}) \tag{9}$$

Eq. 9 and Fig. 16(c) show lower fatigue lives at the mid-plane of 8.00-inch (203-mm) thick plate, as compared to the mid-plane of both the 4.25- and 6.50-inch (108- and 165-mm) thick plate materials. The fatigue data for the 8.00-inch (203-mm) thick plate also showed no evidence of a fatigue limit. It is well known that it is more difficult to break up the mid-plane porosity during processing of 8.00-inch (203-mm) thick plate than it is with thinner plates. Current aluminum plate processing technology allows very substantial sealing of mid-plane porosity in aluminum plates as thin as 4.25 inches (108 mm), but aluminum plates thicker than 6.50 inches (165 mm) offer a much greater challenge in terms of sealing of mid-plane porosity.

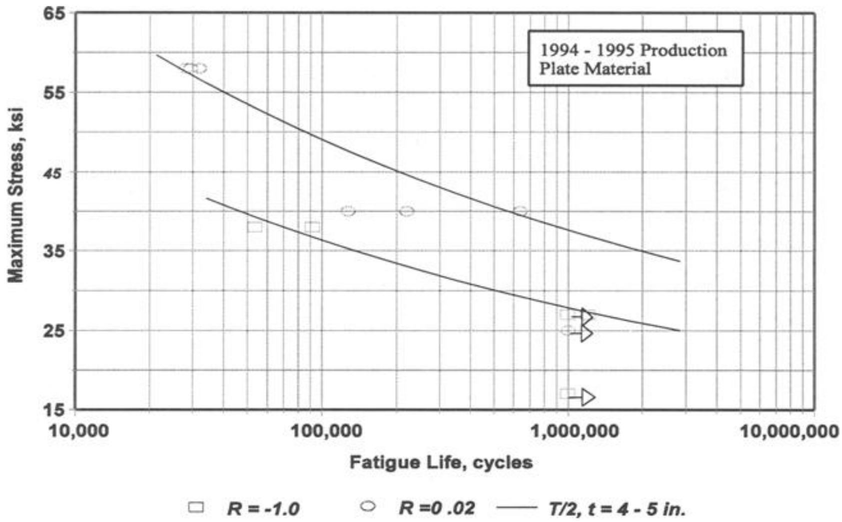

(a)--product thickness of 4.25 inches (108 mm)

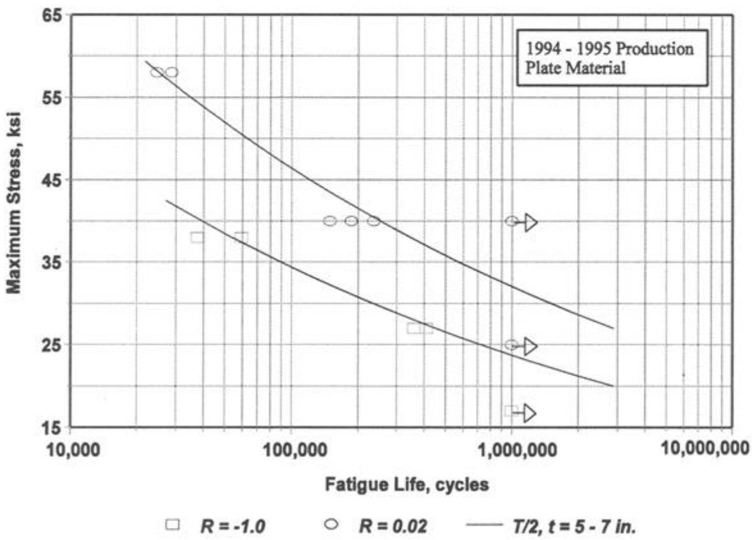

(b)--product thickness of 6.50 inches (165 mm)

FIG. 16—*Maximum stress versus fatigue life for Century 7050-T7451 thick plate, T/2 specimen location.*

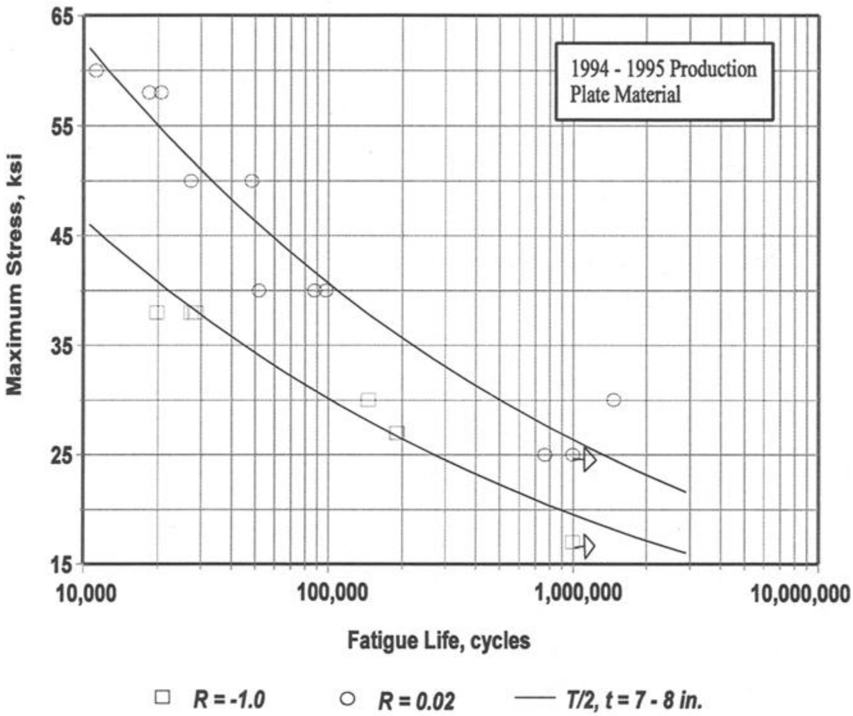

(c)--product thickness of 8.00 inches (203 mm)

FIG 16—*Continued.*

Comparative Assessment of 7050 Fatigue Data

To put the impact of these new aluminum plate processing techniques into perspective in terms of thick plate fatigue properties, some comparisons were made with 7050 thick plate fatigue data available from other sources. Load control fatigue data on 7050-T7451 from three other sources were identified and are documented in this section, and comparisons are made to 1994 to 1995 vintage Century 7050 thick plate fatigue data.

Fatigue Data from Other Sources

MIL-HDBK-5 [*8*] includes load control fatigue data on 1.00 to 6.00-inch (25.4- to 152-mm) thick 7050-T7451 [*9-10*][7] plate representing the same long transverse direction that was characterized in Ref. [*11*]. These data were taken from the T/2 location for plate thicknesses up to 1.5 inches (38 mm) and at the T/4 location for plate thicknesses greater than 1.5 inches (38 mm), as specified in Ref. [*8*]. Comparable plate fatigue data on unnotched specimens taken from the longitudinal direction, as well as comparable hand and die forging data on unnotched specimens, are also included.

A second, very recent and significant source of fatigue data for 7050-T7451 plate, 5.7- to 6.0-inches (145- to 152-mm) in thickness is Ref. [*12*]. This report includes four tables of unnotched, L-T orientation, load control fatigue data on this material representing so-called old-material, now-material, low porosity material, and 1 inch thick plate material. It is important to note that all of these data were generated from specimens excised from the T/2 location. The fatigue life results for these four conditions are summarized in a cumulative distribution plot reproduced in Fig. 17.

Ref. [*12*] also contains detailed information on the size of the micropores or microstructural features that are believed to have caused the fatigue failure. A portion of these data, representing the so-called *old* and *now* technology plate material, were compiled and analyzed as shown in Fig. 18. These two sets of data represent tests run at a maximum stress of 35 ksi (241 MPA) and a stress ratio of 0.10. Although there is substantial scatter in the data, a log-linear trend is evident between maximum pore size and fatigue life. Some very large pores, up to 0.030 inch (760 μm) in diameter are shown to represent the *old* technology plate material. The equation for the mean (solid) line is given by the following expression:

$$\log(N_f) = 3.733 - 0.600 \cdot \log(P_d) \tag{10}$$

where P_d is the pore diameter in inches. The standard error of estimate of the data about the mean regression line is 0.0794. The dashed lines shown in Fig. 18 represent $\pm$ 2.0 SEE; they bound the large majority of the observations, particularly on the lower bound side of the data.

Fig. 18 is replotted in Fig. 19 in more easily interpreted arithmetic units for pore diameter, with Fig. 19(a) displaying the data in terms of inches, and Fig. 19(b) displaying the data in terms of microns.

Comparable pore size versus fatigue life data developed from a sampling of recently produced Century 7050 plate material are shown in Fig. 20. The maximum pore sizes have been normalized, but the positive correlation between micropore size and fatigue resistance is evident, as shown in Fig. 18 [*12*].

---

[7] Unpublished letter to P. Vieth, Battelle, Columbus, Ohio, from Alcoa, "Fatigue Data for 7050 and 7475 Products," Aluminum Company of America, July 17, 1985.

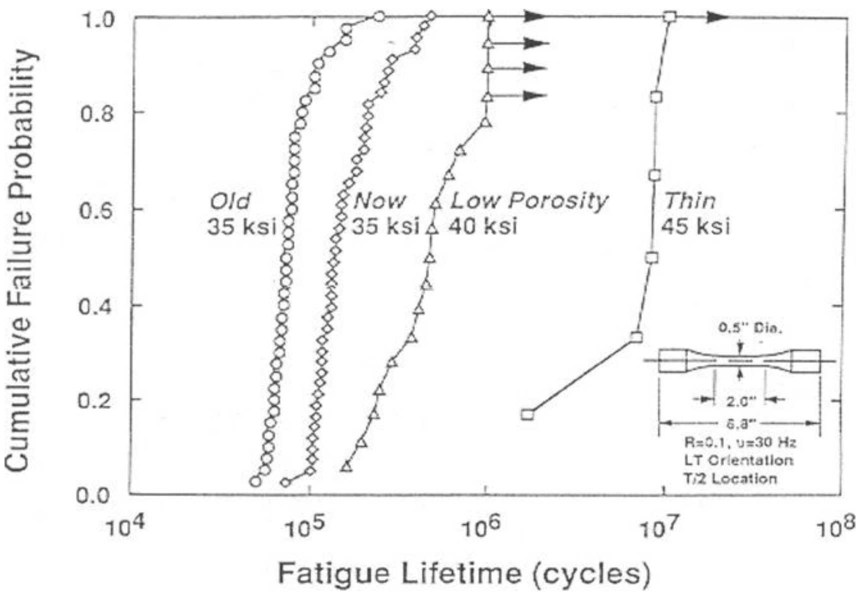

FIG. 17—*Cumulative fatigue lifetime distributions for four microstructural variants (Fig. 2.4 from Ref. [18]).*

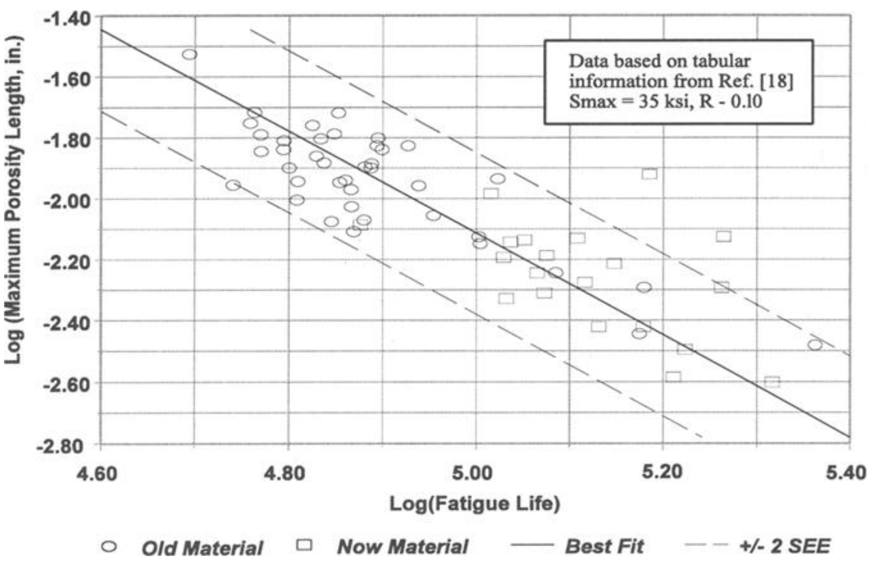

FIG. 18—*Logarithmic display of critical pore size versus fatigue life for 7050-T7451, T/2 specimen location, 5.70-inch (145-mm) thick plate (derived from Ref. [18]).*

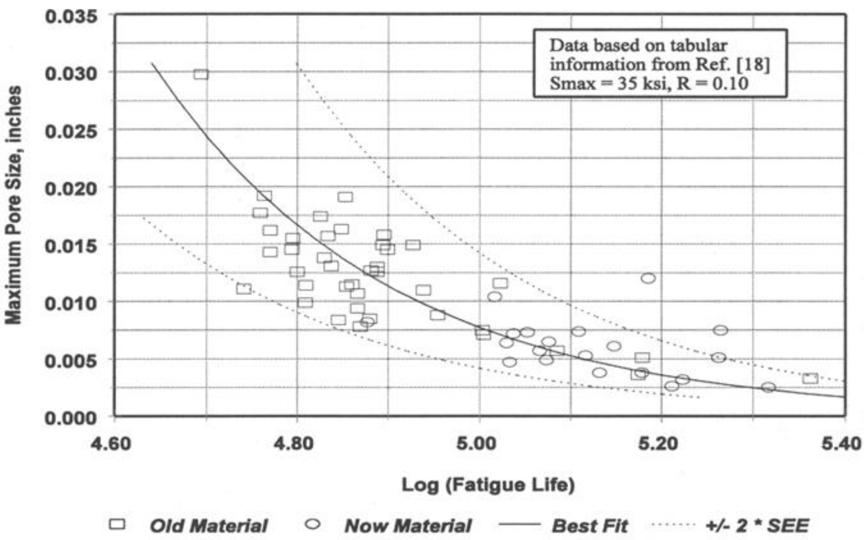

(a)--maximum porosity length in English units

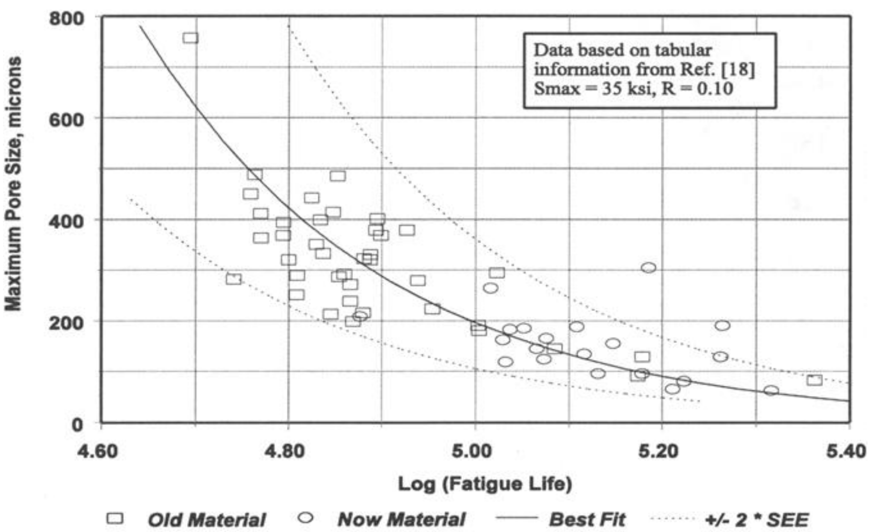

(b)--maximum porosity length in Metric units

FIG. 19—*Semi-logarithmic display of critical pore size versus fatigue life for 7050-T7451, T/2 specimen location, 5.70-inch (145-mm) thick plate (derived from Ref. [18]).*

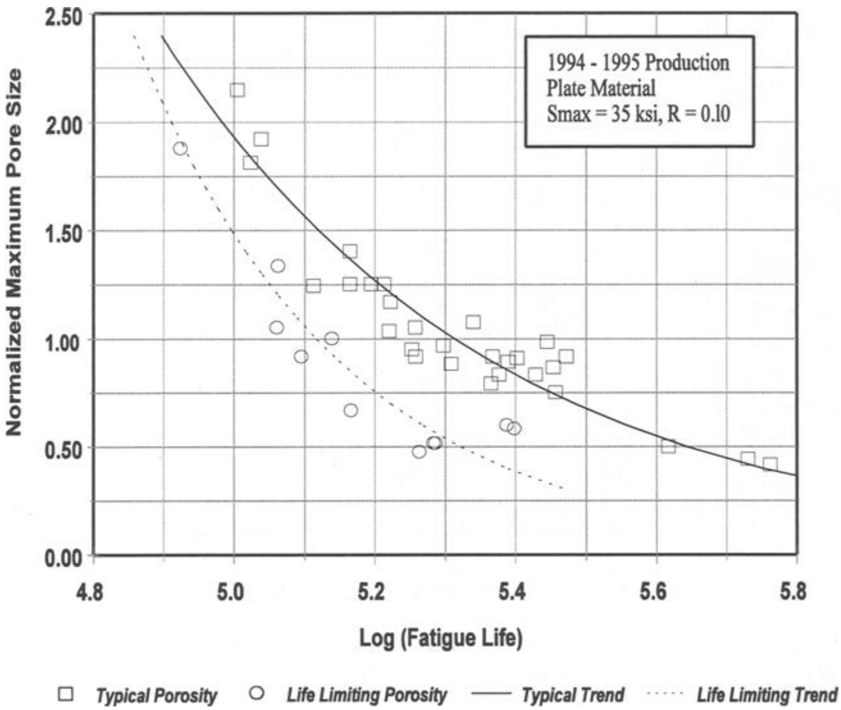

FIG. 20—*Comparison of critical pore size versus fatigue life data trends from Ref [18] with comparable data trends on Century 7050-T7451, 4.25- to 8.50-inch (108- to 216-mm) thick plate.*

The third source of fatigue data for this alloy and product form was obtained from Ref. [*13*], which included a summary diagram from Ref. [*14*]. The fatigue data from Ref. [*14*] represent two different microstructures of the 7050 alloy (a fine, equiaxed grain structure and pancake-shaped grains) as shown in Fig. 21. This source did not identify significant differences in fatigue resistance between these two microstructures. Unfortunately, the stress ratio at which these experiments were performed was not identified, which eliminated these data from further consideration in this study.

Comparison of Fatigue Properties to Data Within Ref. [8]

A comparison of the equivalent stress equation for the fatigue data displayed in MIL-HDBK-5 [*8*] to the one developed to represent the current Century material is shown in Fig. 22. It is important to note, with regard to the MIL-HDBK-5 data, that a large percentage of the data represent the T/2 location for 1 inch (25.4-mm) thick plate. About

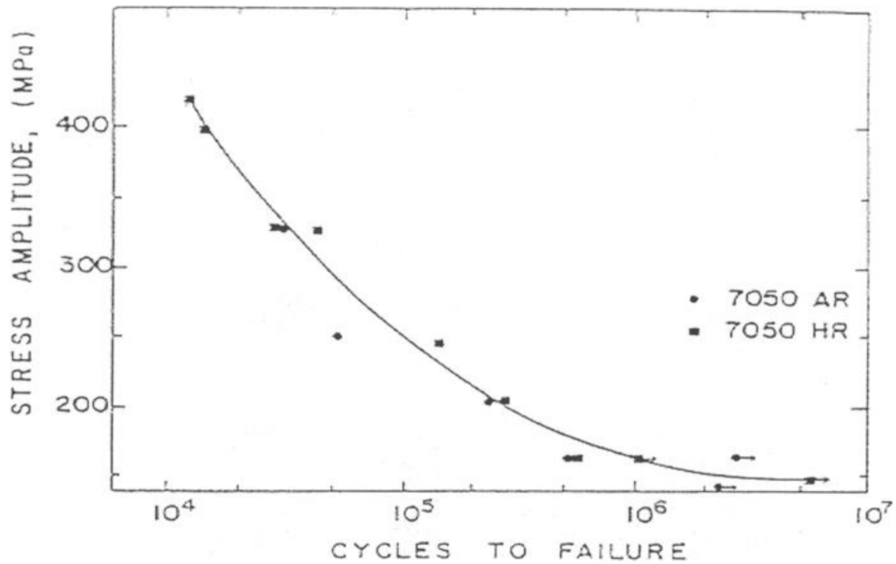

FIG. 21—*Stress-life curves for two 7050 alloys having fine, equiaxed grain (AR) and pancake-shaped grains (HR) (Fig. 12-35 from Ref. [19]).*

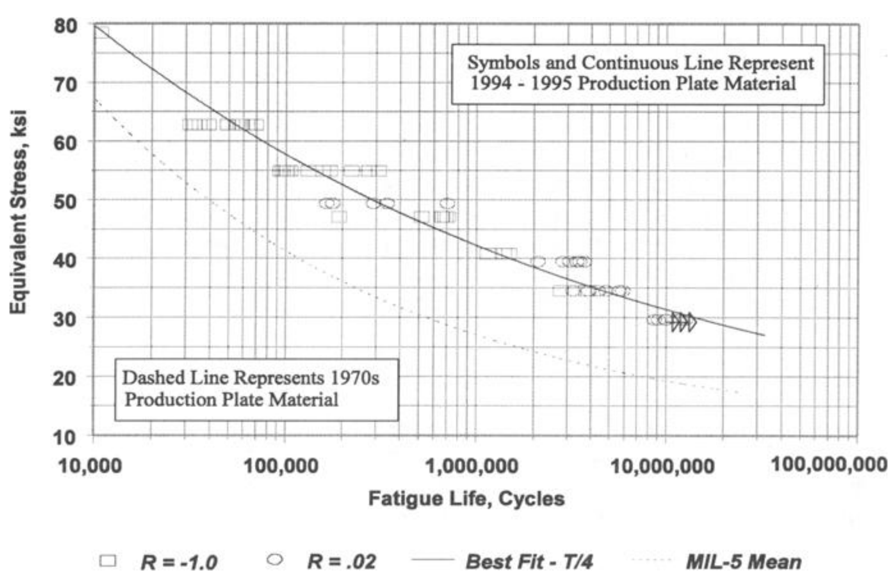

FIG. 22—*Comparison of Century 7050-T7451 thick plate fatigue data trends with comparable L-T orientation data within MIL-HDBK-5 [2].*

15 of the data points represent the T/4 location from thicker plates of 2 to 6 inches (50.8 to 152 mm) in thickness. There are no T/2 location, L-T orientation, fatigue data represented in MIL-HDBK-5 [*8*] for thick plate in the range documented in the present study. Therefore, it was not possible to make a direct comparison between the Century thick plate T/2 data and comparable data from other sources. The point is made in Ref. [*9*] that the T/2 fatigue data for the 1 inch (25.4 mm) thick plate were comparable to the T/4 fatigue data for the 2.00- to 6.00-inch (50.8- to 152-mm) thick plates, which is not surprising since very good (low porosity) mid-section fatigue properties would be expected in a relatively thin, 1 inch (25.4 mm) thick plate. Therefore, it is logical to conclude that the comparison made in Fig. 22 is essentially a comparison between published T/4, L-T orientation, thick plate fatigue properties, and fatigue properties for current Century thick plate production that extends to even greater thicknesses of up to 8.5 inches (216 mm).

Two substantial points can be made with regard to the comparison of fatigue properties shown in Fig. 22. First, the variability in the MIL-HDBK-5 data [*8*], as quantified by an SEE of 0.507, is 2.5 times as great as the Century data for the same alloy, product form, and specimen orientation. Second, the mean trends of the MIL-HDBK-5 data [*8*] fall well below the lower extremes of the Century 7050 thick plate data, with the mean Century curve falling at 3 times the number of cycles to failure as the MIL-HDBK-5 curve at high equivalent stress values and falling at over 10 times the number of cycles to failure at low equivalent stress values.

A broader comparison of the Century 7050 thick plate fatigue data trends is made in Fig. 23 relative to other specimen orientations (grain directions) and product forms represented in MIL-HDBK-5 [*8*]. Five other mean trend lines are displayed relative to the Century mean curve, they represent L and L-T orientation plate data, L and L-T orientation hand forging data, and L-T orientation die forging data. The mean fatigue life trends of the Century data show higher fatigue lives compared to all of the other curves at virtually all equivalent stress levels, regardless of the specimen orientation (grain direction) or product form. However, it is important to remember, as noted earlier, that the data for these other grain directions and product forms is representative of technology that is approximately two decades old; new fatigue data on current technology forgings would probably be significantly superior to that presently shown in MIL-HDBK-5.

Comparison of Fatigue Properties to Data from Other Sources

The fatigue data presented in Ref. [*12*] are relevant to the performance of the Century 7050 thick plate material because this study was done to investigate the linkage(s) between microstructural characteristics and fatigue performance in an aluminum alloy typically used in airframe structural applications, and the alloy studied in detail was 7050-T7451 thick plate.

The unnotched specimen fatigue data documented in Ref. [*12*] represent essentially four different quality levels. These levels, in ascending order of quality, are described as *old* material, *now* material, *low porosity* material, and *thin* material. *Old* material is described as plate fabricated using production practices typical of those used prior to 1984. This quality level is characterized by significant levels of microporosity

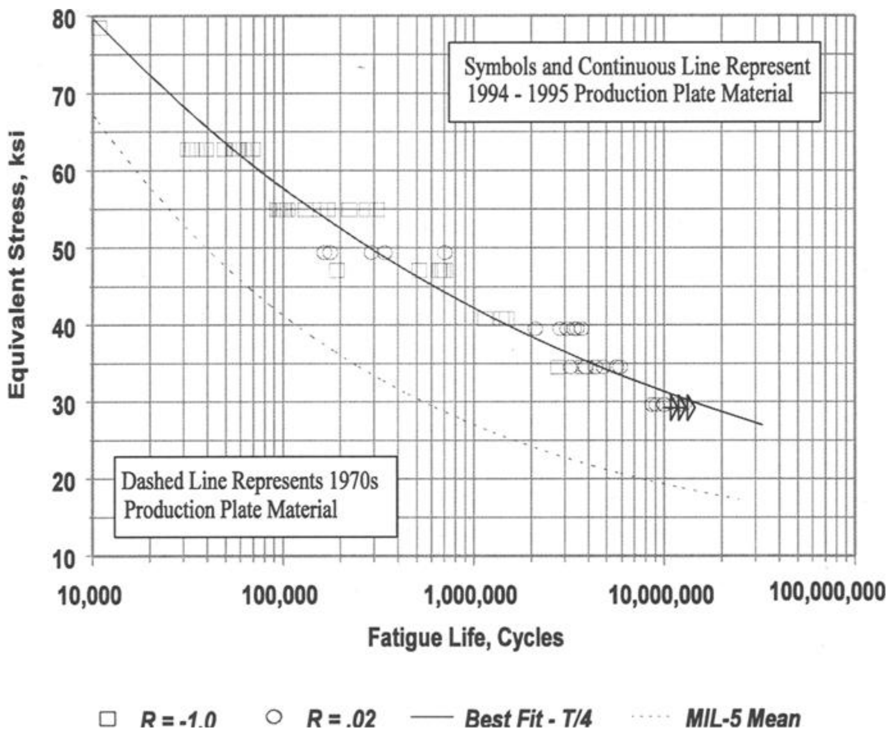

FIG. 23—*Comparison of Century 7050-T7451 thick plate fatigue data trends with other 7050 data within MIL-HDBK-5 [2] representing other grain directions and product forms.*

located at the plate mid-plane (T/2 location). *Now* material is described as plate representative of standard plant production circa 1991. This quality level shows significantly lower levels of mid-plane microporosity compared to *old* material and corresponding better fatigue properties. *Low porosity* material is described as plate material produced by special practices that further reduce mid-plane microporosity compared to the *now* material. *Thin* material is described as 1.00 inch (25.4 mm) thick plate produced according to standard production practices for this product. It is argued that the large thickness reductions that this material receives during rolling to the 1.0 inch (25.4 mm) gauge result in almost no microporosity and a more refined microstructure due to breakage of the original cast structure and flattening of grains.

Through the use of an equivalent stress transformation of the data developed in Ref. [*12*], as summarized in Table 4, it was possible to make fatigue life comparisons with the 1994 to 1995 vintage Century thick plate data. The comparative average results are shown in Fig. 24. The two curves represent the equivalent stress versus fatigue life curves that were defined for the Century 7050 thick plate material. The four data points represent the average fatigue properties from Ref. [*12*] for the four different material conditions noted in Table 5.

The results shown in Fig. 24 support several conclusions regarding the average performance of the Century 7050 thick plate material. The current Century T/2 fatigue data show better fatigue resistance than the comparable fatigue data from Ref. [*12*] said to represent *old* and *now* thick plate production methods for this alloy. The average fatigue properties for the T/2 specimen location as derived from Ref. [*12*], that are said to represent *low porosity* production methods, are comparable to the Century T/2 fatigue properties, but fall below the T/4 fatigue properties by about a factor of two. The T/2 thin

TABLE 4. Calculation of equivalent maximum stresses for the different stress ratios represented in the present study and in Ref. [*18*].

Specimen Location	Stress Ratio	Equivalent Stress[a]	Equivalent Maximum Stress, ksi (MPa)		
	-1.0	S_{max} *	20.84 (143.7)	23.81 (164.2)	26.79 (184.8)
T/4	0.02	S_{max} *	33.12 (228.4)	37.85 (261.1)	42.58 (293.7)
	0.10	S_{max} *	35.00 (241.4)	40.00 (275.9)	45.00 (310.4)
	-1.0	S_{max} *	25.03 (172.6)	28.61 (197.3)	32.18 (221.9)
T/2	0.02	S_{max} *	33.76 (232.8)	38.59 (266.2)	43.41 (299.4)
	0.10	S_{max} *	35.00 (241.4)	40.00 (275.9)	45.00 (310.4)

[a] Computed from $S_{max} * (1 - R)^m$ where m = 0.65 for T/4 location and 0.42 for T/2 location

TABLE 5. Summary of average fatigue properties for 7050 thick plate, T/2 specimen location, derived from Ref. [*18*].

Material Condition	Maximum Stress, ksi (MPa)	Stress Ratio	Log (Fatigue Life) Average	Log (Fatigue Life) Std. Dev.
Old Material	35.0 (241)	0.10	4.889	0.129
Now Material	35.0 (241)	0.10	5.120	0.103
Low Porosity Material	40.0 (276)	0.10	5.703	0.252
Thin Plate Material	45.0 (310)	0.10	6.756	0.270

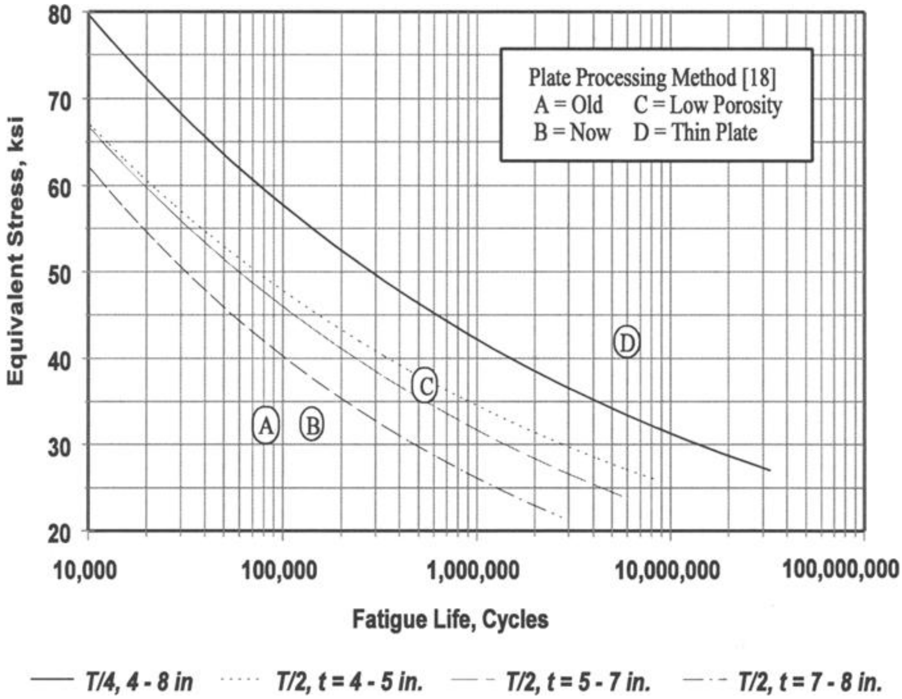

FIG. 24—*Comparison of the T/4 and T/2 average fatigue properties of the Century 7050-T7451 thick plate material with Ref. [18] data representing different "quality" levels.*

plate average fatigue properties derived from Ref. [*12*] fall well above both the T/4 and T/2 fatigue curves for the Century thick plate, but this result shows nothing more than the potential (perhaps never achievable) mid-plane fatigue resistance of thick 7050 plate if porosity can be effectively eliminated and extensive mid-plane cold work can be introduced.

The variability of the Century fatigue data about the equivalent stress fatigue curve, as reflected by the SEE of 0.183, is somewhat higher than the *old* and *now* material variability found in Ref. [*12*], but lower than the *low porosity* and *thin* plate material from the same source. These results show the variability in fatigue properties of the Century plate material in a positive light, because the results from Ref. [*12*] were developed at a single maximum stress level for each material condition.

Conclusions

This paper documents an analysis of load control fatigue data developed on 1994 to 1995 vintage 7050-T7451 thick plate. The fatigue data analysis included an assessment of thickness effects of fatigue life, representation of stress ratio effects through the use of a Walker equivalent stress parameter, and an evaluation of specimen location effects (T/4 versus T/2).

The primary conclusions based on this study can be summarized as follows:

- Microporosity Effects on S/N Fatigue Resistance: Dramatic improvements in mid-plane fatigue resistance of Century produced 7050-T7451 thick plate have been achieved over the past 10 years through processing improvements that have reduced the average size of mid-plane micropores by at least a factor of four.
- Stress Ratio Effects on Fatigue Life: Stress ratio effects on fatigue life were effectively accounted for through the use of a Walker equivalent stress parameter. The smaller separation of the T/4 and T/2, $R = -1.0$ S/N curves (at a given fatigue life) compared to the $R = 0.02$ S/N curves may be primarily due to more extensive microporosity at the mid-plane compared to the T/4 location. This mid-plane microporosity may approximate small pre-existing cracks that lead to more extensive crack growth degradation at $R = 0.02$, where the crack is open for most of the load cycle, compared to $R = -1.0$, where the crack is closed for more than half of the load cycle.
- Product Thickness Effects on T/4 Fatigue Life Properties: Product thickness was found to have a statistically significant effect (at a 90 percent confidence level) on the load control fatigue resistance of the 7050-T7451 thick plate material at the T/4 location, with the 8.00- to 8.50- inch (203- to 216-mm) thick plate showing somewhat lower fatigue resistance than the 4.25-inch (108-mm) thick plate.
- Product Thickness Effects on T/2 Fatigue Life Properties: Product thickness was found to have a statistically significant effect (at a 99 percent confidence level) on the load control fatigue resistance of the 7050-T7451 thick plate material at the T/2 location. This effect increased substantially with increased plate thicknesses and examinations of critical pore sizes show that this trend can be attributed primarily to remaining mid-plane microporosity in the thickest plates.
- Comparative Fatigue Performance of Century 7050 Thick Plate: The fatigue performance of 1994 to 1995 Century produced 7050 thick plate was found to be superior to all of the 7050 plate and forging data currently presented in MIL-HDBK-5 [*8*]. The data currently included in MIL-HDBK-5 represent older plate processing technology (from the 1970's), and there is clear evidence with the current 7050 thick plate data that the processing technology has improved substantially over the past two decades. These fatigue life improvements probably relate directly to reduced levels of microporosity that decrease the number and severity of fatigue crack initiation sites within the 7050 thick plate.

References

[1] Hartley, R., "Meeting Minutes at Northrop, Hawthorne, California, with Alcoa, Kaiser, and Reynolds -- May 15-16, 1984, and June 12, 1984.

[2] Tuegel, E. J., Cochran, R. W., et al., "Fatigue Properties of Several 7050 Thick Products," Presented at Aeromat 95, Anaheim, California, August 8-11, 1995.

[3] Freudenthal, A.M., and Gumbel, E.J., "Advances in Applied Mechanics," AAMCA, Vol. 4, 1956, pp. 117-158.

[4] Bastenaire, F.A., "New Method for the Statistical Evaluation of Constant Stress Amplitude Fatigue-Test Results," Probabilistic Aspects of Fatigue, STP 511, American Society of Testing and Materials, 1972, pp. 3-28.

[5] Lipson, C. And Sheth, N.J., Statistical Design and Analysis of Engineering Experiments, McGraw Hill Book Company, 1973.

[6] Walker, E.K., "The Effect of Stress Ratio During Crack Propagation and Fatigue for 2024-T3 and 7075-T6 Aluminum," Effect of Environment and Complex Load History on Fatigue Life, STP 462, 1970, pp. 1-14.

[7] Rice, R.C., Davies, K.B., Jaske, C.E., and Feddersen, C.E., "Consolidation of Fatigue and Fatigue-Crack Propagation Data for Design Use," NASA Contractor Report, National Aeronautics and Space Administration, NASA CR-2586, October 1975.

[8] MILITARY HANDBOOK - *Metallic Material and Elements for Aerospace Vehicle Structures,* **MIL-HDBK-5G, Change Notice 1**, Department of Defense, November 1994

[9] Davies, R.E., Nordmark, G.E., and Walsh, J.D., "Design Mechanical Properties, Fracture Toughness, Fatigue Properties, Exfoliation, and Stress-Corrosion Resistance of 7050 Sheet, Plate, Hand Forgings, Die Forgings, and Extrusions," Report N00019-72-C-0512, Aluminum Company of America, July 1975.

[10] Deel, O.L., Ruff, P.E., and Mindlin, H., "Engineering Data on New Aerospace Structural Materials," AFML-TR-75-97, June 1975.

[11] Hasse, K. R., **Engineering Properties Section, Test Report No. 11200**, Report from Kaiser Aluminum & Chemical Corp. to Century Aluminum, April 19, 1996.

[12] Magnusen, P.E., Bucci, R.J., Hinkle, A.J., Brockenbrough, J.R., Konish, H.J., and Miyasato, S.M., "The Role of Microstructure on the Fatigue Durability of

Aluminum Aircraft Alloys," Final Report, ONR Contract N00014-91-C-0128, November 1995.

[13] Boyer, H.E. (Ed.), Atlas of Fatigue Curves, American Society of Metals, Metals Park, Ohio, 1986, p. 353.

[14] Starke, E.A., Lutjering, G., "Cyclic Plastic Deformation and Microstructure," in Fatigue and Microstructure, American Society for Metals, Metals Park, Ohio, 1979, p. 238.

APPENDIX A -- SUPPORTING DATA

TABLE A-1. Summary of load control fatigue tests on 4.00 - 8.50 inch thick 7050-T7451 plate

Specimen Identification	Thickness, inches	Specimen Location	Stress Ratio	Max. Stress Ksi	Cycles To Failure	Comments
BXZI-2	4.25	T/4	-1.00	50.0	10,871	
BXZI-5	4.25	T/4	-1.00	40.0	55,859	
BXZI-6	4.25	T/4	-1.00	40.0	69,920	
BXRV-1	6.00	T/4	-1.00	40.0	57,616	
BXRV-2	6.00	T/4	-1.00	40.0	62,501	
BXRY-5	6.50	T/4	-1.00	40.0	49,687	
BXRY-6	6.50	T/4	-1.00	40.0	59,083	
BXRW-2	7.00	T/4	-1.00	40.0	33,425	
BXRW-1	7.00	T/4	-1.00	40.0	55,816	
BXZG-2	8.00	T/4	-1.00	40.0	31,730	
BXZG-1	8.00	T/4	-1.00	40.0	35,422	
BXRX-4	8.50	T/4	-1.00	40.0	39,660	
BXRX-3	8.50	T/4	-1.00	40.0	55,082	
BXZJ-3	4.25	T/4	-1.00	35.0	275,648	
BXZJ-4	4.25	T/4	-1.00	35.0	312,302	
BXRV-5	6.00	T/4	-1.00	35.0	102,345	
BXRV-6	6.00	T/4	-1.00	35.0	106,029	
BXRY-8	6.50	T/4	-1.00	35.0	94,010	
BXRY-7	6.50	T/4	-1.00	35.0	157,863	
BXRW-3	7.00	T/4	-1.00	35.0	102,352	
BXRW-4	7.00	T/4	-1.00	35.0	224,108	
BXZG-6	8.00	T/4	-1.00	35.0	96,693	
BXZG-5	8.00	T/4	-1.00	35.0	101,186	
BXRX-6	8.50	T/4	-1.00	35.0	131,800	
BXRX-5	8.50	T/4	-1.00	35.0	172,230	
BXRV-9	6.00	T/4	-1.00	30.0	192,704	
BXRV-10	6.00	T/4	-1.00	30.0	691,722	
BXRW-8	7.00	T/4	-1.00	30.0	663,700	
BXRW-7	7.00	T/4	-1.00	30.0	711,402	
BXZH-4	8.00	T/4	-1.00	30.0	519,231	
BXZH-3	8.00	T/4	-1.00	30.0	661,268	
135293-1	6.00	T/4	-1.00	26.0	1,406,598	
135298-2	6.00	T/4	-1.00	26.0	1,155,573	
135301-1	6.00	T/4	-1.00	26.0	1,491,489	
135289-1	6.00	T/4	-1.00	22.0	3,894,686	
135297-1	6.00	T/4	-1.00	22.0	2,795,361	
135300-4	6.00	T/4	-1.00	22.0	3,783,325	
BXZI-4	4.25	T/4	0.02	50.0	341,725	

TABLE A-1. (**Continued)**

Specimen Identification	Thickness, inches	Specimen Location	Stress Ratio	Max. Stress Ksi	Cycles To Failure	Comments
BXZI-3	4.25	T/4	0.02	50.0	709,196	
BXRY-4	6.50	T/4	0.02	50.0	291,633	
BXRU-11	8.00	T/4	0.02	50.0	165,210	
BXRU-12	8.00	T/4	0.02	50.0	177,752	
BXRV-3	6.00	T/4	0.02	40.0	2,111,509	
BXRV-4	6.00	T/4	0.02	40.0	3,495,537	
BXZJ-2	4.25	T/4	0.02	40.0	3,096,970	
BXZJ-1	4.25	T/4	0.02	40.0	3,718,529	
BXZG-4	8.00	T/4	0.02	40.0	2,853,862	
BXZG-3	8.00	T/4	0.02	40.0	3,381,154	
BXRV-8	6.00	T/4	0.02	35.0	3,229,657	
BXRV-7	6.00	T/4	0.02	35.0	5,623,522	
BXRW-5	7.00	T/4	0.02	35.0	4,382,353	
BXRW-6	7.00	T/4	0.02	35.0	5,883,721	
BXZH-1	8.00	T/4	0.02	35.0	3,882,916	
BXZH-2	8.00	T/4	0.02	35.0	4,823,835	
BXRV-11	6.00	T/4	0.02	30.0	11,772,958	Did Not Fail
BXRV-12	6.00	T/4	0.02	30.0	12,664,786	Did Not Fail
BXRX-7	8.50	T/4	0.02	30.0	8,647,548	
BXRX-8	8.50	T/4	0.02	30.0	9,936,421	
BYXL-17	8.00	T/4	0.02	30.0	9,114,087	
BYXL-16	8.00	T/4	0.02	30.0	10,000,000	Did Not Fail
BXZH-5	8.00	T/4	0.02	30.0	10,000,000	Did Not Fail
BXZH-6	8.00	T/4	0.02	30.0	10,000,000	Did Not Fail
8763-4	8.00	T/2	-1.00	38.0	19,930	Failed in Radius
2755-4	8.00	T/2	-1.00	38.0	27,436	Failed in Radius
2754-3	8.00	T/2	-1.00	38.0	28,426	
8762-4	8.00	T/2	-1.00	38.0	28,825	Failed in Radius
2772-7	4.25	T/2	-1.00	38.0	53,638	
2770-5	4.25	T/2	-1.00	38.0	91,544	
2779-7	6.50	T/2	-1.00	38.0	37,637	
11904-2	6.00	T/2	-1.00	38.0	59,544	
BYXL-15	8.00	T/2	-1.00	30.0	146,668	
2746-2	8.00	T/2	-1.00	27.0	191,019	
2751-4	8.00	T/2	-1.00	27.0	193,375	
2769-4	4.25	T/2	-1.00	27.0	1,000,000	Did Not Fail
2767-2	4.25	T/2	-1.00	27.0	1,208,620	
2782-10	6.50	T/2	-1.00	27.0	361,252	
2774-2	6.50	T/2	-1.00	27.0	411,557	
11905-2	4.00	T/2	-1.00	17.0	1,000,000	Did Not Fail

TABLE A-1. (Continued)

Specimen Identification	Thickness, inches	Specimen Location	Stress Ratio	Max. Stress Ksi	Cycles To Failure	Comments
2747-3	8.00	T/2	-1.00	17.0	1,000,000	Did Not Fail
2752-1	8.00	T/2	-1.00	17.0	1,000,000	Did Not Fail
2758-3	8.00	T/2	-1.00	17.0	1,000,000	Did Not Fail
2761-3	4.25	T/2	-1.00	17.0	1,000,000	Did Not Fail
2759-1	4.25	T/2	-1.00	17.0	1,000,000	Did Not Fail
2773-1	6.50	T/2	-1.00	17.0	1,000,000	Did Not Fail
2785-13	6.50	T/2	-1.00	17.0	1,000,000	Did Not Fail
2784-12	6.50	T/2	-1.00	17.0	1,000,000	Did Not Fail
BYXK-12	8.00	T/2	0.02	60.0	11,229	
2753-2	8.00	T/2	0.02	58.0	18,494	
2757-2	8.00	T/2	0.02	58.0	20,688	
2762-4	4.25	T/2	0.02	58.0	28,116	
2760-2	4.25	T/2	0.02	58.0	29,469	
2764-6	4.25	T/2	0.02	58.0	31,941	
2778-6	6.50	T/2	0.02	58.0	24,626	
2786-14	6.50	T/2	0.02	58.0	28,718	
BYXK-18	8.00	T/2	0.02	50.0	27,505	
BYXL-6	8.00	T/2	0.02	50.0	48,709	
8764-1	4.00	T/2	0.02	40.0	638,795	
2745-1	8.00	T/2	0.02	40.0	88,052	
2750-3	8.00	T/2	0.02	40.0	97,826	
2763-5	4.25	T/2	0.02	40.0	127,816	Failed in Radius
2765-7	4.25	T/2	0.02	40.0	220,851	
2777-5	6.50	T/2	0.02	40.0	149,530	Failed in Radius
2775-3	6.50	T/2	0.02	40.0	186,520	
2781-9	6.50	T/2	0.02	40.0	236,240	
8765-1	6.00	T/2	0.02	40.0	1,000,000	Did Not Fail
BYXL-12	8.00	T/2	0.02	40.0	52,019	
BYXL-18	8.00	T/2	0.02	30.0	1,472,215	
2748-1	8.00	T/2	0.02	25.0	1,000,000	Did Not Fail
2749-2	8.00	T/2	0.02	25.0	1,000,000	Did Not Fail
2756-1	8.00	T/2	0.02	25.0	768,291	
2766-1	4.25	T/2	0.02	25.0	1,000,000	Did Not Fail
2768-3	4.25	T/2	0.02	25.0	1,000,000	Did Not Fail
2771-6	4.25	T/2	0.02	25.0	1,000,000	Did Not Fail
2776-4	6.50	T/2	0.02	25.0	1,000,000	Did Not Fail
2780-8	6.50	T/2	0.02	25.0	1,000,000	Did Not Fail
2783-11	6.50	T/2	0.02	25.0	1,000,000	Did Not Fail

Ralph I. Stephens,[1] Joshua J. Horn,[2] Dente D. Poland,[2] and Eric A. Sager[2]

INFLUENCE OF DENSITY AND POROSITY SIZE AND SHAPE ON FATIGUE AND FRACTURE TOUGHNESS OF HIGH STRENGTH FL4405 P/M STEEL

REFERENCE: Stephens, R. I., Horn, J. J., Poland, D. D., and Sager, E. A., **"Influence of Density and Porosity Size and Shape on Fatigue and Fracture Toughness of High Strength FL4405 P/M Steel,"** *Effects of Product Quality and Design Criteria on Structural Integrity, ASTM STP 1337,* R. C. Rice and D. E. Tritsch, Eds., American Society for Testing and Materials, 1998.

ABSTRACT: Density and sintering temperature effects were investigated with FL4405 low alloy P/M high strength steel. Monotonic tensile stress-strain, plane strain fracture toughness and fatigue behavior of smooth, notched and cracked specimens were investigated under both constant and variable amplitude loading. Two density levels, 7.0 and 7.4 g/cm^3 and two sintering temperatures, 1120 and 1315°C, were evaluated. The increased density resulted in smaller pore size and pore volume and the increased sintering temperature resulted in greater pore roundness. All final fracture surfaces were brittle at the macro level while containing ductile dimples at the micro level. Fatigue surfaces contained cleavage only, ductile dimples only or mixed cleavage and ductile dimple morphology with no striations nor beachmarks. Increasing the density resulted in significant higher tensile strength, elastic modulus, ductility, fracture toughness and fatigue resistance. Increasing the sintering temperature, and hence increasing pore roundness, resulted in additional enhancement of these properties. However, this increase was not as significant as that of the density increase.

KEYWORDS: powder metal, density, sintering temperature, porosity, low cycle fatigue, fatigue crack growth, constant amplitude, variable amplitude, fractography

Monotonic stress-strain, fatigue and fracture behavior of powder metal (P/M) products depend significantly upon the compacted material density, the distribution of the inherent porosity, and the size and shape of the individual pores [1-3]. Many ferrous P/M products are traditionally sintered at approximately 1100°C, producing sharp and irregular pore geometry. Higher sintering temperatures, 1300°C, improve performance by driving the diffusion of atoms through a reduction in surface area, thereby ameliorating much of the pore angularity via pore rounding. Similarly, the density of a P/M component influences the size of the porosity within the component. Higher densities lead to smaller porosity. As a result, the process of high temperature sintering and/or repressing for higher density is of significant interest to high performance P/M users [4-6].

[1] Professor, Mechanical Engineering Department, The University of Iowa, Iowa City, IA 52242

[2] Research Assistant, Mechanical Engineering Department, The University of Iowa, Iowa City, IA

A research program was established within the SAE Fatigue Design and Evaluation Committee for the purposes of determining the effects of density (pore size) and sintering temperature (pore roundness) using three high strength FL4405 P/M low alloy steels. The parametric test program utilized two nominal material densities of 7.0 g/cm^3 (material A) and 7.4 g/cm^3 (materials B and C) along with two sintering temperatures of 1120°C (materials A and B) and 1315°C (material C) (TABLE 1). Material A with the low density, low sintering temperature had the greatest pore size and volume fraction of void space and the least number of rounded pores. Material B, with the high density, low sintering temperature had less volume space, but possessed a mixture of angular and rounded pores. By increasing both density and sintering temperature, material C had reduced pore size, void space and increased pore roundness. Thus materials A and B could be compared for pore size (density) effects and materials B and C could be compared for pore roundness (sintering) effects.

The research program included the following: composition, microstructure, image analysis of size, shape and distribution of porosity, monotonic tension, cyclic stress-strain, strain life ($\varepsilon - N$), notch sensitivity (S-N), fatigue crack growth (da/dN - ΔK), plane strain fracture toughness (K_{Ic}), and variable amplitude fatigue of smooth, notched and precracked specimens, and macro and micro SEM fractography. This multiplicity of test and evaluation concepts provided a realistic comparison of the parametric goals.

Materials/Specimens

The FL 4405 P/M steel alloy specimens were produced by Burgess-Norton Mfg. Co. of Geneva, Illinois. The alloy blend had the constituents of 98.75% Hoeganaes Ancorsteel 85 HP powder, 0.50% Southwest graphite 1561 and 0.75% Acrawax zinc sterate lubricant. The 85 HP powder consisted of 0.5% carbon, 0.85% molybdenum, 0.12% nickel, 0.13% manganese, 0.09% copper and 98.3% iron. Material A specimens were produced with a single press followed by presintering and materials B and C were produced with a double press with a presinter between presses. The double press procedure involved pressing to a density of 6.8 g/cm^3 and then repressing to a nominal density of 7.4 g/cm^3. Presintering was done at 900°C for 20 minutes in an endothermic atmosphere. Materials A and B were sintered at 1120°C for 20 minutes in a 10% hydrogen and 90% nitrogen atmosphere and material C was vacuum sintered at 1315°C for 30 minutes. Test specimens were then machined to final size (FIG. 1). Axial smooth specimens (FIG. 1(a)) were machined from 13 x 13 x 120 mm rectangular bars with the final 6.4 mm diameter test section polished in the longitudinal direction. Compact disk, DC (T) specimens (FIG. 1(b)) and keyhole notch specimens (FIG. 1(c)) were machined from 101.6 mm diameter disks to a thickness of 9 to 9.5 mm thick. The 6.35 mm diameter keyhole notch was left in the as-drilled condition to better simulate real component conditions. Following machining, all specimen were vacuum austenitized at 843°C for one hour, oil quenched and tempered at 177°C for two hours. A vacuum heat treatment was chosen to minimize any atmosphere-solid reaction that would affect the carbon chemistry.

TABLE 1--*Nominal material description*

Material	A	B	C
Density -- g/cm^3	7.0	7.4	7.4
Sintering Temperature -- °C	1120	1120	1315
Mean Pore Size -- µm	10	8	8
Number of Round Pores	least	intermediate	most

Surface, core and material carbon content varied little with all values between 0.41 and 0.52 percent.

The resulting microstructures for all three materials (A, B and C) were determined by etching with a 2% Nital solution and examined at 500X magnification. A uniform tempered martensitic structure was observed in all materials on both the surface and in the core. The relative size and amount of porosity was also evident in the micrographs. Both apparent hardness and microhardness measurements were made for the three different materials with both axial and disk specimens. Apparent hardness was measured using the Rockwell C hardness scale (HRC) and the microhardness was measured using a Knoop

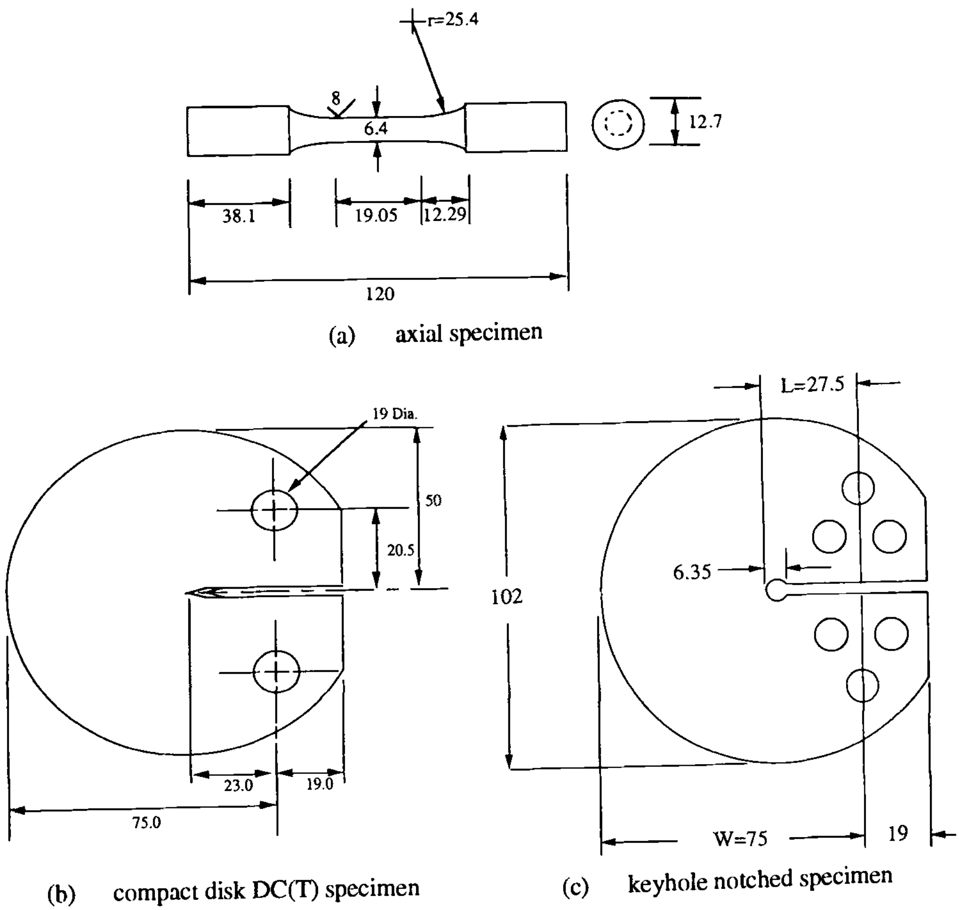

FIG. 1--*Test specimens (all dimensions in mm)*

hardness tester with results converted to HRC (TABLE 2). Apparent hardness is seen to differ for the three materials while the microhardness for a given specimen type is quite similar. The microhardness for the disk specimens is lower than for the axial specimens. On a global scale, the apparent hardness accounts for gross material behavior, including material porosity, while microhardness provides the hardness of a fully dense region in the porous material, indicating the "true" hardness of that material in the absence of porosity [7].

Powder-Tech Associates Inc. performed image analysis on both axial and disk specimens to quantify porosity size, shape and distribution [8]. Ten fields of vision were taken at each of two different locations (near surface and near mid thickness) for each specimen type. The results (TABLE 2) indicate mean pore size for a given specimen type was significantly larger for the lower density material A while materials B and C were similar. Pore roundness values ranged from 0 to 1 with 1 being a perfectly round pore and 0 being an elongated rough pore. The percent number of pores with a roundness value between 0.8 and 1 (TABLE 2) was greatest for material C, intermediate for material B and lowest for material A. Thus the higher sintering temperature of material C did have a desired pore rounding effect.

Monotonic Tensile Stress-Strain

All mechanical testing for this research was performed with a 100 kN closed-loop servohydraulic test system using computer control. Tensile tests were performed using hydraulic grips with the system in strain control. Four or five tensile tests were performed for each of the three material conditions. Scatter for a given material was not significant. Average tensile properties (TABLE 3) and representative stress-strain curves (FIG. 2) indicate significant differences between the three materials. All strengths, deformations at fracture and elastic moduli, E, were highest for material C, intermediate for material B and lowest for material A. Thus both higher density (smaller pore size) and higher sintering temperature (greater pore roundness) resulted in improved tensile stress-strain behavior.

TABLE 2--*Specific material description*

	Axial specimens			Disk specimens		
Material	**A**	**B**	**C**	**A**	**B**	**C**
Sintering Temperature -- °C	1120	1120	1315	1120	1120	1315
Density -- g/cm^3	7.01	7.48	7.51	7.0	7.39	7.44
Apparent Hardness -- HRC	33	45	46	38	40	46
Micro Hardness -- HRC	59	57	56	48	52	48
Mean Pore Size -- μm	9.6	7.3	7.5	11.1	8.7	8.5
% Mean Pore Roundness Between 0.8 and 1.0 Roundness	35	52	55	27	39	54

TABLE 3--*Average monotonic tensile properties*

Material	A	B	C
Tensile Strength, S_u - MPa	1 092	1 810	1 940
Yield Strength, S_y - MPa	1 013	1 440	1 462
Elastic Modulus, E - GPa	139	168	182
Percent Elongation, - %	1.2	2.6	4.4
Percent Reduction in Area, - %	0.8	1.2	2.4
Strength Coefficient, K - MPa	2 770	3 154	3 088
Strain Hardening Exponent, n	0.164	0.125	0.117
True Fracture Strength, σ_f - MPa	1 100	1 832	1 988
True Fracture Ductility, ε_f	0.008	0.012	0.024

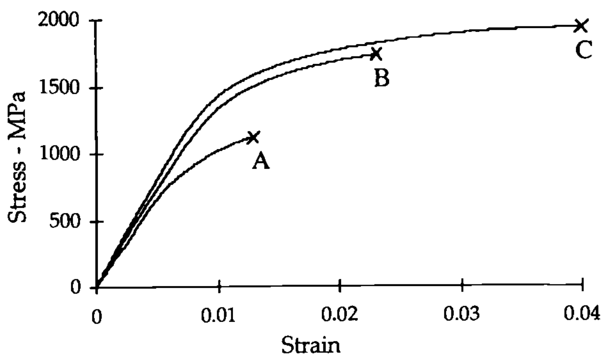

FIG. 2--*Representative monotonic stress-strain curves for materials A, B and C*

At the macro level, all three materials behaved in a brittle fashion with flat fracture surfaces. Tensile percent elongation ranged from 1.2 to 4.4% and reduction in area ranged from 0.8 to 2.4%. No significant macro fracture surface differences existed for the three materials. Scanning electron fractographs of the monotonic tensile tests (FIG. 3) indicate ductile dimple fracture morphology in bonded particles of all sizes, tear ridges and no cleavage for all three material conditions. The large amount of porosity and void space is evident in material A (FIG. 3(a)) leading to higher local stresses in the particle necks. Materials B and C contain much greater amounts of particle fracturing via ductile dimples. The more rounded pore structure for material C, from the higher sintering temperature, is evident (FIG. 3(c)). The above micro fracture morphology is consistent with that described by Mazen and Lade for AISI 1018 steel [9]. The FL 4405 three material conditions, A, B and C, can be classified here as globally brittle and locally ductile.

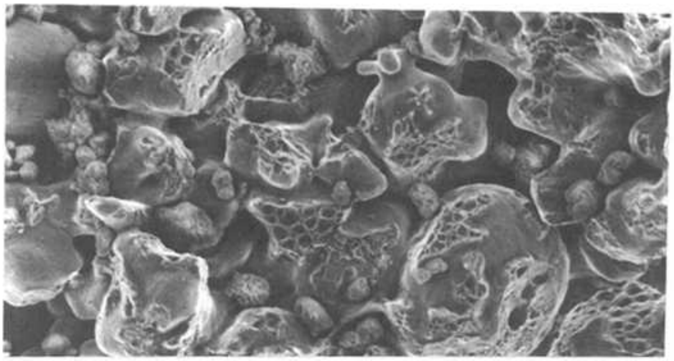

(a) material A

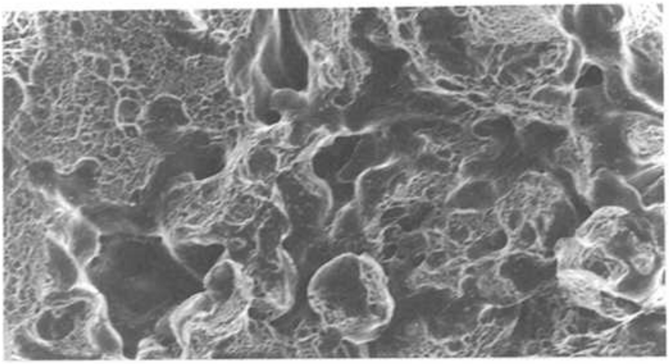

(b) material B

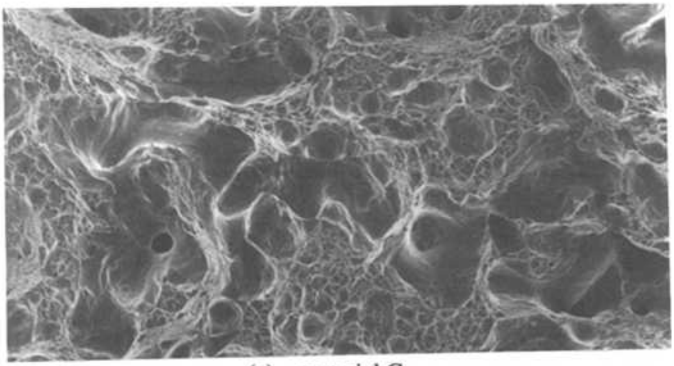

(c) material C

10 μ

FIG. 3--*Monotonic fracture surfaces*

Constant Amplitude Low Cycle Fatigue

Smooth axial specimens (FIG. 1(a)) were subjected to fully-reversed constant amplitude strain cycling in accordance with ASTM Practice for Strain-Controlled Fatigue Testing (E 606). A triangular wave form was used with frequencies between 1 and 10 Hz. Twelve or thirteen specimens were used for each material at seven different strain amplitudes giving between 42 and 46% replication. Failure was defined as fracture, as very little load drop occurred prior to fracture. Fatigue crack growth depth at fracture was ≤ 1.5 mm.

Typical hysteresis loops at first cycle, half-life and near fracture for the largest, intermediate and smallest strain amplitudes (FIG. 4) indicate plastic strain amplitudes for all tests were significantly less than elastic strain amplitudes. Figure 4 is for material B, but similar hysteresis loops were found for materials A and C. A slight amount of cyclic softening occurred in the first few cycles at the intermediate and larger strain amplitudes followed by essentially stable behavior until about fracture for all three materials. Typical plots of σ_a versus applied cycles, N_{app}, normalized by the cycles to fracture, N_f, for three strain levels (FIG. 5) indicate this same stable behavior. The cyclic stress-strain curve was obtained by connecting the tensile half-life hysteresis loop tips. This curve is compared to the monotonic stress-strain curve for material B (FIG. 6) which also indicates only slight cyclic softening which was typical for all three materials. The cyclic strength coefficient, K' and the cyclic strain hardening exponent n' along with the cyclic modulus of elasticity E' were obtained (TABLE 4) for all three materials. All three materials had cyclic stress-strain behavior very similar to their monotonic stress-strain behavior.

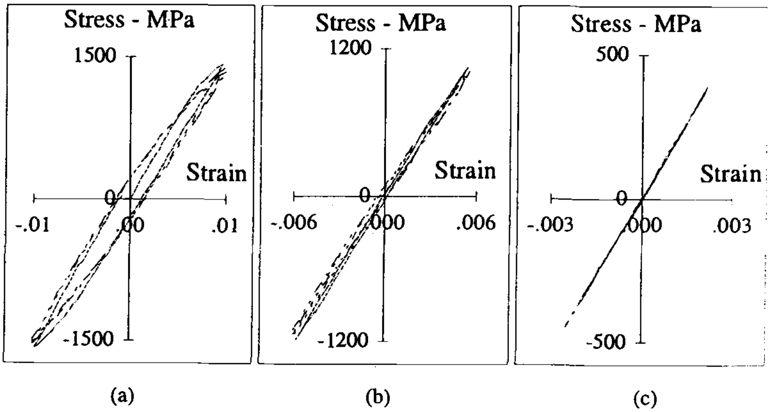

FIG. 4--*Hysteresis loops for material B*
(a) $\Delta\varepsilon/2 = 0.01$ (b) $\Delta\varepsilon/2 = 0.006$ (c) $\Delta\varepsilon/2 = 0.0025$

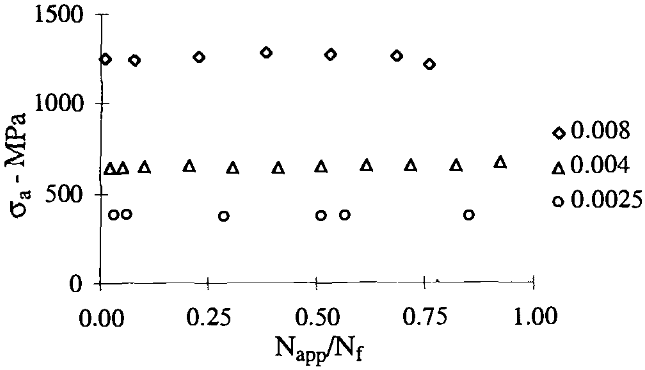

FIG. 5--*Stress amplitude vs. normalized applied cycles for material B*

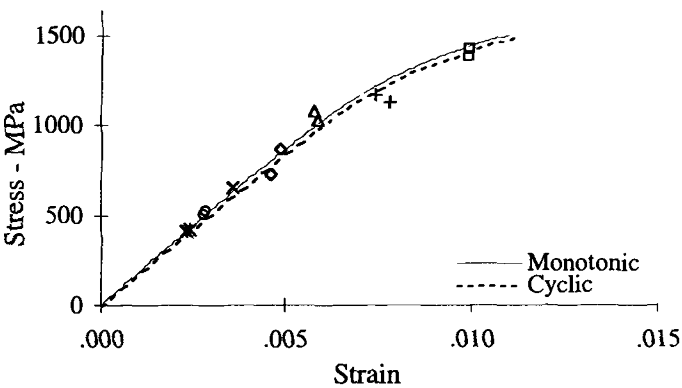

FIG. 6--*Cyclic stress-strain data, curve and monotonic curve for material B*

TABLE 4--***Low cycle fatigue parameters***

Material	A	B	C
Fatigue Strength Coefficient, σ_f' - MPa	1485	3065	4205
Fatigue Strength Exponent, b	-.133	-.156	-.176
Fatigue Ductility Coefficient, ε_f'	.007	.137	.09
Fatigue Ductility Exponent, c	-.593	-.961	-.755
Cyclic Strength Coefficient, K' - MPa	3970	3290	5010
Cyclic Strain Hardening Exponent, n'	.206	.130	.182
Avg. Cyclic Elastic Modulus, E' - GPa	129	169	174

Low cycle fatigue data were broken into total, plastic and elastic strain amplitudes as

$$\frac{\Delta\varepsilon}{2} = \frac{\Delta\varepsilon_p}{2} + \frac{\Delta\varepsilon_e}{2} \qquad (1)$$

and represented on log-log coordinates as

$$\frac{\Delta\varepsilon}{2} = \varepsilon_f'(2N_f)^c + \frac{\sigma_f'}{E}(2N_f)^b \qquad (2)$$

The fatigue coefficients and exponents (TABLE 4) were determined by a log-log linear regression. The low cycle fatigue behavior for material B (FIG. 7) was qualitatively similar to that for materials A and C. Plastic strain amplitudes were essentially one or more orders of magnitude less than elastic strain amplitudes. The plastic and elastic data reasonably satisfied the log-log modeling. Scatter was also reasonable for duplicate tests.

The total strain amplitude versus life data and best fit curves for all three materials (FIG. 8) indicate material A, with its low density, had approximately an order of magnitude less fatigue life than materials B or C for a given strain amplitude. Materials B and C differed by a factor of 3-4 at large strain amplitudes with convergence at low strain amplitudes. Thus higher density and higher sintering temperature were desirable under these low cycle fatigue test conditions.

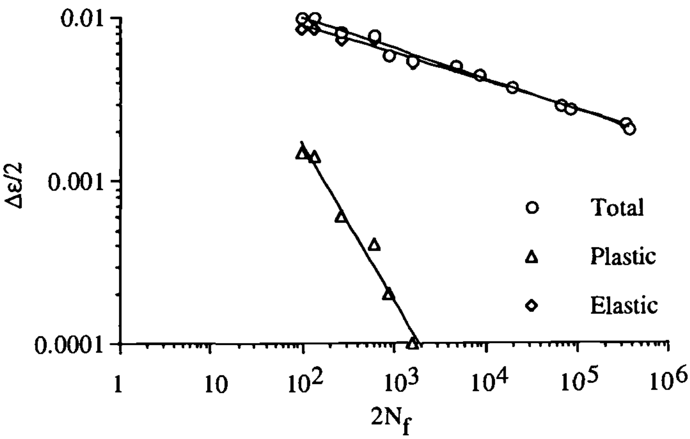

FIG. 7--*Total, elastic and plastic strain amplitude vs. life for material B*

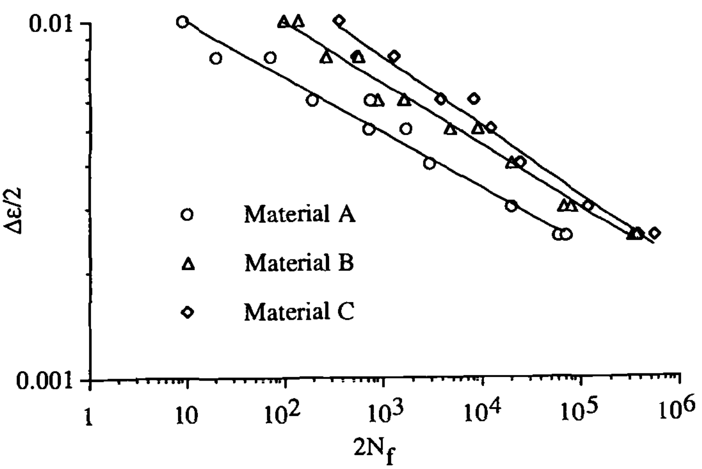

FIG. 8--*Total strain amplitude vs. life for materials A, B and C*

Macroscopic fracture appearance of the three materials subjected to low cycle fatigue was similar for a given strain amplitude. At the larger strain amplitudes, no crack initiation site(s) nor fatigue crack growth was evident and fractures were essentially the same as monotonic fractures. At lower strain amplitudes, surface semi-elliptical fatigue cracks up to 1.5 mm in depth along with river markings existed. All macroscopic fracture surfaces were flat and brittle in appearance. The scanning electron microscope was used to examine fracture surfaces from each material for strain amplitudes of 0.8, 0.4 and 0.25%. This essentially included the total range of low cycle fatigue life. Fatigue crack initiation sites were found at both surface and subsurface voids and metallic and non-metallic inclusions. Fatigue crack growth around the initiation sites was predominantly ductile dimples with an occasional small amount of cleavage. Fatigue crack growth regions were predominantly ductile dimples (FIG. 9) as were final fracture regions. No striations were evident. Significant porosity can be seen (FIG. 9(a)) for material A along with ductile dimples. Both ductile dimples and some cleavage across particle necks can be observed (FIG. 9(b)) for material B. The transition zone bounding between the fatigue crack growth region and the final fracture region is evident (FIG. 9(c)) for material C. The left region is fatigue crack growth and the right region is final fracture. Thus, the low cycle fatigue crack growth morphology for all three materials involved primarily ductile dimples.

Constant Amplitude Notched Fatigue

Keyhole notched fatigue specimens (FIG. 1(c)) were subjected to three different constant load amplitude tests for each of the three materials. The purposes of these tests were to compare the constant amplitude notched fatigue resistance of the three materials and to determine their notch sensitivity. Tests were performed with the load ratio $R = P_{min}/P_{max}$ equal to -1 at a frequency of 10 Hz. The amplitudes were chosen based upon the life of the smooth low cycle fatigue behavior (TABLE 4) and taking into consideration the notched elastic stress concentration factor, K_t. The K_t value was obtained using finite element methods, along with experimental methods by applying small, 0.8 mm gage length, strain gages in the notch for three test specimens. K_t was determined to be 3.5. Local maximum stresses at the notch including the K_t value were less than the 0.2% yield strength for all

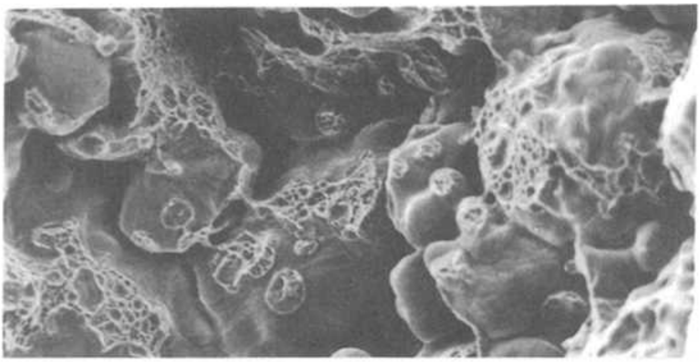

(a) material A

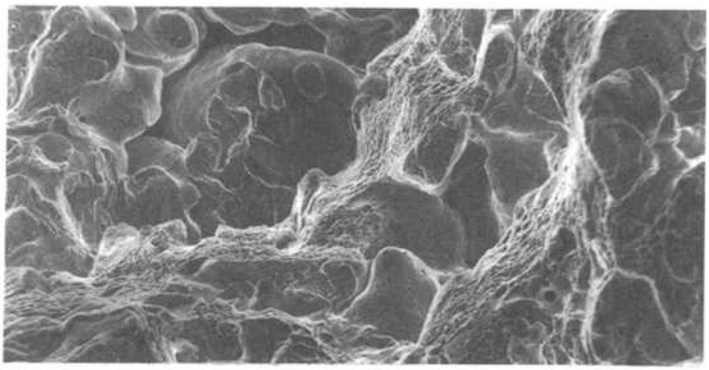

(b) material B

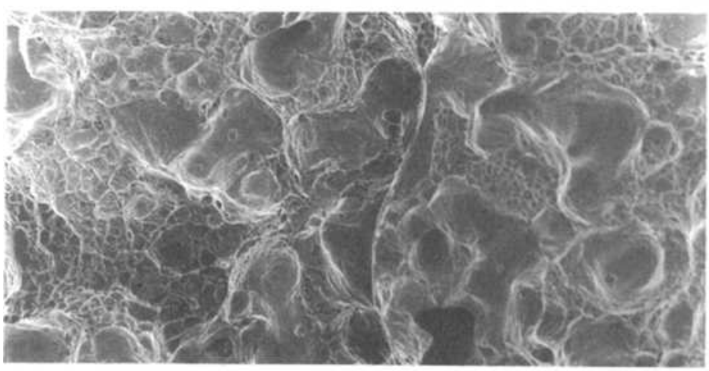

(c) material C

10 μ

FIG. 9--*Low cycle fatigue crack growth surfaces*

tests. Failure of these fatigue tests was based upon the low cycle fatigue results which showed crack lengths at fracture to be about 1.5 mm or less. Fatigue cracks initiated either at the mid-thickness of the notch or at one of the corners. The cracks grew from these sites until a surface crack of 1.5 mm occurred, or fracture, at which time failure was assumed. Thus, a notch sensitivity analysis could be made with these test results and the elastic portion of the smooth specimen low cycle fatigue results.

Nominal stress amplitude versus fatigue life behavior for materials A, B and C (FIG. 10) was very similar to smooth specimen behavior (FIG. 8). Materials B and C had about an order of magnitude greater life than material A. The difference between materials B and C was a factor of two at higher stress amplitude, but the behavior converged at the longer life. Thus for these keyhole notched specimens the higher density was significantly beneficial, but the pore roundness was only slightly beneficial.

The data of FIG. 10 were superimposed with the low cycle fatigue elastic data that provided an indication of notch sensitivity. A typical superposition (FIG. 11) for material B indicates the fatigue notch factor, K_f, at longer life was 3.4 which is approximately equal to K_t. K_f is defined as the ratio of the smooth specimen fatigue strength to the notched specimen fatigue strength at a given life. Values of K_f at long life were 3.3, 3.4 and 3.6 for materials A, B and C respectively. This indicates that all three material conditions were essentially fully notch sensitive at long lives.

The notched specimen fracture surfaces were examined macroscopically and with the scanning electron microscope. Fatigue regions and final fracture regions were flat and brittle in appearance and no shear lips nor permanent deformation was noted. Scanning electron microscopy for the longer life specimens revealed fatigue crack initiation site regions and fatigue crack growth regions were dominated by cleavage for material A and mixed cleavage and ductile dimples for materials B and C. This morphology was somewhat different than the low cycle fatigue morphology, where ductile dimples were more dominant. All notch specimen final fracture regions, however, were ductile dimples.

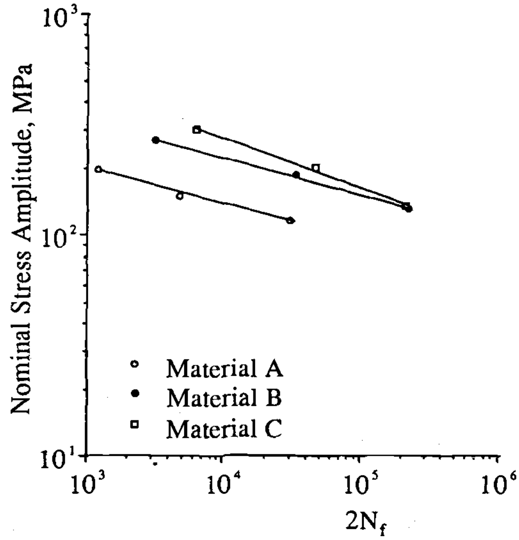

FIG. 10--*Constant amplitude keyhole notch fatigue behavior for materials A, B and C*

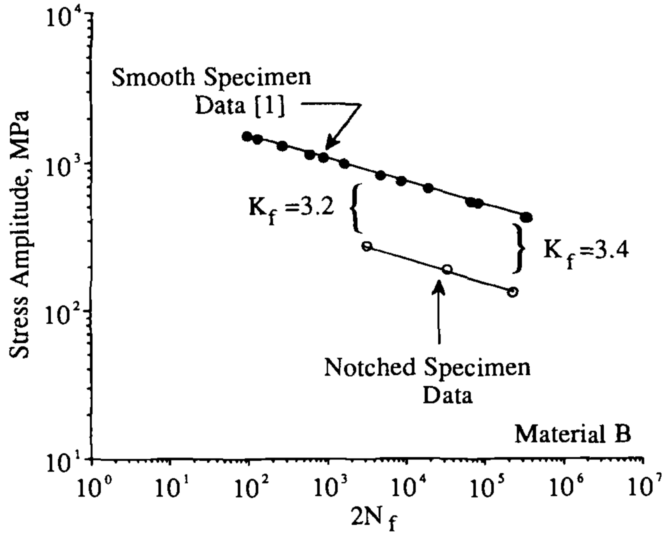

FIG. 11--*Combined smooth LCF and keyhole notch fatigue behavior for material B*

Fracture Toughness, K_{Ic}

Fracture toughness tests were performed using 9.5 mm thick pre-cracked compact disk DC(T) specimens (FIG. 1(b)) following ASTM Test Method for Plane-Strain Fracture Toughness of Metallic Materials (E399). Triplicate tests were performed for each of the three materials, however, one material B specimen fractured during precracking, so only two valid material B valid tests were obtained. Specimens were precracked to an a/w value between 0.45 and 0.55 and tested in ram displacement control with $\dot{K}$ between 0.5 and 2.7 MPa$\sqrt{m}$ /s. A load versus CMOD curve (FIG. 12) was typical of all three material responses. The OP_5 line represents a decrease in slope of 5% and P_Q represents the load used for calculating K_Q. The thickness requirement

$$B \geq 2.5\left(\frac{K_Q}{\sigma_{ys}}\right)^2 \tag{3}$$

and the load ratio requirement

$$P_Q/P_{max} \leq 1 \tag{4}$$

were satisfied in all tests along with other E399 crack requirements. Thus K_Q values represented valid plane strain fracture toughness, K_{Ic}. K_Q was calculated using [10]

$$K = \frac{P}{B\sqrt{w}} f(a/w) \tag{5}$$

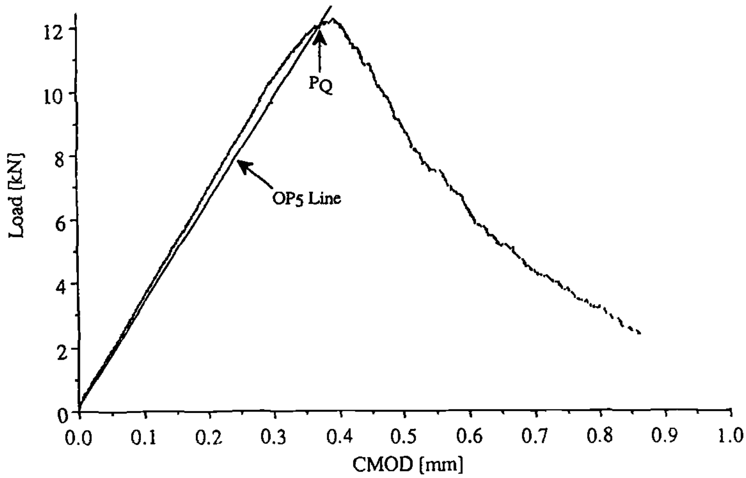

FIG. 12--Representative load vs. CMOD from fracture toughness, K_{Ic}, tests

where

$$f(a/w) = \frac{2 + a/w}{\left[1 - a/w\right]^{3/2}}\left[0.76 + 4.8(a/w) - 11.58(a/w)^2 + 11.43(a/w)^3 - 4.08(a/w)^4\right] \quad (6)$$

Scatter of triplicate tests for materials A and C was less than 10% while scatter for duplicate tests of material B was 30%. Average values of K_{Ic} were 28, 31 and 42 MPa$\sqrt{m}$ respectively for materials A, B and C. Thus increased density and higher sintering temperature enhanced the plane strain fracture toughness with the most significant increase due to the higher sintering temperature. Others have found this same trend of higher fracture toughness with higher yield strength, density or sintering temperatures for P/M materials [1, 11-17].

Macroscopic fracture surface examination showed that all three materials had 100% flat fracture with no shear lips nor visible plastic deformation. Scanning electron fractography revealed all three material fracture regions were ductile dimples. Material A showed courser fracture surfaces with fewer and smaller regions of ductile tearing indicating less contact between particles, larger porosity and lower density. Material C had more rounded pores in the fracture surface. The macro/micro examination revealed that global plane strain fracture was brittle, while local fracture was ductile dimples.

Fatigue Crack Growth, da/dN-ΔK

Fatigue crack growth behavior was obtained using 9.5 mm thick compact disk DC(T) specimens (FIG. 1(b)) following ASTM Test Method for Measurement of Fatigue Crack Growth Rates (E647). Two load ratios $R = P_{min}/P_{max}$ equal to 0.05 and 0.5 were evaluated with crack growth rates between 10^{-10} and 10^{-4} m/cycle. These rates included the complete sigmoidal da/dN versus ΔK behavior, regions I, II and III. Tests were run between 5 and 40 Hz depending upon da/dN. Crack lengths were monitored using a 30x traveling telescope. Load shedding was used in near threshold region I while constant amplitude loading was used for regions II and III. ΔK_{th} was defined at da/dN = 10^{-10} m/cycle as per ASTM E647. Crack length versus applied cycles data were converted to da/dN using a secant method between adjacent data points. ΔK was determined using equations (5) and (6) and replacing P with $\Delta P = P_{max} - P_{min}$. Crack closure was monitored with a CMOD gage with readings taken at both R ratios in regions I and II. Loading and unloading, P vs. CMOD curves were identical with no closure evident in any tests. Thus crack closure for these high strength P/M steels with constant R ratio tests was not present.

da/dN versus ΔK data for material C with R = 0.05 and 0.5 (FIG. 13) was reasonably typical for all three materials. R ratio effects were small or negligible in regions I and II and very distinct in region III. Fatigue crack growth parameters for all three materials (TABLE 5) along with superposition of R = 0.05 results (FIG. 14) and R = 0.5 results (FIG. 15) provide a complete comparison of fatigue crack growth behavior for the three materials. For a given R ratio, regions I and II were similar for all three materials. ΔK_{th} was about 3 MPa$\sqrt{m}$ for all three materials with both R ratios. This is consistent with no closure existing. Region III, however, clearly shows significant material differences. Region III fatigue crack growth and fracture resistance is greatest for material C, intermediate for material B and lowest for material A. For a given material, K_{max} at fracture (TABLE 5) was similar to K_{Ic} despite the significant differences in loading rate and crack length. Paris equation parameters for region II (TABLE 5) where obtained by linear log-log regression of

$$\frac{da}{dN} = A(\Delta K)^m \tag{7}$$

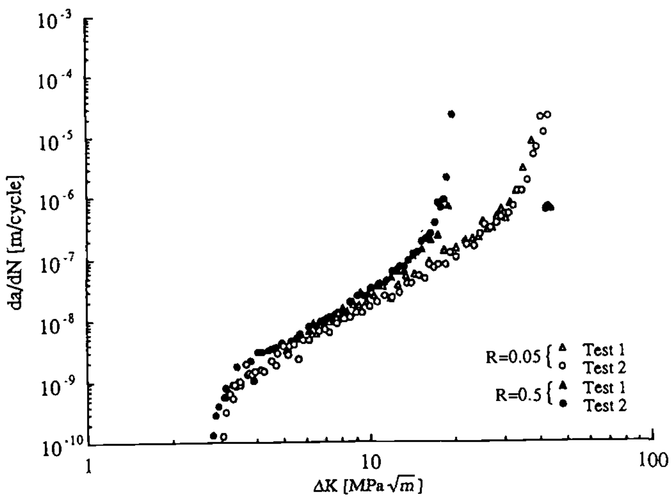

FIG. 13--*da/dN vs. ΔK with R = 0.05 and 0.5 for material C*

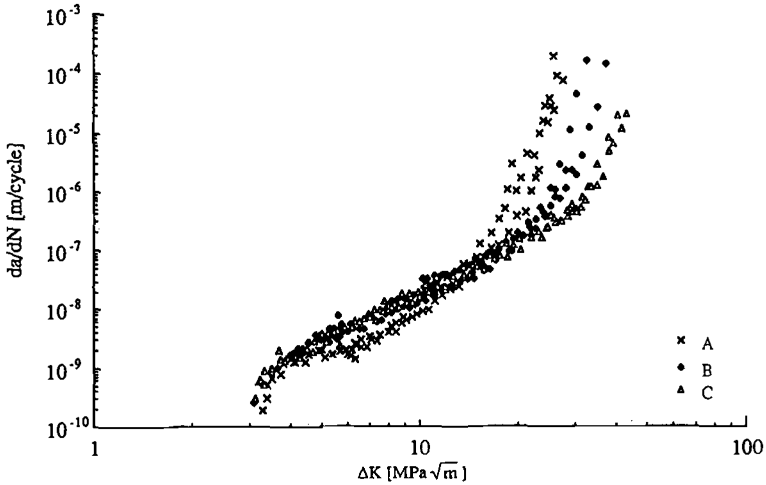

FIG. 14--*da/dN vs. ΔK with R = 0.05 for materials A, B and C*

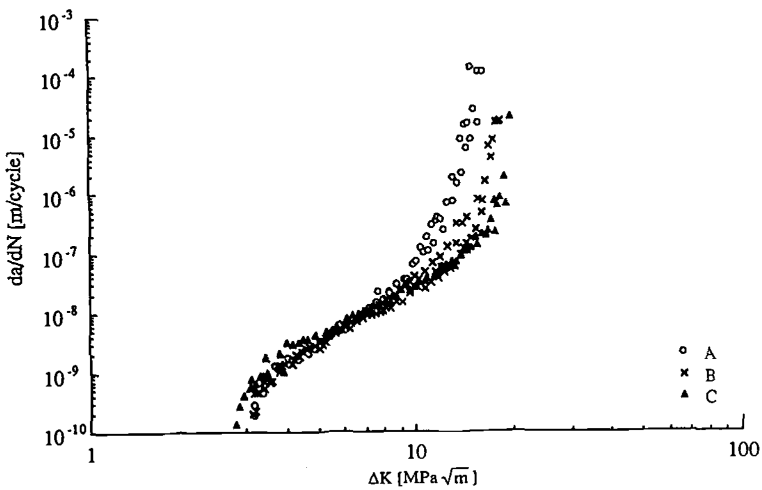

FIG. 15--*da/dN vs. ΔK with R = 0.5 for materials A, B and C*

TABLE 5--*Fatigue crack growth parameters and K_{Ic} units in m/cycle and MPa$\sqrt{m}$*

Material	A	B	C
R = 0.05			
ΔK_{th} - MPa$\sqrt{m}$	3.1	2.8	3.0
A	1.75 x 10^{-12}	3.66 x 10^{-11}	3.47 x 10^{-11}
m	3.84	2.71	2.74
K_{max} at fracture - MPa$\sqrt{m}$	27	37	45
R = 0.5			
ΔK_{th} - MPa$\sqrt{m}$	3.0	2.9	2.7
A	6.89 x 10^{-12}	1.44 x 10^{-11}	3.22 x 10^{-11}
m	3.81	3.31	3.00
K_{max} at fracture - MPa$\sqrt{m}$	32	36	40
K_{Ic} - MPa$\sqrt{m}$	28	31	42

Macroscopic examination of the fatigue crack growth fracture surfaces revealed all flat surfaces with no shear lips for all three materials and both R ratios. Regions I and II were smooth with increased coarseness in region III. Material A with its lower density and greater porosity exhibited greater coarseness than materials B and C. Scanning electron fractography was performed on all three materials. Near threshold region I morphology (FIG. 16) and region II morphology (FIG. 17) indicate all fatigue crack growth for these two regions were transgranular/transparticle cleavage for all three materials. Greater porosity is evident for material A and more rounded pores are evident for material C. Fatigue crack growth in region III (FIG. 18) was mixed with some cleavage and mostly ductile dimples. The final fracture region for all three materials was ductile dimples similar to all previously described final fracture regions. Thus, at low and intermediate ΔK values where plastic zone sizes were small, and cracks grew via cleavage, the fatigue crack growth resistance was similar for all three materials. However, differences existed at the higher ΔK values, and hence larger plastic zone sizes, where some cleavage and mostly ductile dimples existed. This suggests fatigue crack growth via ductile dimples may be a dominant factor in altering fatigue resistance of these P/M materials.

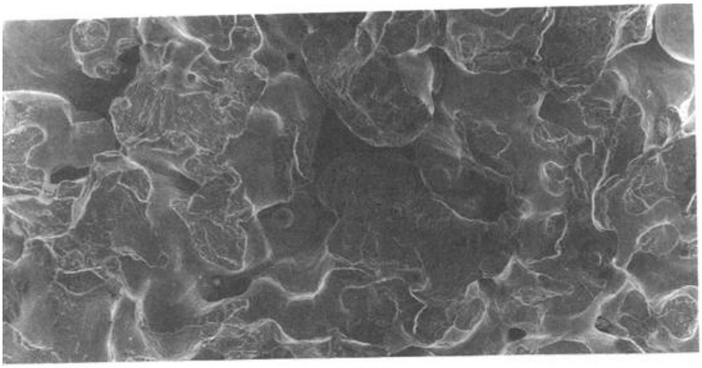

(a) material A

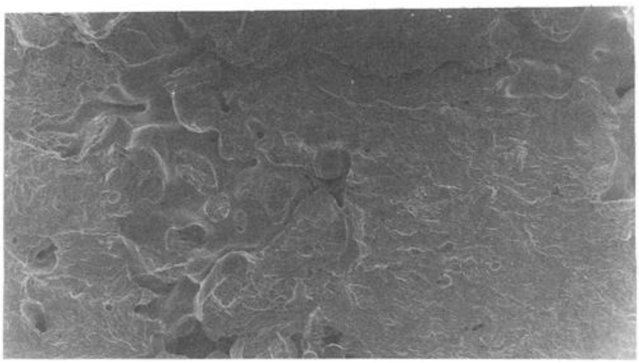

(b) material B

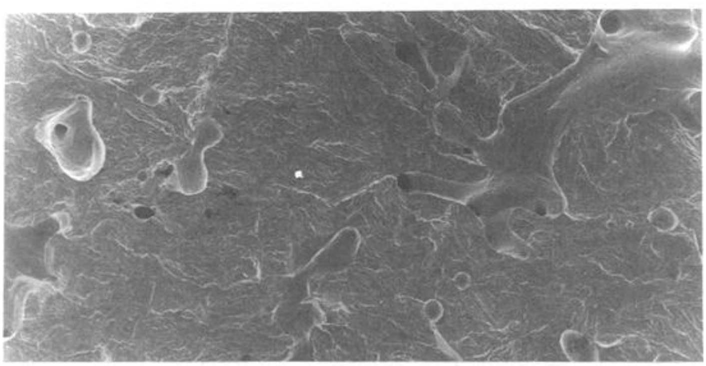

(c) material C

$\lfloor 10\,\mu \rfloor$

FIG. 16--*Fatigue crack growth surfaces in region I (near ΔK_{th})*

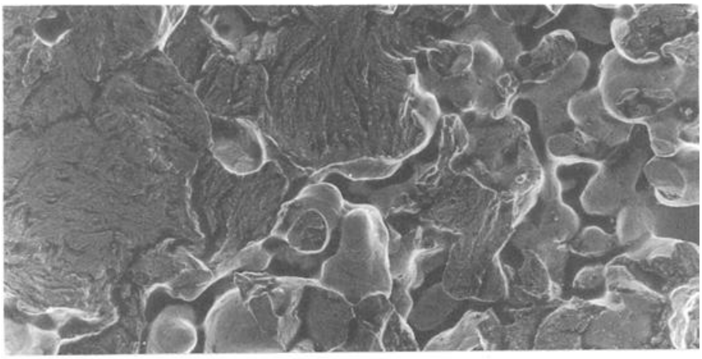

(a) material A

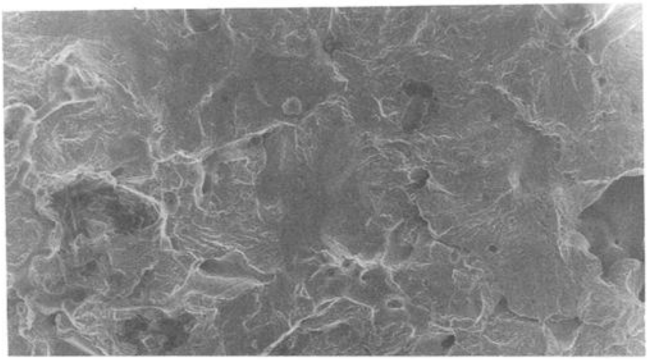

(b) material B

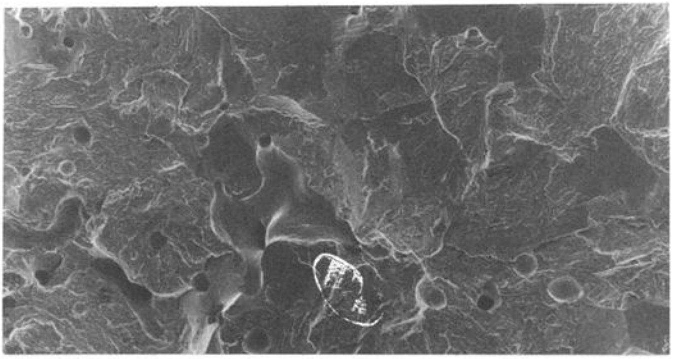

(c) material C

10 μ

FIG. 17--*Fatigue crack growth surfaces in region II (Paris region)*

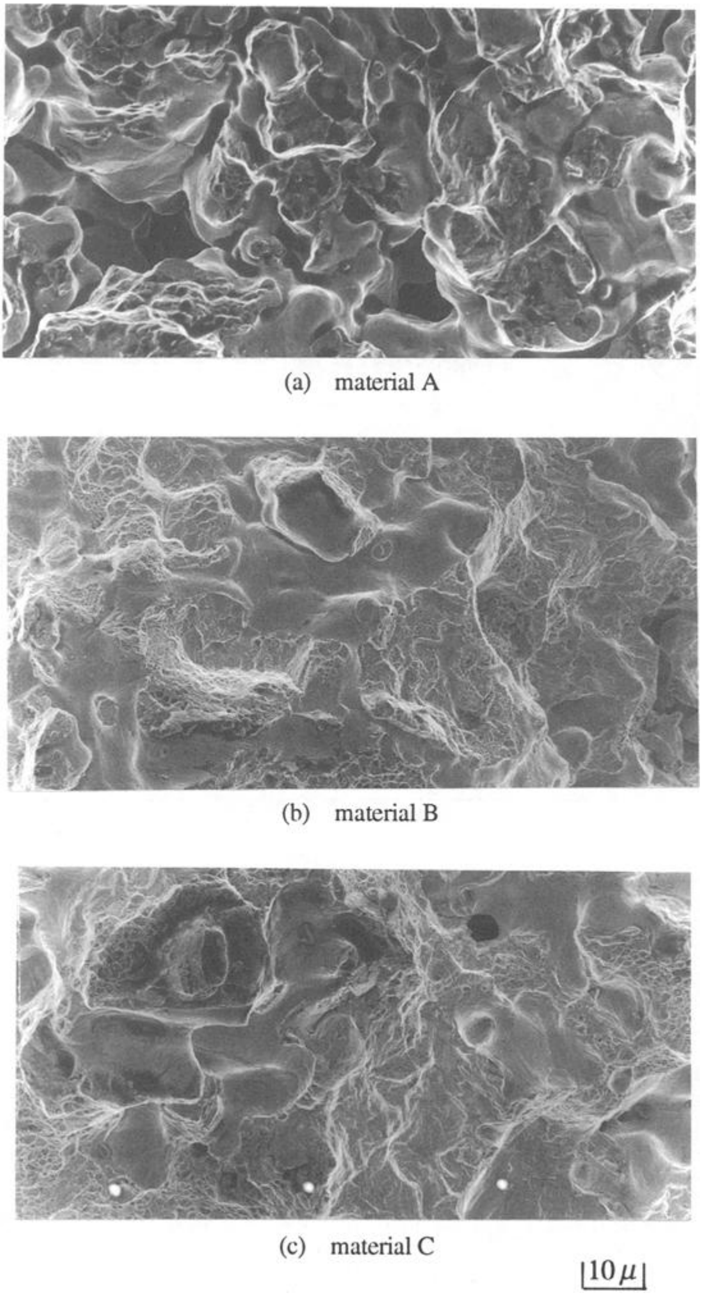

(a) material A

(b) material B

(c) material C

FIG. 18--*Fatigue crack growth surfaces in region III (rapid growth)*

Variable Amplitude Fatigue

Load Spectrum

The load spectrum used for all variable amplitude tests was an edited version of the SAE Fatigue Design and Evaluation Committee's log skidder history [18]. The edited version contained 20127 reversals and included fully-reversed, tensile mean and compressive mean values (FIG. 19). A wide range of amplitudes and mean values existed in the spectrum. Variable amplitude fatigue tests were run involving smooth, keyhole notched and compact disk DC(T) pre-cracked specimens.

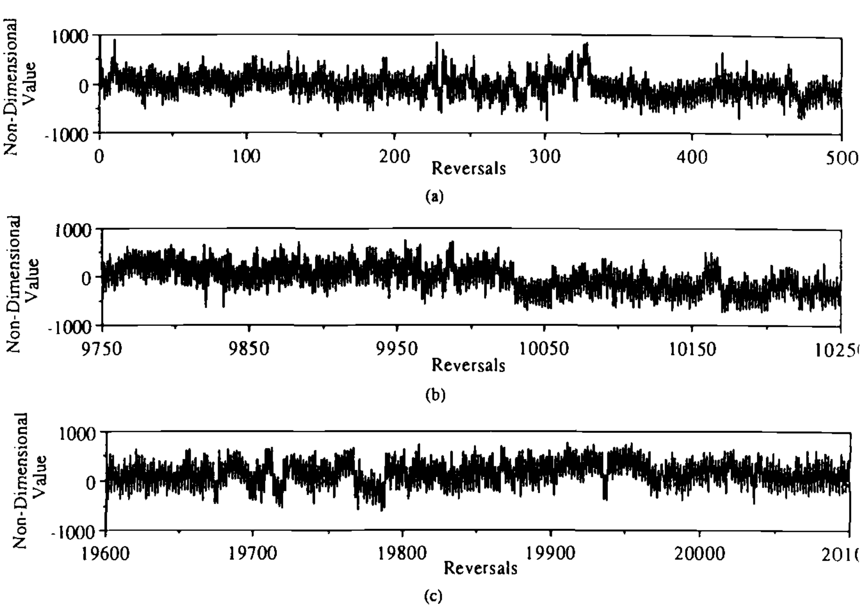

FIG. 19--*Variable amplitude load spectrum*
(a) first 500 reversals (b) middle 500 reversals (c) last 500 reversals

Smooth specimens

Smooth axial specimens (FIG. 1(a)) where tested for each material at two different peak load levels. Duplicate tests were planned for each material and load level, however one material B specimen was ruined during a test malfunction. Hence only three valid fatigue tests existed for material B, while materials A and C had four valid tests. Peak stress levels were calculated based upon obtaining maximum fatigue life of several hundred blocks or less ($<10^7$ reversals). The peak stress levels were less than the tensile yield strength in all cases. Tests were run in load control at 7 Hz until fracture. As with previous smooth specimen strain control tests, crack depths were $\lesssim$ 1.5 mm at fracture and very little scatter in fatigue life existed for duplicate tests. Peak stress versus blocks to fracture (FIG. 20) indicate an appreciable increase in fatigue resistance for materials B and C over material A and only a small increase in fatigue resistance for material C over material B.

Keyhole Notched Specimens

Keyhole notched specimens (FIG. 1(c)) were tested for each material at two different load levels with duplicate tests at each level. Peak load levels were again chosen to have failure within several hundred blocks. Peak stress levels at the notch were less than the tensile yield strength in all cases. Tests were run in load control at about 14 Hz. Failure was defined as a through crack of 1.5 mm from the keyhole notch consistent with smooth specimen low cycle fatigue results. Final fracture was consistent with this crack length criterion. Local peak stress versus blocks to failure (FIG. 21) indicate similar results to the smooth specimen variable amplitude behavior (FIG.20). That is, the material B and C fatigue resistance is significantly better than that of material A, while material C is

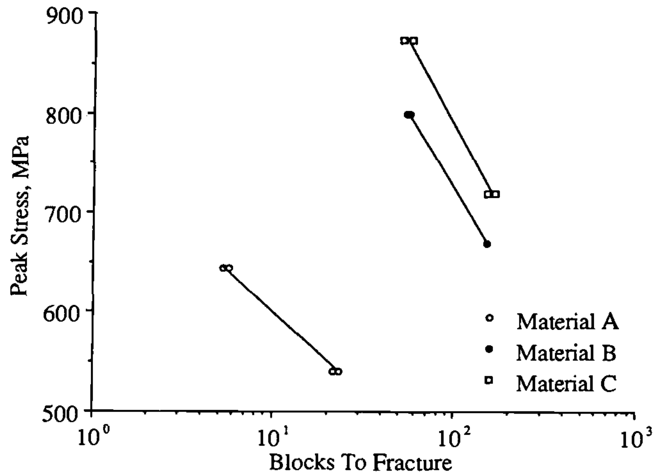

FIG. 20--*Variable amplitude smooth specimen fatigue behavior for materials A, B and C*

only slightly better than material B. Thus for both smooth and notched variable amplitude fatigue loading involving crack growth to about 1.5 mm or less, increasing the density (smaller pore size and volume) caused significant increase in fatigue resistance, while increasing the sintering temperature (greater pore roundness) had a much smaller benefit.

Compact Disk Pre-cracked Specimens

Compact disk DC(T) specimens (FIG. 1(b)) for all three materials were precracked to a_i = 34.5 mm and tested to fracture with the variable amplitude history at one peak load level and duplicate tests. The initial peak stress intensity factor was about 20 MPa$\sqrt{m}$ however, within a given block many amplitudes of loading caused values of ΔK to range throughout regions I, II and III. Crack extension at fracture and blocks to fracture indicated by bar charts (FIG. 22) show that materials B and C had significantly greater crack tolerance at fracture along with significantly greater variable amplitude fatigue crack growth resistance than material A. Differences between materials B and C were smaller. Average blocks to grow the crack from 34.5 mm to fracture are indicated in FIG. 22(b). Average fatigue crack growth extension at fracture was 5, 13 and 17 mm for materials A, B and C respectively. The increased life for materials B or C was not just from higher fracture toughness, but also from lower fatigue crack growth rates.

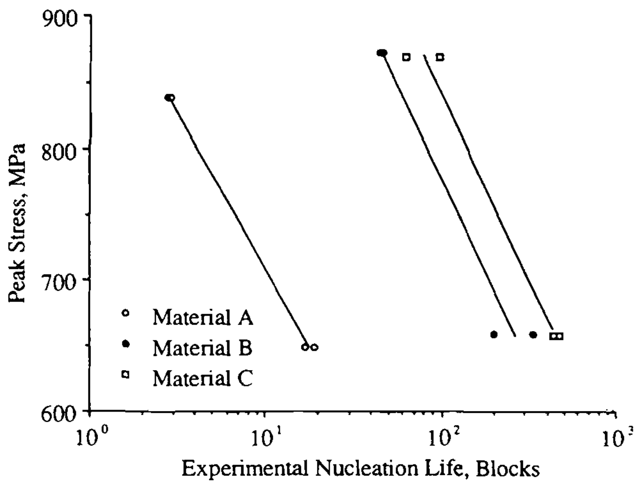

FIG. 21--*Variable amplitude keyhole notch fatigue behavior for materials A, B and C*

Fractography

Macroscopic examination revealed all variable amplitude fatigue crack growth and final fracture regions were brittle and flat without shear lips. No beach marks were evident despite the variable amplitude loading involving both tension and compression. Elliptical surface cracks formed for both smooth and notched specimens. Scanning electron fractography indicated that for the smooth and notched variable amplitude tests the fatigue crack initiation regions, fatigue crack growth regions and final fracture regions were essentially the same as those found for the constant amplitude notched specimens. That is, mostly cleavage for A and mixed cleavage and ductile dimples for B and C near the initiation regions and mixed cleavage and ductile dimples in the fatigue crack growth regions. Final fracture regions were all ductile dimples. For the compact disk variable amplitude fatigue crack growth tests, all three materials showed mostly cleavage with some ductile dimples at short crack length extension (FIG. 23). At mid crack extension (FIG. 24) material A was mostly ductile dimples with some cleavage while materials B and C were mostly cleavage and some dimples. At final fracture all materials were ductile dimples.

Discussion of Results

Both image analysis and scanning electron fractography showed that material A, with its low density and low sintering temperature, did have large porosity size, irregular shapes and high void space. They also showed material B, with its higher density and low sintering temperature, had smaller porosity size, porosity volume and intermediate pore roundness while material C, with its higher density and high sintering temperature, also had smaller porosity size, porosity volume but had the largest amount of pore roundness. In most scanning electron fractography the increased void space showed up in material A and the increased pore roundness showed up in material C. Thus the three test materials contained the planned microstructure/morphology.

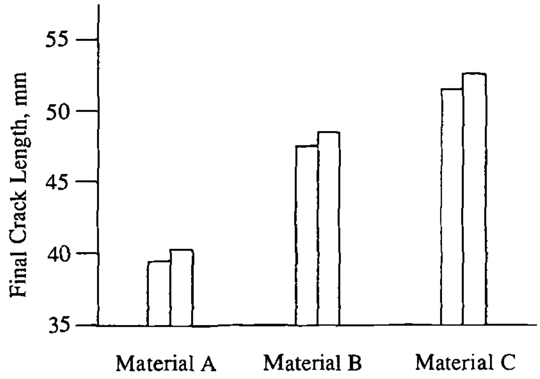

(a) crack length at fracture

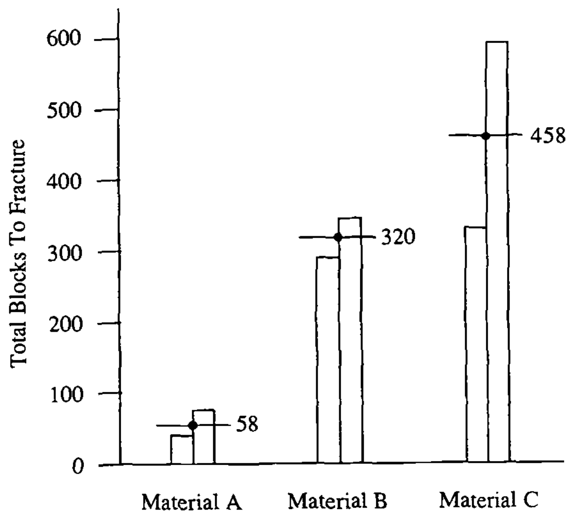

(b) blocks to fracture

FIG. 22--*Variable amplitude fatigue crack growth behavior for materials A, B and C*

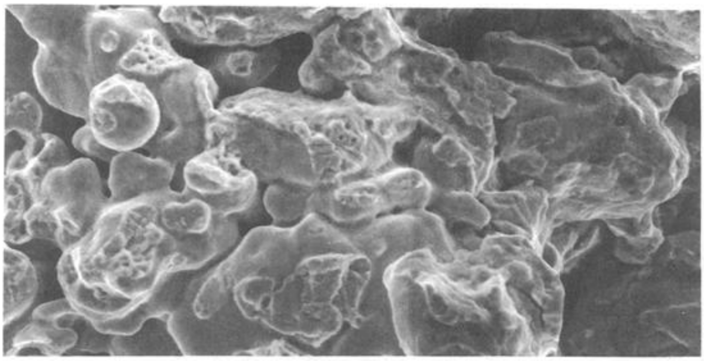

(a) material A

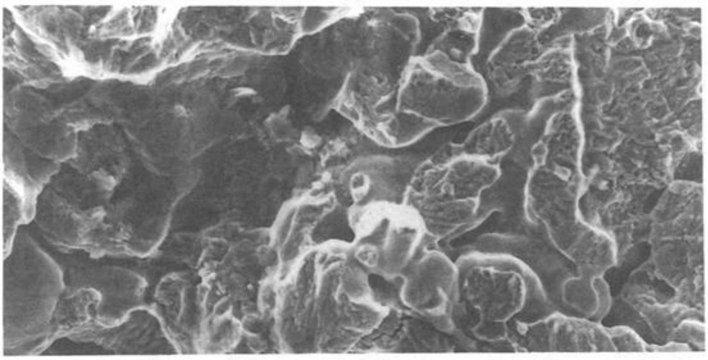

(b) material B

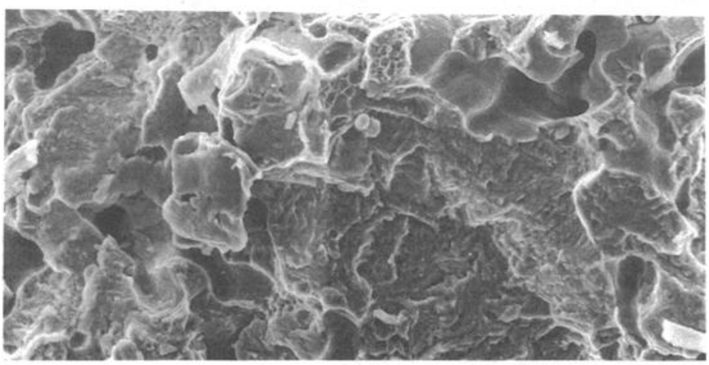

(c) material C

10μ

FIG. 23--*DC (T) variable amplitude fatigue surfaces at short crack extension*

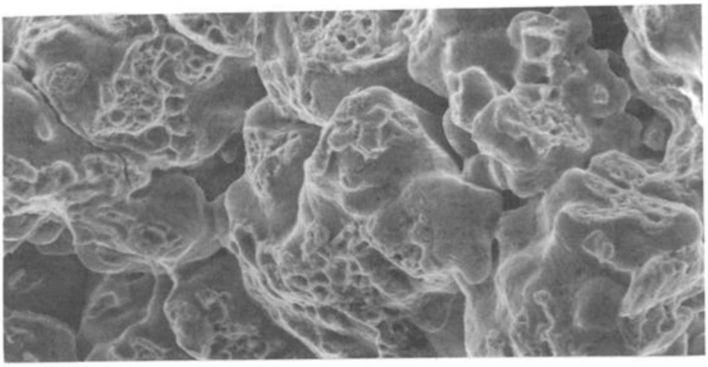

(a) material A

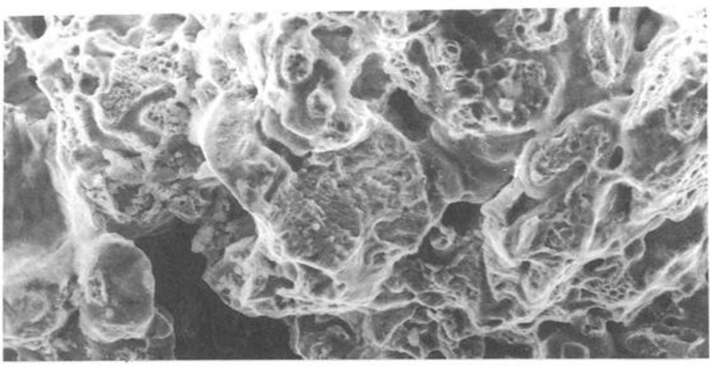

(b) material B

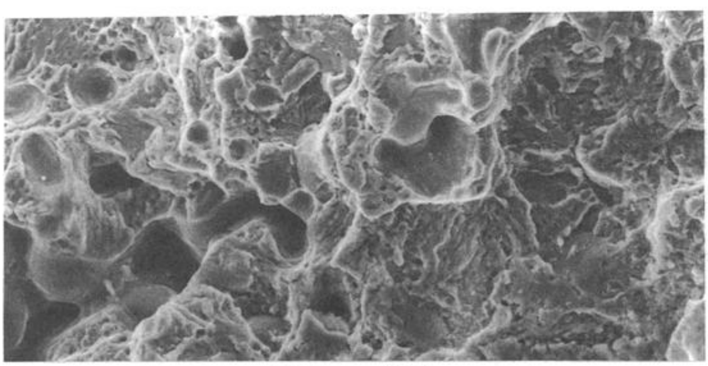

(c) material C

|10 μ|

FIG. 24--*DC (T) variable amplitude fatigue surface at mid crack extension*

Many different comparative tests were performed with the three material conditions. These involved static monotonic stress-strain and plane strain fracture toughness, K_{Ic}, along with fatigue tests involving smooth, notched and cracked specimens. Both constant amplitude and variable amplitude fatigue conditions were employed with all three types of specimens. This wide variety of tests was considered necessary in order to make proper comparisons, but also to obtain common material properties often used in design. Variable amplitude tests are usually considered the most desirable for comparative purposes because they will often involve interaction influences not involved in constant amplitude tests [19-21].

The final fracture region of all three materials for all tests including smooth, notched, cracked, monotonic and constant or variable amplitude fatigue tests involved a macroscopic brittle appearance. This included a flat fracture surface with no shear lip nor slant fracture and no obvious permanent deformation. However, scanning electron fractography revealed all these final fracture surfaces failed at the local microscopic level via ductile dimples. Essentially no cleavage was found in the final fracture areas. Hence, fracture for these three tempered martensitic P/M steels were brittle at the macro level and ductile at the local level. The macro fatigue regions were essentially the same as the macro final fracture regions. That is, they were all flat with no shear lips nor slant fracture and no obvious permanent deformation. Beach marks were not evident on any fatigue surfaces for either constant or variable amplitude tests.

Scanning election fractography of fatigue crack initiation and growth regions revealed two different micro mechanisms. Both cleavage and ductile dimples were found at near initiation sites and in fatigue crack growth regions. They often occurred completely separate or at times mixed cleavage and ductile dimples existed in micro regions. No striations existed for any of the fatigue test conditions. The amount of ductile dimples was often less in material A due to its greater void percentage. The most consistent trend of cleavage versus ductile dimples was with the precracked compact disk, DC(T) specimens under constant R ratio testing where regions I and II fatigue crack growth morphology was dominated by cleavage for all three materials. These are regions of low and intermediate ΔK, da/dN and plastic zone size. In region III, at higher ΔK, da/dN and plastic zone size, ductile dimples were dominant. The variable amplitude DC(T) specimen tests showed mostly cleavage with some ductile dimples at small crack extension and hence lower ΔK, da/dN and plastic zone size. At mid length crack extension and hence higher ΔK, da/dN and plastic zone size, material A was dominated by ductile dimples, while materials B and C showed mostly cleavage with some ductile dimples. It does appear, however, that cleavage morphology was more common at lower fatigue crack growth rates while ductile dimples were dominant at higher fatigue crack growth rates.

The three P/M materials with their two densities and two sintering temperatures had many similarities in this research program such as the macro and micro fracture surface appearance as just described. In addition, all three materials were essentially cyclically stable with only a small amount of cyclic softening occurring. Very little plastic strain was evident in the smooth specimen strain controlled low cycle fatigue behavior. All materials were notch sensitive with K_f values at long life essentially equal to K_t which was 3.5. No crack closure existed in constant R ratio fatigue crack growth tests, and fracture toughness load versus CMOD curves were linearly elastic up to almost fracture instability for all three materials. The most unusual similarity, however, existed in the constant R ratio fatigue crack growth regions I and II where all three materials had essentially the same fatigue crack growth resistance and cleavage crack growth morphology. All other tests however showed significant differences in monotonic tensile stress-strain, plane strain fracture toughness and fatigue behavior. In all these tests, material B with its high density and low sintering temperature significantly outperformed material A with its lower density and low sintering temperature. Material C with its high density and high sintering temperature also significantly outperformed material A, but showed only small improvement over material B. Thus the influence of higher density was of much greater importance than that of higher sintering temperature. Therefore porosity size and void volume had greater influence on tensile stress-strain, fracture toughness and fatigue resistance than the increased pore roundness obtained from high temperature sintering. The higher sintering temperature however did produce the best tensile stress-strain, fracture toughness and fatigue resistance. Its additional cost must be assessed in relation to the benefits from these improvements.

Summary and Conclusions

1. Imaging analysis and scanning electron fractography showed that high temperature sintering (1315°C) increased pore roundness, while low density (7.0 g/cm^3 compared to 7.4 g/cm^3) had larger pore size and shape irregularity, and larger void volume.

2. High density (7.4 g/cm^3 compared to 7.0 g/cm^3) in general caused a significant increase in monotonic strengths, ductility, elastic modulus, plane strain fracture toughness, and fatigue resistance under both constant and variable amplitude loading for both smooth, notched and cracked specimens.

3. High temperature sintering (1315°C compared to 1120°C) in general caused an additional smaller increase in the above mechanical behavior. Thus, even though high temperature sintering produced the most desirable monotonic and fatigue properties, the increases were smaller than those caused by increased density.

4. The only disagreement with the above two general conclusions was in region I (threshold) and region II (Paris) of constant R ratio fatigue crack growth tests where all three materials had essentially the same fatigue crack growth resistance.

5. Based upon plane strain fracture toughness, K_{Ic}, and constant or variable amplitude fatigue crack growth, the high sintering temperature provided the most crack tolerance followed by the high density.

6. No crack closure existed for R = 0.05 and 0.5 and R ratio effects were very small in regions I and II. Region III (high da/dN) showed appreciable R ratio effects.

7. Under strain controlled low cycle fatigue conditions, all three materials were cyclically stable with only a small amount of cyclic softening. Plastic strain amplitudes were essentially an order of magnitude or more less than elastic strain amplitudes.

8. At long lives, 10^5 cycles, using keyhole notch specimens, all three materials were fully notch sensitive with $K_f \approx K_t = 3.5$. This was independent of density and sintering temperature.

9. All macro final fracture surfaces were flat with no shear lip, slant fracture nor permanent deformation and thus brittle in appearance, while all micro final fracture regions involved ductile dimples. Thus macro brittle behavior and micro ductile behavior existed in all three materials at final fracture, independent of sintering temperature and density.

10. Fatigue region fracture surfaces included cleavage only, ductile dimples only or mixed regions of cleavage and ductile dimples. Higher ΔK, da/dN and plastic zone sizes resulted in more ductile dimple morphology. No striations nor beach marks occurred with either constant or variable amplitude loading.

Acknowledgment

The authors would like to thank Mr. Tom Prucher of Burgess-Norton for manufacturing and providing all the test specimens, some grips and imaging analysis for this research, and for many very informative and helpful discussions. Members of the SAE Fatigue Design and Evaluation Committee also contributed to discussions involving this research. The research was also supported by the SAEFDE-University of Iowa Fatigue Concepts in Design short course.

References

[*1*] Fleck, N.A. and Smith, R.A. "Effect of Density on Tensile Strength, Fracture Toughness, and Fatigue Crack Propagation Behavior of Sintered Steel" *Powder Metallurgy*, No. 3, 1981, pp. 121-125.

[*2*] Sanderow, H. and Prucher, T. "Mechanical Properties of Low Alloy Steels: Effect of Composition, Density and Heat Treatment" *Advances in Powder Metallurgy and Particulate Materials, Vol. 7*, Metal Powder Industries Federation, Princeton, NJ, 1994, pp. 355-371.

[*3*] Sonsino, C.M. "Fatigue Design for Powder Metallurgy" Contribution to The Institute of Metals International Conference on Powder Metallurgy, The Institute of Metals, 1990.

[*4*] Sonsino, C., Schlieper, G., and Huppmann, W.J., "Influence of Homogeneity on the Fatigue Properties of Sintered Steels," *The International Journal of Powder Metallurgy and Powder Technology*, Vol. 20, 1984, pp. 45-50.

[*5*] Sanderow, H.I., "High Temperature Sintering of Ferrous P/M Components," In *New Perspectives in Powder Metallurgy: High Temperature Sintering*, Edited by Howard Sanderow, Metal Powder Industries Federation, New Jersey, 1990.

[*6*] Hudson, S.A., Fulmer, J.J., and Griffith, D.R. "Characterization of a High Performance P/M Steel for Use in Fatigue Design," Society of Automotive Engineers, Warrendale, PA, 1990.

[*7*] MPIF Standard 51, "Determination of Microhardness of Powder Metallurgy Materials," Metal Powder Industries Federation, Princeton, NJ, 1994, pp. 1-3.

[*8*] Pease, L.F., "Image Analysis of Materials A, B and C," Powder-Tech Associates, Inc., North Andover, MA, Laboratory Report, June, 1996.

[*9*] Mazen, A.A. and Lade, P.V. "Failure of Porous AISI 1018 P/M Steel Under Different Loading Conditions", *Proceedings of the First International Conference on Failure Analysis*, ASM International, Materials Park, Ohio, 1992, pp. 13-19.

[*10*] Newman, J.C., Jr., "Stress Intensity Factors and Crack Opening Displacements for Round Compact Specimens," *International Journal of Fracture*, Vol. 17, No. 6, December 1981,
pp. 567-578.

[11] Ingelstrom, N. and Ustimenko, V., "The Influence of Porosity and Carbon Content on the Fracture Toughness of Some Sintered Steels," *Powder Metallurgy*, Vol. 18, 1975, pp. 303-322.

[12] DasGupta, P.S., and Queeney, R.A., "Fatigue Crack Growth Rates in a Porous Metal," *The International Journal of Fatigue*, Vol. 2, 1980, pp. 113-117.

[13] Crane, L., and Farrow, R., "Effect of Sintering Conditions on Fracture Toughness of a Commercial Alloy Steel," *Powder Metallurgy*, Vol. 23, No. 4, 1980, pp. 198-202.

[14] Dimascio, P. and Queeney, R., "Fatigue Crack Propagation Rates in a Sintered Aluminum Alloy Powder," *The International Journal of Powder Metallurgy and Powder Technology*, Vol. 19, 1983, pp. 127-135.

[15] Navara, E., and Bengtsson, B., "Fracture Toughness of P/M Steels," *The International Journal of Powder Metallurgy and Powder Technology*, Vol. 20, 1984, pp. 33-43.

[16] Wang, K. and Prucher, T., "Fracture Toughness Evaluation on Iron-Nickel and Iron-Copper P/M Steels," *Advances in Powder Metallurgy and Particulate Materials*, Vol. 1, 1993, pp. 287-301.

[17] Wang, K. and Prucher, T., "Fracture Toughness Measurements of P/M Steels," *Advances in Powder Metallurgy and Particulate Materials*, Vol. 2, 1994, pp. 69-82.

[18] Lease, K.B. and Stephens, R.I., "Verification of Variable Amplitude Fatigue Life Methodologies for a Cast Aluminum Alloy," paper 910163 SAE Transactions, *Journal of Materials and Manufacturing*, Vol. 100, Section S, 1991, pp. 105-123.

[19] Fuchs, H.O. and Stephens, R.I., *Metal Fatigue in Engineering*, Wiley Interscience, New York, 1980.

[20] Hertzberg, R.W., *Deformation and Fracture Mechanics of Engineering Materials*, 4th edition, John Wiley and Sons, New York, 1996.

[21] Dowling, N.E., *Mechanical Behavior of Materials*, Prentice Hall, Englewood Cliffs, NJ, 1993.

Steven M. Tipton[1]

LOW-CYCLE FATIGUE TESTING OF TUBULAR MATERIAL USING NON-STANDARD SPECIMENS

REFERENCE: Tipton, S. M., "**Low-Cycle Fatigue Testing of Tubular Material Using Non-Standard Specimens,**" *Effects of Product Quality and Design Criteria on Structural Integrity, ASTM STP 1337,* R. C. Rice and D. E. Tritsch, Eds., American Society for Testing and Materials, 1998.

ABSTRACT: Coiled tubing life prediction models are based on the use of standard low-cycle fatigue data. However, coiled tubing dimensions and the ultra-low-cycle life regime of interest, combine to complicate "standard" experimental methodology. This paper describes coupon design and testing procedures that alleviate the difficulties inherent to strain-controlled low-cycle fatigue testing of tubular material. Data sets are presented and compared to existing sets generated using smaller specimens. It is shown that the refined approach facilitates the generation of data in the ultra-low-cycle coiled tubing operating regime. The difference between the morphologies of the outer and inner surfaces of the specimens, as manufactured by standard tube rolling techniques, proved to be influential, but could not fully explain the comprehensive tendency for cracks to initiate at the inner surface. The inherently lower fatigue resistance of the inner surface indicates the theoretical existence of a "threshold defect severity" which must be exceeded on the outer surface before it would affect the fatigue life of the tubing.

KEYWORDS: coiled tubing, low-cycle fatigue, tubular materials, surface effects, tube rolling, surface roughness, surface defects

Coiled tubing is used in the petroleum industry to perform a wide variety of production and well service operations, from drilling to logging[1]. Long strings of continuous tubing (up to 25,000 ft. (7.6 km)) are wrapped onto large spools upon fabrication. From these spools, the tubing is deployed into and retrieved from well bores, resulting in severe bending strain fluctuations on the order of 2-3% in strain range. The use of coiled tubing in the petroleum industry is steadily increasing. This growth can be attributed in part to the successful implementation of an algorithm used to successfully monitor plasticity and fatigue behavior under field loading [2-3]. The model is based on

[1]Professor, Mechanical Engineering Department, The University of Tulsa, 600 S. College Avenue, Tulsa, OK.

the use of standard low-cycle fatigue data. However, coiled tubing dimensions and the ultra-low-cycle life regime of interest, combine to complicate standard experimental methodology, as described by the ASTM Recommended Practice for Constant-Amplitude Low-Cycle Fatigue Testing (E 606). Previous low-cycle testing on coiled tubing samples provided useful data sets [3,4], but included very few data points for lives below 1000 cycles, the predominant operating regime for coiled tubing. This was due to the difficulty in avoiding specimen buckling in this ultra-low cycle regime. This paper describes coupon design and testing procedures that alleviate some of the difficulties inherent to strain-controlled low-cycle fatigue testing of tubular material. Most of the testing protocol defined in ASTM E 606 are still pertinent, however, tubing geometry makes the fabrication of cylindrical specimens impractical. Coupons are extracted from the tubing and special grip inserts are used to maintain the tube wall curvature while keeping the centroid of the specimen gage section coincident with the axis of loading. This approach offers the additional advantage of preserving surface profiles imposed by manufacturing processes on both sides of the tubing.

Data sets for three coiled tubing materials are presented and compared to existing sets generated using smaller specimens. It is shown that the refined gripping configuration and specimen design presented in this study (a wider and shorter gage section) was not susceptible to buckling, and thus able to withstand testing in the ultra-low-cycle coiled tubing operating regime. It was observed that cracks initiated exclusively at the inner surface of each specimen tested. Profilometer data are presented which reveal that the standard tube rolling process used to manufacture coiled tubing inner surface induces a rougher profile on the inner surface than on the outer. To investigate this effect, several specimens were tested with polished inner surfaces and lives increased, as expected. However, cracks in these specimens also initiated at the polished inner surface. Therefore, surface roughness is shown only to partially explain the inherently lower fatigue resistance of the inner surface, relative to the outer surface. This observation could be important in the context of evaluating the influence on fatigue strength of external surface imperfections. A defect on the outer surface of the tubing may have to exceed a "threshold severity" before it is expected to degrade the fatigue strength of the tubing. Results from coupon tests with notched external surfaces are used to illustrate this effect.

LCF TESTING OF COILED TUBING COUPONS

Standard low-cycle fatigue testing per ASTM E-606 is usually conducted on specimens with reduced test sections. Reduced sections are ground and longitudinally lapped to a maximum surface roughness of 0.2 μm. In this way, the data are considered to represent fatigue resistance as a "material property," independent from the important influence of surface morphology. However, specimens geometries in ASTM E 606 primarily are intended for round or flat stock material, or material thick enough to be turned into cylindrical form. Coiled tubing wall thicknesses are predominantly well below 0.25 in. (6.3 mm) and not conducive to these geometries. Full body tube testing is a possibility, but was not pursued due to problems with test machine capacity and the avoidance of grip-induced failures. Instead, special specimens and fixturing were designed, which would facilitate testing into the ultra-low-cycle regime (strain ranges up to 3.0%). Specimens were designed such that the surface morphology of the inner and outer tube walls were preserved, thus avoiding the need for additional empirical "surface modification factors" in subsequent fatigue modeling. The specimen design, gripping geometry, testing procedure and results are presented in this section.

Specimen Design

Dog-bone-type specimens were numerically machined from tubing samples with initial dimensions of 1.75 in. (44.5 mm) outer diameter and a wall thickness of 0.156 in. (4.0 mm), as depicted in Fig. 1. Gage section dimensions are 0.7 in. (17.8 mm) width, 0.625 in. (15.9 mm) long with 1.25 in. (31.8 mm) fillet radii in the transition to the grip region. After machining, the edges of each specimen were manually ground and polished longitudinally to avoid fatigue crack initiation at the edges. A 0.5 in. (12.2 mm) gage length extensometer was used to control strain in the gage section.

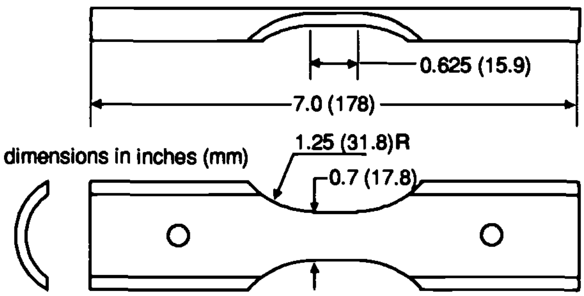

Figure 1 - *Coupon specimen dimensions.*

The exceptionally low length-to-width ratio was chosen to avoid buckling in the gage section. Previous tests on 70 ksi (483 MPa) yield strength tubing [3] and 80 ksi (552 MPa) tubing [4] were conducted using coupons extracted from tubes with a 1.25 in. (31.75 mm) diameter and a 0.087 in. (2.2 mm) wall thickness. The gage section of these specimens were 0.6 in. (15.2 mm) long and only 0.2 in. (5.1 mm) wide. However, specimen buckling inhibited the generation of valid data for lives below 1000 cycles, the predominant regime for coiled tubing. For the 80 ksi (552 MPa) material grade, 2 data points out of 14 were collected in this regime. More low cycle points were collected for the 70 ksi (483 MPa) samples (9 of 20), where shorter gage lengths also were used, however the monotonic properties for the material used to generate that data set differ considerably from the current properties for that grade of material. Therefore, specimens were fabricated from 100 (690 MPa) ksi, 80 ksi (552 MPa) and 70 ksi (483 MPa) yield strength grades of coiled tubing material. These materials will be referred to as 100 grade, 80 grade and 70 grade, respectively, for the remainder of this paper.

Grip Inserts

Special grip inserts were machined to hold the centerline of the gage section coincident with that of the load train while maintaining the as-manufactured curvature and surface profiles of the tubing walls. The inserts are depicted in Figure 2, with the specimen. The dimensions of the inserts were selected based on Eqn. 1, derived for the centroidal location of the gage section cross section,

$$y=\frac{D}{2}-\frac{2w\left(Dt-t^2\right)}{\left[w\sqrt{D^2-w^2}+D^2\sin^{-1}\left(\frac{w}{D}\right)-w\sqrt{(D-2t)^2-w^2}-(D-2t)^2\sin^{-1}\left(\frac{w}{D-2t}\right)\right]} \quad (1)$$

where y is the distance from the outer surface to the centroid, as shown in Fig. 2, and D and t are the outer diameter and wall thickness, respectively. The cross sectional area, A, for this geometry is given by Eqn. 2.

$$A=\frac{1}{4}\left[w\sqrt{D^2-w^2}+D^2\sin^{-1}\left(\frac{w}{D}\right)-w\sqrt{(D-2t)^2-w^2}-(D-2t)^2\sin^{-1}\left(\frac{w}{D-2t}\right)\right] \quad (2)$$

The convex portion of the grip has a countersunk 0.25 in. (6.4 mm) clearance hole and the concave portion is threaded. The purpose of the screw is simply to secure the inserts to the specimens. The inserts serve to transfer the hydraulic gripping force uniformly from the jaws of the grips to the surface of the specimens. The curved surfaces of the inserts, which contact the specimen, were slightly serrated, to assure positive engagement.

Prior to conducting the tests, an alignment gage was constructed to assure alignment of the load train, as depicted schematically in Fig. 3. A ground smooth rectangular bar the same width as the grip insert, was centered in the lower grips using brass shim stock material. The alignment gage, consisting of two dial indicators for the wide side and two more for the narrow side, likewise was centered in the upper grips. The dial indicators were zeroed on a gage block, prior to loading them into the hydraulic grips. Finally, an alignment adjustment device on the upper grip was used to remove angular and transverse misalignment from the load train. Shim stock was used similarly to center each specimen-insert assembly into the grips prior to each test.

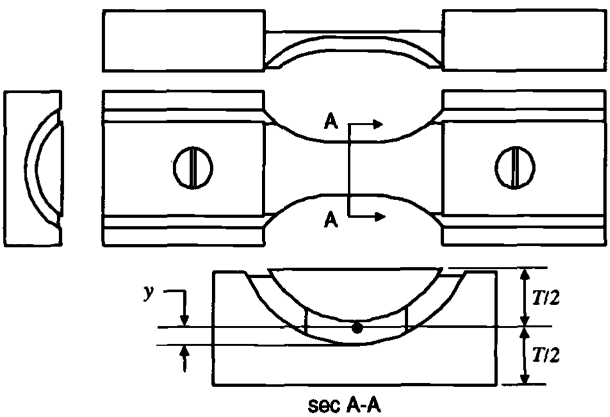

Figure 2 -- *Grip inserts and centroidal location of gage section.*

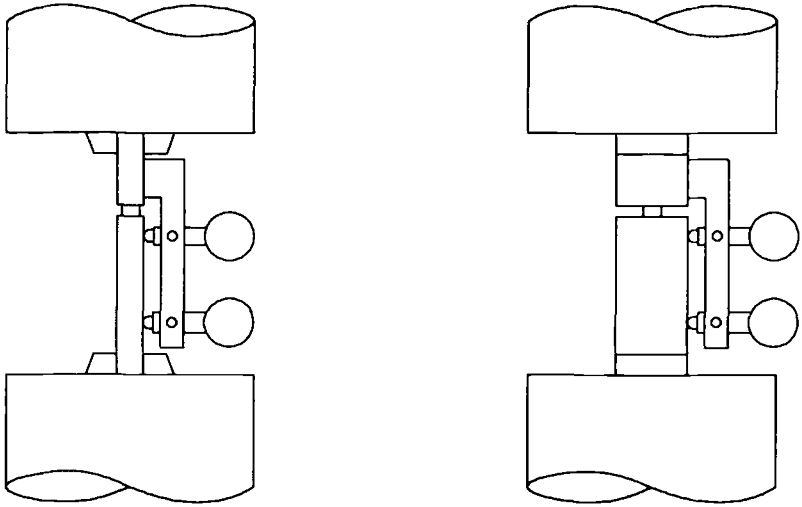

Figure 3 -- *Side view and front view of grip alignment gage set-up.*

Testing Procedure

In spite of the care taken to align the load train, it was noticed upon assembly of the specimen-grip inserts that the specimens were slightly bowed along their axis of curvature. The curvature, resulting from residual stresses released upon fabrication of the coupons, was pronounced in the 100 grade samples and negligible in the 70 and 80 grade samples. Strain gages were placed on the outer and inner surfaces of a 100 grade sample and the bending strains upon gripping were about 1000 $\mu\varepsilon$ (tension on the outer surface and compressive on the inner surface). This misalignment was impossible to avoid and caused buckling to occur when $R_\varepsilon = -1$ (fully reversed) strain controlled loading was imposed. To handle this situation, $R_\varepsilon = 0$ (fully tensile) strain controlled loading was used instead of fully reversed. In addition to alleviating the misalignment problem (by stretching the gage section during the initial loading cycle, essentially straightening the specimen), this type of loading is more typically encountered by coiled tubing material in the field under bending-straightening loading cycles. It should be noted that the 1000 $\mu\varepsilon$ curvature strain is small compared to the majority of the applied strain ranges used in these tests (0.6% to 3.0 %, or 6,000 $\mu\varepsilon$ to 30,000 $\mu\varepsilon$). It also should be noted that under these large strain ranges, the stress fluctuation was nearly fully reversed from the first cycle. That is, following a maximum tensile force required to strain the material to its first peak value, a compressive force of nearly equal magnitude is required to return the plastically deformed gage section to zero strain.

The tests were conducted on a 22 kip (97.9 kN) servohydraulic test machine under strain-control using an extensometer with a gage length of 0.5 in (12.7 mm). Failures associated with the knife edges were avoided by bonding phenolic/copper solder tabs to the edge of the specimen to shield the edge of the specimen from metal-to-metal contact. The extensometer was mounted to the edge of the specimen rather than on the outer (concave) surface in order to average out any bending which occurred during the early cycles of loading.

A trapezoidal wave form was used, with a constant strain rate of 0.2%/sec, and a hold time at each peak and valley of 0.2 seconds. For a test conducted at a strain range of $\Delta\varepsilon$ (in percent), this caused a testing period of

$$T = 10\text{sec}\ (\Delta\varepsilon) + 0.4\ \text{sec}. \tag{3}$$

For example, the smallest strain range tested, (0.6%) had a period of 6.4 seconds. The longest (3%) had a period of 30.4 sec. The 0.2 sec. hold time was used to assure the collection of several data points at each peak and valley.

Data Collection and Results

Strain and axial force data were collected on a computer data acquisition system for individual hysteresis loops at a rate of 250 points per cycle. The first 6 cycles were collected and every third cycle for the remainder of each test. The modified A606 alloy (A607 for the 100 grade material) is extremely fine grained (on the order of ATSM #12, extrapolated beyond the maximum value of #10), ductile and resistant to crack propagation. Under the large strain ranges used in this study, all materials cyclically softened such that the amplitude of stress tended to decay steadily throughout life (after a more rapid transient decay during the first few cycles). Tests were run until the peak load in the specimen dropped to a value of about 30% of its value for the first cycle. Some tests were run until the specimen fractured and it is interesting to note that the peak stress in these cases slowly decreased each cycle until just a tiny ligament of material fractured at the end of the specimen life.

The stress-strain data sets for each hysteresis loop were analyzed with a post-processing algorithm to define the peak and valley stresses. The "crack initiation life" was defined as the cycle count where the stress amplitude dropped to a value 10% less than the amplitude which occurred at 1/2 of that cycle count (the 50%-life, or mid-life). This was observed empirically as the point at which cracking could be observed with a low-power microscope on the surface of the specimen (exclusively on the inner surface, which will be discussed in more detail in a later section). The hysteresis loops corresponding to the initiation and mid-life cycles were written to a separate data file, along with the peak, valley and amplitude values of stress for each of these cycles. From the mid-life hysteresis loop, the program computed the plastic strain amplitude, defined as 1/2 of the loop width through the mean stress point, and the elastic strain amplitude defined as the total strain amplitude minus the plastic strain amplitude. The cyclic modulus of elasticity was defined as the stress amplitude divided by the elastic strain amplitude. For several cases, cyclic moduli also were computed from the slopes of the elastic loading and unloading segments of the 50%-life hysteresis loops. In all cases, these moduli were essentially identical and showed good correlation with the cyclic modulus defined by the data reduction algorithm. Sample hysteresis loops from the first six cycles are presented on the same axes with the separate mid-life loop (bold) in Fig. 4 (a), (c) and (e) for a strain amplitude of 1.6 % and in Fig. 5 (a), (c) and (e) for a strain amplitude of 2.6%. Alongside each set of hysteresis loops, the peak-valley-amplitude profiles are presented for the same test. The amplitude profiles in Figs. 4 and 5, (b), (d) and (f) are almost identical to the peak profile throughout most of the specimen life. This indicates that the stresses are nearly fully-reversed, even though the tests are conducted in fully-tensile strain control.

In total, 27 valid tests were conducted for the 100 grade material, 23 for the 80 grade material and 25 for the 70 grade material. All data points are plotted in terms of elastic, plastic and total strain amplitude versus "life to crack *initiation*," as defined previously, in Figs. 6, 7 and 8. The straight lines in each plot were fit through log-log values of the elastic and plastic strain amplitudes according to the ASTM Standard Practice for Statistical Analysis of Linear or Linearized Stress-Life (S-N) and Strain-Life (ε-N) Fatigue Data (E 739). The curves in Figs. 6-8 represent the total strain amplitude, taken as the sum of the elastic and plastic strain amplitudes. Cyclic stress amplitude versus strain amplitude data points from each test are plotted in Fig. 9 for all three materials, along with curves based on a Ramberg-Osgood relation [5].

To compare data from the current study to data generated previously with smaller specimens, strain-life data points from both are plotted together in Fig. 10. The two sets converge well, with the existing set extending into the longer life region, as previously noted.

Finally, some important observations about cracking behavior need to be made. Four of the five longest life tests on the 100 grade samples failed outside the gage section, on the inner surface at the transition region of the 1.25 in. (31.8 mm) specimen fillet radius. This was difficult to avoid, due to the curvature discussed previously. However, since significant cracking was also visible in the gage section of each of these specimens, the influence of these out-of-gage-section failures was assumed to be insignificant. Their inclusion in the data set serves to add conservatism to their subsequent use in any strain-based life prediction methodology.

INFLUENCE OF SURFACE MORPHOLOGY ON FATIGUE

Fatigue tests on coiled tubing samples routinely produce failure sites that defy conventional engineering intuition. Cracks are expected to initiate at the location experiencing most severe state of stress and strain. For tubing under flexure, this should be the outer surface of the tensile side of the tubing. However, the majority of fatigue cracks in coiled tubing *initiate* on the inner surface of the compressive tube wall [6]. Plasticity theory has been used to explain that the cyclic states of stress and strain on the compressive tube wall can be more severe than on the tensile wall [2]. Radial compression can combine with axial compression to cause a greater rate of circumferential ratcheting and wall thinning at the compressive side of the tubing, relative to the tensile side. However, arguments based on engineering mechanics have not been able to explain the nucleation of the vast majority of fatigue cracks at the inner surface instead of the outer surface (which experiences a more severe strain range than the inner surface).

As mentioned previously, the cracks that led to failure nucleated at the inner surface of 100% of the specimens tested in this study. Usually, cracks nucleated at multiple sites along the inner surface, coalesced and propagated to the side of the

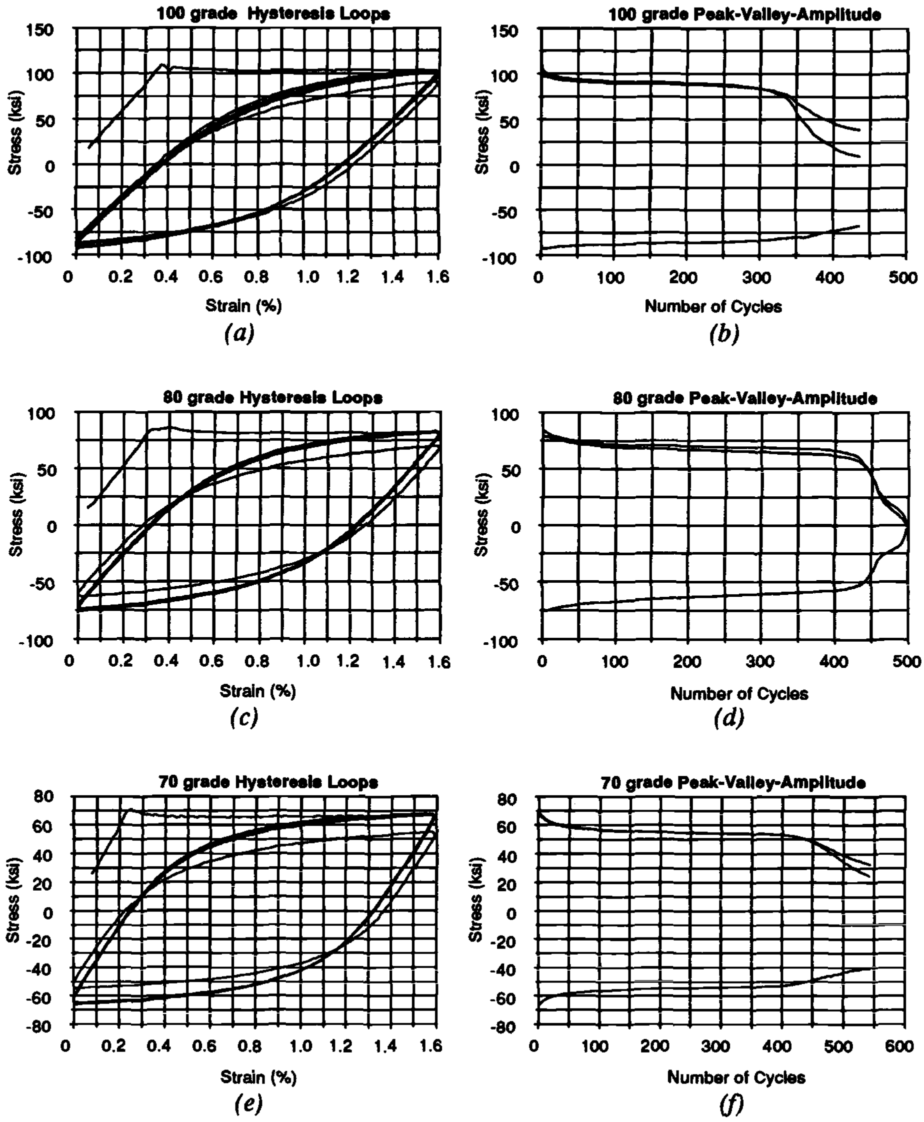

Fig. 4 --*Hysteresis loops and peak-valley-amplitude profiles from tests on the three material grades conducted at a strain range of 1.6%. Loops are presented for the first 6 cycles and a separate loop for the 50% life cycle in (a), (c), and (e). Note that the peak and amplitude profiles are almost identical in (b), (d), and (f), indicating that the stresses are fully-reversed, even though the tests are conducted in R=0 strain control.*

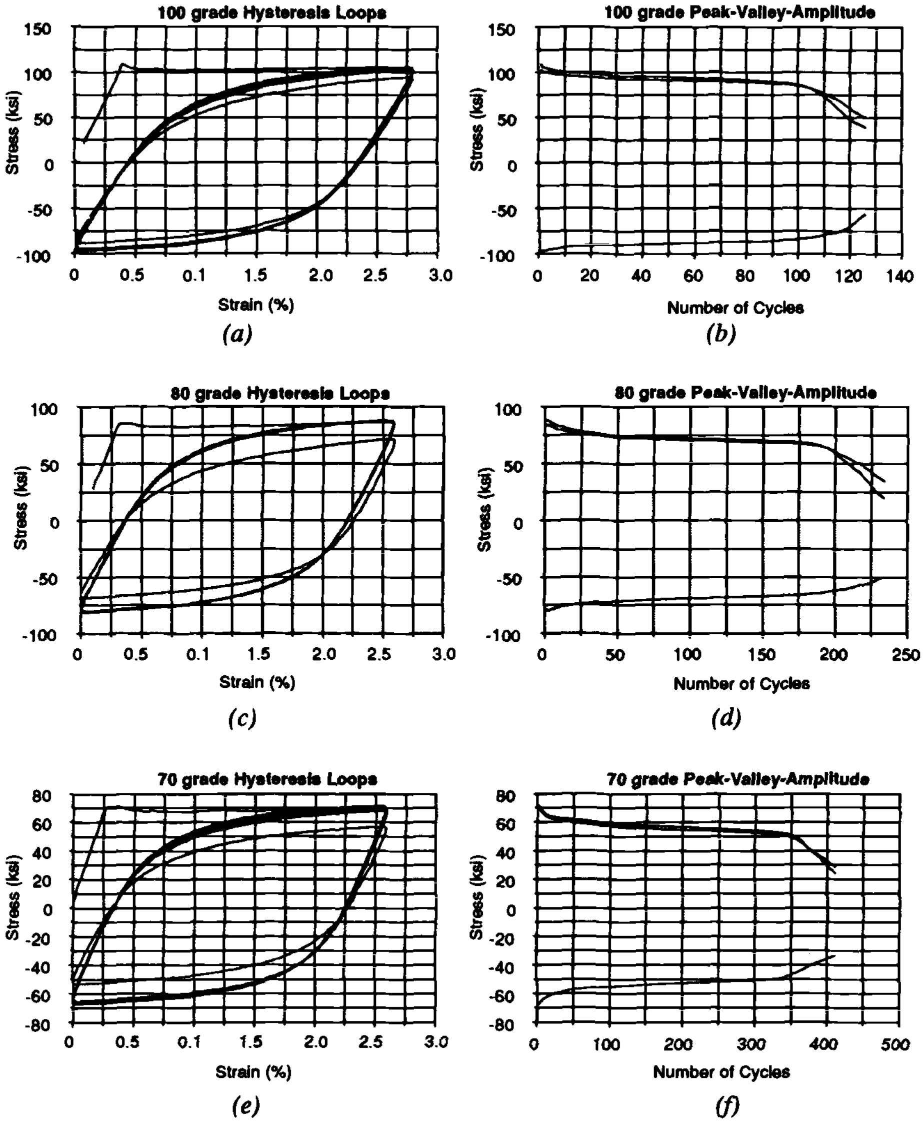

Fig. 5 --*Hysteresis loops and peak-valley-amplitude profiles from tests on the three material grades conducted at a strain range of 2.6%. Loops are presented for the first 6 cycles and a separate loop for the 50% life cycle in (a), (c), and (e). Note that the peak and amplitude profiles are almost identical in (b), (d), and (f), indicating that the stresses are fully-reversed, even though the tests are conducted in R=0 strain control.*

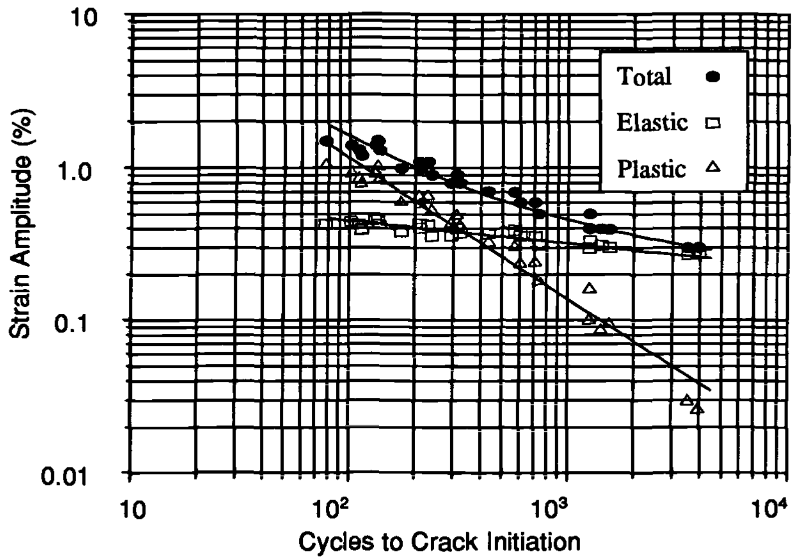

Fig. 6 --*Total, elastic and plastic strain amplitude versus cycles to crack initiation curves for 100 grade material, with data points.*

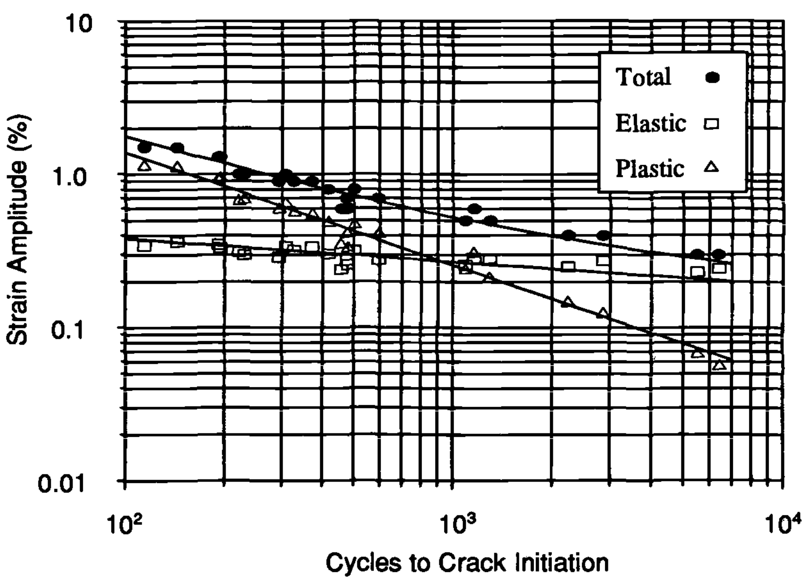

Fig. 7 --*Total, elastic and plastic strain amplitude versus cycles to crack initiation curves for 80 grade material, with data points.*

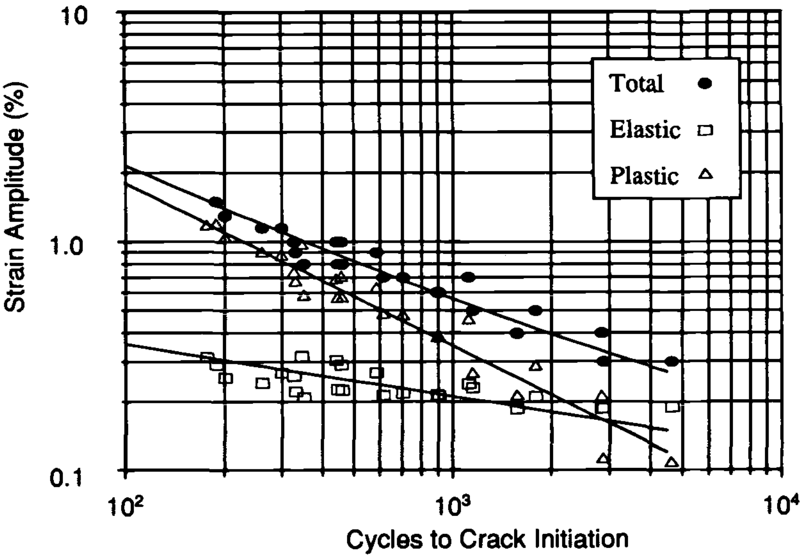

Fig. 8 --*Total, elastic and plastic strain amplitude versus cycles to crack initiation curves for 70 grade material, with data points.*

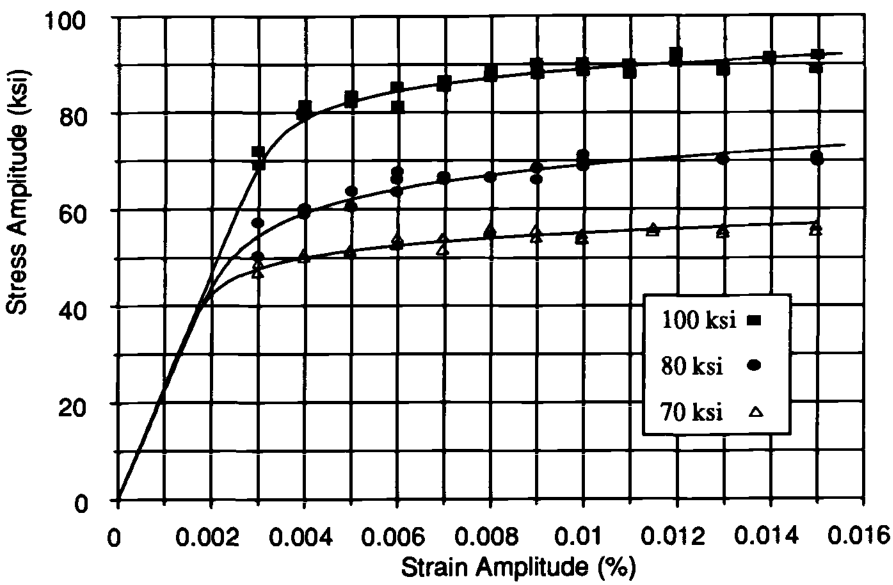

Fig. 9 --*Stress amplitude versus total strain amplitude data for 100, 80 and 70 material grades, shown with curves from Ramberg-Osgood equation [5]..*

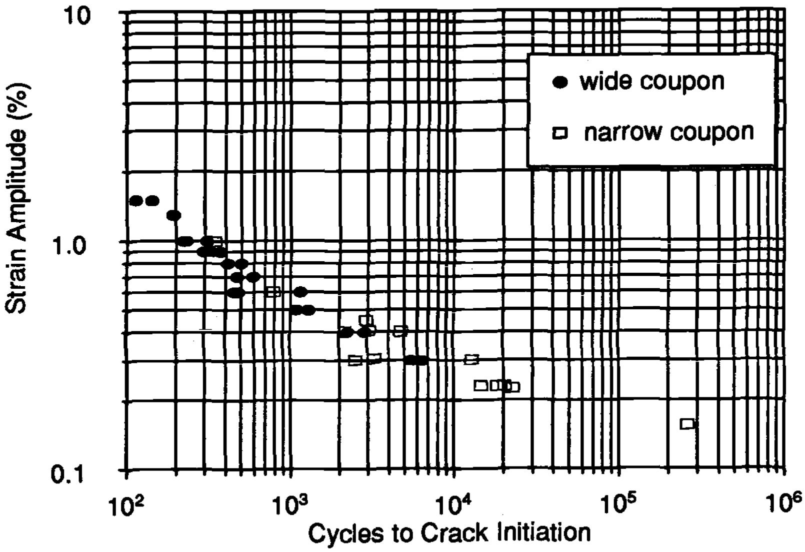

Fig. 10 --*Total strain amplitude versus cycles to crack initiation data for 70 grade material from the current study (wide coupon) and a previous study (narrow coupon).*

specimen. The side to which this propagation occurred was random, indicating good alignment. To explain the overwhelming tendency for inner surface nucleation, it can be observed that the inner surface appears "dull" relative to the more "glossy" texture of the outer tube wall. This observation was confirmed using surface profilometer readings taken on 80 grade material, and summarized in Table 1.

TABLE 1 - *Surface Roughness Measurements*

Location	Ra	Ry	Rv
Inner surface	1.95 μm	18.9 μm	9.8 μm
Outer surface	0.72 μm	8.7 μm	6.7 μm
Polished inner	0.04 μm	0. 40 μm	0.20 μm

The measurements in Table 1 represent the average of several readings. The Ra value is the arithmetic mean of the surface height measurements, Ry is the maximum peak to valley measurement and Rv is the maximum valley depth. The average roughness of the interior surface is nearly 3 times greater than the exterior surface. Scale illustrations of both surface profiles are given in Fig. 11.

The influence of surface roughness on metal fatigue is well documented and it is generally concluded that surface roughness has a stronger effect in the high-cycle life regime, and is less important in the low-cycle regime. To evaluate the effect in the ultra-low cycle-regime associated with coiled tubing strain ranges, a few specimens were polished longitudinally on the inner surface only. Profilometer measurements in Table 1 indicate that the resulting surfaces were more than an order of magnitude smoother than the as-manufactured outer surfaces. Fatigue data from tests at two strain ranges for polished and as-manufactured surfaces are presented in Table 2.

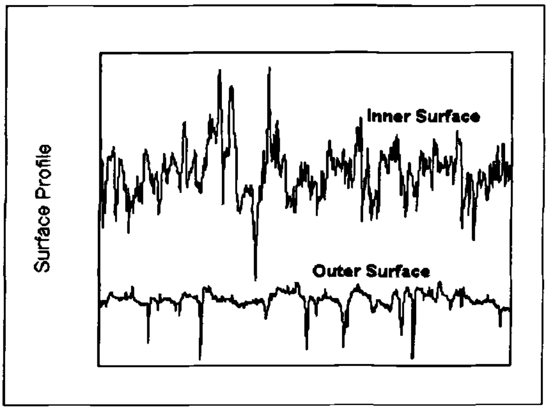

Figure 11 - *As-manufactured inner and outer surface profiles.*

TABLE 2 - *Coupon Fatigue Life Data*

Strain Range	*As-Manufactured*	*Polished ID*
1.6%	501	897
	417	(95% increase)
2.6%	195	321
	192	(66% increase)

The extremely limited data in Table 2 suggest that eliminating surface roughness on the ID has a beneficial effect on fatigue life, almost doubling life for the 1.6% strain range (a range typically encountered by coiled tubing in the field). But, equally interesting is the fact that ***the primary cracks that led to the fracture of the polished samples, still nucleated at the inner surface, in spite of the polishing***. (The "primary crack" refers to the crack that leads to the fatigue failure of a tube or specimen. "Secondary cracks" are cracks which form during the same loading, but do not lead to failure.) This indicates that other factors besides roughness cause the inner surface to be more susceptible to fatigue cracking than the outer surface.

The differences between the inner and outer surfaces can be explained, qualitatively, by considering the manufacturing process for rolled tubing. Coiled tubing begins as strip material that is rolled about the tubing axis and resistance welded along the edges. For the 1.75 x 0.156 in. (44.5 x 4.0 mm) dimensions used to fabricate the axial coupons in this study, a surface strain in the hoop direction of nearly 10% (tensile on the outer surface and compressive on the inner surface) is caused by the rolling process. The large compressive surface strains at the inner surface tend to cause extrusions as well as intrusions to occur along microscopic slip bands, thus roughening the surface. On the outer side, the tensile strains predominantly produce intrusions, which could explain why the Rv measurements in Table 1 for the outer surface differ little from those taken at the inner surface. Based on the nucleation of cracks at ***polished inner surfaces***, factors besides surface morphology appear to be associated with the different strain states. For instance, the nature of dislocation substructures caused just below the surface by compressive hoop strains differs from that caused by tensile hoop strains. The significance of this, in terms of fatigue crack nucleation mechanisms activated by subsequent fluctuating strains in the axial direction, is evidenced by the polished fatigue data. The nature of the rolling process tends to produce an inner surface that is inherently less fatigue resistant than the outer surface.

Finally, it should be noted that the residual stresses from the rolling process could be influential towards the nucleation of cracking at the inner surface. These residual stresses are mitigated to some extent by the heat treating process applied to the tubing when it is manufactured. The longitudinal weld seam is annealed from 1650 °F (899 °C) and a "full body stress relief" is applied by heating the tubing to a region ranging from 900 °F – 1300 °F (482 °C – 704 °C) for a "specified time" depending on the desired properties. The specimen curvature is evidence that the residual stresses are not fully removed, but their influence on cracking behavior has not been assessed.

INFLUENCE OF EXTERNAL SURFACE DEFECTS ON FATIGUE

The existence of an inner surface with an inherently lower fatigue resistance relative to the outer surface leads to the hypothesis ***that a defect on the outer surface must exceed a threshold severity before it will lead to a substantial reduction in fatigue life, relative to the inner surface***. This has importance to the coiled tubing industry with regards to inspection and maintenance of strings in the field. To test this hypothesis, notches with controlled geometry were machined into the outer surfaces of axial coupons of 100 and 80 grade materials. Two different notch geometries were investigated, as depicted in Fig. 12, using an applied strain range, $\Delta\varepsilon$, of 1.6%. A 1/8 in. (3.18 mm)

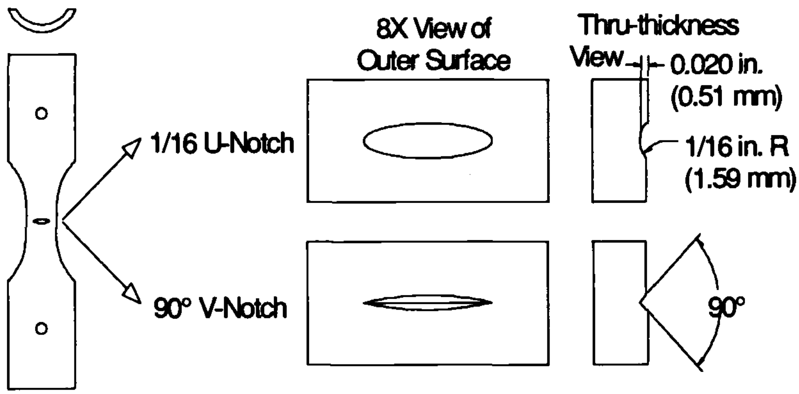

Fig. 12 -- *U and V notch geometries.*

diameter end mill was used to machine rounded notches, referred to as U-Notches, oriented perpendicular to the axis of loading with a root radius of 1/16 in (1.59 mm). A straight end mill was used to cut sharp 90° V-Notches, by fixturing specimens at an angle of 45° and using the corner of the cutter. The root radius of the V-Notch was less than 0.001 in. (0.025 mm). Two notch depths were investigated, 0.01 in. (0.25mm) and 0.02 in. (0.51 mm) (the deeper of these are depicted in Fig. 12), representing about 6% and 12% of the cross sectional wall thickness, respectively. Data from these tests are presented in Table 3.

Many interesting observations can be made from the data in Table 3. (1) Neither of the 0.01 in. (0.25 mm) deep notches in the 100 grade material had an effect on fatigue, relative to specimens without notches. (2) The higher strength material appears to be less sensitive to the presence of a notch than the lower strength material. This is opposite to the usually observed trade-off between strength and fatigue notch-sensitivity. (3) Notice that the only primary cracks nucleating at any notch occurred in the deeper V-Notches. (4) Deeper (12%) U-Notches reduced fatigue life in both material grades, in spite of not being the primary crack initiation site. The deeper notch geometries influenced the state of stress and strain, and thus the fatigue behavior at the inner surface. Again, the effect was much

TABLE 3 - *Fatigue Data from Coupon Samples with Machined Notches in Outer Surface ($\Delta\varepsilon$ =1.6%)*

Mat. Grade	*Surface State*	*depth (in. (mm))*	*Life (cyc.)*	*Primary Crack Nucleation Site*
100	as-mfg.	-	294	inner surface
100	as-mfg.	-	324	inner surface
100	U-Notch	0.01 (0.025)	291	inner surface
100	V-Notch	0.01 (0.025)	363	inner surface *
100	U-Notch	0.02 (0.051)	231	inner surface *
100	V-Notch	0.02 (0.051)	231	OD at notch root
80	as-mfg.	-	501	inner surface
80	as-mfg.	-	417	inner surface
80	U-Notch	0.02 (0.051)	252	inner surface
80	V-Notch	0.02 (0.051)	108	OD at notch root

* - secondary cracking at notch root

more pronounced in the 80 grade samples, than in the 100 grade samples. (The identical lives for the 100 grade samples are coincidental.)

The quantity of data presented in this paper is not adequate to draw definitive conclusions. There is an obvious need to generate more data in full-scale tubular specimens. The coupons provide useful information, but the uniform, tensile strain state through the cross section is not indicative of field conditions. In an actual tube in bending, there is a difference between the magnitude of the fluctuating strain range at the outer and inner surfaces. For example, when 1.75 x 0.156 inch (44.5 x 4.0 mm) tubing is flexed over any radius of curvature, the bending strain is 17.8% greater at the outer surface than at inner surface (assuming plane sections remain plane). This difference could significantly reduce the "threshold" notch severity required to drop the fatigue strength of the outer surface below that of the inner surface. Further investigations should include a combination of full-scale tubular and small-scale coupon testing.

As a final note, machining a notch into the outer surface shifts the centroid of the minimum cross section from the axis of loading, moving it closer to the notch root. This should make the state of straining worse at the notch root than at the inner surface, aside from stress concentration effects. The fact that cracks still nucleated at the inner surface in most of the notched tests further substantiates the observation that the tube rolling process produces an inherently weaker inner surface.

CONCLUSIONS

1. Testing methodology is presented to supplement ASTM E 606 for conducting low-cycle fatigue testing of coupons extracted from coiled tubing material. Special grip inserts are used to align the centroid of the gage section with the axis of loading. The as-manufactured morphologies of the outer and inner surfaces are preserved. Specimens are polished longitudinally along their edges to avoid the nucleation of cracking along the edges.

2. Extracting coupons from higher strength tubing can result in specimens with curvature along the axis of loading, due to residual stresses from the manufacturing process. This causes some bending to occur during early cycles of loading. For this reason, the extensometer was mounted to the edge of the specimen, rather than along the outer (convex) surface, to average out the bending effect.

3. To further mitigate the influence of curvature-induced bending, testing was conducted under fully tensile strain controlled loading ($R_\epsilon = 0$). This is consistent with the nature of coiled tubing loading in the field (bending-straightening). The initial cycle of loading tends to straighten the specimens, thus avoiding buckling at very high strain ranges.

4. In every specimen tested (75 total) primary cracks nucleated along the inner surface. This is consistent with, and helps to explain the nucleation of fatigue cracks at the inner surface of full-scale tubing, tested in bending (in spite of the fact that strain fluctuations are larger at the outer surfaces).

5. Surface profilometer readings confirm and quantify the macroscopic observation that the inner surface appears rougher than the outer surface.

6. Based on very limited data, axial coupons with polished inner surfaces showed life improvements from 66% to 95% relative to coupons with as-manufactured inner surfaces. However, cracks in these specimens still nucleated at the inner surface. This indicates that factors in addition to the expected influence of surface roughness cause the fatigue resistance of the inner surface to be inherently lower than the outer surface. These are most likely microstructural metallurgical factors (dislocation sub-structures, persistent slip band nucleation, etc.) caused by large plastic straining in the circumferential direction, compressive at the inner surface and tensile at the outer surface. Residual stresses from the tube rolling process also may be influential.

7. An inherently weaker inner surface leads to the theoretical existence of a "threshold severity" that must be exceeded before a defect in the outer surface would degrade the life of a section of tubing in service. This has important implications with regards to the inspection and maintenance of coiled tubing. This theory is validated by preliminary tests on axial coupons with notches on the outer surface, but full-scale bending tests are necessary to validate and quantify the threshold severity concept.

ACKNOWLEDGMENTS

The author would like to thank Quality Tubing, Inc., Houston, Texas, and the Fatigue Laboratory at The University of Tulsa, Mechanical Engineering Department for their support of this work. Bill Vesely, of Midstates Analytical in Tulsa, Oklahoma provided helpful input to the design and fabrication of the grip inserts. Phil Dindinger, of Rexnord Technical Associates, Milwaukee, Wisconsin, offered excellent technical advice. Also, thanks to Sharon Grelecki, Shreekanth Jallipallii, Mokhtar Matallah and Dan Lamoreaux for analytical and technical assistance.

REFERENCES

[1] *World Oil's Coiled Tubing Handbook*, Mark E. Teal, Ed., World Oil, Gulf Publishing Co., Houston, Texas, 1993, pp. 7-130.

[2] Tipton, S.M., "Multiaxial Plasticity and Fatigue Life Prediction in Coiled Tubing," *Advances in Fatigue Lifetime Predictive Techniques, 3rd Volume, ASTM STP 1292*, M.R. Mitchell and R.W. Landgraf, Eds., American Society for Testing and Materials, Philadelphia, 1995, pp. 283-304.

[3] Tipton, S.M. and Newburn, D.A., "Plasticity and Fatigue Damage Modeling of Severely Loaded Tubing," *Advances in Fatigue Lifetime Predictive Techniques, ASTM STP 1122*, M.R. Mitchell and R.W. Landgraf, Eds., American Society for Testing and Materials, Philadelphia, 1992, pp. 369-382.

[4] "CoilLIFE Joint Industry Project," Final Report, Vol. 6, 1993.

[5] Ramberg, W. and Osgood, W., "Description of Stress-Strain Curves by Three Parameters," *NACA TN 902*, 1943.

[6] Tipton, S.M. and P.A. Brown, "Monitoring Coiled Tubing Fatigue Life," *Second International Conference on Coiled Tubing Operations*, Gulf Publishing Company and World Oil, Houston Texas, March 28-31, 1994.

Victor K. Champagne[1]

FAILURE ANALYSIS OF AN AGE HARDENABLE, NICKEL BASE SUPERALLOY BARREL NUT FROM AN ARMY ATTACK HELICOPTER

REFERENCE: Champagne, V. K., **"Failure Analysis of an Age Hardenable, Nickel Base Superalloy Barrel Nut from an Army Attack Helicopter,"** *Effects of Product Quality and Design Criteria on Structural Integrity, ASTM STP 1337,* R. C. Rice and D. E. Tritsch, Eds., American Society for Testing and Materials, 1998.

ABSTRACT: During a routine preflight inspection at Ft. Hood, an outboard barrel nut was found to be cracked on an Army helicopter. The part was fabricated from Inconel 718 (UNS N07718) according to AMS 5662F, "Alloy Bars, Forgings, and Rings, Corrosion and Heat Resistant". Subsequent inspections at Ft. Hood and Ft. Rucker revealed an additional seven barrel nuts with large cracks. The components are used in many critical applications. The failures under investigation in this study were relegated to the vertical stabilizer of the aircraft. The failures were all attributed to hydrogen induced cracking. Galling between the unlubricated bolt and the nut threads provided the sustained hoop stress while galvanic corrosion of the carbon steel retaining clip in contact with the barrel nut generated hydrogen. Microstructural analysis of the nut revealed excessive banding consisting of a Widmanstätten phase and MC carbides which ran parallel to the fracture plane. The grains were almost completely surrounded by an undesirable acicular delta phase. No evidence of Laves phase was observed. Recommendations were made to utilize a corrosion inhibitive lubricant on the threads of the barrel nut and mating bolt to reduce galling and the consequential high stresses which result from metal to metal contact during torquing. A stress analysis of the part showed that the high strength level of the material could be reduced to increase fracture toughness and resistance to hydrogen cracking. The acicular delta phase should be avoided in accordance with AMS 5662F and the extrusion direction of the material should be parallel to the principal loading direction. Salt fog testing of the proposed barrel nut configuration revealed that the shoulder height base thickness should be increased. Future vendors should qualify their product by conducting a prescribed salt fog test incorporating the prescribed torque requirements. Finally, the material used to fabricate the retaining clip should be changed to prevent galvanic corrosion.

Keywords: Failure analysis, fractography, hydrogen induced cracking, Inconel 718

[1]Materials Engineer, U.S. Army Research Laboratory, Aberdeen Proving Ground, MD

Background

During the early 1980's several catastrophic failures of high strength H-11 steel fasteners were encountered by the aerospace industry. These failures were attributed to service-induced hydrogen embrittlement. In response to this problem, the FAA issued an advisory against the use of such fasteners in critical applications. The Army Aviation and Troop Command (ATCOM) in turn, issued an engineering order to replace all H-11 fasteners in critical applications on the Apache with those fabricated from Inconel 718 nickel-base superalloy (UNS N07718), in accordance with an engineering change proposal (ECP) submitted by the primary contractor. The ECP required that the UNS N07718 material be heat treated to 220 ksi (1517 MPa) minimum ultimate tensile strength (UTS) and cadmium plated incorporating a vacuum or an electrolytic deposition process. Approximately eight to ten months after the ECP was implemented, an outboard barrel nut was found cracked at Ft. Hood during a routine preflight visual inspection. This incident prompted further inspections at Ft. Hood and Ft. Rucker. An additional seven barrel nuts were found cracked. A total of three cracked barrel nuts were sent to the Army Research Laboratory (ARL) for examination, the first broken part found at Ft. Hood and two barrel nuts detected during visual inspection at Ft. Rucker. All the components were manufactured by the same company (designated within the context of this report as "Contractor A") and were from the same lot number (03). There was also an alternative supplier to these parts (identified as "Contractor B"), but no failures were attributed to nuts made by this company.

In addition to the three failed components examined at ARL, twelve other barrel nut and bolt assemblies were subjected to salt fog testing while loaded. These parts represented three groups. Four parts were fabricated by Contractor A, and four others by Contractor B. The remaining parts represented a newly proposed design which were manufactured by Contractor B. These assemblies were exposed to a salt fog environment over a prescribed period of time or until failure, and were subsequently examined metallurgically. A series of barrel nuts fabricated by Contractor A were also mechanically loaded to failure over a conical mandrel and the resultant fracture surfaces compared to those of the failed components.

Visual Inspection/Light Optical Microscopy

Figure 1 shows the failed barrel nut assembly from Ft. Hood, designated "H", in the as-received condition. The washer, spring clip, cradle and mating bolt have all been identified. A single crack (denoted by arrow) was observed on the barrel nut running perpendicular to the bolt threads. The fracture occurred perpendicular to the maximum hoop stress direction. The cradle was also cracked in two areas. The cadmium plated surfaces of the components displayed typical signs of wear but the shank of the bolt was almost entirely void of the plating from the region located above the barrel nut to the bolt head. The steel spring clip showed a significant amount of corrosion. No other unusual damage was observed.

The crack propagated through the entire thickness of the nut. The manufacturer trademark, part number (84209-820) and lot number (03) was still clearly visible. One of the legs of the cradle had actually bent outward from the component, most likely as a result of a post-fracture incident. The two other barrel nut failures from Ft. Rucker identified as "R1" and "R2", displayed similar features and were also manufactured by Contractor A, lot number (03). The only significant difference was that both cracks in the cradle of the two Ft. Rucker failures were very easily discernible while one of the two cracks in the Ft. Hood cradle was barely visible. Corrosion products were found on the surface of the cradle and the nut. The corrosion was reddish-brown in color and most likely originated from the steel spring clip. One of the two raised sections (legs) of the cradle had bent outward and the barrel nut was no longer square because the crack had widened a significant amount.

Examination of the threads on the barrel nuts revealed evidence of metal debris and wear. However, much of the cadmium plating on the threads was still intact. It is believed that some of this damage may have occurred during final fracture. As the crack propagated through the entire thickness of the barrel nut, the bolt is thought to have pulled out, causing the bolt threads to shear. The two Ft. Rucker bolt threads experienced shearing while the Ft. Hood bolt did not. Some of the galling observed may have also occurred during installation since a lubricant was not used. Wear marks and exposed base material were also observed on the bolt threads that had been inserted into the barrel nut. Frictional forces between the mating threads of the bolt and barrel nut may have been sufficient to have caused some excessive wear and stress concentration areas.

Microstructural Analysis

A radial transverse section (parallel to the fracture plane) was taken from each of the three failed barrel nuts. Figure 2 reveals the extrusion direction of barrel nut R2 which extends parallel to the direction of crack propagation. A radial transverse section of a Contractor B barrel nut was also examined for comparative purposes and the extrusion direction was perpendicular to that of the Contractor A counterpart, which would be more desirable under the loading conditions encountered during service. Banding was also observed in both the Contractor A and Contractor B barrel nuts running in the same direction as their respective flow patterns. The Contractor A material displayed heavy banding which consisted primarily of MC carbides and delta phase in the form of a Widmanstätten structure. An acicular delta phase was also observed surrounding much of the grain boundaries, as shown in Figure 3. The Contractor B material contained only slight evidence of banding which was comprised primarily of MC carbides as shown in Figure 4. The Contractor A sample contained a large concentration of delta phase in the form of a Widmanstätten structure while the Contractor B material did not. The MC carbides which were aligned preferentially in the extrusion direction seemed to be found in clusters more often in the Contractor A material. Figure 5 is an optical micrograph representative of the Contractor A material at high magnification. The grains are almost completely surrounded by an acicular delta phase whereas the Contractor B microstructure contained a more spherodized grain boundary delta phase which surrounded a significantly smaller percentage of the grains, as depicted in Figure 6. The

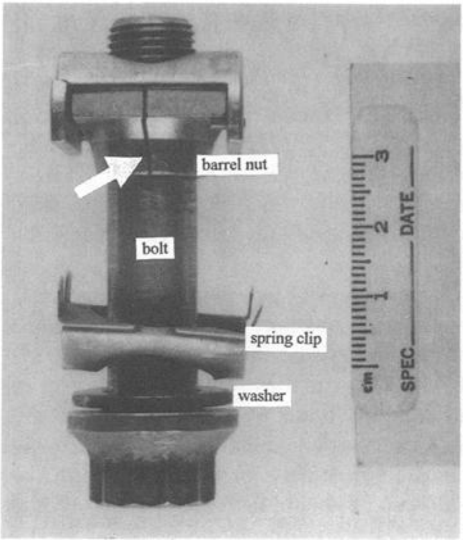

Figure 1. *Barrel nut assembly "H" in the as-received condition.*

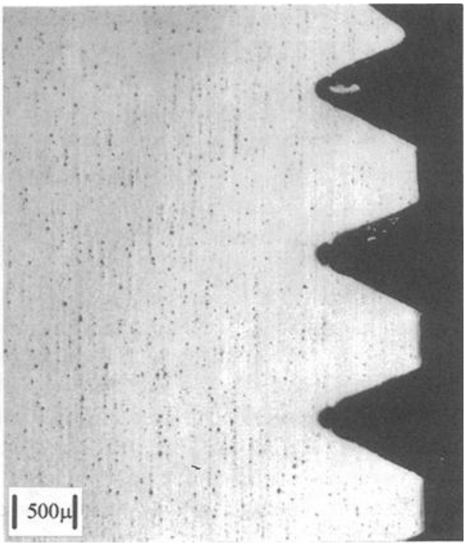

Figure 2. *Extrusion direction of nut "R2", parallel to crack. Mag. 20x.*

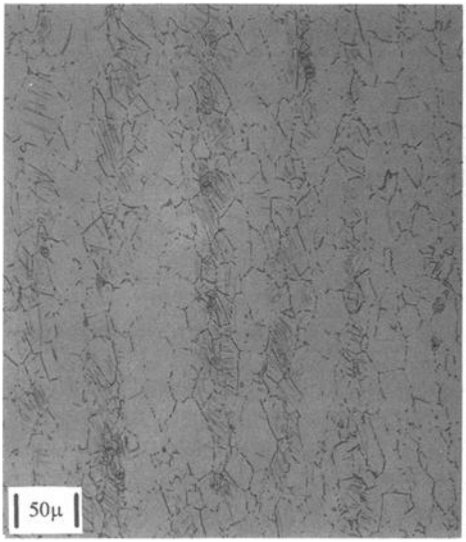

Figure 3. *Nut "H" microstructure showing banding and Widmanstätten delta phase in the extrusion direction. Mag. 200x.*

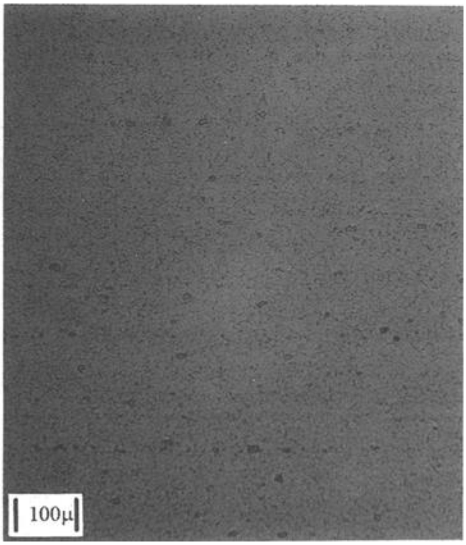

Figure 4. *Contractor "B" nut microstructure showing slight banding and MC carbides in the extrusion direction. Mag. 100x.*

etchant used during this examination consisted of 100 ml of ethyl alcohol added to 100 ml of hydrochloric acid and 5 grams of cupric chloride.

The grain size was required to be 5 or finer (ASTM E112-63, *Test Methods for Determining the Average Grain Size*). The grain size of the Contractor A and Contractor B material was measured utilizing this specification. A reference standard illustrating ranges of grain size (1-8) was superimposed on the photographs for ease in comparison. The Contractor A grain size was approximately 8 while the Contractor B material displayed a much finer grain size than that of the reference standard. However, both materials satisfied the specification requirements.

Carbides which form in UNS N07718 are primarily MC type with a nominal NbC composition, although titanium and molybdenum can substitute for niobium in some circumstances. X-ray mapping was performed within the scanning electron microscope utilizing energy dispersive spectroscopy (EDS) of MC carbides found on both sets of samples. The results indicated a high concentration of Nb and Mo. These carbides are very hard and brittle and are usually considered undesirable because they reduce the ductility of the alloy. In addition, they tie up niobium necessary for the formation of the strengthening phases. There was no evidence of Laves phase found in any of the specimens examined. Chemical segregation can result in the formation of large, blocky intermetallic particles known as Laves phase which is also very brittle and adversely affects the properties of the alloy [1].

A cross-section was taken through the crack origin of the Ft. Hood barrel nut fracture and prepared metallographically for examination. Figure 7 shows the fracture path to be quite intergranular at the origin. The specimen had been polished in relief to highlight the grains.

Chemical Analysis

Material sectioned from a representative failed barrel nut and bolt (both from R1) were subjected to chemical analysis. Atomic absorption and inductively-coupled argon plasma emission spectrometry were used to determine the chemical composition of the alloys. The carbon and sulfur content was analyzed by the Leco Combustion Method. The compositional ranges of the material under investigation compared favorably with the specification requirements.

Hardness Testing

A series of microhardness measurements were performed on cross sections of the three failed barrel nuts and a Contractor B barrel nut from inventory, for comparative purposes. Each nut was sectioned in half transversely and metallographically prepared. Knoop microhardness measurements were taken on the surface. The barrel nuts were required to exhibit a hardness of 42 HRC. The failed nut from Ft. Hood displayed an average hardness of 507 HK or approximately 47.8 HRC, while R1 was 515 HK or approximately 48.3 HRC. Specimen R2 was 525 HK or approximately 48.9 HRC and the Contractor B nut from inventory was 510 HK or approximately 48.0 HRC. All values obtained conformed to the governing specification, and were very close to one another.

Tensile Testing

Tensile specimens were sectioned from two failed barrel nuts (R1 and R2), as well as a Contractor B barrel nut from inventory. Substandard specimens were fabricated according to ASTM E8, *Test Methods of Tension Testing of Metallic Materials*. The specimens were tested in a 20,000-pound (89000 N) capacity Instron universal electromechanical test machine. A 10,000-pound (445000 N) load cell was utilized for the measurement of load. The pull rate was 0.05 inches/minute (1.3 mm/minute). Testing was conducted at room temperature at 50% relative humidity. The ultimate tensile strength was required to be 225,000 psi (1551 MPa) minimum, and 245,000 (1689 MPa) maximum, in accordance with performance requirements, as stated on the engineering drawing. The minimum percent elongation was specified as 8% in 4D. The results of this testing are listed in Table 1.

TABLE 1--*Tensile Test Results*

Specimen	Diameter, in. (mm)	Area, in^2 (mm^2)	Max. Load, lbs (N)	UTS, psi (MPa)	% Elongation
R1	0.066 (1.7)	0.0034 (2.2)	800 (3560)	233,836 (1612)	17.6
R2	0.078 (2.0)	0.0048 (3.1)	1,050 (4670)	219,741 (1515)	*
Contractor B	0.066 (1.7)	0.0034 (2.2)	705 (3140)	206,068 (1421)	16.0

* was not calculated

Fractographic Examination

The three failed barrel nuts were sectioned to separate both fracture halves for examination. Optical and scanning electron microscopy was utilized to identify important features of the fracture surface relating to the failure mechanism. The Ft. Hood barrel nut was determined to be representative of all three service failures and will be used within this discussion to describe the manner of crack propagation. Cracking occurred parallel to the axial loading direction or perpendicular to the threads. A discolored region was observed on the fracture surface near the crack origin. Energy dispersive spectroscopy (EDS) was utilized to characterize the chemistry of the surface within this area. The elements associated with the base material were detected as evidenced by Ni, Fe, Cr, Ti, Nb, Mo and Al peaks. A large Cd peak and small O and Cl peaks were found and most likely represented corrosion product from one of the barrel nut assembly components that had been cadmium plated. Corrosion products of this cadmium plated part and the underlying base material could have seeped into the slowly propagating crack in the barrel nut causing a discolored zone. The reddish brown appearance of this stained region suggests that the corrosion products on this surface were rich in iron and may have originated from a steel component in contact with the barrel nut, such as the spring clip. Even though the EDS analysis supports this deduction an argument can be made that the Fe, Cd and O peaks may represent only the barrel nut material. However, the reddish brown appearance of the discolored region indicates corrosion of an iron rich material. The remaining elements are believed to be contaminants, although Si, S and Ca are acceptable within this alloy in very low concentrations. Figure 8 is an optical macrograph highlighting the fractographic features of the surface. The chevron markings and river pattern converge to an area identified as the crack initiation site as shown by the arrow.

Figure 9 is a schematic illustrating a cut-away section of the barrel nut, bolt and cradle which shows the location of the fracture origin observed on all three service failures. Cracking had initiated near the first thread of the barrel nut adjacent to the cradle. Figure 10 is a schematic illustrating the four distinct zones noted on the fracture surfaces. The fracture originated within the discolored region identified as Zone 1. This region was relatively free from smearing which can occur if the two fracture faces rub against one another in service, but contained surface contamination and debris. Zone 1 was an area of slow crack growth showing little ductility and the morphology was intergranular as shown in Figure 11. These features are typically associated with hydrogen-assisted crack growth under sustained load. Zone 2 was a region where fracture by intergranular decohesion transitioned to a more dimpled mode, as depicted in Figure 12. The fracture mode observed in Zone 3 consisted primarily of equiaxed dimples which is associated with ductility. Zone 4 consisted of shear lips adjacent to the outside perimeter which displayed directional dimples. Crack propagation occurred at a faster rate within Zone 3 and final fracture took place within Zone 4.

Further EDS analysis was performed within the various zones of fracture. The spectrum obtained from Zones 3 and 4 revealed primarily those constituents associated with the base material. There was no significant Cd, Cl, or O peaks detected. A very large concentration of Cd, had been detected along with Cl and O near the crack origin site. The corrosion product observed on the surface of the barrel nut cradle was also analyzed by EDS. A significant concentration of Cl was detected. The Cd peak in this case primarily represents the plating on the surface of the cradle. The small Fe and O peak may represent corrosion product from the steel spring clip or the base material of the cradle. Fracture Zones 3 and 4 primarily contained those elements associated with the base material. No significant concentration of Cd or Cl was detected in these areas.

Mandrel Testing

A series of Contractor A barrel nuts were subjected to mechanical testing to compare overload-induced fracture surface features with those found on the field-cracked barrel nuts. The barrel nuts were mechanically loaded to failure over a conical mandrel. Subsequent fractographic analysis of the failed barrel nuts revealed surfaces which were entirely dimpled. This type of fracture morphology is indicative of a ductile failure. Since the fracture surfaces of the failed barrel nuts displayed significant intergranular regions at the crack origin, it became evident that initial crack growth may have been environmentally induced.

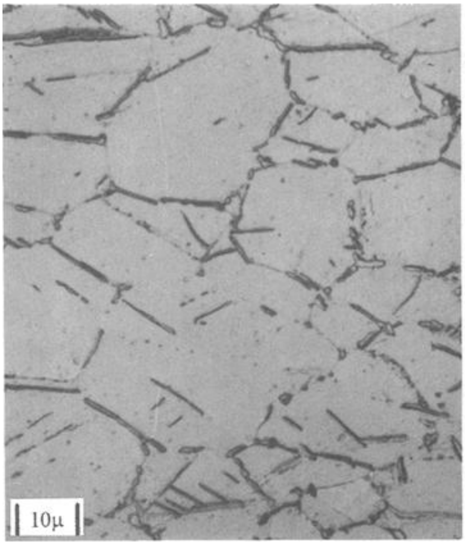

Figure 5. *Contractor "A" microstructure displaying acicular delta phase at grain boundaries. Mag. 1000x.*

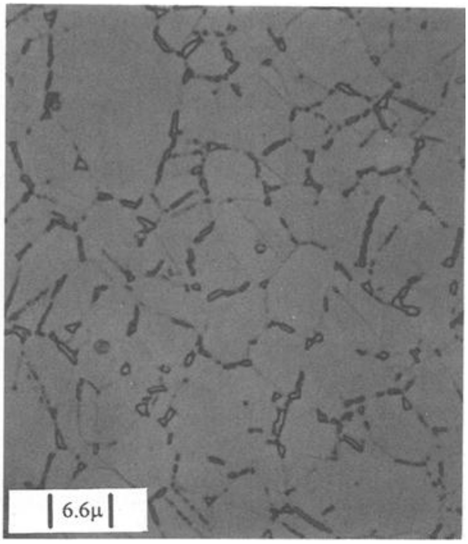

Figure 6. *Contractor "B" microstructure containing a spherodized grain boundary delta phase. Mag. 1500x.*

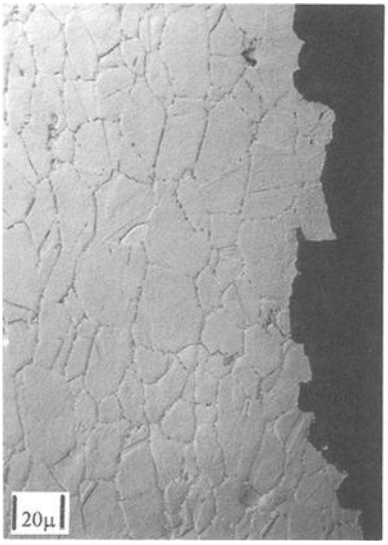

Figure 7. *Cross-section through crack origin of nut "H". Note the intergranular fracture path. Mag. 400x.*

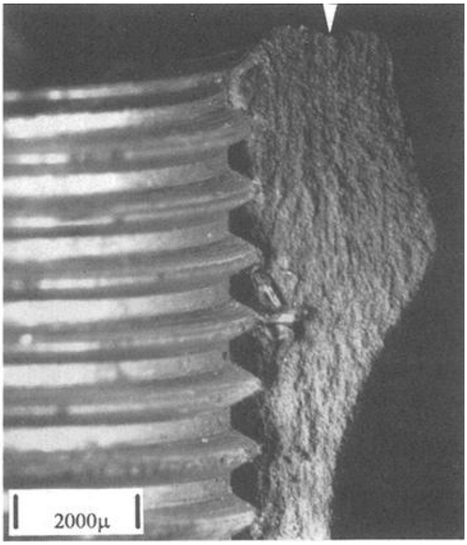

Figure 8. *Fractograph of nut "H" showing crack origin and radial markings. Mag. 10x.*

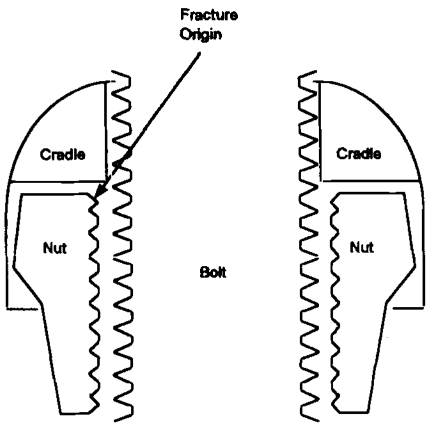

Figure 9. *Cut-away section of the barrel nut, bolt and cradle showing the fracture origin observed on all three service failures.*

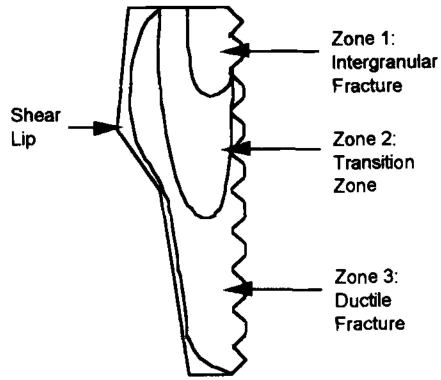

Figure 10. *Schematic illustrating fracture zones observed on each failed nut.*

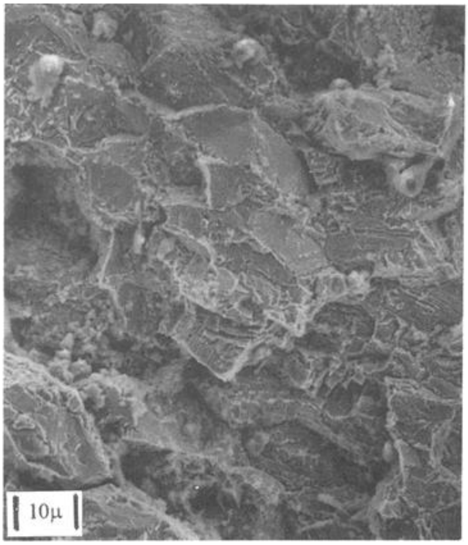

Figure 11. *Intergranular mode of fracture found in Zone 1. Mag. 1000x.*

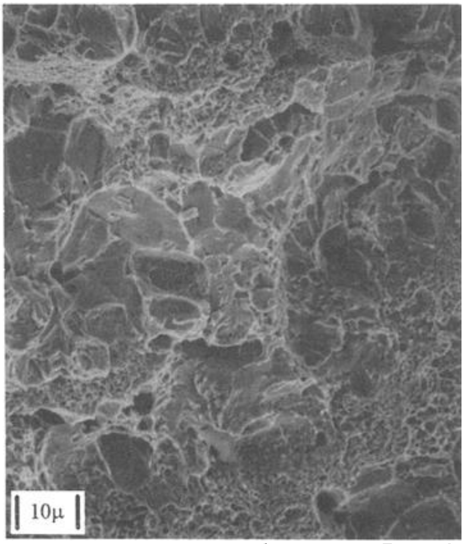

Figure 12. *Fracture indicative of Zone 2 consisting of intergranular decohesion and ductile dimples. Mag. 1000x.*

Salt Spray Testing

A series of three salt spray tests were conducted on Contractor A, B and newly designed barrel nut assemblies, in an effort to reproduce the failure mechanism and to compare the three barrel nut designs. The differences in design included the height of the conical section, the thickness of the base, and the hardness of the material. The assemblies were tested in an actual aluminum fuselage section. Bolts were inserted through a block of 6061-T6 aluminum, which represented the rear vertical stabilizer of the helicopter. Some of the blocks were machined with a 0.6 degree taper, while other blocks were flat and parallel. The taper was designed to induce a bending moment within the nut to replicate the effects of having a bolt inserted at an angle, causing a stress concentration and galling when torqued. The bolts were threaded into the barrel nut assemblies and were then torqued and placed in a salt spray chamber. The bolts were incrementally torqued to higher stress levels at regular intervals following a schedule determined by ATCOM. The chamber maintained a salt fog with 5% NaCl by weight, at 95° F (35°C), and 100% relative humidity. During the torquing process, the assemblies were removed from the chamber for no longer than five minutes. Torquing was conducted utilizing a digital torque wrench, having a capacity of 250 ft-lbs (340 N·m).

Two Contractor A barrel nuts broke while being salt spray tested and the resultant fracture surfaces revealed similar features as the failed components (intergranular fracture at the crack origin and ductility in the area of final fracture). The similarity between these fracture features and those on the field-fractured nuts provides additional evidence that field cracking was due to a corrosion-induced hydrogen-assisted mechanism. The region of intergranular fracture within the barrel nuts broken in the salt spray chamber was smaller than that of the three field failures. This was attributed to the higher torque levels prescribed during the laboratory salt fog test as opposed to those specified in service. It is believed that the higher stresses would result in faster initial crack growth. The Contractor B and newly designed barrel nuts did not experience failure as did the Contractor A nuts tested under identical conditions. The use of tapered blocks, intended to cause a slight mismatch and galling of the threads on the barrel nut and mating bolt, did not contribute to premature failure of loaded barrel nuts during exposure to a salt spray atmosphere.

Discussion

Part geometry, microstructure, mating materials, lubrication and environment all contributed to premature failure, as determined from examining and comparing the three Contractor A barrel nuts that failed in service, the two Contractor A barrel nuts that failed in the salt spray chamber test, the Contractor B barrel nuts from inventory and the proposed redesigned barrel nuts that did not fail the salt spray chamber test. The smaller cross-sectional area at the conical threaded region (shoulder) of the Contractor A barrel nut contained less volume in which to distribute applied loads than the Contractor B and the newly designed barrel nuts. This resulted in higher stresses at this area during service. Another factor contributing to regions of high localized stress was the installation of the bolt into the barrel nut assembly. The wear and metal debris observed within the threaded section of the failed barrel nuts may have been attributable to improper seating of the bolt while torquing. Misalignment of the bolt caused by an uneven mating surface beneath the bolt head would result in surface galling during torquing. This condition would cause highly stressed areas in the barrel nut. Lubricity is also an important issue when uniform torque is required. The use of a corrosion inhibitive dry film lubricant would have helped to insure a uniform and consistent stress distribution within the barrel nut after torquing. High frictional forces as a result of metal-to-metal contact or parts that have a damaged cadmium plating could be avoided. Therefore, the risk of failure due to hydrogen induced cracking would be greater in the Contractor A barrel nuts.

The higher stresses in the Contractor A barrel nuts were compounded further by a higher strength material and an undesirable microstructure. The Contractor A material contained an unacceptable acicular delta phase in the grain boundaries and in the form of a Widmanstätten structure throughout the grains. The ultimate tensile strength of the two Contractor A barrel nuts that failed in service measured higher than the ultimate tensile strength of a Contractor B barrel nut. The higher strength of the Contractor A barrel nuts increased its susceptibility to hydrogen embrittlement and decreased its toughness in comparison to the Contractor B barrel nut at the lower strength level.

The acicular delta phase observed metallographically within the microstructure of the Contractor A barrel nuts is considered a greater stress concentrator than the spheroidal delta phase found in the Contractor B barrel nuts[1]. The delta phase inhibits excessive grain growth in UNS N07718 during the solutionizing and aging treatments, but it is a brittle phase and decreases the toughness of the material [2]. Metallography also revealed MC carbides in both versions of the barrel nuts. These MC carbides are brittle (many were cracked when examined as a result of prior forming) and are stress concentrators. These carbides were preferentially orientated in the direction of extrusion and occurred in bands. The Contractor A material also contained a high concentration of Widmanstätten structure within these regions of banding. Banding in the Contractor A barrel nut occurred parallel to the plane of fracture, which is undesirable. Banding in the Contractor B barrel nut ran more favorably, in the direction of extrusion perpendicular to the Contractor A fracture plane. The MC carbides in the Contractor A material seemed to be found more in clusters than in the Contractor B material. Together, the higher tensile strength, the acicular delta phase, and the banding decreased the toughness of the Contractor A barrel nuts.

Inspection of the Contractor A spring clips revealed that the cadmium plating and the steel clip were completely corroded. The cadmium plating of the spring clip was either scratched during installation or corroded during service eventually leaving the steel spring clip unprotected. Corrosion of the spring clip occurred when water was entrapped in the barrel nut receptacle machined in the aluminum fuselage. Oxidation occurred at the steel clip surface while nascent hydrogen was produced at nearby cathodic sites as part of the electrochemical corrosion process. The high state of stress, grain boundary chemistry (acicular delta phase) in the Contractor A barrel nut is thought to have increased the susceptibility of this material to hydrogen embrittlement. In addition, nickel is cathodic to

---

[1]Conversation with R. R. Biederman, Worcester Polytechnic Institute, Professor, Department of Mechanical Engineering, 100 Institute Rd., Worcester, MA, 1991.

steel in the presence of ionized water. The hydrogen would have preferentially migrated to sites of highest stress and disorder in the grain boundaries. Fractography of the Contractor A barrel nuts that failed in service showed that intergranular decohesion occurred at the crack initiation sites suggesting that cracking in these areas was environmentally assisted. Laboratory testing of Contractor A barrel nuts in a salt spray environment caused similar intergranular fracture at the crack origin. When testing was performed in the absence of an aggressive environment, as when the Contractor A barrel nut was forced over a conical mandrel during overload testing, fracture occurred in the same plane as the service and salt spray failures. However, the resultant morphology consisted entirely of ductile dimples. There was no initiation region of intergranular decohesion. Therefore, the salt spray chamber and conical mandrel testing showed that fracture of the Contractor A barrel nuts in service would not have occurred in an intergranular mode if an aggressive environment was not present. Further evidence of the presence of an aggressive environment in the service failures of the Contractor A barrel nuts was found by EDS on the surface of the Ft. Hood cradle and fracture surface of the barrel nut at the crack origin. Characteristic X-rays of chlorine, calcium and iron were collected that indicated chlorine and calcium ions were most likely present in water that caused the oxidation of iron (most likely the steel spring clip), both of which collected on the cradle surface as the water evaporated or drained out of the barrel nut receptacle in the aluminum fuselage.

Failure Scenario

According to the original engineering drawing, the only requirement placed on the barrel nut was its ability to withstand a specific load of 37,800 pounds (168000 N). Each manufacturer had considerable latitude in designing the conical threaded region (shoulder). Contractor A chose to design this region thinner than Contractor B, yet they both met the original drawing requirements. Based on salt fog tests and microscopic examination of the fracture surfaces, the following hypothesis was developed. UNS N07718 alloy, being a nickel base alloy, is highly prone to galling. Absence of any lubricant during installation causes galling debris to wedge between the threads and in turn provides a source of constant hoop stress in the nut. The presence of a steel clip used for alignment purposes created a galvanic couple in which the nut became a cathode and the clip the anode. As a result, hydrogen was being charged into the nut through galvanic corrosion during service. Consequently, after a period of time, a service induced hydrogen stress crack developed and grew until the hoop stress overloaded the remaining material. Since the failure was not in the thread, any sustained stress from the pre-load was ruled out as a potential cause. Since Contractor B nuts did not fail, the magnitude of the hoop stress was suspected to be important. However, the testing conducted to evaluate the effect of misalignment showed no significant detrimental effect.

Conclusion

The failure of the barrel nuts was attributable to hydrogen induced cracking. Galling between the unlubricated bolt and the nut thread provided the sustained hoop stress. Design of the nut shoulder may also have contributed to high stresses. Galvanic coupling with the carbon steel retaining clip provided the source of hydrogen necessary for this mode of failure in the cold worked and aged microstructure.

Recommendations

1. A minimum height for the threaded conical section (shoulder) of the barrel nut should be specified and the thickness of the base increased to reflect the new proposed design.

2. The barrel nut and mating bolt should be wet installed utilizing MIL-T-83483, a molybdenum disulfide, anti-seize thread compound, to reduce galling and the consequential high tensile stresses which result from metal-to-metal contact during torquing (torque values would have to be re-adjusted from 1,850 to 975 in-lbs which is equivalent to 209 to 110 N·m).

3. The strength of the barrel nut should be reduced, if deemed feasible by stress analysis, to increase the fracture toughness and resistance to hydrogen induced cracking of the material.

4. The acicular delta phase and excessive banding should be avoided in accordance with AMS 5662F.

5. The carbon steel spring clip should be coated or fabricated from such material as stainless steel to avoid galvanic corrosion with the barrel nut and the resultant mitigation of atomic hydrogen.

6. The extrusion direction should be aligned parallel to the principal stress.

References

[1] P. J. DiConza, R. R. Biederman, J. L. Burger, "Microstructural Characterization of Alloy 718," Microstructural Science, Vol. 18, Worcester, MA, pp. 91-92, 1989

[2] J. L. Burger, R. R. Biederman, W. H. Coots, "The Effects of Starting Condition on the Aging Response of As-Forged Alloy 718," Superalloy 718 - Metallurgy and Applications, Worcester, MA, p. 216, 1989.

Edward R. Duffy [1]

Effects of Wear-Resistant Coatings on the Fatigue Strength of 4340 Steel

REFERENCE: Duffy, E. R., **"Effects of Wear-Resistant Coatings on the Fatigue Strength of 4340 Steel,"** *Effects of Product Quality and Design Criteria on Structural Integrity, ASTM STP 1337,* R. C. Rice and D. E. Tritsch, Eds., American Society for Testing and Materials, 1998.

ABSTRACT: For applications using 4340 steel where hardened surfaces are required in a marine environment, surface coatings are necessary. Coatings that resist corrosion and provide wear resistance generally degrade the fatigue performance of the substrate metal. Shot peening before plating was ineffective in preventing a loss of fatigue life of plated steel bars compared to bare steel test bars which were not shot peened. The maximum residual compressive strength produced by shot peening was measured and was less than the maximum applied tensile stress in fatigue. As-plated electroless nickel has poor sliding wear resistance compared to either electroplated nickel or chromium in sliding wear at a contact stress of 37 Mpa. The tensile strength decreased in proportion to the volume fraction of coating applied to the steel substrate.

Keywords: chromium plating, electroless nickel, fatigue, tensile strength, shot peening, residual stress, sliding wear,4340 steel

When Depot level maintenance is required during the life cycle of U.S. Naval aircraft, the replacement of worn and/or corroded components is desirable but in many cases not practical to meet a scheduled rapid return to service for the Fleet. Plating provides wear

[1] Materials Engineer, Naval Aviation Depot North Island, Code 43410, San Diego, CA 02135

and corrosion protection but is not intended to compensate for the decrease in strength from the loss of underlying steel. Cracks in brittle coatings can penetrate into the steel substrate and reduce the strength and fatigue life of the part [1]. Shot peening can minimize or prevent this crack propagation by providing a compressive layer on the steel surface before plating [*1*,2]. The ability of shot peening to extend the fatigue life of chromium plated steel was demonstrated in reverse bending of rotating beam fatigue specimens having a relatively thin (89 microns) plating [*2*]. This investigation repeats the application of shot peening before plating but evaluates thicker (250 microns) coatings under tension-tension fatigue loading.

In an effort to comply with the Aerospace National Emission Standards for Hazardous Air Pollutants (NESHAP), alternates to chromium plating are being evaluated. Electroless nickel is a coating being evaluated as a substitute for chromium in the short term future. The immersion of parts in a tank of different chemistry is a much easier process dislocation than the current concentrated effort of fixturing parts for plasma sprayed or High Velocity Oxygenated Fueled (HVOF) sprayed coatings to replace hard chromium plate.

In addition to tensile and fatigue testing both electroplated chromium and electroless nickel, wear tests were performed with thinner coatings for a specific F/A-18 wear problem. (The F/A-18 is a fighter/attack jet that is overhauled at the Naval Aviation Depot North Island.) For these tests 20 to 25 micron thick coatings of electrodeposited nickel, chromium and electroless nickel were tested against heat treated (1250 Mpa tensile strength) 4130 steel in lubricated sliding wear.

Experimental Method

Tensile and Fatigue Test Specimens

Figure 1 is a sketch of a finished fatigue test specimen . Guidelines for specimen geometry as given in ASTM Practice for Constant Amplitude Axial Fatigue Tests of Metallic Materials (E466) were followed. For plated specimens, a uniform milled undercut similar to that shown for tensile specimens in Figure 2 was used to allow a deposit of 250 to 315 microns to be applied. The minimum width and thickness was measured and recorded for each specimen prior to plating. Baseline bare steel specimens were finish machined to the configuration shown in Figure

1 and then heat treated to a tensile strength of 1940 Mpa. No shot peening was performed. After heat treatment, all test specimens which were to be plated (both tensile and fatigue) were shot peened with a nominal 425 micron ceramic shot per MIL-S-13165, Shot Peening of Metal Parts and AMS 2431/7, Peening Media Ceramic Shot to an intensity of 100 to 150 micron height on Almen A test strips. This intensity was chosen based on fatigue tests of 300M steel using different shot media by Lee [*3*].

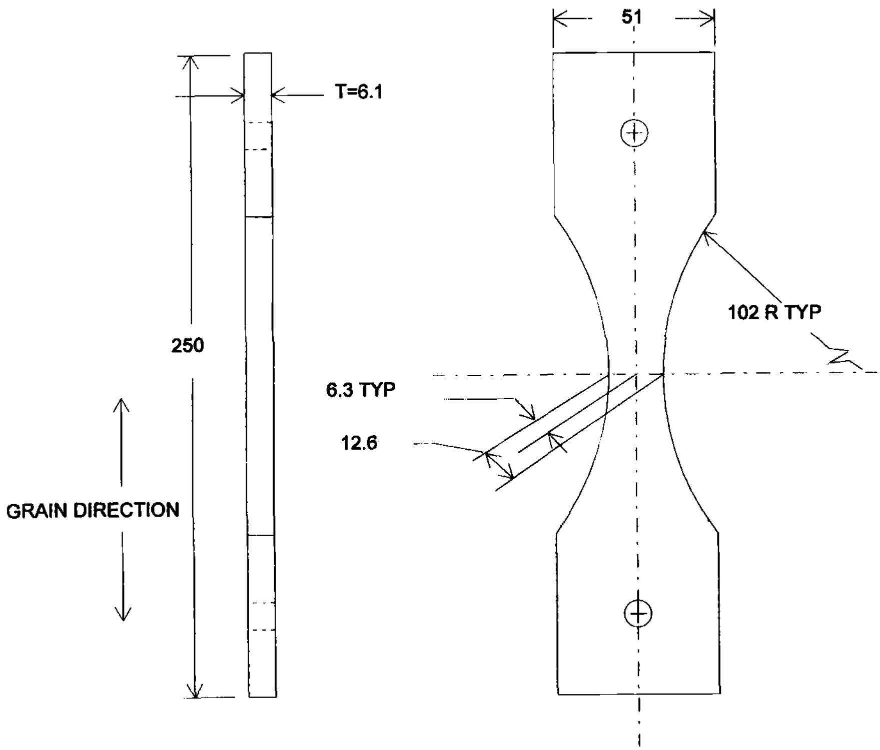

FIG. 1 -- Fatigue Specimen. Dimensions in millimeters.

Lee [*3*] had referenced earlier work performed at Grumman which demonstrated higher residual compressive surface stresses produced by hard (HRC 65) steel shot compared to standard (HRC 46) steel shot. Since Lee's investigation showed that residual compressive surface stresses produced by ceramic media were equal to that produced by hard steel shot, ceramic media was selected since ceramic media and not hard steel shot is available at NADEP North Island.

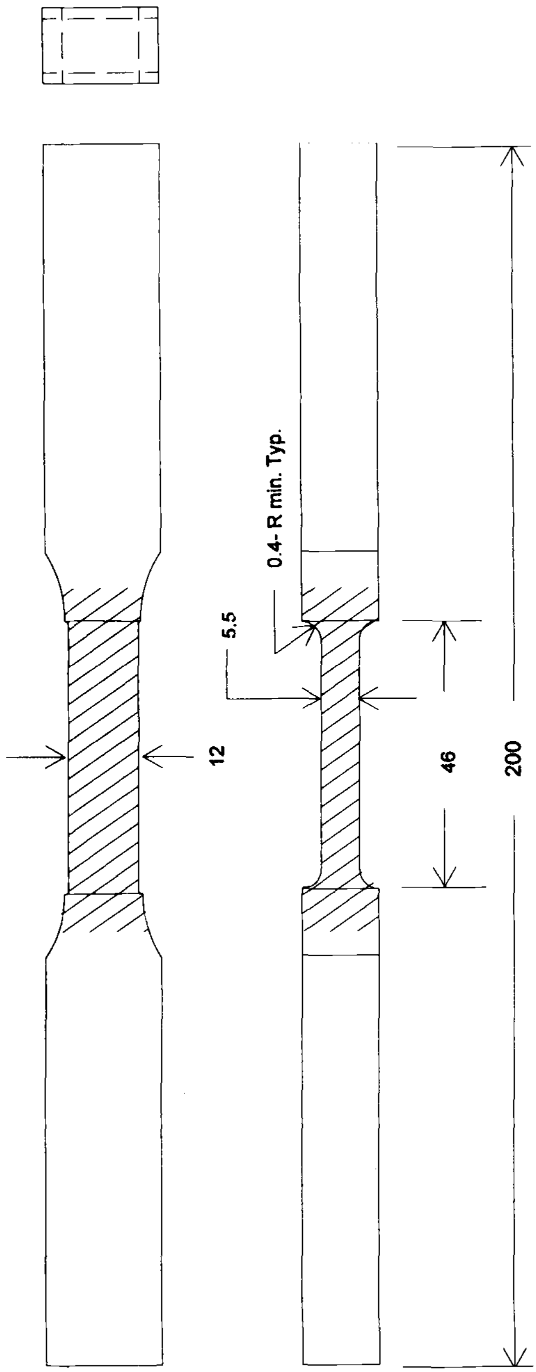

FIG. 2 --Tension test specimen. Cross hatched areas to be plated. Dimensions in millimeters.

Figure 2 is a sketch of a tensile specimen milled from 4340 steel plate prior to heat treating, shot peening and plating. The cross hatched area indicates where the chromium was subsequently deposited. Thinning of electrodeposits near edges required plating beyond the boundaries of the undercut, milled areas. Electroless nickel can be plated to a uniform specified thickness and was therefor tested in the as-plated condition. Chromium plated specimens were ground to produce a 250 micron plating thickness.

Cross sectional area measurements for calculating the applied stress were made after plating (for chromium plated specimens, after finish grinding). The ratio of minimum to maximum stress during the fatigue test (the R value) was 0.2 so that the data generated could be directly compared to that in MIL-HDBK-5. Data in MIL-HDBK-5 was used as a guide to estimate applied stresses for a targeted fatigue life of 10^5 cycles. The higher loads at lower cycles more accurately reflect the severe conditions encountered by high strength steel aircraft parts. High maximum applied stresses were used by Lee [*3*] to simulate F-14 arresting gear conditions.

Steel Analysis

The availability of 4340 steel plate and fatigue data at high strength levels were reasons for choosing 4340 steel plate. A variant of 4340, 300M, is now being used on aircraft landing gears.

Steel chemistry was confirmed by optical emission spectroscopy for conformance to AMS 6359 Steel, Strip and Plate 0.80 Cr - 1.8 Ni - 0.25 Mo (0.38 -0.43 C). The inclusion content was rated as a uniform severity level 2, heavy category D per Method A in ASTM Standard Test Methods for Determining the Inclusion Content of Steel (E45). The material rolling direction was confirmed by metallographic inspection. The grain size was measured to be ASTM No. 8 to 9 using ASTM Test Method for Determining the Average Grain Size (E112).

Plating Processes

Table 1 lists the electroplating parameters used to apply the chromium plating. All specimens were baked within 4 hours of plating at 190° C. for 23 hours to prevent hydrogen embrittlement. Table 2 lists the electroless nickel process parameters. The same baking treatment was given to all specimens which were nickel plated. The electroless nickel bath provides a phosphorus level of 11 to 12 per cent in the nickel deposit with the hypophosphite ions acting as the reducing agent.

TABLE 1 Process parameters for electroplating chromium

Parameter	Concentration or Result
chromic acid	250 g/l
CrO_3 / SO_4	100:1
amperage	0.3 A/cm^2
temperature	54^o C.
thickness/time	20 microns/h

TABLE 2 Process parameters for electroless nickel

Parameter	Concentration or Result
nickel chloride	30 g/l
sodium hypophosphite	9.7 g/l
pH	4.6 - 4.8
temperature	85 - 90^o C.
thickness/time	15 microns/h

Surface Roughness

A surface roughness gage using a diamond stylus drawn across the surface was used to measure surface irregularities. The conical diamond stylus had a 10 micron radius tip. The rougness average or arithmetic height of roughness irregularities measured from a mean line within the evaluation length was found to be 1 to 1.2 microns. This same measurement was found on as-milled steel plate and as-plated chromium and electroless nickel. V- block specimens for wear testing were purchased with a surface finish (roughness average) of 0.1 to 0.2 microns.

Wear Testing

Wear tests were conducted per ASTM D2625, Method for Determining Endurance (Wear) Life and Load -Carrying Capacity of Dry Solid Film Lubricants (Falex Method). Figure 3 schematically illustrates the method of applying a load to a rotating pin or journal in this type of wear test. Thin (20 to 25 micron) coatings of electroless nickel, electroplated chromium and electroplated nickel were applied to heat treated (1300 Mpa tensile strength) pins of 4130 steel. Uncoated V-blocks of the same steel and heat treat condition as the mating surface were used. The wear couple (rotating pin and 2 stationary V-blocks) were immersed in ambient temperature MIL-L-23699 lubricating oil during the test. A contact stress of 37 Mpa was chosen to match as nearly as possible a particular wear condition that was being encountered in the F/A-18 airframe mounted accessory drive (AMAD) gear box. The total test time was limited to 4 minutes since detectable wear was observed by the relative motion of the wear test loading mechanism during this time period.

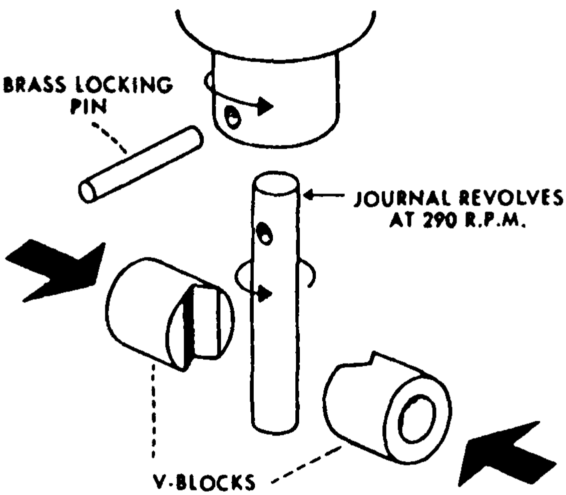

Figure 3 -- Schematic of wear test

Results

Residual Stress

Figure 4 is a histogram showing the number of fatigue test specimens having the average surface compressive stress measured with X-ray diffraction. A separate legend is included for those test specimens which were tested 13 months after shot peening. Note the shift to a lower surface compressive stress on these same specimens. The measured shift has allowed their surface stress to be nearly indistinguishable from that of specimens which were not shot peened. Chromium on selected specimens was electrochemically stripped after fatigue testing to expose the steel substrate for residual stress measurement.

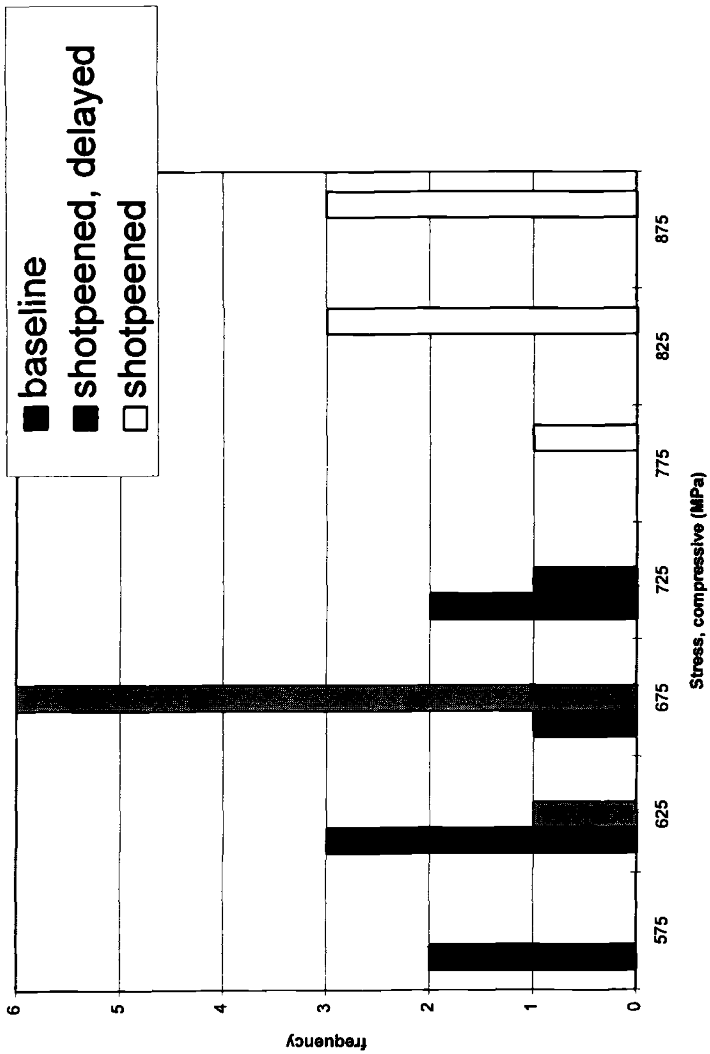

Figure 4. Histogram of Residual Stress Measurements

Tensile Tests

Tables 3, 4 and 5 list average tensile properties for the baseline steel plate, electroless nickel and chromium plated steel tensile specimens respectively. For the plated tensile specimens, the load bearing area was calculated using the entire cross sectional area including the plating. Plating was applied on all four sides of each tensile specimen as shown in Figure 2. Both nickel and chromium plating produced a weaker composite strength than the bare uncoated steel plate. From the review of stress strain curves it was apparent that the maximum stress used in fatigue testing (965 Mpa) was above the elastic limit for the nickel plated tensile specimens but below that for bare steel and chromium plated tensile specimens.

TABLE 3 -- Tensile test results on bare steel

Property	Average	standard deviation
tensile strength (MPa)	1949	7.6
yield strength	1536	7.6
per cent elongation	8.3	0.9

Average values listed are for six data points.

TABLE 4 -- Tensile test results on electroless nickel- plated steel

Property	Average	standard deviation
tensile strength (MPa)	1714	6.2
yield strength (MPa)	1408	26.
per cent elongation	6.3	0.5

Average values listed are for five data points.

TABLE 5 -- Tensile test results on chromium-plated steel

Property	Average	standard deviation
tensile strength (MPa)	1639	78
yield strength (MPa)	1473	17.
per cent elongation	5.5	

Average values listed are for three data points except elongation (one datum point).

Fatigue Tests

Bare fatigue test bars were cycled with maximum stresses ranging from 930 to 1100 Mpa. before a maximum stress of 965 Mpa. was selected as the maximum stress for evaluating plated fatigue bars. This stress was chosen so that fatigue lives would not exceed 10^6 cycles for reasons previously explained.

During tests of the electroless nickel specimens, a network of visible surface cracks was observed after 1000 cycles. The number of visible cracks increased as the specimen accumulated more loading cycles. This phenomenon was not observed on bare steel or chromium plated test specimens.

Figure 5 is a bar graph showing the test results for the single fatigue loading condition (maximum stress of 965 Mpa and an R of 0.2) used on all plated specimens. Results for bare specimens also exposed to these conditions are included on the same bar graph. Note that testing was stopped on one bare steel specimen after the specimen had accumulated more than 10^6 cycles. From surface features of the failed specimens, most failures were found to originate at a corner of the substrate steel. Several specimens from each group (baseline, nickel plated and chromium plated) were examined in a scanning electron microscope for evidence of defects at the steel surface or subsurface which could have caused failure. None were found.

Wear Tests

Table 6 lists the average weight loss on rotating pins and pairs of V-blocks used for each test. Two tests were conducted on nickel plated pins and one on a chromium plated pin. For each test conducted with electroplated nickel (nickel sulfamate), one steel V-block gained weight and the opposing block lost weight.

TABLE 6 -- Wear test results

Pin Coating	pin weight loss (mg)	V-block weight loss (mg)
chromium	0.0	1.4
electroless nickel	45.1	1.2, 0.8
electroplated nickel	0.3	+0.2, 0.1

Plus sign indicates a weight gain.

Microhardness tests were performed on cross sections of plated pins and a V-block. A 100 gram load was used so that hardness impressions were contained within the plating thickness. Results are listed in Table 7.

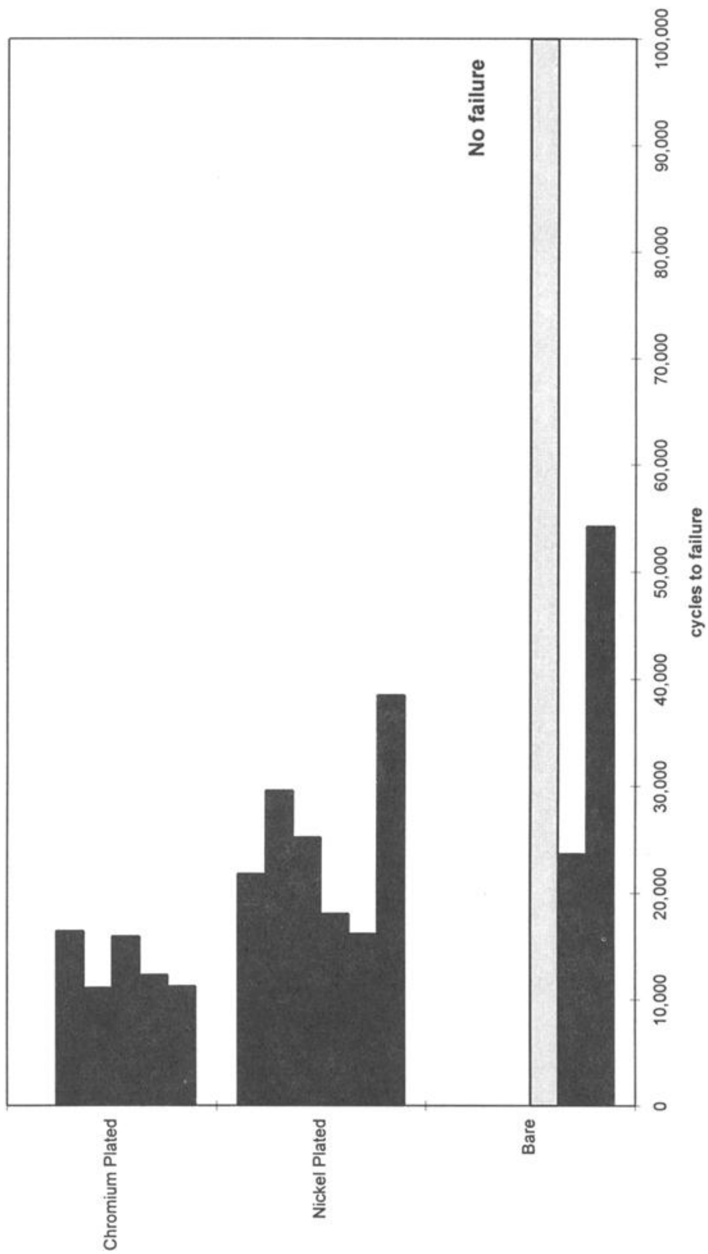

Figure 5. Bar graph of fatigue test results at 965 MPa.

TABLE 7 -- Microhardness, 100 gram load

Material	Vickers Hardness
chromium	900
electroplated nickel	610
electroless nickel	432
4130 steel	405

Discussion of Results

Tensile Tests

The drop in tensile strength (by 12 per cent) of nickel plated tensile specimens follows closely with the measured volume per cent of nickel plating (11.6 per cent). A higher reduction (16 per cent) in tensile strength for chromium plated tensile specimens was measured for just a slightly higher volume per cent (12.8) of chromium plate measured in the reduced cross section of the tensile specimens.

When dealing with low elongations (less than 10 per cent) any reduction is greatly magnified if compared on a percentage basis. For both nickel plated and chromium plated tensile specimens, lower elongations were observed. The lack of ductility in either coating has reduced the measured elongation of a steel heat treated to a condition of marginal ductility.

Residual Stress

Using the Student's t statistic to evaluate small samples, the measured values of the residual surface stress on machined test specimens was compared to test specimens which had been shot peened. A student t of 5.8 was calculated using the method to verify if two separate populations of data are present [*4*]. This t value indicates that shot peening did significantly change the surface stress with a certainty of 99 per cent..

The fatigue tests in this investigation were initially performed at the Naval Aviation Depot Alameda. Due to base closure constraints, the completion of the testing had to be delayed over a year to have the test equipment moved to San Diego. This resulted in delaying fatigue tests on chromium plated specimens for 13 months. Figure 4 shows the measured drop in residual surface stress. To answer the question if this drop in residual stress was due to fatigue loading and/or specimen fracture, one bare steel specimen which had not been shot peened was peened in an identical manner as the other shot peened specimens. The residual surface stress was measured before fatigue testing. After fatigue testing at a maximum stress of 993 Mpa , the specimen failed after nearly two million cycles. The residual surface stress was measured after testing. The results are reported in Table 8. The total stress error includes counting statistics and goodness of fit of the plot of icident angle of radiation to metal lattice d-spacing.

TABLE 8 -- Residual surface stress, before and after testing

	Stress (MPa)	error (MPa)
Before testing	834	45
After testing	793	55

It is apparent from Table 8 that there is no change in the measured residual stress taking into account the total stress error. The drop in residual stress after a 13 month delay shown in Figure 5 therefor is not due to fatigue loading. Speculation on the cause of this drop in stress is outside the scope of this investigation.

Fatigue Tests

MIL-HDBK-5 reports four fatigue data points with the same material (4340 steel), heat treatment and test stress levels used in this investigation. In addition to one specimen which did not fail in 10^7 cycles, MIL-HDBK -5 reports the following fatigue lives for a maximum stress of 965 Mpa and an R ratio of 0.2:

72 000 cycles
85 000 cycles
and 190 000 cycles.

In this investigation, there was one baseline specimen which did not fail after 2 $\times 10^6$ cycles. The other two 4340 stel specimens (bare, no plating) machined from plate stock failed at 23 700 and 54 200 cycles. The MIL-HDBK-5 data is for bar stock..

A reason for lower fatigue lives reported for chromium plated specimens may be the higher maximum stresses used in fatigue testing. The maximum stress used by Cohen [2] was 827 Mpa. Since most investigators are concerned with fatigue strength usually defined as a maximum stress below which failure does not occur after a million fatigue cycles or more , they would be using lower applied stresses than in a low cycle fatigue study such as this one. There is an interaction between the magnitude of the residual compressive surface stress for shot peened components and fatigue strength [5]. The fact that the applied stress used in this investigation is larger than the maximum residual surface stress is believed an important influence on fatigue.

The fact that an appreciable loss in fatigue strength occurred for nickel plated specimens despite no delay in testing may be due to the applied tension load in fatigue being higher than the measured elastic limit (880 Mpa) for nickel plated tensile specimens. Testing at a stress 85 Mpa higher than the elastic limit would have dissipated some of the imposed residual compressive stress [6].

Wear Tests

The higher hardness of electroplated nickel and chromium are believed responsible for the superior wear resistance compared to electroless nickel plating.

Summary

Tensile properties of high strength 4340 steel were reduced when coated with thick (250 micron) electroless nickel or electroplated chromium.

The low cycle fatigue life of uncoated 4340 steel plate was reduced when plated with thick (250 microns) coatings of electroless nickel and electroplated chromium.

The sliding wear resistance of as-plated electroless nickel rubbing against 4130 steel was inferior to either electroplated nickel or electroplated chromium, as expected due to higher coating hardness.

Recommendations

To confirm a dependence of the magnitude of residual surface stress to the maximum applied stress, fatigue tests should be run with maximum applied stresses just above and below the maximum measured residual surface stress on uncoated but shot peened steel specimens. The tests should then be repeated with coated specimens which were identically shot peened before coating.

Acknowledgements

The author wishes to acknowledge the contributions of E. Lopez, M. Oliver, D. Ottino and M. Poirier at the Naval Aviation Depot North Island.

The author also wishes to thank M. Zulim formerly with the Naval Aviation Depot Alameda for initial tensile and fatigue tests.

References

1. Powell, G. and Mahmoud, S., edits., *Failure Analysis and Prevention, Metals Handbook, Ninth Edition,* ASM, Metals Park, OH., 1986, p. 126.

2. Cohen, B., " Effect of Shot Peening Prior to Chromium Plating on the Fatigue Strength of High Strength Steel," Wright Air Development Center, Technical Note 57-178, June 1957.

3. Lee, S., " Hard Steel Shot Peening and Ceramic Shot Peening Effects on Fatigue of High Strengrh Steel," Grumman Aerospace Corp., Report M&ME -TS441A-86R-041, 1986.

4. McClave, J. and Benson, P., *Statistics for Business and Economics*, Dellen Publishing, New York, 1982, p. 337.

5. Koster, W.P. et al, " Surface Integrity of Machined Materials," AFML-TR-74-60, April 1974.

6. Almen, J.O. and Black, P.H., *Residual Stresses and Fatigue in Metals*, McGraw-Hill, New York, 1963, p. 80.

Michael F. Petrou[1] and Philip C. Perdikaris[2]

DESIGN OF REINFORCED CONCRETE BRIDGE DECKS UNDER MOVING LOADS

REFERENCE: Petrou, M. F. and Perdikaris, P. C., "**Design of Reinforced Concrete Bridge Decks Under Moving Loads,**" *Effects of Product Quality and Design Criteria on Structural Integrity, ASTM STP 1337,* R. C. Rice and D. E. Tritsch, Eds., American Society for Testing and Materials, 1998.

ABSTRACT: This paper presents design recommendations of non-composite reinforced concrete bridge decks subjected to fatigue due to moving loads. These recommendations are based on test results of 1/3- and 1/6.6- scale physical models of a full-scale 21.6-cm (8.5 in.) thick and 15.24-m (50-ft) long simply supported non-composite reinforced concrete deck. Concrete bridge decks should be designed to transfer the load in a two-way action. Experimental results show that the two-way slab action in the decks changes to a one-way action (transverse direction) as fatigue damage due to a moving wheel-load accumulates. It is recommended to adopt an isotropic steel reinforcing pattern. An isotropic reinforcing pattern with a steel ratio of 0.3 % (each top and bottom layer) in each direction appears to be adequate. A similar reinforcing amount and pattern is required by the Ontario bridge design Code. The required steel content is therefore reduced resulting in substantial savings in the bridge deck construction costs and improving the corrosion resistance in decks, especially in the presence of deicing chemicals. It appears that flexural cracking in the deck and bond failure at the steel-concrete interface are necessary and sufficient conditions for deck failure under traffic loads. It is, thus, highly desirable to preclude or at least limit cracking and maximize the bond strength of the steel rebars.

KEYWORDS: bridge deck, fatigue, design, moving load, pulsating load, reinforced concrete, static load.

Concrete is one of the most consumed materials on earth, second only to water; one ton of concrete is manufactured for each person on earth each year. It is a very good construction material because it is inexpensive, durable, can be easily formed into

[1] Assistant Professor, Department of Civil and Environmental Engineering, University of South Carolina, Columbia, SC 29208

[2] Professor, Department of Civil Engineering, Case Western Reserve University, Cleveland, OH 44106

different shapes and sizes, and has reasonably high compressive strength. Concrete's "Achilles heel", however, is its tensile strength and lack of ductility. Steel reinforcement is added to carry the tensile stresses and provide some of the needed ductility.

Fatigue of reinforced concrete is a complex problem because it involves fatigue of plain concrete, steel reinforcement, bond at the concrete-steel interface and the interaction of these mechanisms. Bridge decks is an example of reinforced concrete structures subjected to fatigue loading conditions due to moving loads. Several researchers have been working in this field for many years [1-8]. The research, however, has been focused on fatigue of plain concrete or steel reinforcement or bond at the concrete-steel interface instead of the actual fatigue of reinforced concrete [1-5]. Hawkins et al., Chang et al. and Kormeling et al. conducted limited research on the fatigue behavior of reinforced concrete beams under pulsating loading conditions [6-8].

The reinforced concrete bridge decks (slabs) are currently designed according to the American Association of State Highway and Transportation Officials (AASHTO) Code requirements [9 and 10]. According to the AASHTO Standard Code Specifications [9], concrete bridge decks are designed as beams transverse to the traffic direction and carrying the traffic load in flexure. This approach does not take into account fatigue and the enhancement of the shear and flexural ultimate capacity of the bridge deck due to the two-way load transfer and the compressive membrane action in the deck [11-13].

Small-scale models have been tested under concentrated static and stationary pulsating loads in Canada and the US [14 and 15]. The Ontario Highway Bridge Deck Design Code [16] adopted an "isotropic" steel reinforcement pattern with equal amount of steel reinforcement in both the transverse and longitudinal direction based on static and stationary pulsating fatigue tests [14 and 17]. The amount of steel required by the Ontario Code is approximately 60% lower than that required by the AASHTO Standard Code Specifications[9]. An empirical design procedure similar to the Ontario Design is introduced in the AASHTO LRFD Bridge Design Specifications [10]. A preliminary fatigue study of bridge decks under moving constant wheel-loads [15] indicated a substantial reduction in the bridge deck fatigue life.

The objective of this paper is to present some results on the response of non-composite reinforced concrete bridge decks under moving constant wheel-loads and recommend some design modifications. Details regarding the experimental program, instrumentation, and experimental results can be found elsewhere [12].

Experimental Results-Discussion

Small-scale (1/6.6) physical models of concrete bridge decks of a simply supported non-composite 15.24-m (50-ft) long bridge with a 21.6-cm (8.5-in.) thick concrete deck supported on four steel girders spaced at 2.13 and 3.05 m (7 and 10 ft) were subjected to concentrated static, stationary pulsating (cyclic), and moving constant wheel-loads. The stationary pulsating load was applied at the center of one of the nine deck regions shown in Fig. 1 using a 222.5 kN (50-kip) actuator. The moving constant wheel-load was applied at the center of one of the three lanes (see Fig. 1) using a specially designed wheel-load setup. Two deck designs were studied: (a) "orthotropic" (AASHTO standard design method) with steel ratios (steel reinforcement area to concrete area ratio) of ρ_t=0.7% (transverse) and ρ_l=0.35% (longitudinal) and (b) "isotropic" (Ontario design method) with ρ_t=ρ_l=0.3%.

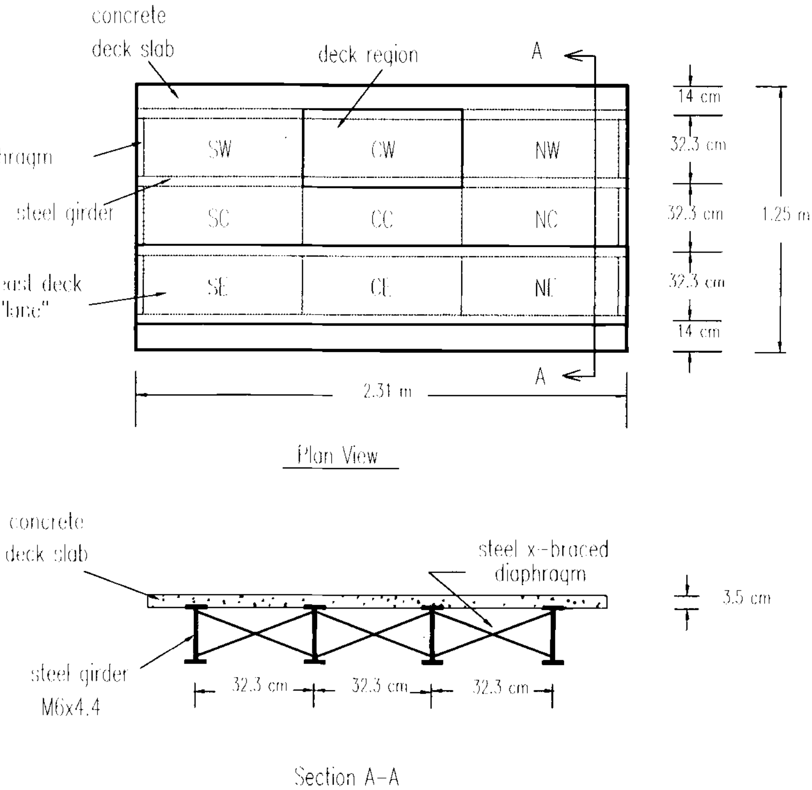

FIG. 1-- Dimensions of the 1/6.6-scale bridge deck model with a prototype girder spacing of 2.13 m (7 ft).

Static Load

The presence of membrane compressive forces (arching action) in the deck due to lateral and rotational restraint enhances its static ultimate strength. The measured static ultimate strength for the decks, P_u, reached values up to 3 times the yield-line theory predictions which corresponds to safety factors against static strength between 8 and 21. A combined membrane and bending action occurs in the deck slabs. Although some of the decks failed in flexure, all the decks eventually punched through at a maximum deck deflection of less than half the deck thickness. Punching shear failure in the deck appears to be interrelated with a "snap-through" instability of a compressive "arch" mechanism activated in the deck due to the lateral restraint. The American Concrete Institute (ACI)

Code equations [18] (recommended also by AASHTO) clearly underestimate the ultimate capacity of the decks, especially for the "orthotropic" deck design.

The relatively high safety factors and the general response of the reinforced concrete bridge decks under static loads suggest that the design procedure should be modified and required amount of reinforcement be significantly reduced. The bridge decks should be analyzed as two-way slabs taking into account the compressive membrane action and not as transverse beams which leads to designs with unnecessarily large amounts of steel reinforcement. More information about the behavior of bridge decks under static loads is included in a previous paper [13].

Stationary Pulsating Load

Stationary pulsating load tests were performed using load control at a frequency of 7 Hz. The pulsating load varied sinusoidally with a minimum load level of 2.2 kN (500 lb) and a maximum load equal to that selected for each test. The frequency of 7 Hz was selected to simulate the passage of a truck over a bridge. The time it takes a truck to cross a 24-m (80-ft) bridge is about 1 sec (speed of about 55 miles/hr). Since for the deck models tested in this study the frequency is scaled as the scale factor of length, the frequency of the applied load for the 1/6.6-scale model decks should be about 7 Hz.

The type of applied fatigue loading has a profound influence on the fatigue behavior of the decks. The behavior of reinforced concrete bridge decks under a stationary pulsating load is similar to that under a static load. The stationary pulsating load is transferred in both the two major directions (transverse and longitudinal) of the deck along which steel reinforcement is placed. This two-way deck slab action is maintained until failure occurs which helps to extend the fatigue life of the bridge deck. Punching shear failure occurred in almost all the specimens as a secondary failure while yielding of reinforcement is considered the primary cause of failure. All bridge decks exhibited a flexure radial cracking pattern very similar to that observed in bridge decks subjected to static loads (see Fig. 2). The maximum stationary pulsating load was applied statically after a certain number of load cycles in order to measure the deflection of the bridge deck and assess the accumulation of damage. The total deck deflection that includes the permanent deformation during fatigue of bridge decks tested under stationary pulsating load varies between 63% and 108% of the ultimate static deflection (average of 88%). The variation is due to the effect of the applied load, steel reinforcement ratio, girder spacing, and restraint conditions. The total deck deflection value is actually closer to the ultimate static deflection since the deck deflection right at failure is never recorded.

Moving Constant Wheel-load

An experimental moving constant wheel-load setup [12, 15] was developed. It consists of a moving steel trailer bolted to a 30-kip hydraulic actuator which applies a constant wheel-load to the deck specimen through a steel reaction frame attached to the floor. A hydraulic motor enables the jack-wheel assembly to move back and forth at a maximum speed of about 0.6 m/sec (1.4 miles/hr). The average time to complete one

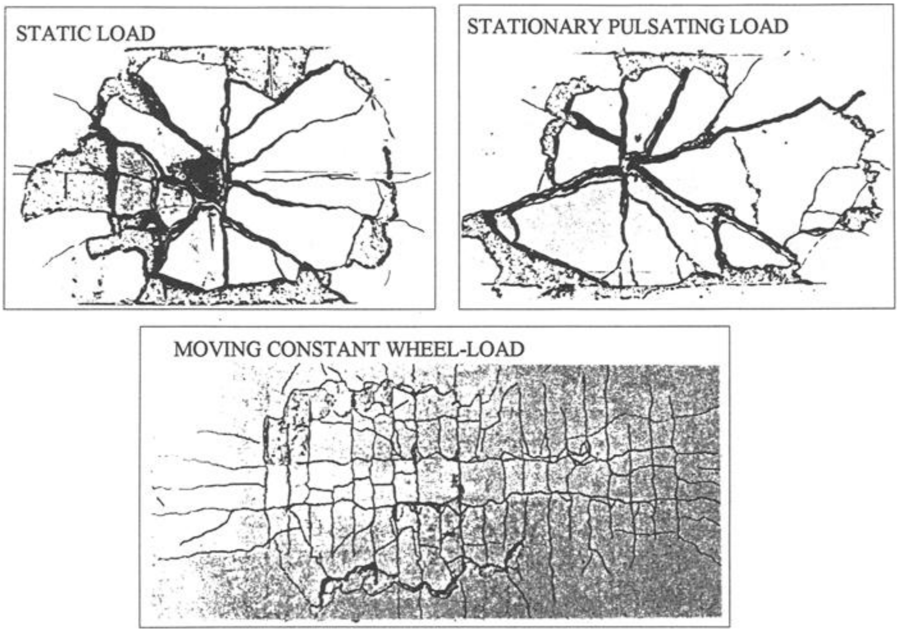

FIG. 2--Cracking patterns of reinforced concrete bridge decks

wheel passage on the deck specimen is about 4 sec., which is equivalent to a frequency of 0.25 Hz, instead of 0.43 sec. that is required for a 1/6.6-scale model deck. The speed of the wheel-load was not scaled properly because of limitations in the loading system. Since the speed of the model wheel-load is extremely low, the present study on the fatigue response of the concrete bridge decks does not include any possible dynamic effects.

Bridge decks subjected to moving constant wheel-load exhibited a behavior different than under static or stationary pulsating loads. Under moving constant wheel-load, the initial two-way deck slab action changes to a one-way slab action as failure is approached. This accelerates the damage accumulation and lowers considerably the fatigue life of the decks. For a given applied fatigue load level, the decks subjected to a stationary pulsating loading regime exhibited higher fatigue life than those subjected to a constant moving load of equal maximum load level (see Fig. 3). Stationary pulsating load tests are therefore not adequate in predicting the fatigue strength of reinforced concrete bridge decks subjected to traffic loads. Under a moving constant wheel-load a flexural grid-like pattern similar to the bottom flexural steel mesh is formed (see Fig. 2). The damage accumulation in bridge decks subjected to moving constant wheel-loads takes place in three stages: (a) the damage increases very rapidly at the first stage; (b) the rate of increase of damage is practically constant at the second stage; (c) approaching failure damage increases rapidly at the third stage. This typical sigmoidal fatigue damage

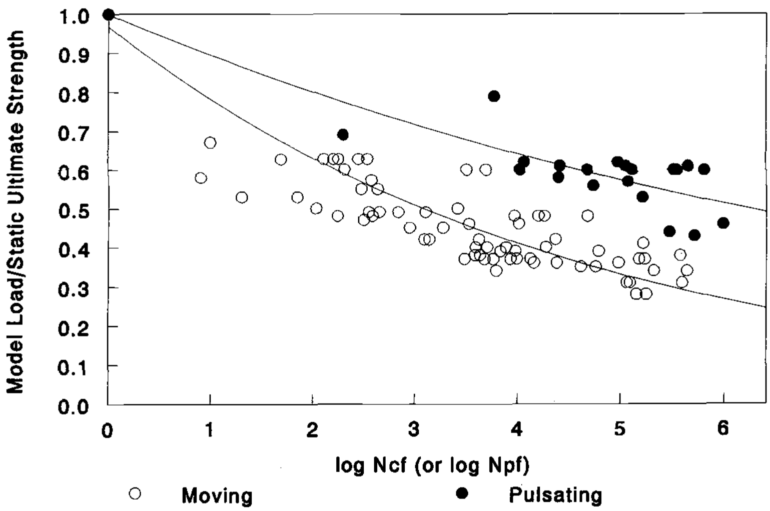

FIG. 3--Comparison of the fatigue life of bridge decks tested under stationary pulsating and moving constant wheel-load.

accumulation curve is depicted in the total deck deflection measurements with respect to the number of passages of the moving constant wheel-load over "orthotropically" and "isotropically" reinforced bridge decks with 3.05 m (10 ft) and 2.13 m (7 ft) girder spacing respectively (see Fig. 4). Such behavior can be used as a non-destructive evaluation tool to assess the condition of a bridge deck and estimate its remaining life. The total deck deflection values for bridge decks subjected to moving constant wheel-loads varies between 22% and 58% of the ultimate static deflection (average of 37%). These values depend on the maximum applied load, steel reinforcement ratio, girder spacing, and restraint conditions.

As shown in Fig. 5 (log P/P_u vs. $\log N_{cf}$ or $\log N_{pf}$), based on an exponential curve fit of the fatigue data the 2.5-million load cycle fatigue strength of the deck models under a stationary pulsating load ranges between $0.47P_u$ and $0.54P_u$ (safety factor of 5 to 12, as shown in Table 1; see Fig. 5). The 2.5-million wheel-load passages fatigue strength, on the other hand, estimated to range between 0.21 and $0.28P_u$ (safety factor of 3 to 4, as shown in Table 1; see Fig. 5).

It should be noted that while the fatigue strength of the bridge decks under a moving constant wheel-load is in the same range as the cracking load level, the fatigue strength under a stationary pulsating load is similar to the yielding load level for the steel reinforcement. If the efficiency of the fatigue deck design is measured by the number of wheel-load passages the deck can sustain for a given load level P/P_u without failing, the "Ontario" deck design appears to be more efficient than the "orthotropic" design (see Fig. 5). The use of fiber-reinforcement in a higher tensile strength concrete should improve the fatigue response of reinforced concrete bridge decks.

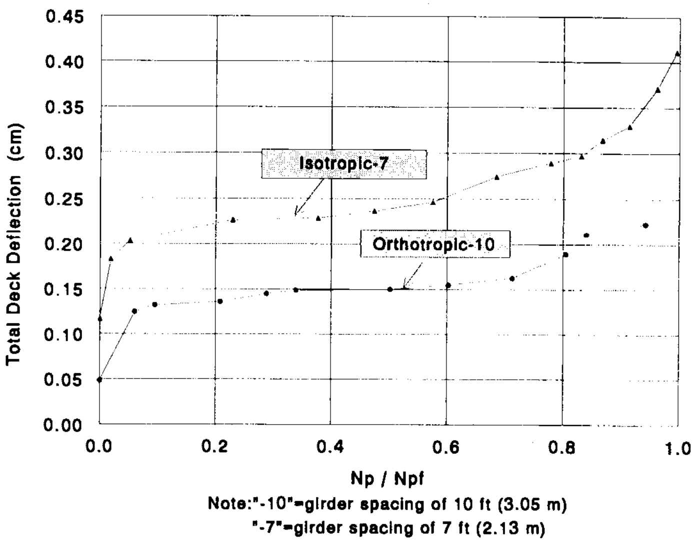

FIG. 4--Total deck deflection under moving constant wheel-load with respect to ratio of the number of wheel-load passages to the number of wheel-load passages to failure, N_p/N_{pf}

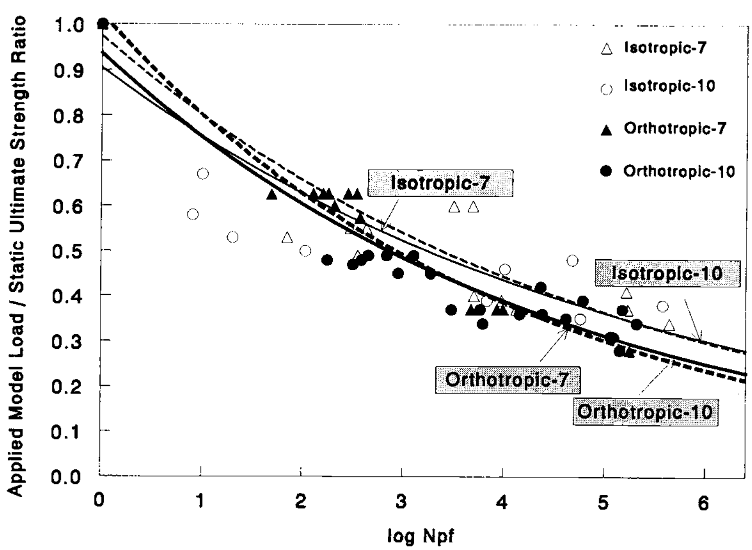

FIG. 5-- S-N curves under moving constant wheel-load.

TABLE 1--Predicted deck fatigue strength based on exponential curve fitting of the experimental data.

Specimen	Predicted Fatigue Strength (P/P_u)		Safety Factor	
	Pulsating Load	Moving Load	Pulsating	Moving
	N_{cf} = 2.5 mil.	N_{pf} = 2.5 mil.	N_{cf} = 2.5	N_{pf} = 2.5
Orthotropic-7	0.52	0.21	12.2	4.4
Orthotropic-10	0.54	0.23	8.3	3.6
Ontario-7	0.47	0.28	6.9	3.9
Ontario-10	0.47	0.28	5.4	3.0

Notes: P = applied load; P_u = static ultimate strength

N_{cf} = number of load cycles to failure; N_{pf} = number of wheel-load passages to failure

Fatigue Failure Mechanism(s) of a Concrete Bridge Deck Under Traffic Loads

During the service life of a concrete bridge structure, its deck is subjected to high-cycle low stress level fatigue due to traffic loading (moving loads). Based on the present test results, the collapse of concrete decks is expected to occur due to steel-concrete bond failure. As soon as cracking occurs, the steel stress (and strain) increases substantially, whereas the concrete stress in the close vicinity of the crack is reduced. The differential strains cause high bond stresses, resulting in the debonding of the steel bars. This phenomenon in conjunction with the gradual transition of the two-way action in the deck into a one-way action leads to a punching type deck.

The following conclusions are based on experimental measurements and observations:

1. The fatigue failure of the non-composite reinforced concrete bridge decks tested under moving constant wheel-loads is directly associated with the cracking of concrete.
2. Cracking of concrete occurs in a grid-type pattern very similar to the steel reinforcing mesh.
3. The total deck deflection at failure for the bridge decks subjected to moving constant wheel-loads is considerably lower than the deck deflection measured at failure for the bridge decks subjected to static loads. This indicates that a different fatigue mechanism than yielding of steel reinforcement or shear failure of concrete observed under static loading conditions causes the deck to fail under moving load conditions.

Design of Concrete Bridge Decks Under Moving Loads

Fatigue of reinforced concrete structures is not addressed by any design code in the US. Fatigue of reinforced concrete bridge decks, in particular, is becoming increasingly critical due to the increase of the intensity and magnitude of traffic loads and the tendency to use more slender bridge decks with fewer supporting steel girders.

Several modifications of the existing design procedures for the design of concrete bridge decks under fatigue loading conditions are justified:

1. Reinforced concrete bridge decks should be designed to transfer the load in a two-way action. Fatigue experimental results show that the two-way slab action in the decks changes to a one-way (transverse) action as fatigue damage due to the moving wheel-load accumulates. The bridge decks designed according to the AASHTO standard specifications carry the traffic load mainly in the transverse direction (perpendicular to the traffic) since twice as much amount of steel reinforcement is present in the transverse direction compared to that in the longitudinal (traffic) direction. In these decks, the transition from a two-way action to a one-way action is accelerated. It is recommended to adopt an isotropic reinforcing pattern.
2. A reinforcing steel ratio of 0.3 % in an isotropic reinforcing pattern, such as that required by the Ontario bridge design code and allowed in the AASHTO LRFD bridge design specifications according to the empirical design method, appears to be adequate. This reinforcing pattern reduces the steel content and not only results in substantial savings in the construction costs of bridge decks but more importantly it improves the corrosion resistance of the decks.
3. Since it appears that initiation of flexural cracking in the deck is a necessary and sufficient condition contributing to the failure of the decks under moving wheel-load fatigue, it is highly desired to limit or preclude cracking. The use of fiber-reinforcement in a higher tensile strength concrete should improve the fatigue response of reinforced concrete bridge decks.
4. The fatigue life of reinforced concrete bridge decks subjected to traffic loading conditions directly depends on the fatigue life of the interface bond between concrete and steel. Addition of concrete admixtures that improve bond and use of as small size steel rebars as possible will improve the bond behavior between steel and concrete and the fatigue performance of the decks.

Acknowledgments

This research was funded by the Ohio Department of Transportation and the Federal Highway Administration. Their support is greatly appreciated. The contents of this paper reflect the views of the authors, who are responsible for the findings and conclusions presented herein, and do not necessarily reflect the views of the Ohio Department of Transportation or the Federal Highway Administration.

References

[1] Shah, S.P., and Chandra, S., "Fracture of Concrete Subjected to Cyclic and Sustained Loading", ACI Journal, Oct., 1970.

[2] ACI Committee 215, "Considerations for Design of Concrete Structures Subjected to Fatigue Loading", ACI Journal, Vol. 71, No. 3, March 1974, pp. 97-121.

[3] Holmen, J., "Fatigue of Concrete of Constant and Variable Amplitude Loading", American Concrete Institute, Detroit, 1982, pp. 71-110.

[4] Hanson, M., Burton, K.T., and Hognestad, E., "Fatigue Tests of Reinforcing Bars-Effect of Deformation Pattern", Portland Cement Association, 1968.

[5] Balazs, G.L., "Fatigue of Bond", ACI Materials Journal, Nov.-Dec., 1991.

[6] Hawkins, N.M., "Fatigue Characteristics in Bond and Shear of Reinforced Concrete Beams", SP-41, Fatigue of Concrete, American Concrete Institute, Detroit, MI, 1974.

[7] Chang, T.S., and Kesler, C.E., "Fatigue Behavior of Reinforced Concrete Beams", Journal of ACI, Aug., 1958.

[8] Kormeling, H.A., Reinhardt, H.W., and Shah, S.P., "Static and Fatigue Properties of Concrete Beams Reinforced with Continuous Bars and with Fibers", ACI Journal, Jan.-Feb., 1980.

[9] AASHTO Standard Specifications of Highway Bridges, 15th Ed., American Association of State Highway and Transportation Officials, Washington, D.C., 1992 (Interims 1993-1995).

[10] AASHTO, LRFD Bridge Design Specifications, 1st Ed., American Association of State Highway and Transportation Officials, Washington, D.C., 1994.

[11] Perdikaris, P.C. and Petrou, M.F., "Code Predictions vs. Small Scale Bridge Deck Model Test Measurements", Transportation Research Record, No. 1290, TRB, Vol. 1, March 10-13, 1991, pp. 179-187.

[12] Perdikaris, P.C., Petrou M.F., and Wang, A., "Fatigue Strength and Stiffness of Reinforced Concrete Bridge Decks", Final Report-FHWA/OH-93/016, Ohio D.O.T., March, 1993.

[13] Petrou, M.F., Perdikaris, P.C., and Duan, M., "Static Behavior of Non-Composite Concrete Bridge Decks Under Concentrated Loads", ASCE Journal of Bridge Engineering, Vol. 1, No. 4, November, 1996, pp. 143-154.

[14] Batchelor, B. deV., Hewitt, B. E., and Csagoly, P., "An Investigation of the Fatigue Strength of Deck Slabs of Composite Steel/Concrete Bridges", Transportation Research Record ,No. 664, TRB, 1978, pp. 153-161.

[15] Perdikaris, P.C., and Beim, S.R., "Design of Concrete Bridge Decks", Final Report-FHWA/OH/RR-88-004, Ohio D.O.T., August, 1988.

[16] OHBDC Highway Bridge Design Code, 2nd Ed., Highway Engineering Division, OHBDC Ministry of Transportation and Communications, Downsview, OHBDC, p. 357, 1983.

[17] Batchelor, B. deV., and Hewitt, B.E., "Are Composite Bridge Slabs Too Conservatively Designed?-Fatigue Studies", Fatigue of Concrete, ACI Special Publication SP4-15, 1974, pp. 331-346.

[18] ACI 318-95 Building Code Requirements for Structural Concrete, American Concrete Institute, Detroit, Michigan, 1995.

Patrick A. Le Delliou,[1] Patrick Sémété,[1] and Salvatore Ignaccolo[2]

FRACTURE MECHANICS ANALYSIS OF CAST DUPLEX STAINLESS STEEL ELBOWS CONTAINING A SURFACE CRACK

REFERENCE: Le Delliou, P. A., Sémété, P., and Ignaccolo, S., "**Fracture Mechanics Analysis of Cast Duplex Stainless Steel Elbows Containing a Surface Crack,**" *Effects of Product Quality and Design Criteria on Structural Integrity, ASTM STP 1337*, R. C. Rice and D. E. Tritsch, Eds., American Society for Testing and Materials, 1998.

ABSTRACT: Some components of the primary loop of a PWR are made of cast duplex stainless steel. This kind of steel may age even at relatively low temperatures, (below 400°C, which is within the temperature range of PWR service conditions), leading to a significant decrease of its toughness. This is why a large research program was initiated on the fracture behaviour of aged duplex stainless steel elbows in France. The main task of this program was to test three 2/3-scale models of aged PWR primary loop elbows. The first two tests (called SEM1 and SEM2) were conducted under in-plane closure bending at 320°C ; the third (called SEM3) was conducted under constant internal pressure and in-plane closure bending at 60°C. The first two elbows contained a semi-elliptical notch machined into the outer surface of one flank, oriented either longitudinally (SEM1 test) or circumferentially (SEM2 test) ; the third elbow contained both notches described above, one on each flank. This paper presents the results of the experiments, the finite element calculations and the ductile fracture mechanics analyses that were performed.

KEYWORDS: fracture mechanics, elbows, duplex stainless steel, surface crack, crack initiation, crack stability, toughness, J-integral, finite element analysis

Introduction

Some components of the primary loop of Pressurized Water Reactors (pump casings, some elbows, pipes, fittings and valve casings) are made of cast duplex stainless steel. Since the beginning of the 1980s it has been known that this kind of steel may age even at relatively low temperatures, (below 400°C, which is within the temperature range of PWR service conditions), due to a microstructural evolution of the ferritic phase. An important consequence of this ageing process is the decreasing of the toughness of the duplex material. It is feared that this embrittlement, associated with the occurrence of casting defects, may increase the risk of failure. This is why an extensive program was set up to determine the criteria of the acceptability of ageing of cast stainless steel components on the primary circuit. An overview of the research program on the fracture behaviour of aged cast duplex stainless components conducted in France is presented in [*1*].

[1] Research engineer, Electricité De France (EDF), Direction des Etudes et Recherches, Département MTC, Les Renardières, 77818 Moret Sur Loing Cedex, FRANCE

[2] Engineer, Electricité De France (EDF), Direction de l'Equipement, SEPTEN, 12-14 avenue Dutrievoz, 69628 Villeurbanne Cedex, FRANCE

One important task of this program was to test three large diameter elbows containing analytical notches (semi-elliptical shape). The first two tests were conducted under in-plane closure bending only, at 320°C [*2*]. For the third test, the elbow was loaded by a constant internal pressure combined with in-plane bending moment at 60°C [*3*]. This paper presents the results of the experiments, the numerical computations and the fracture mechanics analyses that were performed.

Test description

Description of the elbows

The elbows were made of Z3 CND 19-10M duplex stainless steel (French standard equivalent to CF8M). Table 1 shows the elements responsible for the sensitivity of the duplex stainless steel to the thermal ageing phenomenon, chromium, silicium and molybdenum, their sum - the equivalent chromium content Cr* - and the δ ferrite content.

TABLE 1--*Chemical composition of the elbow steels (by weight %).*

Material I.D.	C	Si	Mn	Ni	Cr	Mo	Cr*	δ ferrite
SEM1	0.027	1.13	1.03	10.00	21.70	2.72	25.5	34.7
SEM2	0.027	1.19	1.07	10.15	21.95	2.71	25.8	35.6
SEM3	0.044	1.23	0.95	10.20	22.30	2.73	26.3	33.5

The elbows were thermally aged at 400°C for 3 000 hours (SEM1 and SEM2 tests) or 1 000 hours (SEM3 test), prior to the bending test. Their chemical composition led to fast thermal ageing and low toughness, equivalent to, or lower than, the end-of-life properties of in-service cast duplex stainless steel components.

Their dimensions are as follows :
- outer diameter : 580 mm
- thickness : 44 mm
- bend radius : 900 mm
- bend angle : 90 degrees.

The elbows in the first two tests contained a semi-elliptical notch on the outer surface of one flank and were loaded under in-plane closure bending. For the SEM3 test, the elbow contained both cracks described above (one on each flank) and was loaded with constant internal pressure of 15.5 MPa and under in-plane closure bending. In each case, the crack was located so that it was submitted to tensile stresses. The characteristics of the notches are given in Table 2 and are represented in Fig. 1.

The notches were manufactured by electric discharge machining and were not fatigue sharpened. The effect of using blunt notches instead of sharp cracks was investigated on CT specimens. No significant notch radius effect could be found.

TABLE 2--*Characteristics of the machined notches.*

Test I.D.	Notch location	Notch orientation	Length 2c (mm)	Max. depth a (mm)	c/a ratio
SEM1	Flank	Longi.	210	10.5	10
SEM2	Near flank[a]	Circum.	88	14.7	3
SEM3	Flank	Longi.	210	10.5	10
SEM3	Near flank[a]	Circum.	88	14.7	3

[a] 15° towards extrados

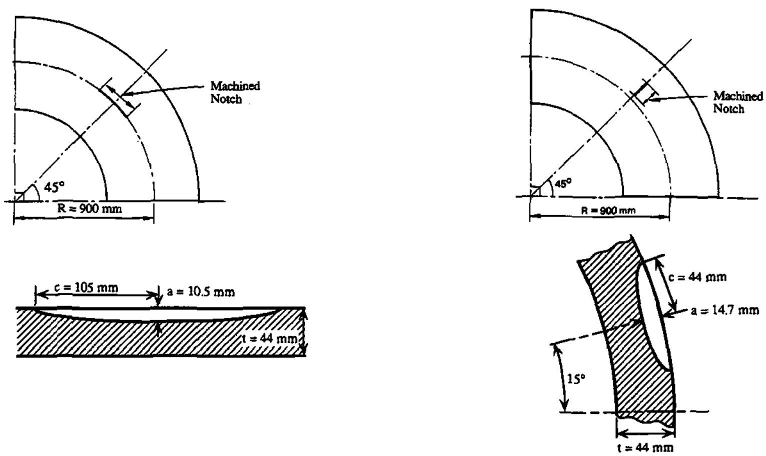

SEM1 and SEM3 tests
semi-ellipse : c/a = 10 a/t = 1/4

SEM2 and SEM3 tests
semi-ellipse : c/a = 3 a/t = 1/3

FIG. 1--*Notch location and shape.*

Description of the test conditions

The experimental installation used to perform the tests - called "SEM" - is shown in Fig. 2 : one end of the elbow is fixed to a rigid welded frame embedded in the ground, the other one is fitted with a 6-m long straight pipe used as a moment arm. The moment loading is generated by pulling on the arm pipe with a long stroke ram. The bending load was applied at a quasi-static rate, with the displacement rate of the ram at 2 mm/min. The length of the arm pipe remained constant during the tests because the loading saddle was allowed to slip under the mobile frame.

For the first two tests, two connecting pipes were inserted ; one between the elbow and the arm pipe and the other between the elbow and the flange. For the SEM3 test, in addition to the moment loading an internal pressure was applied, and two flat heads were inserted ; one between the elbow and the flange (replacing the lower connecting pipe) and the other one between the upper connecting pipe and the arm pipe. The water inside the elbow, was first pressurized up to 15.5 MPa, then the bending moment was applied in the manner described above.

In the first two tests, the elbow and the connecting pipes were heated to 320°C, while for the SEM3 test, the elbow, the flat heads, and the connecting pipe were maintained at 60°C.

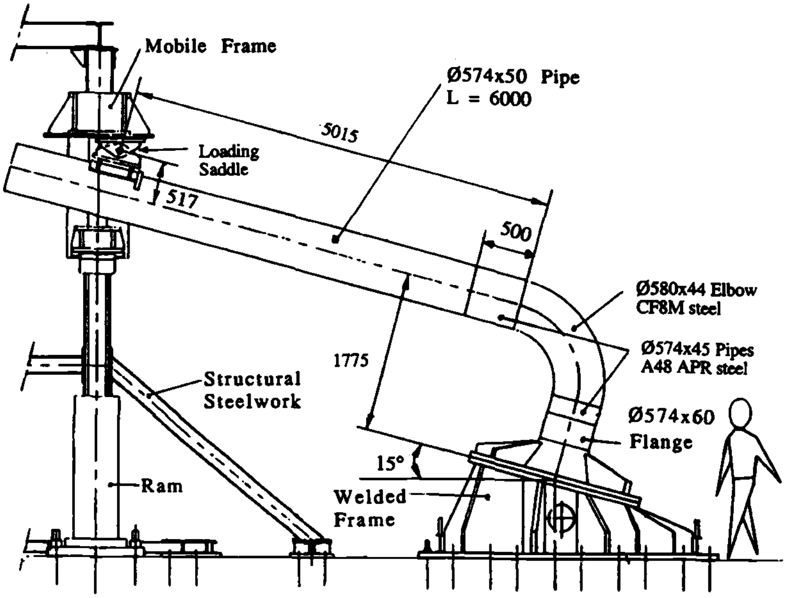

FIG. 2--*Schematic drawing of the test installation (first test configuration).*

Material data

For the elbows, the material characterisation program included chemical analysis, tensile tests and J-resistance curves determined on 1T-CT specimens (thickness : 25 mm) with 20 % side grooves.

The connecting pipes, the flat heads, the arm pipe, the flange, and the loading saddle were made of carbon steel. For the elbows, the connecting pipes and the flat heads which exhibited plasticity, conventional tensile properties are given in Table 3 and true stress - true strain curves are shown in Fig. 3. For the other components (flange, loading saddle and arm pipe) which remained elastic during the tests, only the Young's modulus is given in Table 3.

J-resistance tests (at 320°C for SEM1 & 2 and 60°C for SEM3) on aged 1T-CT specimens gave the values of $J_{0.2}$ (value of J for 0.2 mm of crack extension) and a J-R curve fitted with a power-law, $J = C(\Delta a)^n$. The multiple specimen technique was used to produce the data. For the first two elbows, three kinds of CT specimens were used : specimens without fatigue-precracking sampled on elbow with C-A orientation, specimens without fatigue-precracking with C-R orientation and finally, fatigue precracked specimens with C-R orientation. It was not possible to observe either notch radius effect or orientation effect because of the wide scatter observed on this type of material. For the third test, specimens without fatigue precracking sampled on C-A orientation were used.

TABLE 3--*Mechanical properties of the three test materials.*

Material I.D.	Test temperature (°C)	Young's modulus (MPa)	0.2% offset yield strength (MPa)	Ultimate tensile strength (MPa)
SEM1 cast elbow	320	176 500	258	670
SEM2 cast elbow	320	175 500	259.5	662
SEM3 cast elbow	60	188 000	321	743
Connecting pipes SEM1 & 2	320	188 000	223	545
Connecting pipe SEM3	60	201 000	278.4	...
Flat heads - SEM3	60	201 000	460	...
Arm pipe SEM1 & 2 & 3	20	204 000	...	...
Flange SEM1 & 2	320	183 000	...	...
Flange - SEM3	60	201 000	...	...
Loading saddle SEM1 & 2 & 3	20	204 000	...	...

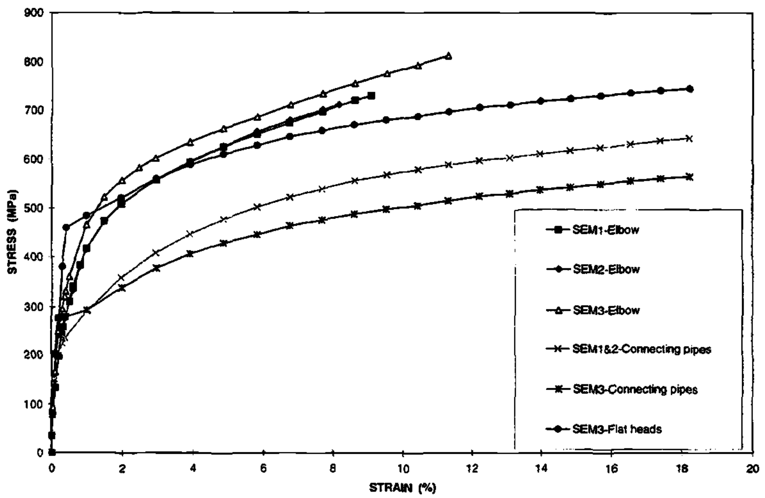

FIG. 3--*True stress - true strain curves for SEM1, SEM2 and SEM3 tests.*

The J-R curves exhibit some scatter and a statistical analysis of the data was used to produce the results given in Table 4, where C and n are the parameters of the power-law fit. The scatter is related to the coarse solidification macrostructure of cast duplex steel.

TABLE 4--*Toughness properties of the three elbows.*

Material I.D.	Test temperature (°C)	$J_{0.2}$ mean value (kJ/m^2)	C mean value (kJ/m^2)	n mean value (Δa in mm)
SEM1 cast elbow	320	68	97.2	0.2497
SEM2 cast elbow	320	51	66.6	0.1796
SEM3 cast elbow	60	56	84.13	0.2698

Test results

During the tests, the machined notches were submitted to tensile stresses, so that they initiated and subsequently grew by ductile tearing. The direct-current electric potential method permitted the interruption of the test when a large amount of stable crack growth was reached. The final crack extension reached 8 mm (SEM1 test), 13 mm (SEM2 test), 2.6 mm (SEM3 test, circumferential notch) and 6 mm (SEM3 test, longitudinal notch).

During the tests, a variety of measurements were made : applied load, ram displacement, elbow diameter variations (for ovalization), structure rotation (with inclinometers), CMOD in several points along the crack length, and strains in the elbow mid plane. The electric potential drop method was used to detect crack initiation and to conduct the tests, in order to obtain a given amount of stable crack extension.

Applied load versus ram displacement curves are shown for the three tests in Fig. 4, where Fy and Uy are, respectively, the applied load and the displacement of the loading point normal to the moment arm. The first two tests curves are very close together, due to the similarity of the stress-strain curves (see Fig. 3). This proves that the effect of the notch on the global load versus displacement curve is quite limited. The third test curve is higher than the others, because the internal pressure and the flat heads limited the ovalization of the elbow, and also because the lower test temperature (60°C instead of 320°C) increased its stress-strain curve.

Figure 5 shows the evolution of the center-crack electric potential drop versus ram displacement and the location of the crack initiation point for the three tests. Table 5 shows the main results of the three tests. The moment is evaluated in the mid-section of the elbow, taking into account the moment induced by the dead weight of the structure.

TABLE 5--*Main results of the tests.*

Test I.D.	Crack initiation Fy (kN)	End of test Fy (kN)	End of test moment (kN.m)	End of test Δa (mm)
SEM1	363 / 378	448	2705	8
SEM2	336 / 353	483	2900	12
SEM3	365 / 391 (longi. notch)	531	3150	6.3 (longi. notch)
SEM3	405 / 426 (circum. notch)	531	3150	2.6 (circum. notch)

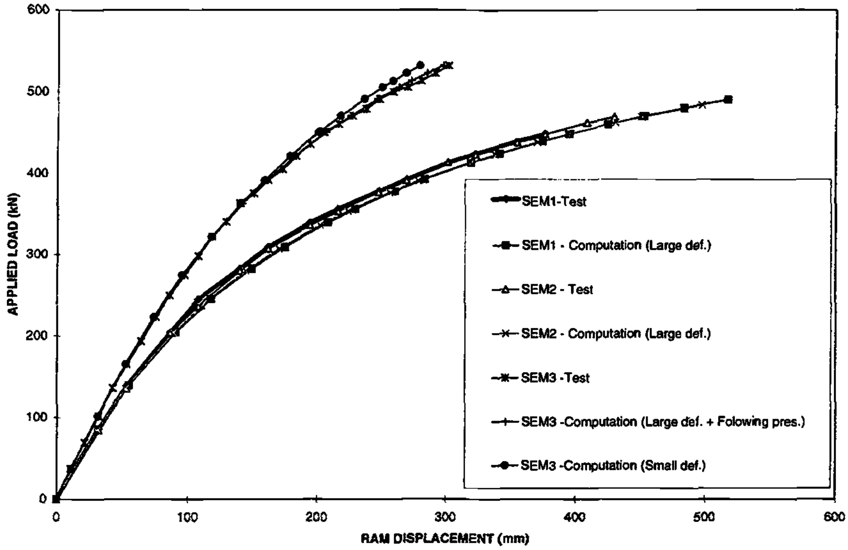

FIG. 4--*Applied load versus ram displacement curves.*

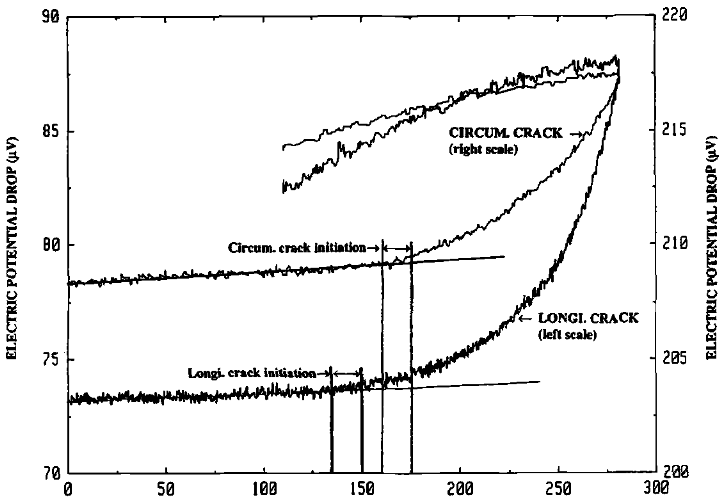

FIG. 5--*Electric potential drop versus ram displacement curves (SEM3 test).*

For the crack examination, the notch area was cut away from the elbow, then thermally marked, cooled in liquid nitrogen to ensure brittle fracture, and finally broken open. The final crack shape was measured optically and, because of its irregular shape, was smoothed by a semi-ellipse for the purpose of the analyses. The final shapes that were obtained for the three tests are shown in Fig. 6 and 7.

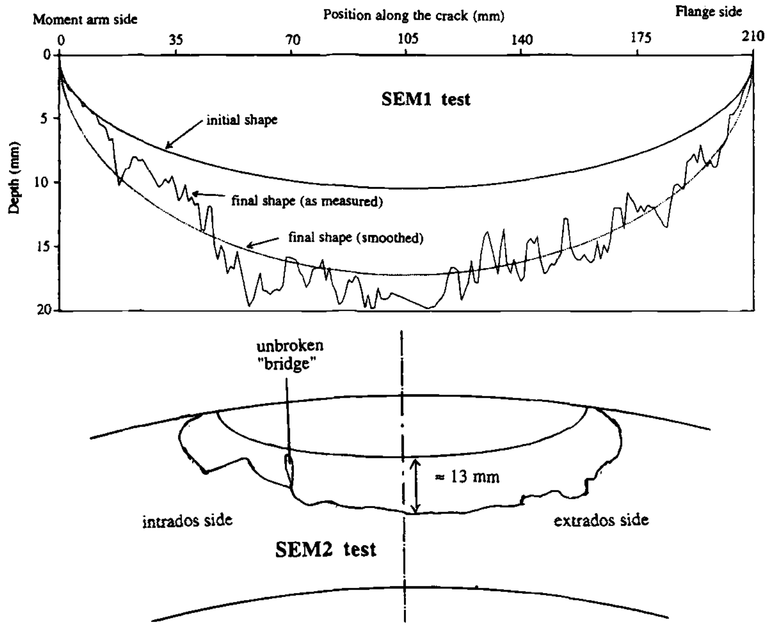

FIG. 6--*Final crack shapes (SEM1 and SEM2 tests).*

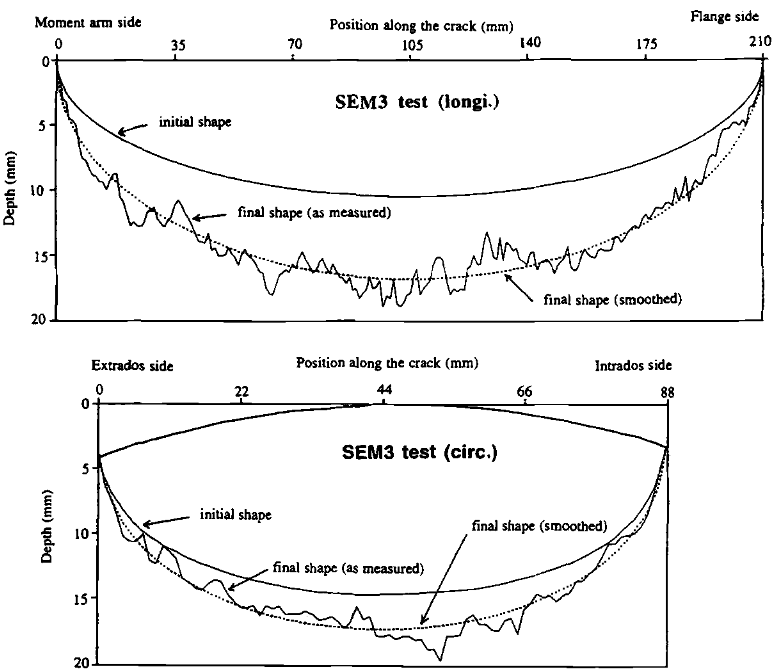

FIG. 7--*Final crack shapes (SEM3 test).*

Numerical analysis

Description of the FE models

The aim of the computations was to show their ability to accurately simulate the tests by conducting systematic comparisons of the results of the experiments and the calculations. The calculations were made with the FE program named *Code_Aster®* [*4*].

The meshes of the tested structures were built up with solid elements (15 and 20 node elements) and, in addition for the third test, with shell elements (6 and 8 node elements) in order to apply internal pressure. A normal integration scheme was used.

The meshes were built from a cracked block (see Fig. 8) which is characterised by a refinement relevant to fracture mechanics analyses. Due to the small size of the notch, it was assumed that its presence had no influence on the global behaviour of the structure (in terms of load versus displacement curve). This was verified by an elastic-plastic computation of the uncracked structure and by the test results (see previous paragraph). Therefore, the FE model was limited to the half structure containing the notch (this means that the corresponding full model actually has two symmetrical cracks). The third test mesh included the flat heads as shown at the top of Fig. 8. The meshes of the three (half) test structures contained from 12 000 to 16 000 nodes.

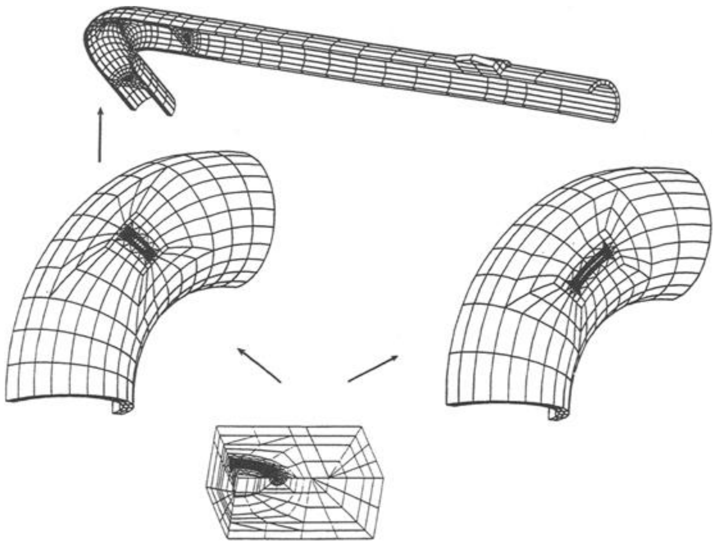

FIG. 8--*View of the finite element mesh (SEM3 test).*

Global behaviour of the tested structure

In this section, the global behaviour of the structure is assessed in terms of load versus ram displacement curves (Fig. 4).

The investigations that were carried out during the first calculations allowed for improvement of the model. It was verified than the large displacement formulation gave better results than the small displacement, because it takes into account the effect of softening due to the elbow ovalization. The dead weight of the moment arm was also included in the loading conditions because its contribution to the moment is significant (about 160 kN.m).

For the third test, the application of internal pressure on the updated geometry, within the framework of the large displacement formulation, provided another improvement for the global behaviour simulation. However, in this particular case, the internal pressure and the flat heads limited the elbow ovalization, so that the small displacement formulation also gave very good results. Finally, as shown in Fig. 4, the similarities between experimental and numerical load-versus-ram displacement curves are stricking for the three tests.

Crack initiation evaluation

The crack initiation evaluation was done by comparing the toughness $J_{0.2}$ measured on CT specimens to the energy-release rate G in the center of the crack, calculated for the experimental initiation load.

The 3-D energy-release rate was calculated using the G-THETA method [*5*, *6*]. A new formulation for this parameter G was developed to be consistent with the "large deformation" option [*7*], and was used for the first two test computations. For the third test, G was computed with the small displacement formulation.

In all three tests, the crack initiation is well predicted, falling each time in the scatter band of the parameter $J_{0.2}$. The overall accuracy of the analysis is actually limited by the scatter on the J material data. Those results are presented in Fig. 9 for the longitudinal and the circumferential cracks of SEM3 test ; the figures relative to SEM1 and SEM2 can be found in [*2*]. Fig. 9 shows that, until the initiation load is reached, the G value is higher for the longitudinal crack than for the circumferential. This is quite consistent with the test results where the longitudinal crack initiated first. Formally, this calculation with the initial crack mesh is no longer valid once the crack begins to propagate. Therefore, the computations with deeper cracks (accounting for crack growth) presented in the following paragraph will confirm that during this third test the longitudinal crack grew faster than the circumferential one.

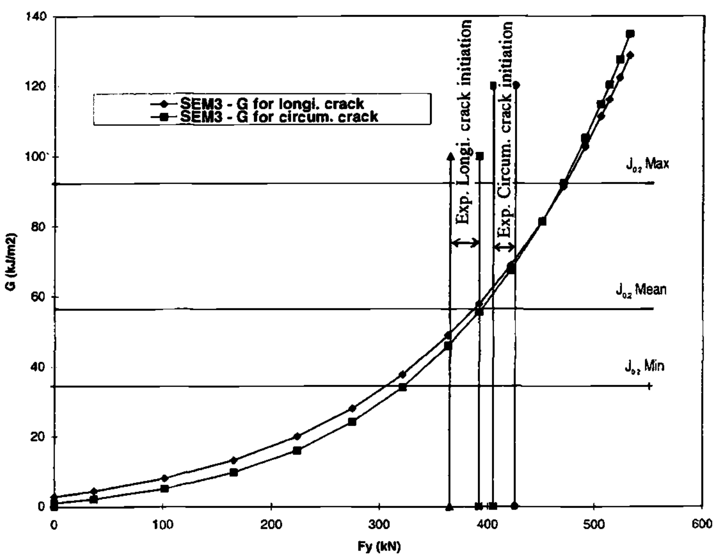

FIG. 9--*G versus applied load curves (SEM3 test).*

Crack growth evaluation

The evaluation of the crack propagation is made by comparing "applied J" curves to the material J-R curve obtained on CT specimens. The "applied J" curves are obtained by considering different crack depths. For each crack, besides the initial depth, the final depth measured at the end of the test and an intermediate value were used (Table 6). The numerical simulation of the crack growth was modelled by remeshing.

TABLE 6--*Cracks depths used for the calculations.*

Test I.D.	Initial depth a (mm)	Intermediate growth Δa (mm)	Final growth Δa (mm)
SEM1	10.5	4	8
SEM2	14.7	6	12
SEM3 (longi. notch)	10.5	3	6
SEM3 (circum. notch)	14.7	1.3 and 2	2.6

The material J-R curves were extrapolated beyond 3 mm (which is the validity limit for 1T-CT specimens) with the same power-law fit as the one determined within the validity range (Table 4). For each material, three curves were assessed : a "mean" curve, a "minimum" curve (-2 σ) and a "maximum" one (+2 σ).

The results of the crack growth evaluation are shown in Fig. 10 for the longitudinal notch of the SEM3 test and in Fig. 11 for the circumferential one ; the figures relative to SEM1 and SEM2 can be found in [2].

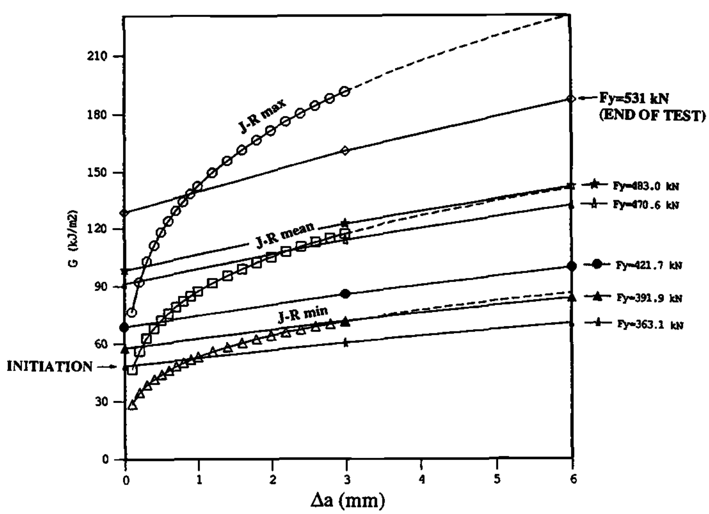

FIG. 10--*Crack growth analysis (SEM3 test - longitudinal crack).*

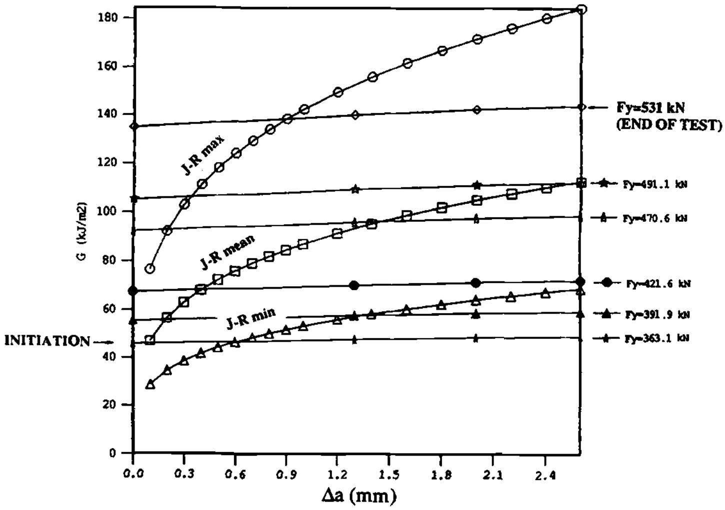

FIG. 11--*Crack growth analysis (SEM3 test - circumferential crack).*

For the SEM1 test, the numerical prediction is conservative with the "mean" J-R curve (the calculated load Fy = 413 kN corresponding to the final crack extension of 8 mm is lower than the end-of-test experimental load Fy = 448 kN) and agrees well with the "maximum" J-R curve. On the other hand, for the SEM2 test, the prediction is very conservative, even with the "maximum" J-R curve. The reason for this difference between both tests is probably related to the "constraint" effect, the through-wall stress distribution being mostly a bending one for the SEM1 test (like in the CT specimens) and a membrane one for the SEM2 test. However this explanation must remain qualitative, considering the uncertainty coming from the scatter and the power-law extrapolation of the J-R data.

For the longitudinal notch of the SEM3 test (Fig. 10), the prediction is conservative with the "mean" J-R curve : the calculated load (483 kN) corresponding to the final crack extension of 6 mm is lower than the end-of-test experimental one (531 kN). For the circumferential notch of the SEM3 test (Fig. 11), the prediction is also conservative with the "mean" J-R curve : the calculated load (491 kN) corresponding to the final crack extension of 2.6 mm is lower than the end-of-test experimental one (531 kN).

Conclusions

Three bending tests were performed on large diameter aged cast duplex stainless steel elbows containing either one or two semi-elliptical notches on the outer surface of the flank. The first two elbows were loaded under in-plane closure bending moment, while the third was loaded by an in-plane closure bending moment combined with an internal pressure of 15.5 MPa.

The tests showed that it was possible to obtain a large amount of stable crack growth (up to 13 mm) despite the low toughness of the aged material. Owing to the efficiency of the d-c electric potential drop method, the crack initiation was accurately detected and the final crack extension was correctly estimated.

The finite element analyses of the three tests accurately simulated the global behaviour of the tested structure, and gave in each case a good prediction of the crack initiation. The crack growth analysis was conservative, compared with the experimental results. Three reasons are proposed to explain this fact : the scatter of the J-R data, the extrapolation of J-R curves from standard CT specimens to longer crack extension, and a constraint effect in the ligament.

These tests contribute to the integrity assessment of in-service cast duplex stainless steel components. First, they have proven that even in low toughness aged steel, the propagation of a large crack remains stable after a large amount of tearing (5 to 10 mm). Secondly, they have shown the accuracy and the conservatism (this means being on the safe side) of flaw assessment analysis by 3-D finite element calculations.

Work is on-going to study the mechanical behaviour of casting defects [*8*], in order to assess the conservatism and the soundness of current safety analyses, where casting defects are modelled by envelope semi-circular surface cracks (radius of 20 mm).

References

[1] Massoud, J. P., Jayet-Gendrot, S., et al., "Thermal ageing of cast duplex stainless steel primary components. Overview of the research program conducted by EDF", *Proceedings* of Icone-5, Nice, May 26-30, 1997, paper #2497.

[2] Le Delliou, P., Sémété, P., and Ignaccolo, S., "Fracture mechanics analysis of cast duplex stainless steel elbows containing a surface crack", *Proceedings* of the 1996 PVP Division Conference, Vol. 323, pp 117-123.

[3] Sémété, P., Le Delliou, P., and Ignaccolo, S., "Fracture resistance of cracked duplex stainless steel elbows under bending with or without internal pressure", *Proceedings* of the 1997 PVP Division Conference, Orlando, Vol. 350, pp 117-127

[4] *Code_Aster®* Version 3, Report HI-75/96/073 (information brochure in French), EDF, Research and Development Division.

[5] Suo, X. Z., and Combescure, A., "On the application of G(θ) method and its comparison with De Lorenzi's approach", *Nuclear Engineering and Design*, 1992, Vol. 135, pp. 207-224.

[6] Wadier, Y., and Malak, O., "The THETA method applied to the analysis of 3-D elastic-plastic cracked bodies", *Transactions* of the 10th International Conference on Structural Mechanics in Nuclear Technology (SMIRT), Vol. G, pp. 13-18, Anaheim, August 1989.

[7] Mialon, P., and Visse, E., "An energy release rate formulation for large deformation problems" (in French), *Proceedings* 2ème Colloque National en Calcul des Structures, Giens, France, May 1995, Vol. 1, pp 89-94.

[8] Jayet-Gendrot, S., Gilles, P., and Migné, C., "Behaviour of duplex stainless steel casting defects under mechanical loadings", *Proceedings* of the 1997 PVP Division Conference, Orlando, Vol. 350, pp 107-116.

Roy T. Watanabe[1], Troy D. Scheumann[2]

STRUCTURAL INTEGRITY CRITERIA FOR COMMERCIAL TRANSPORT AIRCRAFT

REFERENCES: Watanabe, R. T. and Scheumann, T. D., "**Structural Integrity Criteria for Commercial Transport Aircraft,**" *Effects of Product Quality and Design Criteria on Structural Integrity, ASTM STP 1337,* R. C. Rice and D. E. Tritsch, Eds., American Society for Testing and Materials, 1998.

ABSTRACT: The criteria and procedures used to develop and maintain commercial transport aircraft have produced long-life structure with credible service records. These criteria have evolved over time and address a multitude of regulatory and manufacturer-specific requirements to ensure long-term structural integrity of these aircraft. Structure designed to meet these requirements must balance detail design, manufacturing processes, and ease of maintenance, and must be expected to operate at high stresses because of weight objectives. Static strength requirements ensure that any failure due to static overload is unlikely. Operator service period expectations are met with durability requirements, while detection of damage prior to compromising structural safety is ensured by damage tolerance and fail-safety criteria.

The evolution of structures design criteria is briefly reviewed with major focus on current guidelines for structural durability and damage tolerance.

KEYWORDS: fail-safe, durability, damage tolerance, detectability, inspection program, airworthiness initiatives.

Design of structures is an interactive process aimed at achieving a practical balance between state-of-the-art structural capability and the intended usage requirements. These capabilities and requirements are typically addressed through a disciplined design process that includes design requirements, methods and analysis, databases and validation tests.

Modern airplanes operate under a complex combination of operating conditions, environments, and economic requirements. Aircraft structural components are designed to

[1]Manager, Structural Damage Technology, Boeing Commercial Airplane Group, Seattle, WA 98124-2207
[2]Structures engineer, Boeing Commercial Airplane Group, Seattle, WA 98124-2207

specific static and dynamic loading conditions, deformation, and functional criteria. Operating service loading criteria for design and verification of durability and damage tolerance are equally important. With structural weight an important parameter, fatigue and consequent cracks have been a continuous challenge for the airplane industry.

Structural integrity criteria for aircraft structure have evolved as new technologies have been proven by extensive verification tests and accumulation of operating experience. Both regulatory and manufacturer-specific requirements have shaped the way in which airplane structure is designed today. This review is focused on the evolution of structural integrity criteria, in particular durability and damage tolerance principles.

Static Strength Criteria

Structural design criteria to ensure structural strength in the absence of accidental, corrosion, and fatigue damage are based on design limit loads for maneuvers, gust, and ground-loading conditions. These requirements were implemented very early in aviation history and are still in use today.

Regulations [*1*] require the manufacturer to demonstrate that the airplane structure is capable of carrying the design limit load without causing detrimental permanent deformation of the structure and that it will not fail at ultimate load, which is commonly 150% of limit load. The strength limitations of an airplane are presented in the form of envelope conditions that relate load factor (n) to airspeed (V). A typical case is shown in a V-n diagram (fig. 1). The applicant for certification must also satisfy regulatory requirements to ensure that specified conditions are met.

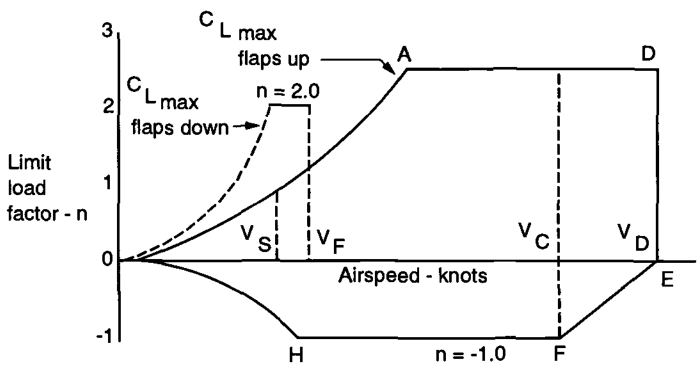

FIG. 1—*Design Loads Are Based on Load Factors*

Proof of structural integrity and safety is typically established by analysis and supported by structural test results. There is very little regulatory guidance given on stress analysis methods for structures subjected to these loads. Such analysis tools have evolved based on cumulative experience to a point where it is exceptional for airframes not to attain design limit/ultimate load levels in full-scale verification tests. Test verification has historically been based on a "building-block" approach, as shown in figure 2. These tests range from small "coupon" tests used for developing material property data, to structural elements such as fuselage stringers, to subcomponents like the wing upper surface panel, to components including major fuselage sections, to full-scale airplane tests.

The full-scale static test consists of a structurally complete airframe subjected to numerous design loads in order to meet certification requirements and verify structural analysis methods. Static validation tests often occur simultaneously with a flight test program. Initially, temporary operating limitations are imposed on the flight test airplanes that limit the operating envelope to a percentage of the design limit loads. Flights in these critical test conditions are permitted only after certain static tests successfully prove the structure can withstand the design limit loads.

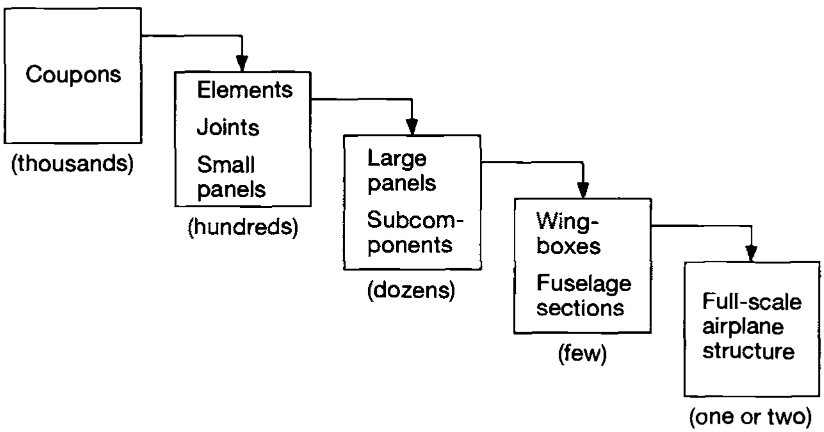

FIG. 2—*Structural Test Building Block Approach*

Safe-Life Philosophy

The capability of transport aircraft advanced significantly during World War II, spawning a revolution in commercial air travel shortly after peace was declared. With extended use of essentially wartime designs in the 1950s, it became clear that static strength criteria had to be supplemented by estimated replacement times for some critical structural elements.

In the pursuit of high performance, the use of high-strength aluminum alloys without corresponding increase in fatigue strength produced an environment where fatigue failures could occur. Further compounding the problem were improved stress analysis methods which often eliminated past hidden static strength margins. The knowledge of actual operating conditions also became more extensive, providing more precise static strength load conditions based on rational ultimate design conditions. Reliance on safe-life policies, where fatigue was controlled by limited service lives for components in early commercial airplanes, was to some degree successful. This was primarily due to rapid technology developments rendering airplanes obsolete before serious challenges of the established life limits.

As important lessons were learned, fatigue test requirements emerged. Repeated load testing was, for instance, performed on the Comet I in 1950. It was also recognized through experience that first defects in the fleets could occur at a fraction of the test demonstrated life. The use of imprecise and inaccurate fatigue analyses coupled with inherent material scatter characteristics often resulted in unnecessarily short lives, and many sound structures were retired prematurely. The overall problem with the safe-life principles was, indeed, that an acceptable commercial airliner safety standard could not be economically achieved

Today, safe-life design principles are typically limited to ground-loaded structure, such as high-strength landing gear steel components, for which substantial fatigue test verification is required.

Fail-Safe Design

The industry addressed the inherent problems of the safe-life principles by adoption of fail-safe concepts in the late 1950s. The containment of potential structural failures was the goal of fail-safe design. Considerable testing was conducted to verify design concepts. Fail-safe structures achieved safety levels equivalent to prudent safe-life designs more economically, but specific limits on the maximum risk that eventually would be experienced were not quantified.

Structural fail-safety is the ability of a critical component to maintain design load capability and functionality with (a) one of its elements completely failed or (b) with an obvious partial failure of a single element. This design envelope criteria was intended to represent more critical conditions than would normally be encountered by partial failures and adjacent structural cracking. To ensure safety by timely detection of structural damage, the damaged structural element must be detectable by in-service observations. The primary means of achieving fail-safety relied on multiple structural members with established strength requirements for failure of a single structural element or an obvious partial failure. Fail-safe verification was typically based on static strength evaluations for different structural member failures scenarios.

The concept of redundancy has stood up well for these types of damage. In terms of fatigue damage, particularly in cases of aging airplanes, structural redundancies are not always effective because of damage at multiple sites. Back-to-back fittings may have excellent structural capability if one element is accidentally damaged and/or impaired by corrosion, whereas crack initiation in adjacent, redundant members is likely and similar unless the elements are totally independent or significantly different. Thus, accepting the existence of the circumstances that necessitated redundancy also means accepting that the redundancy may not be very effective in some instances to provide structural reliability.

Another universally accepted means of achieving fail-safety is by the incorporation of crack-arresting features into the design of the structure. In the strictest sense, crack-arrest capability is the ability of a structure to stop a dynamically propagating crack in a single element before that element completely fractures. A practical definition of crack arrest, however, is the ability of a structure to significantly slow down the growth rate of a propagating crack. This is achieved when the geometric features of the structure result in a drop in the stress intensity factor at the crack tip as the crack increases in length. Some examples of these features include tear straps and padded-up skins. Ideally, the length of the crack should be large enough to detect during the period of time for which its growth is retarded. This provides adequate time for detection of such damage.

Experience has shown that the fail-safe design philosophy has generally been effective in allowing sufficient opportunities for timely detection of structural damage. However, failure modes were not always predicted with sufficient accuracy to ensure that structural failures would be obvious and within safety limits. Further, structural failures could progress in unanticipated ways and a number of older airplanes were found with quite unexpected defects.

Damage Tolerance and Durability

The design approach in the 1950s and 1960s was essentially based on multi-structural member concepts, with strength requirements for the failure or obvious partial failure of a single structural element. These fail-safe design concepts, supported by considerable testing, have worked well in the past and required diligent performance by the designer/manufacturer, operators, and regulatory agencies for continued safe operation. Fatigue analyses and tests provided indications of early, unexpected cracking requiring modifications to ensure a long economic service period. It was the responsibility of the operators to provide continuous vigilance of airplane structure to detect and report damage, and to perform prompt repairs as required.

By the 1970s it was clear that airline operators were sometimes expected to find cracks that were difficult to detect, and inspection planning was recognized as a safety issue. This prompted industry and airworthiness authorities to focus more on the adequacy of inspection programs for timely detection in support of fail-safe principles. Combined industry and airworthiness authority activities in the late 1970s resulted in changes to the regulatory requirements to reflect state-of-the-art developments. In addition to residual strength evaluations, damage growth and inspection requirements with considerations of damage at multiple sites were incorporated in FAR/AC 25.571, Amendment 45 [*1*] for new airplanes (fig. 3), and in CAA Notice 89 and AC 91-56 for development of supplemental inspections of aging airplanes.

A multitude of design considerations are involved in achieving structural integrity in commercial aircraft, and structural design objectives must be currently satisfied jointly by:

Damage tolerance—Ability of structure to sustain anticipated loads in the presence of fatigue, corrosion, or accidental damage, until such damage is detected through inspections or malfunctions and repaired.

Analysis	FAR 25.571 (before 1978)	FAR 25.571 (after 1978)
Residual strength	• Single element or obvious failure 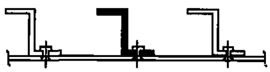	• Multiple active cracks 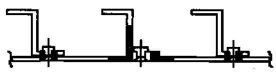
Crack growth	• No analysis required	• Extensive analysis required
Inspection program	• Based on service history • FAA air carrier approval 1	• Related to structural damage characteristics and past service history • Initial FAA engineering and air carrier approval

1 Supplemental damage tolerance inspection. Performed per AC91-56.

FIG. 3—*Damage Tolerance Regulation Comparison*

Durability—Ability of the structure to sustain degradation from such sources as fatigue, accidental damage, and environmental deterioration, to the extent that they can be controlled by economically acceptable maintenance and inspection programs.

Interaction between structural damage tolerance and durability characteristics must be recognized in design, manufacturing, and operation of modern jet transports. While these aspects are difficult to separate entirely, damage tolerance is primarily governed by minimum certification requirements jointly developed by the manufacturer, operator, and the regulating agency. Durability characteristics of damage tolerant structures mainly influence the economics of in-service operation, maintenance, and repair, and are dictated by the requirements of a competitive international market.

Damage tolerance is the present method of achieving structural operating safety. The damage tolerance method provides for damage detection prior to loss of structural integrity by employing up to three separate but related technologies, as shown for structural Category 3 (fig. 4). The structural categories are shown in descending order of preference whenever a practical design choice is available. Safe-life is restricted to structure that cannot be designed as damage tolerant, and usually employed for landing gear structure. Adequate contributions from all elements are usually required to achieve the desired level of damage tolerance. The best design has safety provided by structural characteristics and requires only a small contribution from inspections (fig. 5). In extreme cases, where these elements combined provide insufficient contributions, a safe-life classification is the only alternative.

Structural category			Technique of ensuring safety	Safety analysis requirements	Structural classification examples
Other structure	Damage tolerant design	1 Secondary structure	Design for loss of component or safe separation	• Continued safe flight	Wing spoiler segment (safe separation or safe loss of function)
Structurally significant items or principal structural elements (primary structure)	Damage tolerant design	2 Damage obvious or malfunction evident	Adequate residual strength with extensive damage obvious during walkaround or indicated by malfunction	• Residual strength	Wing fuel leaks
	Damage tolerant design	3 Damage detection by planned inspection	Inspection program matched to structural characteristics	• Residual strength • Crack growth • Inspection program	All primary structure not included in categories 2 or 4
	Safe-life design	4 Safe life	Conservative fatigue life	• Fatigue	Landing gear structure (conservative fatigue life)

FIG. 4—*Categories of Structure*

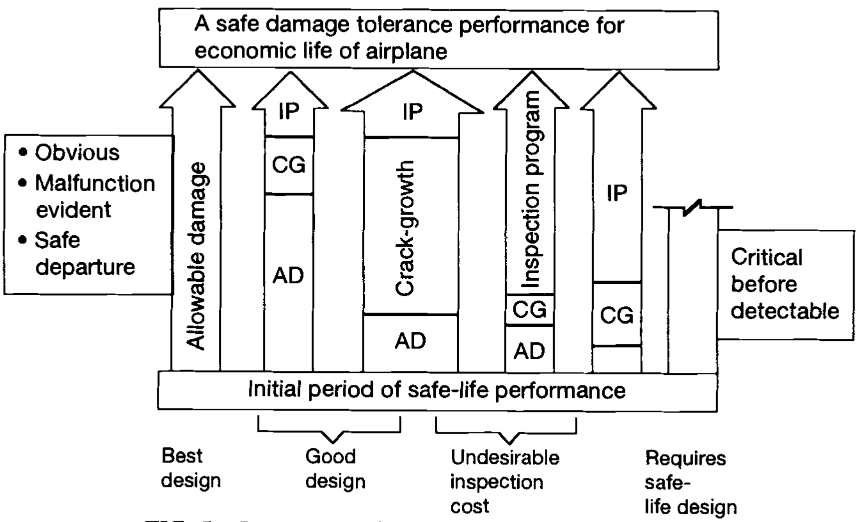

FIG. 5—*Interaction of Damage Tolerance Elements*

The key element of damage tolerance is the ability to detect damage, shown schematically as detection opportunities in figure 6. A short crack growth period with high detectability can provide as many opportunities for damage detection as a long crack growth period with low detectability. Damage tolerance comprises three distinct elements of equal importance for achieving a desired level of safety:

Allowable Damage is the maximum damage, including multiple secondary cracks, that the structure can sustain under fail-safe load conditions. Linear elastic fracture mechanics theory is relied upon for a comparison of calculated stress intensities in cracked structure with material fracture toughness properties. This theory is widely used on aircraft structure, supplemented by an inventory of fracture toughness and standard stress intensity solutions. Methods based on elastic plastic elongation and allowables are used for details where this theory does not apply.

- Structure is damage tolerant when damage, if it should occur, will be discovered and repaired before residual strength falls below specified levels.

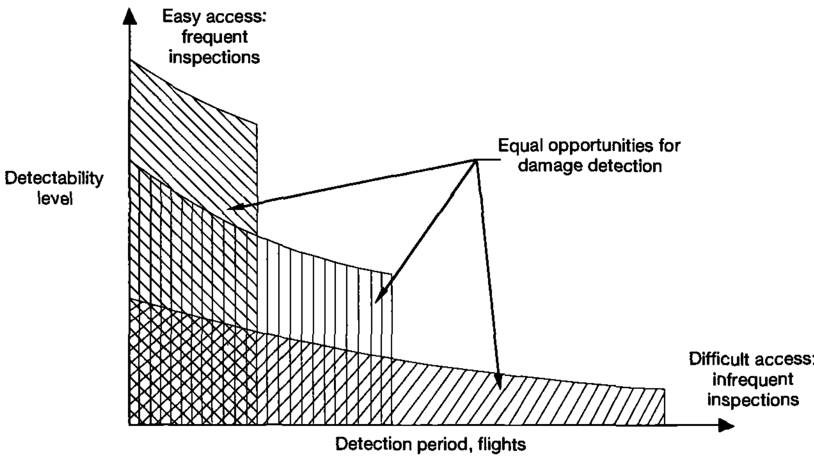

FIG. 6—*Opportunities for Damage Detection*

Damage Growth Period is the interval in which damage progresses from a detectable threshold to maximum allowable, based on proper recognition of operating service loads, load sequencing, and environmental effects. The basis of assessing crack growth is the crack growth rate data which permits separation of the three influences affecting crack growth; namely, cyclic stresses, material properties, and detail geometry. The cyclic stress analysis is based on an expansive inventory of fleet-recorded data and is readily performed by computer. Material crack growth rates are adjusted for various aircraft environments. The influence of detail can be derived from known stress intensity solutions to reflect the unique behavior of a structural configuration.

Inspection Programs define a sequence of inspections in a fleet of aircraft, with methods and frequencies aimed at timely damage detection. Structural inspections are required for both safety and timely economic repair. The discussion here is limited to the inspections necessary to maintain safety of damage tolerant structure. The key to inspection program evaluation methods is matching the inspection to the structural characteristics. These characteristics have such a wide range that the required type of inspections can vary from casual observations during routine maintenance to intensive NDT techniques at frequent intervals. The inspection program evaluation methods are classified as a technology because of the complexities of fleet operations. A key objective of this evaluation is to determine the probability of damage detection within a safe period, and is measured as an equivalent number of opportunities for damage detection. Inspectability and accessibility characteristics of the structure must be such that general visual methods of damage detection can be confidently employed for the majority of the structure. Directed inspections, involving sophisticated damage-detection equipment, may be acceptable in areas where inaccessibility dictates infrequent inspections.

It is important to recognize that all structure, whether classified as safe-life or damage tolerant has a limited period of safe performance. Several combinations of the primary damage tolerance parameters can provide safety beyond this initial service period. If allowable damage is obvious in terms of detection prior to flight, or permits safe operation for the remainder of a flight, there is no need for additional damage growth substantiation and inspection program analysis. Examples of this case would be foreign object impact, with the fuselage resulting in controlled decompression, or splice-to-splice wing skin damage with extensive fuel leakage.

Early jets were very successful, and offered long, useful service periods. This kept efforts to prevent fatigue cracking as a primary design consideration. Fatigue evaluations of early commercial jet transports depended heavily on experience, engineering judgment, and tests during the design and analysis process. As technology progressed and competitive pressures for long-life economic structures increased, fatigue specialists were forced to apply more sophisticated analysis methods [2]. However, the timing of such evaluations was often incompatible with the detail design and drawing release process because fatigue evaluations involved time-consuming analyses and lacked visibility of key parameters. Logistics involved in managing large teams of engineers to effectively use cumulative design experience and apply disciplined fatigue methods prompted development of durability systems in the early 1970s. The key elements of such systems usually included

- Retention of test and service experience.
- Durability design guides.
- Quantitative fatigue analysis methods and allowables.
- Computerized and hand-check analysis procedures.

Industry durability systems serve as a corporate memory of past designs with highly visible key parameters, and provide the means of timely extension and transfer of experience to new design and/or operating usage. The result has been a transfer of the fatigue check responsibility from specialists to stress and design engineers who perform systematic checks as part of a total structural integrity evaluation.

Component and full-scale airplane fatigue tests have served well to validate fatigue analyses. The primary benefit of the fatigue test is leading the fleet in accumulated flight cycles for locating areas that might exhibit early fatigue problems. This fatigue testing also provides opportunities to develop and verify proposed inspection, maintenance, and repair procedures. In addition, full-scale fatigue testing verifies the absence of widespread damage due to metal fatigue. However, the test is not an alternative to inspections required by the basic maintenance program to ensure structural integrity over the life of an airplane in service.

Continued Airworthiness

Continuing airworthiness concerns about aging jet transports have received attention over the last 15 years [3]. Supplemental structural inspection programs were developed in accordance with damage tolerance concepts in the late 1970s to address fatigue crack detection in airplanes designed to the fail-safe principles. Damage at multiple sites was also addressed in terms of dependent damage-size distributions in relation to assumed lead cracks in different structural members. Structural audits were performed in the mid 1980s to ascertain whether these supplemental inspection programs addressed independent multiple site damage in similar structural details subjected to similar stresses. The safe-decompression concepts were challenged in these reviews of different manufacturer damage tolerance philosophies, but no major changes occurred.

Extensive industry actions were initiated in 1988 to address aging fleet airworthiness concerns prompted by the explosive decompression of a 737 over Hawaii. Model-specific structures working groups were formed, and five initiatives were developed within and across models and throughout the industry. The cooperative achievements have been impressive, in accomplishing five original tasks chartered by the Airworthiness Assurance Working Group (AAWG), as shown in figure 7.

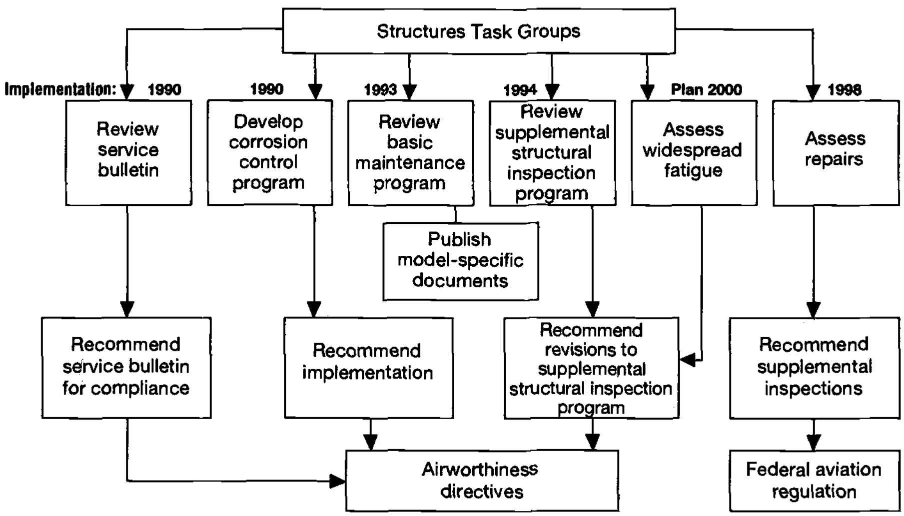

FIG. 7—*Continued Airworthiness Industry Initiatives*

Service bulletins are issued to address a known cracking event that has occurred in the operating fleet. These bulletins define inspection procedures, but may recommend modification/rework that would eliminate the problem. These were reviewed, and recommendations for mandatory incorporation were made.

While corrosion has always been recognized as a major factor in airplane maintenance, each airline has addressed it differently, according to its operating environment and perceived needs. Manufacturers have reviewed and published corrosion-prevention manuals and guidelines to assist the operators, but until now there have never been mandatory corrosion-control programs.

Supplemental structural inspection programs were initiated soon after damage tolerance regulations were enacted in the late 1970s. Their purpose was to ensure continued safe operation of the aging fleet by timely detection of new fatigue-damage locations. In the light of current aging fleet concerns, these inspection programs were reviewed and updated to ensure adequate protection.

Airplanes are susceptible to damage and are inevitably repaired many times in service. The manufacturer provides considerable guidance in the form of structural-repair manuals and instructions for specific damage. Traditionally, these repairs have met static strength, durability and fail-safe criteria. The industry developed a program for consistent guidelines for evaluating and maintaining damage tolerance of the structure.

While multiple-site concerns were addressed in the updates of Supplemental Structural Inspection Programs (SSIP), a sixth industry initiative was chartered in 1991 to identify potential widespread fatigue damage (WFD) before it occurred in the commercial fleet. Widespread fatigue damage in a structure is characterized by the simultaneous presence of cracks at multiple structural details that are of sufficient size and density whereby the structure will no longer meet its damage tolerance requirement. Dependent types of multiple-site damage (MSD) and multiple-element damage (MED) that are within the extent of existing damage tolerance regulation are labeled "local." The concern for widespread fatigue damage thus exists for large regions of similar structural details with similar high stress levels. Considerable activities were undertaken by AAWG to address WFD concerns and recommended alternate means of ensuring that the fleet is free from widespread cracking. These activities have resulted in comprehensive reports and formation of industry/operator/regulatory agency teams to develop recommendations for audits of structures with regard to WFD and recommended inspection/modification programs.

Conclusions

As technology and service experience have expanded in the aviation industry, structural integrity criteria have evolved to produce structure with an excellent safety record. Each new principle continues to supplement established technology based on years of experience. It was recognized that static strength, safe-life, fail-safe and damage tolerance principles each have some inadequacies and that a combination of all four philosophies is needed in some cases. Fracture mechanics enabled analysts to more accurately predict residual strength and crack growth characteristics for structural details. However, experience has taught the industry that the incorporation of fail-safe design features is the cornerstone for achieving damage tolerant structure. Each successive advancement in the evaluation of structural integrity is applied with the successful achievements that have been learned in the past. Thus, structural integrity criteria is an evolution of principles based on proven experience and implemented through one or a combination of regulations, proprietary criteria, and industry action. The result has been a steady improvement in the fleet safety record, as shown in figure 8.

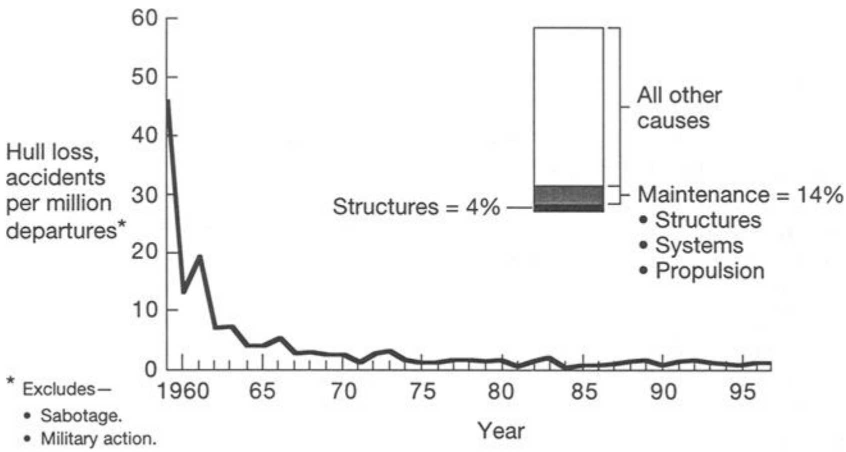

FIG. 8—*Jet Fleet Safety Record*

References

[1] *Federal Aviation Regulations, Part 25 - Airworthiness Standards: Transport Category Airplanes*, Federal Code of Regulations.

[2] Goranson, U. G., et al., *"Long Life Damage Tolerant Jet Transport Structures,"* ASTM Special Technical Publication 71, American Society for Testing and Materials Fatigue and Fracture Resistant Structures, Bal Harbour, Florida, November 1980.

[3] Goranson, U. G., *"Damage Tolerance: Facts and Fiction,"* 17th Symposium of the International Committee on Aeronautical Fatigue (ICAF), Stockholm, Sweden, June 1993.

Christoph S. Wiesner[1], Stephen J. Garwood[2] and J. Barry Denham[3]

THE SPECIFICATION OF CRACK ARREST PROPERTIES FOR STORAGE TANKS: BACKGROUND AND RECOMMENDATIONS

REFERENCE: Wiesner, C. S., Garwood, S. J., and Denham, J. B., **"The Specification of Crack Arrest Properties for Storage Tanks: Background and Recommendations,"** *Effects of Product Quality and Design Criteria on Structural Integrity, ASTM STP 1337,* R. C. Rice and D. E. Tritsch, Eds., American Society for Testing and Materials, 1998.

ABSTRACT:
Existing storage tank fracture prevention design criteria aim at the avoidance of fracture initiation. However, catastrophic failures have shown that the avoidance of crack initiation can never be guaranteed in any absolute sense. Consequently, European specifications increased initiation toughness requirements to reduce further the risk of failure and modified tank design concepts to alleviate the consequences of failure. It could be argued on safety and economic grounds that the use of crack arrest concepts for storage tanks may be the better option. In the present paper, the comparison of a collection of structurally representative large-scale test results with small-scale material characterisation tests shows that there is now a wealth of data available supporting the use of the 'Pellini' drop-weight test as a proxy for structural crack arrest behaviour, which is therefore recommended as design criterion for crack arrest during storage tanks fabrication. It is noted that, for a complete structural integrity evaluation of storage tanks, it is necessary to also consider the ductile tearing stability of long arrested cracks.

KEYWORDS: Storage tanks, crack arrest, design criteria, fracture avoidance, drop-weight test.

Introduction

Existing European and US low temperature storage tank design criteria for the prevention of brittle failures aim at the avoidance of fracture initiation. The Charpy V notch test is used as a proxy for initiation toughness and is specified in the relevant fabrication standards, such as API 620, BS 7777 and the forthcoming European storage tank code.

[1] TWI, Abington Hall, Abington, Cambridge, CB1 6AL, UK
[2] TWI, present address: Rolls Royce and Associates, PO Box 31, Derby, DE24 8BJ, UK
[3] Retired (formerly with British Petroleum Co plc), Oxton House, 66 Towers Road, Cheshire, SK12 1DE, UK

Although failures have been, fortunately, rare, a number of catastrophic failures in the 1970s has shown that the avoidance of crack initiation can never be guaranteed in any absolute sense. These failures also demonstrated that the consequences of releasing large quantifies of liquefied hydrocarbon gases into the environment can be devastating in terms of loss of life and of capital plant. The reaction to these events was the start of a marked divergence in the design of low temperature tanks between Europe and USA. API 620 has changed little since then whilst BS 7777 has incorporated the concepts of single, double and full containment and some increase in fracture initiation toughness to reduce further the risk of failure as well as the consequences of failure. However, many saw the provision of crack arrest capability of the primary container as the better option.

If crack arrest concepts are combined with the fracture initiation avoidance philosophy, additional safety can be ensured, which is especially important for accidental circumstances. It is surprising that the extensive research and testing programmes of the 1980s to investigate crack arrest for storage tanks, led by the US Gas Research Institute programme [*1*] has not resulted in more active usage in the USA, and only in recent years is beginning to be seriously pursued by European operating companies.

This paper outlines the background of existing, fracture-related storage tank design criteria; reviews application of crack arrest concepts to storage tanks and the demonstration of crack arrest capability of primary containment materials by structurally representative large-scale tests; and presents the wealth of data now available supporting the use of the 'Pellini' drop-weight test as a proxy for structural crack arrest behaviour. Finally, it gives recommendations as to how to specify crack arrest properties for steels aimed at storage tanks fabrication.

Existing Storage Tank Fracture Requirements

Background

Because of the consequences of a catastrophic failure of storage tanks, an essential consideration in the design and operation of tanks, particularly those operating at low temperatures, is the avoidance of the possibility of brittle failure. The specification of material requirements to minimise this risk, for both carbon steel tanks operating at low temperatures (generally considered to be at or below 0°C), and when using alloy steels which are selected for operation below -50°C, is therefore an essential part of all relevant specifications.

Fabrication codes began to be developed by the American Society of Mechanical Engineers (ASME, founded 1880), in response to the high incidence of boiler explosions in the US at the turn of the century. The avoidance of failure in the majority of codes is achieved by reducing stress concentrations, minimising the incidence of flaws, and specifying adequate toughness to prevent initiation of fracture. The toughness requirements of carbon and C-Mn steels have their origins in studies on welded ship casualties after the Second World War [*2*]. A Charpy energy of 20J in plate material seemed to minimise the risk of failure. To improve margins of safety, 27J became a common specification for low strength steels at ambient temperature. These recommendations were carried over into the pressure vessel and storage tank industries;

however, a spate of brittle failures of vessels and tanks under hydrotest in the UK in the late 1950s and 1960s (e.g. [3]) led to recognition of the influence of material thickness, and residual stresses on the risk of brittle fracture.

In the search of a more quantitative approach to material selection in pressurised components, a series of wide plate tests was commissioned by UK industry at the British Welding Research Association (the forerunner to TWI) in the early 1960s [4]. These tests on 1 metre by 1 metre square panels were conducted with notches, located transverse to a weld, of length approximately equivalent to a 10mm through-thickness crack. The requirement set for adequate performance, was the achievement of 0.5% plastic strain as measured across a gauge length of between 20 and 39 inches (500 to 760mm). Materials with different Charpy properties were tested at various temperatures in the as-welded condition, in addition to unwelded plate. The temperature at which 0.5% plastic strain was achieved was then defined by these tests. These results, together with engineering practice current at the time, were drawn together to derive operating temperature/impact test temperature/material thickness relationships, know as design lines. A Charpy requirement for steels allowed by the standard was set at 27J for material with an ultimate strength <450N/mm^2 and 40J for higher strength levels. For plate materials, these requirements were related to the Charpy properties in the longitudinal orientation.

Following the establishment of the design lines concept in BS 1515:Part 1, Appendix C in 1965, various revisions occurred, leading to the publication of BS 5500:1979 Appendix D 'Recommended practice for carbon and carbon manganese steel vessels required to operate at low temperature'. With continued research, and in particular further surveys of wide plate results, Appendix D was revised in 1989 and became mandatory. The background to the latest requirement have been given by Garwood and Denham [5].

Approaches for Storage Tanks

The oil industry has a long tradition of developing standards for storage tanks particularly through the American Petroleum Institute (API). The API 12C and successor API 650 standards have long been recognised around the world for the construction of oil storage tanks and even European equivalents like BS 2654 have their origins with respect to design in the API standards. API was also the first to develop specific requirements for LPG and LNG tanks using AP 620 as the base and adding appendices R & Q, respectively. Again, British Standards followed in the wake of these API developments with BS 4741 for refrigerated gases down to -50°C and BS 5287 for temperatures down to -196°C.

The material toughness specifications of British and API standards for the construction of oil storage tanks are based on Charpy requirements derived from experience with ships and the specifications developed for pressure vessels. The fracture toughness design lines of BS 2654 are deviates of BS 5500 Appendix D, although various criteria have influenced the reason for differences between the two British codes. Firstly, storage tanks are subjected to different proof test conditions; secondly, the construction of tanks can ensure that all plates are oriented such that the major stress axis is parallel with the longitudinal properties of the plate; and lastly, the thickness of the plate varies with the height of the tank in proportion to the loading experienced. European code developments for atmospheric storage tanks are under consideration by CEN TC/265. However, in the wake of the failure of the LPG tank at the QGPC NGL plant at Umm Said, Qatar on 3 April 1977, which led to the complete destruction of the plant by fire and the loss of seven lives, the development of double and full containment designs became dominant and overtook these standards.

The Engineering Equipment & Materials Users Associated (EEMUA), a UK based trade organisation of major user companies, formulated new rules for refrigerated tanks with the assistance of major UK designer/constructor companies. These were published as EEMUA 147 and were widely adopted for application around the world.

As outlined by Denham [*6*], requirements for refrigerated tanks have developed via EEMUA 147, which has evolved into BS 7777. In these specifications, C-Mn steels are restricted to operation down to -35°C. Below this temperature, low nickel, 9% nickel and austenitic steels are required for single containment tanks for liquid propane (-50°C), ethane (-105°C) and nitrogen (-196°C) operations, respectively. For double containment tanks, improved toughness C-Mn steels can be used down to -50°C, and 9% nickel steels to -165°C. Improved 9% nickel or austenitic steels must be used below -105°C if the plate thickness exceeds 30mm, however. All requirements are based on Charpy tests to prevent fracture initiation. BS 7777 adopts a temperature shift (ΔT) concept to allow for the possibility of degradation of Heat Affected Zone (HAZ) properties for certain steel types. This is designed to ensure a HAZ value of 27J at the design temperature for all production welds.

Crack Arrest Considerations

Philosophy

In the past ten years or so, it became clear that despite considerable effort, the prevention of crack initiation could not be guaranteed in any absolute sense. This is especially so for welded steel structures in which weld flaws, locally embrittled regions, geometric stress concentrations and welding residual stresses can combine to make crack initiation a distinct possibility. The crack arrest approach is especially useful for strategic applications, such as storage tanks, where additional integrity is required because of the dramatic consequences of failure. Alternatively, the use of crack arresting steels would allow considerable cost saving if double or full containment designs, which have become the norm following the Qatar failure in 1977, could be replaced by single containment tanks made from crack arresting steels. This possibility had already been recognised in 1986 by Cotton and Denham [*7*], but has not yet been accepted universally, although some operators use a crack arrest approach in addition to the fracture initiation avoidance concept.

For crack arrest to occur, the materials used must have a sufficient so-called crack arrest toughness to ensure that brittle, fast propagating cracks, initiated in regions of low toughness and/or high stress, are arrested when they emerge from the critical zone. One advantage from a practical point of view is that attention can be withdrawn from the microscale (i.e. from the local brittle zone and the local stress concentration) and refocused onto the intermediate scale (i.e. the properties of the parent plate, weld metal, or heat affected zone, and the nominal applied stress). A related advantage is the extra security that this approach gives against unforeseen conditions.

Much of the early work was carried out in naval laboratories in the UK and in the USA and was concerned with determining the conditions for crack arrest. Other industries were also interested in crack arrest (for storage tanks, nuclear pressure vessels and pipelines), but the fracture initiation approach to structural integrity was also being developed and became dominant. Two primary reasons for this were that fracture initiation conditions were inherently simpler to define and there was a significant cost-penalty associated with steels capable of arresting fast running cracks. With the development of modern steels, designing for crack arrest has become an economically viable option, especially if their use would facilitate design simplifications.

Crack Arrest Concepts for Failure Prevention in Storage Tanks

Because storage tanks can operate at low temperatures and the consequences of possible failures are serious, fracture prevention has always been an important issue in the design and construction of large storage tanks. Nevertheless, failures have occurred. However, it is postulated that most of these could have been avoided if the constructions were made from steels with the ability to arrest cleavage cracks under the relevant conditions. Therefore, a number of recent research efforts have been directed to the applicability of crack arrest concepts to the failure prevention in storage tanks.

One example of crack arrest methods applied to storage tank structures has been to carry out tests to simulate the escape of cold gas from a through-thickness crack in an outer containment tank [*8*]. Local cooling causes thermal stresses which can lead to crack initiation. However, it was demonstrated that the crack was arrested in the warmer surrounding regions exhibiting increased crack arrest fracture toughness.

Willoughby and Kawaguchi [*9*] discussed test requirements and analyses for obtaining crack arrest of long, fast running cracks in storage tank structures. They concluded that arrest of long cracks requires the consideration of both arrest conditions and the subsequent stability of the cracks, i.e. whether or not they will continue to propagate by a stable tearing mechanism. The latter mechanism was identified as the limiting factor for a 2.5%Ni steel for typical tank geometries. The need for resistance to ductile tearing following crack arrest was also recognised by Tanaka et al. [*10*] who presented an integrated safety assessment for storage tanks using fracture initiation prevention, crack arrest and ductile tearing stability concepts.

In a major co-operative research programme, funded by the GRI [*1*], the ability of 9%Ni steels and welds to arrest cracks initiated at weld flaws in liquified natural gas (LNG) storage tanks was investigated. In a contribution to this project, Kanninen et al.[*11*] showed that even the lowest toughness materials were able to arrest cracks of up to 300mm in length at LNG temperature.

Crack Arrest Testing

Crack arrest experiments may be divided in three groups: (i) large-scale, structurally representative tests, (ii) small-scale tests which correlate empirically with crack arrest properties to be used as design criteria and (iii) fracture mechanics based crack arrest toughness tests.

Large-scale experiments are carried out to model the geometry and the loading of the actual structure as closely as possible. If the test set-up is such that conditions representative of the actual structure can be achieved, the experiment can be described as 'structurally representative'. The most common large-scale experiments are wide

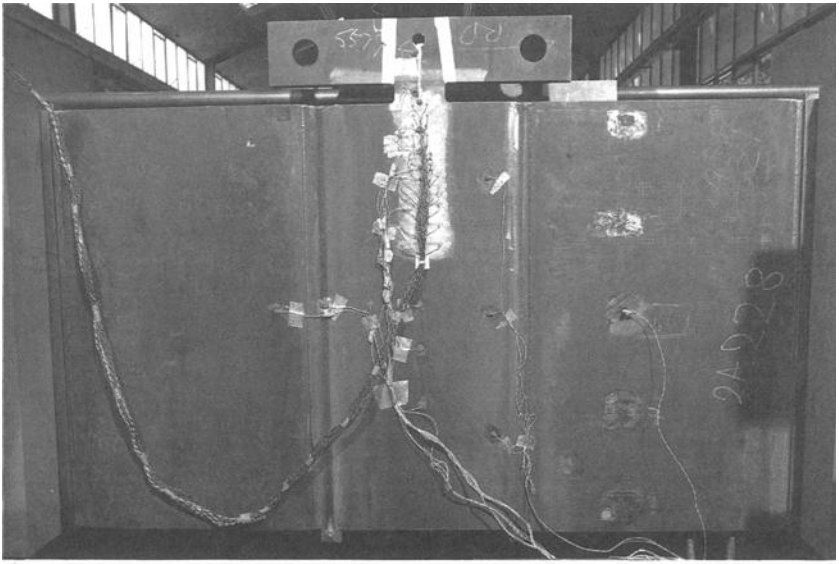

500mm

Fig. 1 Double Tension Crack Arrest Wide Plate Test

plate tests such as the Robertson, ESSO, double tension and short crack arrest (SCA) tests. An example of a double tension test plate, as used by TWI, is shown in Fig.1.

In isothermal wide plate tests, the main test section is cooled to the temperature and loaded to the stress level of interest. A running crack is then initiated into the edge or surface of the plate in a crack starter region which is embrittled by local cooling or by various welding methods. The test result is a statement whether, at a given combination of applied stress, length of crack starter region and temperature, the running brittle crack is arrested when it enters the test section proper or not. The lowest temperature at which arrest occurs is termed the crack arrest temperature (CAT).

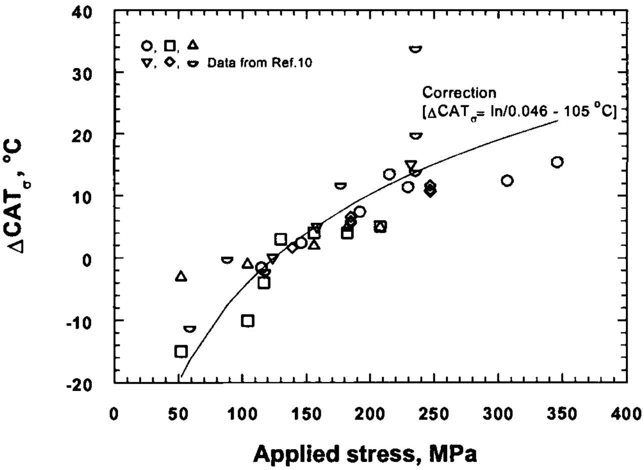

(a)

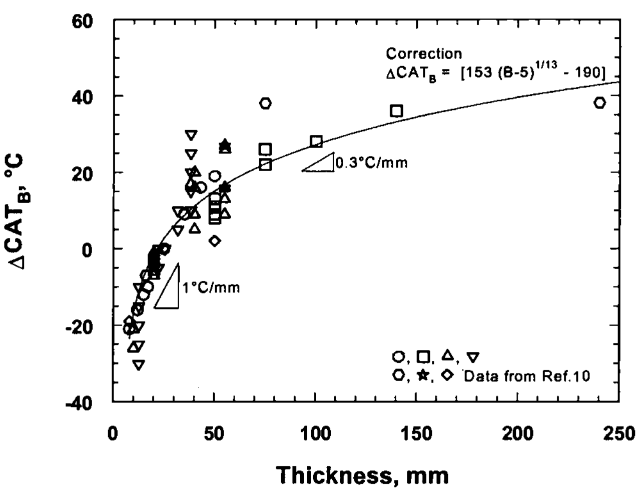

(b)

Fig. 2 Effect of Stress Level (a) and Thickness (b) on the Crack Arrest Temperature (CAT)

The CAT is affected by the thickness of the test plate or component, and the applied stress, as is evident from the collection of large-scale results shown in Fig.2. This CAT concept of crack arrest is consistent with a fracture mechanics approach to crack arrest in that the CAT is the temperature for which crack arrest will take place at a given applied stress intensity factor or, alternatively, for which the crack arrest toughness value has a given value (typically 70 to 150MPa√m) [*13,14*]. A distinct advantage of the CAT approach is that it can be correlated with other transition temperatures from small-scale material characterisation tests, as will be shown in the following.

All large-scale tests mentioned above can be employed to obtain information on structurally representative crack arrest behaviour. Because of their cost, these tests are nowadays normally employed as validation tests for fracture assessment purposes or to establish correlation with standardised small-scale tests.

Prediction of Crack Arrest Temperature Using Small-Scale Tests

To predict crack arrest properties on a day-to-day basis, cost effective small-scale tests are required, such as the well known Charpy and 'Pellini' drop-weight tests.

Regarding the Charpy test, it has been shown [*12,15*] that, although rough estimates of crack arrest properties can be made using Charpy V-notch transition temperatures, the inherent scatter in the results is considerable. The main factor producing the large scatter in correlations between Charpy properties and crack arrest behaviour is that the Charpy energy is a measure of both crack initiation and crack propagation behaviour. More recently, instrumented Charpy tests have been carried out to separate the initiation and propagation stage in the tests, and improved correlations were obtained between measures of the instrumented Charpy and crack arrest tests [*12,16,17*].

However, whilst the development of instrumented Charpy testing is ongoing, the most suited simple small-scale tests to characterise crack arrest behaviour available at present is the 'Pellini' drop-weight test, as specified in (ASTM E208) "Test Method for Conducting Drop-Weight Test to Determine NDTT of Ferritic Steels". The drop-weight test specimen consists of a rectangular coupon with a brittle weld bead deposited on one face. The weld contains a notch, from which a crack is initiated by impact loading the specimen to a fixed amount of deformation under three point bend. Tests are carried out at a variety of temperatures, the nil-ductility transition temperature (NDTT) being defined as the maximum temperature at which the brittle crack spreads completely across one or both of the tension surfaces on either side of the brittle weld bead. The test is also suitable for testing weld metal and heat affected zone (HAZ) by carefully placing the notch in the weld bead over the region of interest. An example of crack propagation along the HAZ of a submerged arc weld in a structural steel is shown in Fig.3.

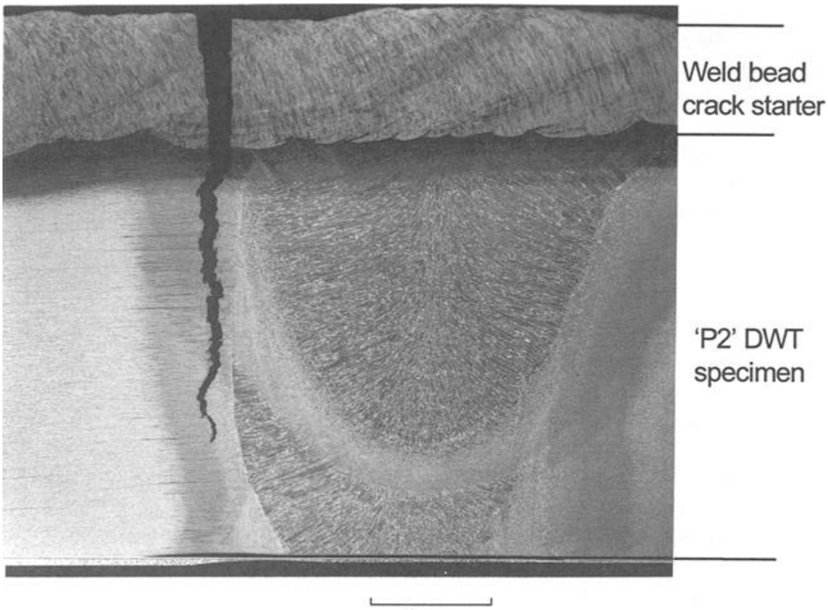

Fig.3 Application of Drop-Weight Testing to HAZ: Longitudinal Section Through Weld Bead Crack Starter

Correlations were established between the CAT and the NDTT throughout the 1960s and 1970s which showed that CAT equals approximately NDTT + 30°C, however, substantial scatter was also apparent. Smedley [*18*] and Wiesner [*12*] suggested semi-empirical corrections for CAT, with respect to the effect of plate thickness and applied stress (see Fig.2 for comparison between correction terms and experimental results):

i. CAT = [NDTT + 10] for 25mm thick plate and an applied stress of 124MPa;
ii. $\Delta CAT_\sigma = [\ln\sigma/0.046 - 105]$, correction for applied stress, σ, (Fig.2a);
iii. $\Delta CAT_B = [153\,(B - 5)^{1/13} - 190]$, correction for plate thickness, B, in the range B = 5 to 250mm (Fig.2b).

Thus:

$$CAT = [NDTT + 10] + [\ln\sigma/0.046 - 105] + [153\,(B - 5)^{1/13} - 190] \quad (1)$$

(CAT and NDTT in °C, σ in MPa and B in mm)

The application of this predictive equation to estimate the structurally representative CAT from measured NDTT values and comparison with a comprehensive data base of experimental results, showed that the CAT, for a large number of steels, can be predicted from NDTT within ± 15°C, see Fig.4, over a wide range of temperatures.

Although Eq.1 provides an accurate estimation scheme for CAT from NDTT, it would be desirable in the design and feasibility stages of a storage tank project to have a simpler relation to estimate crack arrest properties from material characterisation tests.

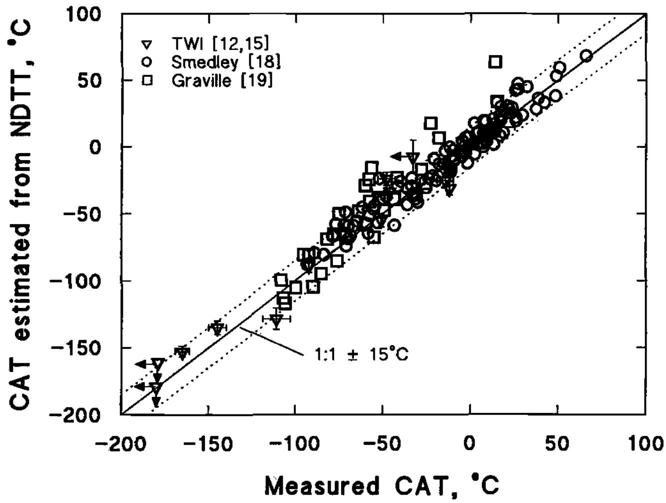

Fig. 4 Comparison of Estimated (Eq. 1) With Measured CAT

simpler relation to estimate crack arrest properties from material characterisation tests. Previous work [*12,15*] has shown that for typical design conditions of storage tanks, the crack arrest temperature can be safely approximated by:

$$\text{CAT} = \text{NDTT} + 40°\text{C} \tag{2}$$

To further validate this relation, all structurally representative CAT data available to the authors were plotted directly against NDTT (Fig.5). It is obvious that the vast majority of results lie below the NDTT + 40°C line. (It should be noted that the data by Kawaguchi and Willoughby [*22*] are ranges of possible CATs as determined in 'go'/'no-go' double tension tests and that arrest was achieved at the lower limit of the band shown, so that the NDTT + 40°C relation is not put into question by these results).

Recommended Design Criterion for Crack Arrest

Crack arrest in storage tanks can be ensured provided that the minimum operation temperature is higher than the highest CAT determined on the storage tank materials, including weld metal and HAZ. The CAT of the storage tank materials can be determined by carrying out large-scale crack arrest tests, or it can be estimated from the NDTT determined in 'Pellini' drop-weight tests (see previous Section).

Equation 1 can be used to calculate required NDTT values when applied stresses and the thickness is known. For instance, consider a LPG storage tank with a minimum operating temperature, T_{min}, of -50°C. The thickness of interest is assumed to be 40mm, the maximum applied stress during operation is assumed to be 180MPa (approximately

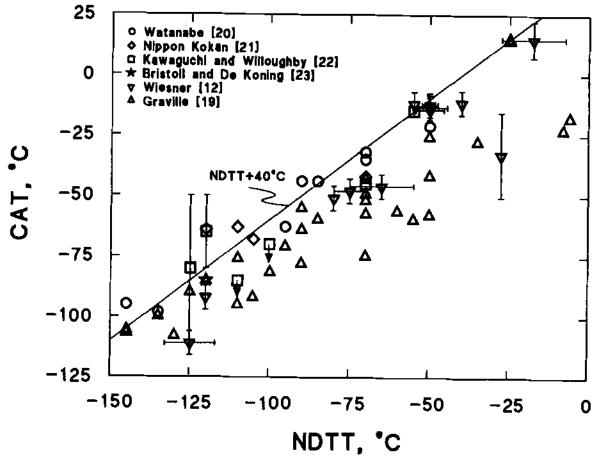

Fig. 5 Crack Arrest Temperatures (CAT) From Structurally Representative Tests Versus the Nil-Ductility Transition Temperature (NDTT)

half the yield strength of a medium strength steel. Equation 1 can be rearranged to give:

$$NDTT_{required} = CAT - 10 - [\ln\sigma/0.046 - 105] - [153\,(B - 5)^{1/13} - 190] \qquad (3)$$

with CAT = T_{min} = -50°C, σ= 180MPa and B = 40mm it follows that
$NDTT_{required} = (T_{min} - 29°C) = -79°C$

A somewhat more conservative result would be achieved by rearranging Eq. 2:

$$NDTT_{required} = CAT - 40°C \qquad (4)$$

with CAT = T_{min} = -50°C it follows that
$NDTT_{required} = (T_{min} - 40°C) = -90°C$.

It can be seen that for typical LPG conditions and assuming an upper bound thickness of 40mm, Eq.4 is about 10°C more conservative for the set of conditions considered. For lower applied stresses and thinner plate, the use of Eq.3 would result in even warmer NDTT requirements, in the range of (T_{min} -15°C) to (T_{min} -25°C).

Whatever relation is used, the data presented provide ample empirical evidence that the 'Pellini' drop-weight test can be used as a proxy for structural crack arrest behaviour. In fact, recent computational studies [*14*] have shown that the CAT = NDTT + 40°C relationship can be reconciled with fracture mechanics principles in that NDTT +40°C is the approximate temperature, where the brittle crack in the 'Pellini' drop-weight specimen arrests immediately after emerging from the crack starter weld bead. The crack arrest toughness associated with that crack shape is between 70 and 150MPa$\sqrt{m}$ which compares very favourably with arrest toughness results obtained at NDTT +40°C in structurally representative tests, see Fig.6.

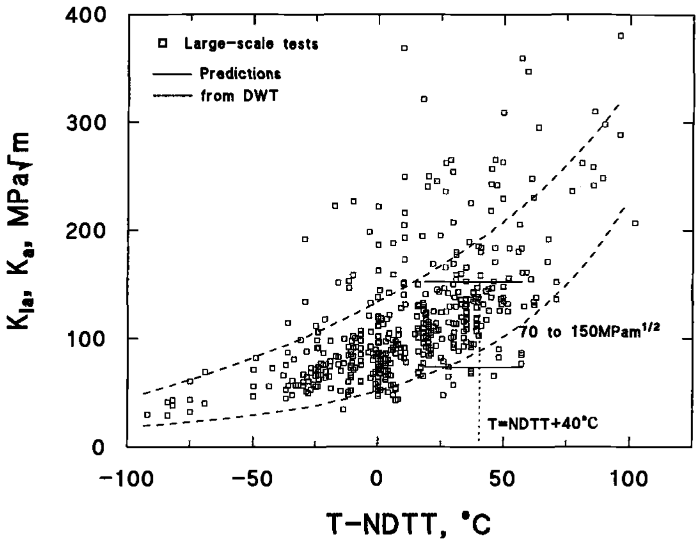

Fig. 6 Collection of Crack Arrest Toughness Transition Curve Data From Structurally Representative Tests [24], Compared With Predictions From Drop-Weight Tests at NDTT +40°C.

In view of the above, guidance has recently been drafted to be considered as an informative appendix for CEN TC265 for the use of steels with crack arresting properties [*25*]. The guidance is based on the 'Pellini' drop-weight test, and steels and their weldments are assumed to be able to arrest brittle cracks if their NDTT is 40°C lower than the minimum design temperature of the storage tank under consideration.

For LNG tanks, the minimum design temperature of about -162°C would necessitate an NDTT of -202°C. This temperature is difficult to achieve by most test laboratories. However, if a clear 'no break' result is achieved during drop-weight testing at liquid nitrogen temperature(-196°C), the implication is that the NDTT will be at least -201°C (possibly lower), since the test protocol in ASTM E208 requires steps of 5°C and NDTT is the lowest temperature where a 'break' is recorded. The difference of 1°C between required and demonstrated NDTT is small enough to be compensated by the inherent conservatism to Eq.2. In fact, applying Eq.3 to typical conditions for LNG tanks would give a required NDTT of only -191°C.

The consideration of crack arrest concepts to enhance existing design criteria for storage tanks based on the 'Pellini' drop-weight test is not part of existing European (e.g. BS 7777) or US (API 620) specification. Although it may be possible to develop correlations between Charpy transition temperatures and NDTT so that Charpy values could be as a proxy, it should be borne in mind that these two tests are different. The measured Charpy energy includes both components of crack initiation (which is known to depend critically on the cleanness of a steel) and crack propagation. The NDTT, on the other hand, is a measure of the crack propagation resistance. This means that Charpy

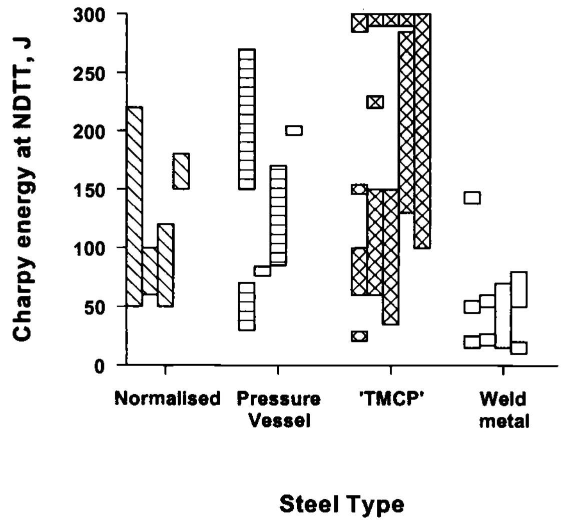

Fig.7 Charpy Energy Levels Determined at NDTT For Various Parent Steels and Weld Metals

versus NDTT correlations are suspect and subject to change for new steel developments. A demonstration of the wide range of Charpy energies determined at NDTT for different types of modern parent steel and weld metal is shown in Fig.7.

Whilst the NDTT in 1940s to 1960s steel used to define the onset of the Charpy brittle to ductile transition temperature corresponding to Charpy energy levels of about 10 to 30J, it can lie on the upper shelf of the transition curve for modern clean steels. This is especially the case for some of the thermomechanically processed steels (designated TMCP in Fig.7). Whilst the specification of a Charpy energy of, say, 27J for older, less clean steel, possibly meant that this requirement subsumes the requirement of NDTT at a similar test temperature, the NDTT for modern steel can be considerably higher than the 27J Charpy energy transition temperature. This trend has also been confirmed by comparing structurally representative crack arrest tests directly with Charpy results [*12*].

As mentioned previously, the shortcomings of conventional Charpy testing may be overcome by carrying out instrumented Charpy experiments [*12,16*] and these may be able to replace drop-weight testing following further validation.

Before concluding, it should be noted that, for a comprehensive structural integrity assessment of storage tanks, the requirement of crack arresting steels for primary containment material should be complemented by an analysis of the tearing stability of the arrested cracks (as mentioned before [*9,10*]), and also by a fluid flow analysis of the product loss rate from the arrested crack [*26*].

Conclusions

From the data presented, it is concluded that a more encompassing approach to storage tank integrity than the prevention of fracture initiation alone would be to include crack arrest requirements. The use of 'Pellini' drop-weight testing to determine the nil-ductility transition temperature (NDTT) is recommended for quality assurance purposes since a large database has demonstrated that NDTT +40°C can be used to make safe estimates of the crack arrest temperature (CAT) of ferritic steel for conditions typical of storage tanks. For modern steels it has been shown that Charpy transition temperatures are unsuitable as proxy for the NDTT. Large-scale crack arrest testing is recommended to validate the correlation between CAT and NDTT for new steel developments. The need to consider ductile tearing stability for long arrested cracks is noted.

References

[*1*] Stout, P.E. and Wiersma, S.J., "Crack Arrest Properties of 9%Ni Steels Used in LNG Storage Vessels," *Proc. Conf. Fracture Safe Design for Large Storage Tanks*, The Welding Institute, 1986, pp. 169-178.

[*2*] Hodgson, J. and Boyd, G. M., *Irons Institute of Naval Arch,* Vol. 100, 1958 p. 141

[*3*] Hayes, B., "Classic brittle failures in large welded structures" and "Six case histories of pressure vessel failures," *Engineering Failure Analysis,* Vol. 3, Nos.2 and 3, 1996, pp. 115-127 and 157-170.

[*4*] Woodley, C. C., Burdekin, F. M., and Wells, A. A., "Mild Steel for Pressure Equipment at Sub-zero Temperatures," *British Welding Journal,* March 1964, pp. 123-136.

[*5*] Garwood, S. J. and Denham, J. B., "The Fracture Toughness Requirements of BS 5500," *ASME PVP Conference*, Paper 88, 1988.

[*6*] Denham, J. B., "LPG & LNG Storage Tanks - Developments in Design and Construction," *Proc. Conf. Bulk Storage Tank Conference,* Abu Dhabi, March 1995.

[*7*] Cotton, H. C., and Denham, J. B., "A review of developments of fracture safe designs and codes for Oil and LPG storage tanks," *Proc. Conf. Fracture-Safe Designs for Large Storage Tanks,* The Welding Institute, 1986, pp. 41-58.

[*8*] Fearnehough, G.D., "Progressive Crack Extension due to Local Cooling of a Crack in LNG Storage Tank Material," *International Journal of Pressure Vessels & Piping, Vol.* 19, (1985), pp. 283-292.

[*9*] Willoughby, A. A., and Kawaguchi, Y., "Arrest of long cracks in storage tanks," *Proc. Conf. Fracture Safe Design for large storage tanks,* The Welding Institute, 1986, pp. 137-150.

[*10*] Tanaka, K., Sato, M., and Ishikawa, T., "Integrated safety assessment of large storage tanks," *Nippon Steel Technical Report*, January, 1987, No. 32, pp. 37-43.

[*11*] Kanninen, M.F., Dexter, R.J., Polch, E.Z., and Popelar, C.H., "The Analysis of Crack Propagation and Arrest in Welded LNG Storage Tanks," GRI Report GRI-86/0006, Gas Research Institute, 1986.

[*12*] Wiesner, C. S., "Predicting Structural Crack Arrest Behaviour Using Small-scale Material Characterisation Tests," *International Journal of Pressure Vessels & Piping*, Vol. 69, 1996, pp. 185-196.

[*13*] Wiesner, C. S., Hayes, B., Smith, S. D., and Willoughby, A. A., "Investigations into the Mechanics of Crack Arrest in Large Plates of 1.5%Ni TMCP Steel," *Fatigue Fracture Engineering Material Structure,* Vol. 17, 1994, pp. 221-233.

[*14*] Wiesner, C. S. and Smith, S. D., "Investigations into the 'Pellini' drop-weight test for characterising structural crack arrest behaviour," *Proc. Conf. ECF11,* EMAS, 1996, pp. 2013-2018.

[*15*] Wiesner, C. S., Hayes, B., and Willoughby, A. A., "Crack Arrest in Modern Steels and their Weldments - Comparison Between Small and Large-scale Experiments," *International Journal of Pressure Vessels & Piping,* Vol. 56, 1993, pp. 369-38.

[*16*] Berger, C., Ewald, J., Wiemann, W., and Wojaczyk, H-G., "Ermittlung von Sprödbruch und bruchmechanischen Kennwerten Mittels Kerbschlagproben". *Proc.Conf. Sitzung DVM AK Bruchvorgänge*, pp.182-195, DVM, 1979 (in German).

[*17*] Planman, T., Wallin, K., and Rintammaa, R., "Comparison of some indirect measures of crack arrest," *Proc. Conf. Crack Arrest Concepts for Failure Prevention and Life Extension,* Paper 6, Abington Publishing, 1996.

[*18*] Smedley, G. P., "Prediction and specification of crack arrest properties of steel plate," *International Journal of Pressure Vessels & Piping,* Vol. 40, 1989, pp. 279-302.

[*19*] Graville, B. A., "Crack Arrest requirements for arctic structures," Graville Associates Inc. Report, March 1989.

[*20*] Watanabe, I., "Thermo-mechanically controlled rolled steels and their properties," *Proc. Conf. Fracture Safe Designs for Large Storage Tanks,* The Welding Institute, 1986, pp. 195-204.

[*21*] Anon, , "EH36 MOD Steel Plates Produced by OLAC for Arctic Marine use Structures", *Nippon Kokan K. K. Technical Bull. No. 242-031,* Nippon Kokan, Tokyo, 1984.

[*22*] Kawaguchi, Y., and Willoughby, A. A., "Crack arrest tests and their use for evaluating material properties," *Proc. Conf. Fracture Safe Designs for Large Storage Tanks,* TWI, 1986, pp. 179-94.

[*23*] Bristoll, P., and de Koning, A. C., "Crack arrest capability of a controlled rolled, quenched tempered 3.5%Ni steel," *Proc. Conf. Fracture Safe Design for Large Storage Tanks,* The Welding Institute, 1986, pp. 151-68.

[*24*] Wiesner, C.S., and Hayes, B., "A Review of Crack Arrest Tests Models and Applications," *Proc.Conf. Crack Arrest Concepts for Failure Prevention and Life Extension*, Paper 3, Abington Publishing, 1996.

[*25*] BSI PV/1/18 proposal for amending CEN/TC265 Document N223, BSI, 1996.

[*26*] Kanninen, M.F. and Dexter, R.J., "Towards the Development of a Crack Arrest Fracture Mechanics Technology for Welded Storage Tank Integrity," *Proc. Conf. Weld Failure*, Paper 28, The Welding Institute, 1988.